

量子机器学习与信息处理
Quantum Machine Learning and
Information Processing

(申请清华大学理学博士学位论文)

培 养 单 位： 交叉信息研究院

学 科： 物理学

研 究 生： 沈 培 鑫

指 导 教 师： 邓 东 灵 助理教授

二〇二二年五月

Quantum Machine Learning and Information Processing

Dissertation submitted to

Tsinghua University

in partial fulfillment of the requirement

for the degree of

Doctor of Philosophy

in

Physics

by

Pei-Xin Shen

Dissertation Supervisor: Assistant Professor Deng Dong-Ling

May, 2022

答辩委员会名单

主席	于海峰	研究员	北京量子信息 科学研究院
委员	段路明	教授	清华大学
	孙麓岩	副教授	清华大学
	邓东灵	助理教授	清华大学
	宋祎璞	研究员	清华大学
	郑东宁	研究员	中国科学院 物理研究所
秘书	于立伟	助理研究员	清华大学

关于学位论文使用授权的说明

本人完全了解清华大学有关保留、使用学位论文的规定，即：

清华大学拥有在著作权法规定范围内学位论文的使用权，其中包括：（1）已获学位的研究生必须按学校规定提交学位论文，学校可以采用影印、缩印或其他复制手段保存研究生上交的学位论文；（2）为教学和科研目的，学校可以将公开的学位论文作为资料在图书馆、资料室等场所供校内师生阅读，或在校园网上供校内师生浏览部分内容；（3）根据《中华人民共和国学位条例暂行实施办法》及上级教育主管部门具体要求，向国家图书馆报送相应的学位论文。

本人保证遵守上述规定。

作者签名： _____

导师签名： _____

日 期： _____

日 期： _____

摘 要

量子力学为信息处理带来新的方法与机遇。近几年量子计算与机器学习的快速发展催生了一个新的研究前沿——量子机器学习。在这篇博士论文中，我们介绍了量子机器学习的架构优化，以及量子自旋链中的信息处理。

我们首先回顾了量子计算、凝聚态物理和机器学习领域的一些基本概念。随后我们介绍了量子机器学习中一些著名的量子算法和量子模拟技术。在嘈杂中等规模量子时代，搜索具有较小深度的、性能良好的量子线路对于量子机器学习实验演示至关重要。我们引入了一种量子神经进化算法，该算法可以自动地为不同的机器学习任务找到接近最优的量子神经网络。为展示此算法的优势，我们设计了一个量子分类器进行手写字体和拓扑态的识别。我们的结果展示了神经进化算法在量子架构搜索中的巨大潜力。

远距离无耗散地传输信息和能量是物理学的重要研究方向之一。我们详细讨论了一维量子 **Ising-XY-Ising** 自旋链的自旋输运。通过运用对称性分析、数值模拟和解析方法，我们揭示了几种与涌现的马约拉纳费米子有关的分数自旋约瑟夫森效应。我们进一步分析了自旋电流对自旋纠缠的影响。我们提出使用腔量子电动力学装置中的色散读出技术来探测自旋约瑟夫森效应。我们可以通过操控腔中的光子来进行量子信息处理。最后，我们展望了一些新的量子机器学习架构和算法。

关键词：量子机器学习；量子分类器；量子架构搜索；拓扑材料；腔量子电动力学

ABSTRACT

Quantum mechanics provides new methods and opportunities for information processing. Recent rapid developments in quantum computing and machine learning have spawned a new cutting-edge research frontier—quantum machine learning. In this doctoral dissertation, we introduce the architecture optimization for quantum machine learning, together with the information processing in quantum spin chains.

We first review some basic concepts in the field of quantum computation, condensed matter physics, and machine learning. We then introduce some renowned quantum algorithms and quantum simulation techniques for quantum machine learning. In the noisy intermediate-scale quantum era, searching a well-performing quantum circuit with a smaller depth is of crucial importance for the experimental demonstration of quantum machine learning. We introduce a quantum neuroevolution algorithm that autonomously finds near-optimal quantum neural networks for different machine learning tasks. To benchmark the effectiveness, we design a quantum classifier for the classification of both handwritten digits and topological states. Our results showcase the vast potential of neuroevolution algorithms in quantum architecture search.

The ability to transmit information and energy without dissipation over large distances is one of the important research directions in physics. We specifically investigate the spin transport through a one dimensional quantum Ising-XY-Ising spin link. Using a combination of symmetry analysis, numerical calculations, and analytical approaches, we have revealed several types of fractional spin Josephson effects that pertain to the emergent Majorana fermions. We further analyzed the entanglement between pairs of spins in the presence of spin currents. We proposed to use a cavity QED setup for detecting the spin Josephson effects by dispersive readout methods. This detection proposal could be used to control the quantum information processing through photons in cavity QED setups. Finally, we provide an outlook for some new architectures and algorithms of quantum machine learning.

Keywords: quantum machine learning; quantum classifier; quantum architecture search; topological materials; cavity quantum electrodynamics

TABLE OF CONTENTS

摘 要.....	I
ABSTRACT	II
TABLE OF CONTENTS	III
LIST OF FIGURES AND TABLES	VI
LIST OF SYMBOLS AND ACRONYMS	VIII
CHAPTER 1 PRELIMINARIES	1
1.1 Introduction	1
1.1.1 Background	1
1.1.2 Outline of the Dissertation	2
1.2 Quantum Computation.....	3
1.2.1 Qubits	4
1.2.2 Quantum Circuits.....	5
1.2.3 Physical Realization	6
1.3 Condensed Matter Theory.....	6
1.3.1 Quantum Spin Chains	7
1.3.2 Topological Band Theory	9
1.3.3 Jordan-Wigner Transformation.....	16
1.3.4 Exactly Solvable Models.....	19
1.3.5 Cavity Quantum Electrodynamics	21
1.3.6 Open Quantum Systems.....	23
1.4 Machine Learning	24
1.4.1 Supervised Learning	24
1.4.2 Unsupervised Learning.....	25
1.4.3 Reinforcement Learning.....	25
1.4.4 Artificial Neural Networks.....	27
1.4.5 Towards Explainability	36

TABLE OF CONTENTS

CHAPTER 2 QUANTUM MACHINE LEARNING IN THE NISQ ERA	37
2.1 Quantum Simulation in the NISQ Era	38
2.1.1 Analog Quantum Simulation	39
2.1.2 Digital Quantum Simulation	39
2.2 Quantum Algorithms for Machine Learning	40
2.2.1 Quantum Algorithms for Linear Algebra	41
2.2.2 Variational Quantum Algorithms	43
2.3 Quantum Artificial Neural Networks	45
2.3.1 The Expressibility	46
2.3.2 Barren Plateau	48
2.3.3 Adversarial Learning	49
CHAPTER 3 QUANTUM ARCHITECTURE SEARCH	51
3.1 Neuroevolution of Augmenting Topologies Algorithm	51
3.2 The Quantum Neuroevolution Algorithm	54
3.2.1 Algorithm Overview	56
3.2.2 The Scaling of the Gate-Block Library	59
3.2.3 Towards the High-Order Markovian Process	63
3.3 Performance Benchmark	64
3.3.1 Classification of Handwritten-Digit Images	64
3.3.2 Classification of Symmetry-Protected Topological States	66
3.3.3 Classification of Cancer Diagnostic Data	69
3.3.4 Parameter Settings	71
3.4 Discussion and Summary	72
CHAPTER 4 INFORMATION PROCESSING IN QUANTUM SPIN LINKS	73
4.1 General Properties of the Quantum Spin Chain	73
4.2 The Ising-XY-Ising Spin Link	76
4.2.1 Model Hamiltonian	77
4.2.2 The Spin Current Operator	78
4.3 Symmetry Analysis	80
4.3.1 Spin \mathbb{Z}_2 Symmetry	81
4.3.2 Real Time-Reversal Symmetry	81
4.3.3 Inversion Time-Reversal Symmetry	83

TABLE OF CONTENTS

4.4 Low-Energy Theory	85
4.4.1 Spectra Near the Critical Point	85
4.4.2 Wave Functions Near the Critical Point	87
4.4.3 Boundary Conditions Near the Critical Point	89
4.4.4 Spectra in the Deep Topological Regime	91
4.4.5 Wave Functions in the Deep Topological Regime	93
4.4.6 Lattice Diagonalization	94
4.5 The Spin Josephson Effect	96
4.5.1 Fractional Spin Josephson Effect	96
4.5.2 Continuum Scenarios	97
4.5.3 Lattice Odd-Even Effect	98
4.6 The Spin Entanglement	100
4.6.1 Metrics for Entanglement	100
4.6.2 Texture of Spin Entanglement	101
4.6.3 Spin Correlation Functions	103
4.7 Detection and Robustness	107
4.7.1 General Expression of the Susceptibility	107
4.7.2 Longitudinal Susceptibility	109
4.7.3 Transverse Susceptibility and Spin Noise	112
4.8 Discussion and Summary	113
CHAPTER 5 CONCLUSION AND OUTLOOK	115
REFERENCES	117
APPENDIX A MATHEMATICAL BACKGROUND	143
APPENDIX B THE HONEYCOMB ISING MODEL	150
APPENDIX C INTRODUCTION TO X-RAY BINARIES	159
ACKNOWLEDGEMENTS	160
声 明	163
RESUME	164
COMMENTS FROM THESIS SUPERVISOR	165
RESOLUTION OF THESIS DEFENSE COMMITTEE	166

LIST OF FIGURES AND TABLES

Figure 1.1	The Bloch sphere.....	4
Figure 1.2	A quantum circuit that performs teleportation of a qubit.....	5
Figure 1.3	A cavity QED setup for detecting observables in quantum spin chains.	21
Figure 1.4	A feedforward neural network.	28
Figure 1.5	A convolutional neural network for classifying the MNIST dataset.....	29
Figure 1.6	The flow of data and hidden state inside the RNN cell.	30
Figure 1.7	Samples of handwritten digits in the MNIST dataset.	31
Figure 1.8	The structure of capsule networks with three essential layers.	33
Figure 1.9	An illustration of the classical dynamic routing.	34
Figure 2.1	The quantum circuit for Grover's algorithm.	41
Figure 2.2	The quantum circuit for quantum phase estimation.....	42
Figure 2.3	The structure of parametrized quantum circuits.	46
Figure 3.1	The performance of the genetic algorithm in the MNIST dataset.....	53
Figure 3.2	The loss and accuracy of the genetic algorithm for the tenth-generation...	54
Figure 3.3	A schematic illustration of the MQNE algorithm.	58
Figure 3.4	The size of the gate-block library under default restrictions.	61
Figure 3.5	The size of the gate-block library under further restrictions.	62
Figure 3.6	The architecture of quantum classifiers.....	63
Figure 3.7	Numerical results of handwritten-digit images by the MQNE algorithm. .	65
Figure 3.8	The optimal quantum circuit generated by the MQNE algorithm.....	66
Figure 3.9	The performance of the MQNE algorithm for classifying SPT states.	67
Figure 3.10	Numerical results of SPT states by the MQNE algorithm.	68
Figure 3.11	The performance of the MQNE algorithm with fixed initial parameters.	69
Figure 3.12	The loss and accuracy of the MQNE algorithm for the sixth-generation.	70
Figure 3.13	Numerical results of the cancer dataset by the MQNE algorithm.	71
Figure 4.1	The mapping between the IXI spin chain and the SNS structure.....	77
Figure 4.2	The spectra of the IXI spin chain as a function of the twisting angle.....	95
Figure 4.3	The spectra of the IXI spin chain under two types of interactions.	97
Figure 4.4	The odd-even effect in the IXI spin chain.	99
Figure 4.5	Comparisons of three quantum entanglement metrics.	101

LIST OF FIGURES AND TABLES

Figure 4.6	The concurrences in the XY sector for ground states.	102
Figure 4.7	The longitudinal susceptibility as a function of the twisting angle.....	110
Figure 4.8	The spectra of the IXI spin chain under random perturbations.	112
Table 1.1	Comparisons for different types of neural networks	27
Table 2.1	Elementary operations for quantum algorithms.....	41
Table 2.2	Subroutines for quantum algorithms.	41
Table 2.3	The complexity of quantum algorithms and subroutines.	43
Table 3.1	An illustration of the graph-encoding method.	55
Table 3.2	The connection rules for gate blocks.	57
Table 4.1	A summary of conclusions, contrasted with the electronic counterpart. ..	113

LIST OF SYMBOLS AND ACRONYMS

ABS	Andreev Bound State
AI	Artificial Intelligence
ANN	Artificial Neural Network
BdG	Bogoliubov-de Gennes
CapsNet	Capsule Network
CNN	Convolution Neural Network
GRU	Gate Recurrent Unit
IXI	Ising-XY-Ising
JE	Josephson Effect
JWT	Jordan-Wigner Transformation
LSTM	Long Short-Term Memory
MBS	Majorana Bound State
MDP	Markovian Decision Process
MNIST	Modified National Institute of Standards and Technology
MQNE	Markovian Quantum Neuro-Evolution
NEAT	NeuroEvolution of Augmented Topologies
NISQ	Noisy Intermediate Scale quantum
PCA	Principal Component Analysis
PHS	Particle-Hole Symmetry
QAOA	Quantum Approximate Optimization Algorithm
QED	Quantum Electrodynamics
QFT	Quantum Fourier Transformation
QML	Quantum Machine Learning
QNN	Quantum Neural Network
QPE	Quantum Phase Estimation
QRAM	Quantum Random Access Memory
QSH	Quantum Spin Hall
RNN	Recurrent Neural Network
SNS	Superconducting-Normal-Superconducting
SPT	Symmetry-Protected Topological
SVM	Support Vector Machine
TRS	Time-Reversal Symmetry

CHAPTER 1 PRELIMINARIES

1.1 Introduction

1.1.1 Background

Quantum information processing exploits the quantum features of superposition and entanglement to process information^[1-3], offering the intriguing potential to outperform their classical counterparts in the near future^[4-6]. This opens up new paradigms for scientists to design algorithms with quantum speedup^[7-8], simulate quantum many-body systems^[9-10], and secure communication with quantum key distribution^[11], etc. Although existing quantum devices remain far from perfect, recent experiments (e.g., random circuit sampling and Gaussian boson sampling) have demonstrated a potential separation between the power of quantum and classical devices^[12-14].

Condensed matter physics studies the macroscopic and microscopic physical properties of matter^[15-16]. This field aims to address scientific problems encountered in solids, liquids, plasmas and more complex matter^[17-18]. To realize a quantum computer, one should not only find some robust physical representation of qubits, but also build a system in which they can be easily controlled. In this vein, condensed matter physics offers a broad playground to engineer controllable hardware to implement quantum information processing. There are numerous solid-state schemes for quantum computing^[19], e.g., electron spin-based qubits in semiconductors^[20] and superconducting circuits with Josephson junctions^[21], Majorana fermions in topological materials^[22], etc.

Machine learning is a branch of artificial intelligence and computer science that enables systems to learn from the underlying pattern of data without being explicitly programmed^[23-29]. With the aid of statistical tools and optimization methods, machine learning models are trained to make predictions for new data samples. Nowadays, artificial intelligence is a thriving field with many practical applications, such as playing Go game^[30-31], predicting the protein structure^[32], guiding mathematical intuition^[33], controlling the nuclear fusion^[34], etc.

In recent years, the interplay between quantum physics and machine learning gives rise to a new research frontier—quantum machine learning^[35-40]. On the one hand, a plethora of tools and ideas from machine learning can be adopted to tackle intricate quantum problems^[39,41-51]. On the other hand, quantum computing could also bring unprece-

mented opportunities to enhance, speed up, or innovate machine learning^[52-59]. However, qubits on current quantum devices are rather fragile, which are very sensitive to the noise from the environment. In the near term, we may only have noisy intermediate-scale quantum (NISQ) devices with hundreds of imperfect qubits^[60]. It is of crucial importance to search for well-performing quantum circuit architectures and maximize the computational power for quantum machine learning tasks on NISQ devices.

The ability to transmit quantum information without dissipation over large distances is one of the Holy Grail in quantum science and technology^[61]. The phenomena of superfluidity, superconductivity, and spin superfluidity which amounts to the flow of matter, charge, and spin without any resistance, respectively, might hold the physics answers to this technological question^[62-63]. The latter in particular, can turn out of crucial importance in spintronics, or electronics with spin^[64-65]. While studies of such spin superfluidity have been carried out for classical magnets, the quantum realm remains largely unexplored. Investigating the spin transport in the anisotropic quantum spin chain might pave the way to unveil the underlying physics.

1.1.2 Outline of the Dissertation

This dissertation will elaborate on two aspects: the quantum architecture search for machine learning^[66], and the quantum information processing in quantum spin chains^[67]. To begin with, we first introduce some basic concepts of quantum computation, condensed matter theory, and machine learning in the following sections of this Chapter 1, which forms the cornerstone of the ongoing projects. In Chapter 2, we introduce the field of quantum machine learning. Therein, we will mainly focus on quantum simulations, quantum algorithms, and quantum classifiers in the NISQ era.

In Chapter 3 we introduce an efficient Markovian quantum neuroevolution (MQNE) algorithm to search for optimal ansatz quantum circuits for different machine learning tasks^[66]. Specifically, we have proposed a graph-encoding method to injectively map quantum circuits to directed graphs. In the directed graphs, the nodes of the graph represent the elementary gate-blocks, and the directed edges correspond to the allowed connection between gate-blocks. Consequently, the problem of designing a proper quantum circuit reduces to a task of searching an appropriate directed path of the corresponding graph in a Markovian fashion. One striking advantage is that we can flexibly impose some further restrictions on building possible gate-blocks to reduce the size of the graph. Through concrete examples including classifications of real-life images and symmetry-

protected topological quantum states, we have demonstrated that our MQNE algorithm performs excellently in searching appropriate quantum classifiers with notably smaller depths, while maintaining a comparable classification accuracy. This work not only provides a valuable guide for experimental implementations of quantum machine learning on NISQ devices, but also would mitigate the possible barren plateau problem.

In Chapter 4, we study the spin transport in a quantum Ising-XY-Ising spin link subject to magnetic twists at their boundaries^[67]. When the twisting angle of the right Ising part is nonzero, there is a spin current flowing through the middle sector. Using a combination of symmetry analysis, numerical calculations, and analytical approaches, we have revealed several types of fractional spin Josephson effects that pertain to the emergent Jordan-Wigner Majorana fermions. We have rigorously proved and generalized the results of Laflamme et al.^[68], where only the special case of one spin in the middle sector was demonstrated. We showed that the \mathbb{Z}_4 Josephson effect is always valid for an odd number of spins, even without many-body interactions. We further analyzed the entanglement between pairs of spins by evaluating the concurrence, and extended the previous results in the literature on spin correlators^[69] to account for the presence of spin currents. Finally, we proposed to use a cavity QED setup for detecting the aforementioned Josephson effects by dispersive readout methods, and showed that the \mathbb{Z}_2 spin Josephson effect is immune to any local magnetic perturbations. Our detection proposal could be conversely used to control the quantum spin current by means of photons in cavity QED setups. We conclude the dissertation in Chapter 5 with several future directions. The source code for the analytical deduction and the numerical calculation can be found in the online GitHub repository^[70].

1.2 Quantum Computation

Quantum computation is a computational paradigm based on the laws of quantum mechanics. Originating from 1982, Feynman suggested to utilize highly controllable quantum devices, later to become known as quantum computers, for the simulation of other complex quantum systems^[4]. One decade later, two pioneering works demonstrated that quantum computers are able to factor integers^[5] and search unstructured database^[6] much more efficiently than the classical machines. Since then, quantum computation has received considerable attention, and become one of today's most active and rapidly expanding fields of research and development.

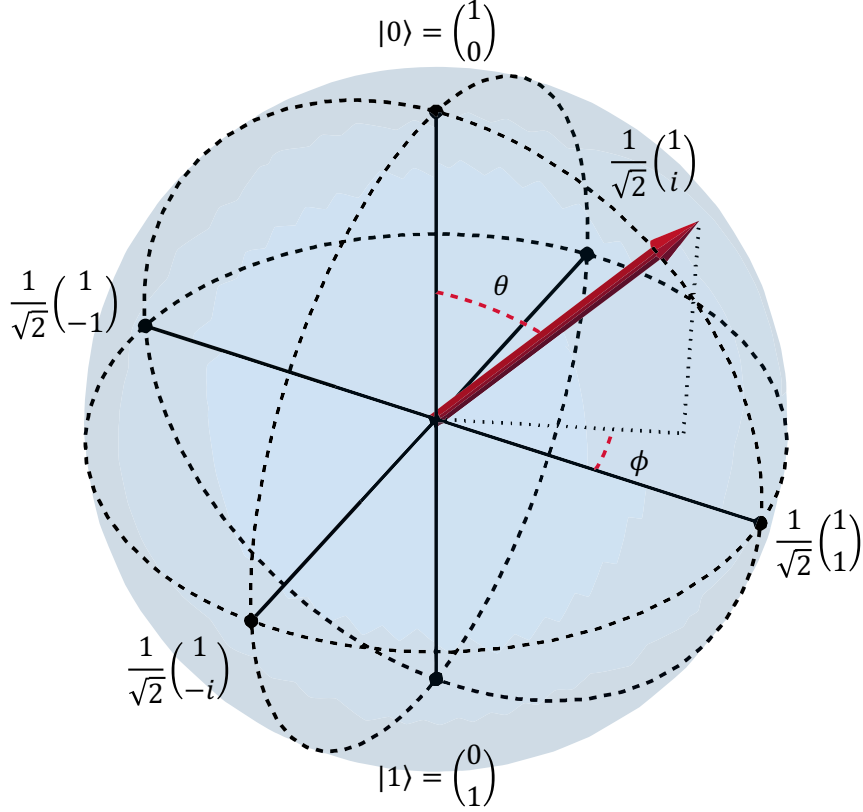


Figure 1.1 The Bloch sphere.

1.2.1 Qubits

For an isolated quantum system, the fundamental unit of information is a qubit, i.e., a quantum two-level system such as the spin of an electron or the polarization of a photon. In contrast to a classical bit which can only stay in one of these two states 0 and 1, the state of a qubit can be prepared in a coherent superposition state of 0 and 1:

$$|\psi\rangle = \alpha |0\rangle + \beta |1\rangle, \quad (1.1)$$

where α and β the complex amplitudes of qubit states $|\psi\rangle \in \mathbb{C}^2$ under the computational basis $|0\rangle$ or $|1\rangle$. The evolution of $|\psi\rangle$ is governed by the Schrödinger equation $i\hbar\partial_t |\psi\rangle = \hat{H} |\psi\rangle$ with a system Hamiltonian \hat{H} . Once measuring the qubit, such a superposition is collapsed into either a definite state $|0\rangle$ or $|1\rangle$ with respective probabilities $|\alpha|^2$ and $|\beta|^2 = 1 - |\alpha|^2$. One intuitive way to visualize the state of a single qubit is through the Bloch sphere,

$$|\theta, \phi\rangle = \cos \frac{\theta}{2} |0\rangle + e^{i\phi} \sin \frac{\theta}{2} |1\rangle, \quad (1.2)$$

where θ and ϕ define a point on the unit sphere. The state of an n -qubit state can be represented by a normalized vector in a tensor-product space \mathbb{C}^{2^n} .

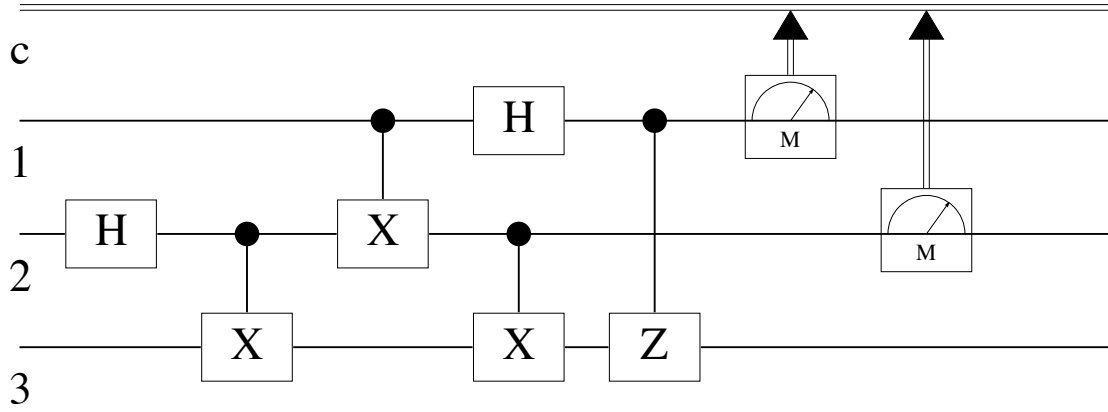


Figure 1.2 A quantum circuit that performs teleportation of a qubit.

1.2.2 Quantum Circuits

There are several theoretical frameworks for quantum computation, including the quantum circuit model^[1], quantum Turing machine^[71], adiabatic quantum computer^[72], measurement-based quantum computer^[73], quantum cellular automata^[74], etc. The most widely used one is the quantum circuit (see Figure 1.2 for the quantum circuit for the quantum teleportation algorithm). Just like classical algorithms at the lowest level are made of primitives such as AND, NOT and OR gates, quantum algorithms are built from a handful of elementary quantum gates. For one qubit gate, there are three Pauli gates along x, y, z directions,

$$X = \hat{\sigma}^x = \begin{bmatrix} 0 & 1 \\ 1 & 0 \end{bmatrix}, \quad Y = \hat{\sigma}^y = \begin{bmatrix} 0 & -i \\ i & 0 \end{bmatrix}, \quad Z = \hat{\sigma}^z = \begin{bmatrix} 1 & 0 \\ 0 & -1 \end{bmatrix}, \quad (1.3)$$

whose corresponding single-qubit rotations of angle θ are

$$e^{i\theta X} = \begin{bmatrix} \cos(\theta) & i \sin(\theta) \\ i \sin(\theta) & \cos(\theta) \end{bmatrix}, \quad e^{i\theta Y} = \begin{bmatrix} \cos(\theta) & \sin(\theta) \\ -\sin(\theta) & \cos(\theta) \end{bmatrix}, \quad e^{i\theta Z} = \begin{bmatrix} e^{i\theta} & 0 \\ 0 & e^{-i\theta} \end{bmatrix}. \quad (1.4)$$

Other three frequently used gates are Hadamard gate H , phase gate S , $\pi/8$ gate T :

$$H = \frac{1}{\sqrt{2}} \begin{bmatrix} 1 & 1 \\ 1 & -1 \end{bmatrix}, \quad S = \begin{bmatrix} 1 & 0 \\ 0 & i \end{bmatrix}, \quad T = \begin{bmatrix} 1 & 0 \\ 0 & e^{i\pi/4} \end{bmatrix}. \quad (1.5)$$

The representative two-qubit gate is the controlled-NOT (CNOT) gate:

$$\text{CNOT} = |0\rangle\langle 0| \otimes I + |1\rangle\langle 1| \otimes X = \begin{bmatrix} 1 & 0 & 0 & 0 \\ 0 & 1 & 0 & 0 \\ 0 & 0 & 0 & 1 \\ 0 & 0 & 1 & 0 \end{bmatrix}. \quad (1.6)$$

We note that $\{H, T, \text{CNOT}\}$ form a gate set for universal quantum computation^[75]. In addition, the Clifford gate set $\{S, T, \text{CNOT}\}$ are the generators Clifford group. By the Gottesman-Knill theorem, quantum circuits built on the Clifford gate set can be effectively simulated with classical computers^[76].

1.2.3 Physical Realization

In 2000, DiVincenzo^[77] proposed five criteria that are necessary to build a quantum computer in a real experimental setup:

- (i) A scalable physical system with well characterized qubit;
- (ii) The ability to initialize the state of the qubits to a simple fiducial state;
- (iii) Long relevant decoherence times;
- (iv) A universal set of quantum gates;
- (v) A qubit-specific measurement capability.

There are a plethora of proposals and platforms fulfill the above conditions, such as superconducting qubits^[78-79], trapped ions^[80-84], quantum dots^[85-88], electron spins in silicon^[20,89-93], ultracold atoms^[94-97], nitrogen-vacancies in diamonds^[88,98], polarized photons^[99-101], topological qubits^[102], etc. Each platform has its own advantages and limitations with respect to the scaling ability, individual control and readout. Among these setups, superconducting system and trapped ion hold the largest number of qubits for a universal quantum computation hitherto.

1.3 Condensed Matter Theory

Condensed matter theory explores the macroscopic and microscopic phenomena that emerge in both natural and synthetic materials. Apart from the elementary particles (e.g., fermion, boson, photon, proton), condensed-matter systems provide a broad playground for emergent quasi-particles (e.g, phonon, polaron, plasmon, excitons, magnon, spinon), which were uncovered from numerous exotic phases. Typical examples include superconducting phase, the ferromagnetic and antiferromagnetic phases in quantum spin chains, the Bose-Einstein condensate in ultracold atomic systems, many-body localization, time crystals, etc. There are a plethora of analytical techniques for theoretical analysis^[103-104]: mean field theory, linear response theory, Green's function, transfer matrix method, Bethe ansatz, path integral, Feynman diagram, etc. Yet, for non-integral systems, one should turn to the use of modern numerical techniques^[105], such as tensor networks, density ma-

trix renormalization group, time-evolving block decimation, quantum Monte Carlo, etc. In the following subsections, we will introduce some of analytical techniques. To begin with, we will first review some basics of quantum spin chains and the p -wave topological superconductors, which are connected by the renowned Jordan-Wigner transformation^[106]. We also briefly discuss possible experimental detection using cavity quantum electrodynamics techniques.

1.3.1 Quantum Spin Chains

Quantum spin chains are paradigmatic models used in the study of critical points and phase transitions of magnetic systems. They can be physically realized in quasi one-dimensional magnetic insulators. In such materials, the magnetic ions are placed in coupled linear arrays that are well separated and magnetically screened from each other^[107]. It has been recently demonstrated that specifically designed anisotropic spin chains offer a promising platform for quantum computation^[108], and even for the simulation of Majorana fermions on the IBM quantum machines^[109-110]. In the following contexts, we will introduce the mathematical framework for quantum spin chains.

1.3.1.1 Pauli matrices

Before introducing the N sites spin-1/2 chain models, let us refresh the basic algebraic properties of the Pauli matrices. They obey commutation and anti-commutation relations, which can be quickly proved by simple matrix multiplication:

$$[\hat{\sigma}^a, \hat{\sigma}^b] = 2i\epsilon_{abc}\hat{\sigma}^c, \quad \{\hat{\sigma}^a, \hat{\sigma}^b\} = 2\delta_{ab}\mathbb{1}. \quad (1.7)$$

We can verify that the Pauli matrices are involutory:

$$(\hat{\sigma}^x)^2 = (\hat{\sigma}^y)^2 = (\hat{\sigma}^z)^2 = \mathbb{1}. \quad (1.8)$$

Defining the raising and lowering operators as

$$\hat{\sigma}^+ = (\hat{\sigma}^x + i\hat{\sigma}^y)/2, \quad \hat{\sigma}^- = (\hat{\sigma}^x - i\hat{\sigma}^y)/2, \quad (1.9)$$

one can check that they have following relations:

$$[\hat{\sigma}^+, \hat{\sigma}^-] = \hat{\sigma}^z, \quad \{\hat{\sigma}^+, \hat{\sigma}^-\} = \mathbb{1}, \quad (1.10)$$

$$[\hat{\sigma}^z, \hat{\sigma}^\pm] = \pm 2\hat{\sigma}^\pm, \quad \{\hat{\sigma}^z, \hat{\sigma}^\pm\} = 0. \quad (1.11)$$

These matrices $i\hat{\sigma}^x, i\hat{\sigma}^y, i\hat{\sigma}^z$ form a basis for the Lie algebra $\mathfrak{su}(2)$, which generate the special unitary group $SU(2)$ (see Appendix A.1.3).

1.3.1.2 General Hamiltonian

The general anisotropic 1D spin-1/2 chain of N sites with nearest-neighbor exchange couplings under the open boundary condition:

$$\frac{\hat{H}}{J} = - \sum_{i=1}^{N-1} (\hat{\sigma}_i^x \hat{\sigma}_{i+1}^x + \alpha \hat{\sigma}_i^y \hat{\sigma}_{i+1}^y + \beta \hat{\sigma}_i^z \hat{\sigma}_{i+1}^z) - g \sum_{i=1}^N \hat{\sigma}_i^z, \quad (1.12)$$

where α, β are dimensionless variables quantifying the relative strength of the remaining terms. With different parameter settings, the above Hamiltonian describes,

- an Ising chain in transverse field g when $\alpha = \beta = 0$;
- an XY chain in transverse field g when $\alpha = 1, \beta = 0$;
- an ferromagnetic Heisenberg chain when $J > 0, \alpha = \beta = 1, g = 0$;
- an antiferromagnetic Heisenberg chain when $J < 0, \alpha = \beta = 1, g = 0$.

The emergent quasi-particles for the elementary excitations in the one-dimensional spin-1/2 Heisenberg ferromagnet and anti-ferromagnet are magnons and spinons, respectively^[111]. In particular, the antiferromagnetic Heisenberg Hamiltonian can be derived from Hubbard's model in the strong correlation limit at half filling. Specifically, the Fermi-Hubbard model on a one-dimensional lattice of N sites with nearest-neighbor hopping under open boundary conditions is defined by the Hamiltonian^[112]:

$$\hat{H} = -t \sum_{j=1}^N \sum_{\sigma=\uparrow,\downarrow} \left(\hat{c}_{j,\sigma}^\dagger \hat{c}_{j+1,\sigma} + \hat{c}_{j+1,\sigma}^\dagger \hat{c}_{j,\sigma} \right) + U \sum_{j=1}^N \hat{n}_{j\uparrow} \hat{n}_{j\downarrow}. \quad (1.13)$$

Here $\hat{c}_{j,\sigma}^\dagger$ and $\hat{c}_{j,\sigma}$ are creation and annihilation fermionic operators of electrons with spin degrees of freedom $\sigma = \uparrow, \downarrow$ localized in an orbital at site j of a one-dimensional lattice, and $\hat{n}_{j,\sigma} = \hat{c}_{j,\sigma}^\dagger \hat{c}_{j,\sigma}$ is the spin-density operator for spin σ on the j -th site. These fermionic operators satisfy the anti-commutation relations:

$$\{\hat{c}_{j,a}, \hat{c}_{k,b}\} = \{\hat{c}_{j,a}^\dagger, \hat{c}_{k,b}^\dagger\} = 0, \quad \{\hat{c}_{j,a}, \hat{c}_{k,b}^\dagger\} = \delta_{jk} \delta_{ab}. \quad (1.14)$$

The hopping term t describes particles tunneling between neighboring sites, U quantifies the strength of the onsite interactions. At half filling and $t \ll U$, this model describes a Mott insulator. Under this regime, electrons are tightly bound to a single site and each site is only occupied by a single electron, which effectively simulates a spin-1/2 degree of freedom for each site. The underlying antiferromagnetic exchange interactions stem from virtual hoppings between neighboring electrons^[18]. Likewise, the Bose-Hubbard model can be obtained by replacing the spinfull fermionic operators with the spinless bosonic

operators, $\hat{c}_{j,\sigma} \rightarrow \hat{b}_j$, satisfying the commutation relations:

$$[\hat{b}_j, \hat{b}_k] = [\hat{b}_j^\dagger, \hat{b}_k^\dagger] = 0, \quad [\hat{b}_j, \hat{b}_k^\dagger] = \delta_{jk}. \quad (1.15)$$

1.3.2 Topological Band Theory

Traditionally, the phase of matter was described by the Ginzburg-Landau theory with spontaneously broken symmetries and local order parameters^[113]. Yet, it was later shown that the fractional quantum Hall effect^[114], high-temperature superconductors^[115] and chiral spin liquids^[116] go beyond this paradigm. To circumvent this difficulty, the concept of topological order has been adopted in condensed matter physics for classifying phases of matter^[117]. In mathematics, topology is concerned with the properties of a geometric object that are preserved under continuous deformations (see Appendix A for a formal definition of topology and its relevant mathematical concepts)^[118]. In condensed matter physics, topological theory aims to address the question whether the Hamiltonians of two quantum systems can be continuously transformed into each other, and find a topological invariant that characterizes the phases of matter^[102,119-121].

There are two prevalent classes of topological phases of matter being extensively investigated^[122]: the intrinsic ones and the symmetry-protected ones, which belong to long-range entangled states and short-range-entangled states, respectively. In particular, the symmetry-protected topological (SPT) phases are gapped quantum phases that are protected by system symmetries, which means that they cannot be smoothly connected to the trivial phases under perturbations that respect the same kind of symmetries^[123]. However, once the corresponding symmetry is broken, all these phases can be smoothly connected to the trivial phase of product states. For free fermions, one can use K-theory^[124] and homotopy group^[125-126] to classify topological phases for topological insulators and superconductors. As for interacting bosons and fermions, the mathematical tools are much more sophisticated, which involve group cohomology^[127-128] and group supercohomology^[122,129].

1.3.2.1 The p -wave superconductor

Among the topological materials, topological insulators and superconductors are probably among the most scrutinized^[119-120,130-132]. Notably because they can host Majorana fermions, quasi-particles that are their own antiparticle, which occur as exotic excitations—Majorana zero modes^[133]. Thanks to their non-Abelian statistics, Majorana

zero modes are crucial ingredients for a functional topological quantum computer: a set of distant, non-interacting Majorana zero modes allow, through the process of braiding, to implement a category of topologically protected gates, albeit not universal^[102,134-135].

To obtain the essence of topological phases, here we give a pedagogical introduction to a toy model proposed by Kitaev^[136], i.e., the one-dimensional tight-binding p -wave superconductor, whose Hamiltonian reads

$$\hat{H} = - \sum_{i=1}^n \left[t_i \hat{c}_i^\dagger \hat{c}_{i+1} + t_i^* \hat{c}_{i+1}^\dagger \hat{c}_i + \Delta_i \hat{c}_i^\dagger \hat{c}_{i+1}^\dagger + \Delta_i^* \hat{c}_{i+1} \hat{c}_i + \mu_i \left(\hat{c}_i^\dagger \hat{c}_i - \frac{1}{2} \right) \right], \quad (1.16)$$

where \hat{c}_i is the electron annihilation operator for site i , t is the hopping term, Δ is the superconducting gap, and μ is the chemical potential. This spinless Hamiltonian can be effectively engineered by spin-polarizing with a magnetic field. One more realistic setup is the spin-orbit coupled nanowire subjected to a magnetic field and in the proximity of an s -wave superconductor^[137-139]. The above second quantized Hamiltonian can be written in a Bogoliubov-de Gennes (BdG) form,

$$\hat{H} = \frac{1}{2} \vec{c}^\dagger \mathcal{H} \vec{c} = \frac{1}{2} \vec{c}^\dagger \begin{bmatrix} S & A \\ -A^* & -S^* \end{bmatrix} \vec{c}, \quad (1.17)$$

with the Nambu spinor $\vec{c} \equiv (\hat{c}_1, \hat{c}_2, \dots, \hat{c}_n, \hat{c}_1^\dagger, \hat{c}_2^\dagger, \dots, \hat{c}_n^\dagger)^\top$, a Hermitian matrix $S = S^\dagger$ and a skew-symmetric matrix $A = -A^\top$. We can further write down \mathcal{H} in an explicit form,

$$\begin{bmatrix} -\mu_1 & -t_1 & 0 & \cdots & -t_n^* & 0 & -\Delta_1 & 0 & \cdots & +\Delta_n \\ -t_1^* & -\mu_2 & -t_2 & \ddots & \vdots & +\Delta_1 & 0 & -\Delta_2 & \ddots & \vdots \\ 0 & \ddots & \ddots & \ddots & 0 & 0 & \ddots & \ddots & \ddots & 0 \\ \vdots & \ddots & -t_{n-2}^* & -\mu_{n-1} & -t_{n-1} & \vdots & \ddots & +\Delta_{n-2} & 0 & -\Delta_{n-1} \\ -t_n & \cdots & 0 & -t_{n-1}^* & -\mu_n & -\Delta_n & \cdots & 0 & +\Delta_{n-1} & 0 \\ \hline 0 & +\Delta_1^* & 0 & \cdots & -\Delta_n^* & +\mu_1 & +t_1^* & 0 & \cdots & +t_n \\ -\Delta_1^* & 0 & +\Delta_2 & \ddots & \vdots & +t_1 & +\mu_2 & +t_2^* & \ddots & \vdots \\ 0 & \ddots & \ddots & \ddots & 0 & 0 & \ddots & \ddots & \ddots & 0 \\ \vdots & \ddots & -\Delta_{n-2}^* & 0 & +\Delta_{n-1}^* & \vdots & \ddots & +t_{n-2} & +\mu_{n-1} & +t_{n-1}^* \\ +\Delta_n^* & \cdots & 0 & -\Delta_{n-1}^* & 0 & +t_n^* & \cdots & 0 & +t_{n-1} & +\mu_n \end{bmatrix}.$$

By using the commutator relationships in Equation (1.14),

$$\begin{aligned} [\hat{c}_i^\dagger \hat{c}_j, \hat{c}_k] &= \hat{c}_i^\dagger \hat{c}_j \hat{c}_k - \hat{c}_k \hat{c}_i^\dagger \hat{c}_j = \hat{c}_i^\dagger \hat{c}_j \hat{c}_k - (\delta_{ik} - \hat{c}_i^\dagger \hat{c}_k) \hat{c}_j \\ &= \hat{c}_i^\dagger \hat{c}_j \hat{c}_k - \delta_{ik} \hat{c}_j - \hat{c}_i^\dagger \hat{c}_j \hat{c}_k = -\delta_{ik} \hat{c}_j, \\ [\hat{c}_i^\dagger \hat{c}_j, \hat{c}_k^\dagger] &= \hat{c}_i^\dagger \hat{c}_j \hat{c}_k^\dagger - \hat{c}_k^\dagger \hat{c}_i^\dagger \hat{c}_j = \hat{c}_i^\dagger \hat{c}_j \hat{c}_k^\dagger + \hat{c}_i^\dagger \hat{c}_k^\dagger \hat{c}_j \end{aligned} \quad (1.18)$$

$$= \hat{c}_i^\dagger \hat{c}_j \hat{c}_k^\dagger + \hat{c}_i^\dagger (\delta_{jk} - \hat{c}_j \hat{c}_k^\dagger) = +\delta_{jk} \hat{c}_i^\dagger, \quad (1.19)$$

$$\begin{aligned} [\hat{c}_i \hat{c}_j, \hat{c}_k^\dagger] &= \hat{c}_i \hat{c}_j \hat{c}_k^\dagger - \hat{c}_k^\dagger \hat{c}_i \hat{c}_j = \hat{c}_i \hat{c}_j \hat{c}_k^\dagger - (\delta_{ik} - \hat{c}_i \hat{c}_k^\dagger) \hat{c}_j \\ &= -\delta_{ik} \hat{c}_j + \hat{c}_i \hat{c}_j \hat{c}_k^\dagger + \hat{c}_i (\delta_{jk} - \hat{c}_j \hat{c}_k^\dagger) = +\delta_{jk} \hat{c}_i - \delta_{ik} \hat{c}_j, \end{aligned} \quad (1.20)$$

$$\begin{aligned} [\hat{c}_i^\dagger \hat{c}_j^\dagger, \hat{c}_k] &= \hat{c}_i^\dagger \hat{c}_j^\dagger \hat{c}_k - \hat{c}_k \hat{c}_i^\dagger \hat{c}_j^\dagger = \hat{c}_i^\dagger \hat{c}_j^\dagger \hat{c}_k - (\delta_{ik} - \hat{c}_i^\dagger \hat{c}_k) \hat{c}_j^\dagger \\ &= -\delta_{ik} \hat{c}_j^\dagger + \hat{c}_i^\dagger \hat{c}_j^\dagger \hat{c}_k + \hat{c}_i^\dagger (\delta_{jk} - \hat{c}_j^\dagger \hat{c}_k) = +\delta_{jk} \hat{c}_i^\dagger - \delta_{ik} \hat{c}_j^\dagger, \end{aligned} \quad (1.21)$$

we calculate the following commutators,

$$[\hat{H}, \hat{c}_i] = -(t_{i-1}^* \hat{c}_{i-1} - \mu_i \hat{c}_i - t_i \hat{c}_{i+1} + \Delta_{i-1} \hat{c}_{i-1}^\dagger - \Delta_i \hat{c}_{i+1}^\dagger), \quad (1.22)$$

$$[\hat{H}, \hat{c}_i^\dagger] = -(+t_{i-1} \hat{c}_{i-1}^\dagger + \mu_i \hat{c}_i^\dagger + t_i^* \hat{c}_{i+1}^\dagger - \Delta_{i-1}^* \hat{c}_{i-1} + \Delta_i^* \hat{c}_{i+1}), \quad (1.23)$$

and obtain the equation of motion with the BdG Hamiltonian:

$$\dot{\vec{c}} = i[\hat{H}, \vec{c}] = -i\mathcal{H}\vec{c} \iff \vec{c}(t) = \exp(-i\mathcal{H}t)\vec{c}(0). \quad (1.24)$$

which describes the time evolution of the single-particle mode.

1.3.2.2 Momentum Space

As mentioned in the previous subsection, although all terms in Equation (1.16) are quadratic, there are coupling terms of neighboring sites. In order to circumvent this problem and obtain the bulk properties of the model, we apply a discrete Fourier transformation to momentum space:

$$\hat{c}_k = \frac{1}{\sqrt{N}} \sum_j \hat{c}_j e^{+ikaj}, \quad \hat{c}_k^\dagger = \frac{1}{\sqrt{N}} \sum_j \hat{c}_j^\dagger e^{-ikaj}, \quad (1.25)$$

and the inverse Fourier transformation is given by

$$\hat{c}_j = \frac{1}{\sqrt{N}} \sum_k \hat{c}_k e^{-ikaj}, \quad \hat{c}_j^\dagger = \frac{1}{\sqrt{N}} \sum_k \hat{c}_k^\dagger e^{+ikaj}, \quad (1.26)$$

where a is the lattice spacing, and $k = \frac{2\pi n}{Na} \in (\pi, \pi]$ is the wave number. Here we impose the periodic boundary conditions, which does not affect bulk properties, and n takes following values:

$$n = \begin{cases} -\frac{N-1}{2}, -\frac{N-3}{2}, \dots, 0, \dots, \frac{N-1}{2}, & \text{if } N \text{ is odd;} \\ -\frac{N}{2} + 1, -\frac{N}{2} + 1, \dots, 0, \dots, \frac{N}{2}, & \text{if } N \text{ is even.} \end{cases} \quad (1.27)$$

Using transformation in Equation (1.26), we can check that:

$$\sum_j \hat{c}_j^\dagger \hat{c}_j = \sum_{k,k'} \hat{c}_k^\dagger \hat{c}_{k'} \left[\frac{1}{N} \sum_j e^{i(k-k')aj} \right] = \sum_{k,k'} \hat{c}_k^\dagger \hat{c}_{k'} \delta_{k,k'} = \sum_k \hat{c}_k^\dagger \hat{c}_k,$$

$$\begin{aligned}
 \sum_j \hat{c}_j^\dagger \hat{c}_{j+1} &= \sum_{k,k'} \hat{c}_k^\dagger \hat{c}_{k'} e^{-ik'a} \left[\frac{1}{N} \sum_j e^{i(k-k')aj} \right] = \sum_{k,k'} \hat{c}_k^\dagger \hat{c}_{k'} e^{-ik'a} \delta_{k,k'} = \sum_k \hat{c}_k^\dagger \hat{c}_k e^{-ika}, \\
 \sum_j \hat{c}_{j+1}^\dagger \hat{c}_j &= \sum_{k,k'} \hat{c}_k^\dagger \hat{c}_{k'} e^{ika} \left[\frac{1}{N} \sum_j e^{i(k-k')aj} \right] = \sum_{k,k'} \hat{c}_k^\dagger \hat{c}_{k'} e^{ika} \delta_{k,k'} = \sum_k \hat{c}_k^\dagger \hat{c}_k e^{ika}, \\
 \sum_j \hat{c}_{j+1} \hat{c}_j &= \sum_{k,k'} \hat{c}_{-k} \hat{c}_{k'} e^{ika} \left[\frac{1}{N} \sum_j e^{i(k-k')aj} \right] = \sum_{k,k'} \hat{c}_{-k} \hat{c}_{k'} e^{ika} \delta_{k,k'} = \sum_k \hat{c}_{-k} \hat{c}_k e^{ika}, \\
 \sum_j \hat{c}_j^\dagger \hat{c}_{j+1}^\dagger &= \sum_{k,k'} \hat{c}_k^\dagger \hat{c}_{-k'}^\dagger e^{-ik'a} \left[\frac{1}{N} \sum_j e^{i(k-k')aj} \right] = \sum_{k,k'} \hat{c}_k^\dagger \hat{c}_{-k'}^\dagger e^{-ik'a} \delta_{k,k'} = \sum_k \hat{c}_k^\dagger \hat{c}_{-k}^\dagger e^{-ika}.
 \end{aligned}$$

With above equations, we can transform the p -wave Hamiltonian in Equation (1.16) to momentum space (we set $t_i = t_i^* = t$, $\Delta_i = \Delta_i^* = \Delta$ and $\mu_i = \mu$ for simplicity):

$$\begin{aligned}
 \hat{H} &= - \sum_i \left[t(\hat{c}_i^\dagger \hat{c}_{i+1} + \hat{c}_{i+1}^\dagger \hat{c}_i) + \Delta(\hat{c}_i^\dagger \hat{c}_{i+1}^\dagger + \hat{c}_{i+1} \hat{c}_i) + \mu(\hat{c}_i^\dagger \hat{c}_i - \frac{1}{2}) \right] \\
 &= - \sum_k \left[t(\hat{c}_k^\dagger \hat{c}_k e^{-ika} + \hat{c}_k^\dagger \hat{c}_k e^{ika}) + \Delta(\hat{c}_k^\dagger \hat{c}_{-k}^\dagger e^{-ika} + \hat{c}_{-k} \hat{c}_k e^{ika}) + \mu \hat{c}_k^\dagger \hat{c}_k \right] + \frac{1}{2} \mu N \\
 &= - \sum_k \left[(2t \cos ka + \mu) \hat{c}_k^\dagger \hat{c}_k + \frac{\Delta}{2} (\hat{c}_k^\dagger \hat{c}_{-k}^\dagger e^{-ika} + \hat{c}_{-k} \hat{c}_k e^{ika}) + \text{H.c.} \right] + \frac{1}{2} \mu N \\
 &= - \sum_k \left[(2t \cos ka + \mu) \hat{c}_k^\dagger \hat{c}_k + \frac{\Delta}{2} e^{ika} (\hat{c}_{-k}^\dagger \hat{c}_k^\dagger + \hat{c}_{-k} \hat{c}_k) + \frac{\Delta}{2} e^{-ika} (\hat{c}_k^\dagger \hat{c}_{-k}^\dagger + \hat{c}_k \hat{c}_{-k}) \right] + \frac{1}{2} \mu N \\
 &= - \sum_k \left[(2t \cos ka + \mu) \hat{c}_k^\dagger \hat{c}_k + \frac{\Delta}{2} (e^{ika} - e^{-ika}) (\hat{c}_{-k}^\dagger \hat{c}_k^\dagger + \hat{c}_{-k} \hat{c}_k) \right] + \frac{1}{2} \mu N \\
 &= - \sum_k \left[(2t \cos ka + \mu) \hat{c}_k^\dagger \hat{c}_k + i\Delta \sin ka (\hat{c}_{-k}^\dagger \hat{c}_k^\dagger + \hat{c}_{-k} \hat{c}_k) \right] + \frac{1}{2} \mu N. \tag{1.28}
 \end{aligned}$$

1.3.2.3 Bogoliubov Transformation

We note that the fermion number of the p -wave superconducting model is not conserved, which implies we should define new set of operators $\{\hat{a}_k\}$ to fulfill the conservation of particle numbers. This can be achieved by the Bogoliubov transformation:

$$\hat{a}_k = u_k \hat{c}_k - i v_k \hat{c}_{-k}^\dagger, \tag{1.29}$$

$$\hat{a}_k^\dagger = u_k \hat{c}_k^\dagger + i v_k \hat{c}_{-k}, \tag{1.30}$$

In order to make $\{\hat{a}_k\}$ satisfy the anti-commutation relations for fermions, i.e.

$$\{\hat{a}_k, \hat{a}_l^\dagger\} = \delta_{kl}, \quad \{\hat{a}_k, \hat{a}_l\} = \{\hat{a}_k^\dagger, \hat{a}_l^\dagger\} = 0, \tag{1.31}$$

u_k and v_k are required to follow

$$u_k^2 + v_k^2 = 1, \quad u_{-k} = u_k, \quad v_{-k} = -v_k. \tag{1.32}$$

which gives

$$\hat{a}_{-k} = u_k \hat{c}_{-k} + i v_k \hat{c}_k^\dagger, \quad (1.33)$$

$$\hat{a}_{-k}^\dagger = u_k \hat{c}_{-k}^\dagger - i v_k \hat{c}_k, \quad (1.34)$$

Combining Equation (1.29) and Equation (1.33) together, the inverse Bogoliubov transformation is given by

$$\hat{c}_k = u_k \hat{a}_k + i v_k \hat{a}_{-k}^\dagger, \quad (1.35)$$

$$\hat{c}_k^\dagger = u_k \hat{a}_k^\dagger - i v_k \hat{a}_{-k}, \quad (1.36)$$

$$\hat{c}_{-k} = u_k \hat{a}_{-k} - i v_k \hat{a}_k^\dagger, \quad (1.37)$$

$$\hat{c}_{-k}^\dagger = u_k \hat{a}_{-k}^\dagger + i v_k \hat{a}_k. \quad (1.38)$$

With the above transformation, the Hamiltonian is transformed into

$$\begin{aligned} \hat{H} &= - \sum_k \left[(2t \cos ka + \mu) \hat{c}_k^\dagger \hat{c}_k + i \Delta \sin ka (\hat{c}_{-k}^\dagger \hat{c}_k^\dagger + \hat{c}_{-k} \hat{c}_k) \right] + \frac{1}{2} \mu N \\ &= - \sum_k \left\{ (2t \cos ka + \mu) (u_k \hat{a}_k^\dagger - i v_k \hat{a}_{-k}) (u_k \hat{a}_k + i v_k \hat{a}_{-k}^\dagger) \right. \\ &\quad + i \Delta \sin ka \left[(u_k \hat{a}_{-k}^\dagger + i v_k \hat{a}_k) (u_k \hat{a}_k^\dagger - i v_k \hat{a}_{-k}) \right. \\ &\quad \left. \left. + (u_k \hat{a}_{-k} - i v_k \hat{a}_k^\dagger) (u_k \hat{a}_k + i v_k \hat{a}_{-k}^\dagger) \right] \right\} + \frac{1}{2} \mu N \\ &= - \sum_k \left\{ (2t \cos ka + \mu) \left[u_k^2 \hat{a}_k^\dagger \hat{a}_k + v_k^2 \hat{a}_{-k} \hat{a}_{-k}^\dagger + i u_k v_k (\hat{a}_k^\dagger \hat{a}_{-k}^\dagger - \hat{a}_{-k} \hat{a}_k) \right] \right. \\ &\quad + i \Delta \sin ka \left[\left(u_k^2 \hat{a}_{-k}^\dagger \hat{a}_k^\dagger + v_k^2 \hat{a}_k \hat{a}_{-k} + i u_k v_k (\hat{a}_k \hat{a}_k^\dagger - \hat{a}_{-k}^\dagger \hat{a}_{-k}) \right) \right. \\ &\quad \left. \left. + \left(u_k^2 \hat{a}_{-k} \hat{a}_k + v_k^2 \hat{a}_k^\dagger \hat{a}_{-k}^\dagger + i u_k v_k (\hat{a}_{-k} \hat{a}_{-k}^\dagger - \hat{a}_k^\dagger \hat{a}_k) \right) \right] \right\} + \frac{1}{2} \mu N \\ &= - \sum_k \left\{ (2t \cos ka + \mu) \left[u_k^2 \hat{a}_k^\dagger \hat{a}_k - v_k^2 \hat{a}_{-k}^\dagger \hat{a}_{-k} - i u_k v_k (\hat{a}_{-k}^\dagger \hat{a}_k^\dagger + \hat{a}_{-k} \hat{a}_k) + v_k^2 \right] \right. \\ &\quad + i \Delta \sin ka \left[\left(u_k^2 \hat{a}_{-k}^\dagger \hat{a}_k^\dagger - v_k^2 \hat{a}_{-k} \hat{a}_k - i u_k v_k (\hat{a}_k^\dagger \hat{a}_k + \hat{a}_{-k}^\dagger \hat{a}_{-k}) + i u_k v_k \right) \right. \\ &\quad \left. \left. + \left(u_k^2 \hat{a}_{-k} \hat{a}_k - v_k^2 \hat{a}_{-k}^\dagger \hat{a}_k^\dagger - i u_k v_k (\hat{a}_{-k}^\dagger \hat{a}_{-k} + \hat{a}_k^\dagger \hat{a}_k) + i u_k v_k \right) \right] \right\} + \frac{1}{2} \mu N \\ &= - \sum_k \left\{ (2t \cos ka + \mu) \left[(u_k^2 - v_k^2) \hat{a}_k^\dagger \hat{a}_k - i u_k v_k (\hat{a}_{-k}^\dagger \hat{a}_k^\dagger + \hat{a}_{-k} \hat{a}_k) + v_k^2 \right] \right. \\ &\quad + i \Delta \sin ka \left[(u_k^2 - v_k^2) (\hat{a}_{-k}^\dagger \hat{a}_k^\dagger + \hat{a}_{-k} \hat{a}_k) - 4 i u_k v_k \hat{a}_k^\dagger \hat{a}_k + 2 i u_k v_k \right] \right\} + \frac{1}{2} \mu N \\ &= - \sum_k \left\{ \left[(2t \cos ka + \mu) (u_k^2 - v_k^2) + 4 u_k v_k \Delta \sin ka \right] \hat{a}_k^\dagger \hat{a}_k \right. \\ &\quad \left. - i \left[(2t \cos ka + \mu) u_k v_k - (u_k^2 - v_k^2) \Delta \sin ka \right] (\hat{a}_{-k}^\dagger \hat{a}_k^\dagger + \hat{a}_{-k} \hat{a}_k) \right\} \end{aligned}$$

$$+ (2t \cos ka + \mu)v_k^2 - 2u_k v_k \Delta \sin ka \} + \frac{1}{2} \mu N. \quad (1.39)$$

In order to eliminate the off-diagonal terms, we should set

$$(2t \cos ka + \mu)u_k v_k - (u_k^2 - v_k^2)\Delta \sin ka = 0. \quad (1.40)$$

Supposing $u_k = \cos \theta_k$, $v_k = \sin \theta_k$, we get $u_k^2 - v_k^2 = \cos 2\theta_k$, $2u_k v_k = \sin 2\theta_k$. From Equation (1.40), θ_k is restricted to

$$\theta_k = \frac{1}{2} \arctan \left(\frac{2\Delta \sin ka}{2t \cos ka + \mu} \right). \quad (1.41)$$

Then we have

$$u_k^2 - v_k^2 = \cos 2\theta_k = \frac{2t \cos ka + \mu}{\sqrt{(2t \cos ka + \mu)^2 + 4\Delta^2 \sin^2 ka}}, \quad (1.42)$$

$$2u_k v_k = \sin 2\theta_k = \frac{2\Delta \sin ka}{\sqrt{(2t \cos ka + \mu)^2 + 4\Delta^2 \sin^2 ka}}, \quad (1.43)$$

$$u_k^2 = \frac{1}{2} (1 + \cos 2\theta_k) = \frac{1}{2} \left(1 + \frac{2t \cos ka + \mu}{\sqrt{(2t \cos ka + \mu)^2 + 4\Delta^2 \sin^2 ka}} \right), \quad (1.44)$$

$$v_k^2 = \frac{1}{2} (1 - \cos 2\theta_k) = \frac{1}{2} \left(1 - \frac{2t \cos ka + \mu}{\sqrt{(2t \cos ka + \mu)^2 + 4\Delta^2 \sin^2 ka}} \right). \quad (1.45)$$

Plugging back into Equation (1.39), we obtain the diagonalized Hamiltonian as

$$\begin{aligned} \hat{H} = & - \sum_k \left[\sqrt{(2t \cos ka + \mu)^2 + 4\Delta^2 \sin^2 ka} \hat{a}_k^\dagger \hat{a}_k \right. \\ & \left. + \frac{1}{2} \left(2t \cos ka + \mu - \sqrt{(2t \cos ka + \mu)^2 + 4\Delta^2 \sin^2 ka} \right) \right] + \frac{1}{2} \mu N. \end{aligned} \quad (1.46)$$

Then the energy bands of the p -wave superconductor are given by

$$\varepsilon(k) = \sqrt{(2t \cos ka + \mu)^2 + 4\Delta^2 \sin^2 ka}. \quad (1.47)$$

1.3.2.4 Marjorana Representation

In the above section, we have solved out the bulk properties of p -wave superconductor by transforming their Hamiltonian in momentum space, with the periodic boundary condition imposed. In order to investigate the coupling effects under finite N sites with free ends, we need to go to the Majorana representation and solve it numerically^[136]. From quantum field theory, we have already known that any fermion can be written as a combination of two Majorana fermions, which basically corresponds to splitting a fermion

into a real part and an imaginary part:

$$\hat{c}_i = (\hat{\gamma}_{2i-1} + i\hat{\gamma}_{2i})/2, \quad \hat{c}_i^\dagger = (\hat{\gamma}_{2i-1} - i\hat{\gamma}_{2i})/2. \quad (1.48)$$

Each Majorana fermion is an equal superposition of an electron and a hole state:

$$\hat{\gamma}_{2i-1} = \hat{c}_i^\dagger + \hat{c}_i, \quad \hat{\gamma}_{2i} = i(\hat{c}_i^\dagger - \hat{c}_i). \quad (1.49)$$

Obviously, the Majorana operators themselves are Hermitian. We can verify that the Majorana operators satisfy the anti-commutation relation:

$$\{\hat{\gamma}_i, \hat{\gamma}_j\} = 2\delta_{ij}. \quad (1.50)$$

Hence, Majorana fermions are elements of a Clifford algebra (see Appendix A.1.4 for a formal definition)^[140]. Combining Equation (1.16) and Equation (1.48), we can transform the Hamiltonian of the p -wave superconducting model from fermionic representation to Majorana representation (we set $t_i = t_i^* = \Delta_i = \Delta_i^* = t$ and $\mu_i = \mu$ for simplicity):

$$\begin{aligned} \hat{H} &= -t \sum_i \left(\hat{c}_i^\dagger \hat{c}_{i+1} + \hat{c}_{i+1}^\dagger \hat{c}_i + \hat{c}_i^\dagger \hat{c}_{i+1}^\dagger + \hat{c}_{i+1} \hat{c}_i \right) - \mu \sum_i \left(\hat{c}_i^\dagger \hat{c}_i - \frac{1}{2} \right) \\ &= -\frac{t}{4} \sum_i \left[(\hat{\gamma}_{2i-1} - i\hat{\gamma}_{2i})(\hat{\gamma}_{2i+1} + i\hat{\gamma}_{2i+2}) + (\hat{\gamma}_{2i+1} - i\hat{\gamma}_{2i+2})(\hat{\gamma}_{2i-1} + i\hat{\gamma}_{2i}) \right. \\ &\quad \left. + (\hat{\gamma}_{2i-1} - i\hat{\gamma}_{2i})(\hat{\gamma}_{2i+1} - i\hat{\gamma}_{2i+2}) + (\hat{\gamma}_{2i+1} + i\hat{\gamma}_{2i+2})(\hat{\gamma}_{2i-1} + i\hat{\gamma}_{2i}) \right] \\ &\quad - \frac{\mu}{4} \sum_i \left[(\hat{\gamma}_{2i-1} - i\hat{\gamma}_{2i})(\hat{\gamma}_{2i-1} + i\hat{\gamma}_{2i}) - 2 \right] \\ &= -\frac{t}{4} \sum_i \left(\hat{\gamma}_{2i-1} \hat{\gamma}_{2i+1} + \hat{\gamma}_{2i-1} \hat{\gamma}_{2i+2} - i\hat{\gamma}_{2i} \hat{\gamma}_{2i+1} + \hat{\gamma}_{2i} \hat{\gamma}_{2i+2} \right. \\ &\quad \left. + \hat{\gamma}_{2i+1} \hat{\gamma}_{2i-1} + i\hat{\gamma}_{2i+1} \hat{\gamma}_{2i} - \hat{\gamma}_{2i+2} \hat{\gamma}_{2i-1} + \hat{\gamma}_{2i+2} \hat{\gamma}_{2i} \right. \\ &\quad \left. + \hat{\gamma}_{2i-1} \hat{\gamma}_{2i+1} - i\hat{\gamma}_{2i-1} \hat{\gamma}_{2i+2} - i\hat{\gamma}_{2i} \hat{\gamma}_{2i+1} - \hat{\gamma}_{2i} \hat{\gamma}_{2i+2} \right. \\ &\quad \left. + \hat{\gamma}_{2i+1} \hat{\gamma}_{2i-1} + i\hat{\gamma}_{2i+1} \hat{\gamma}_{2i} + \hat{\gamma}_{2i+2} \hat{\gamma}_{2i-1} - \hat{\gamma}_{2i+2} \hat{\gamma}_{2i} \right) \\ &\quad - \frac{\mu}{2} \sum_i \left(i\hat{\gamma}_{2i-1} \hat{\gamma}_{2i} - i\hat{\gamma}_{2i} \hat{\gamma}_{2i-1} + \hat{\gamma}_{2i-1}^2 + \hat{\gamma}_{2i}^2 - 2 \right) \\ &= i \left(t \sum_i \hat{\gamma}_{2i} \hat{\gamma}_{2i+1} - \frac{\mu}{2} \sum_i \hat{\gamma}_{2i-1} \hat{\gamma}_{2i} \right). \end{aligned} \quad (1.51)$$

It can be shown that the system is in a symmetry-protected topological phase when $|\mu| < 2t$, and in a topologically trivial phase when $|\mu| > 2t$ ^[136]. Specifically when $\mu = 0$, two Majorana operators $\hat{\gamma}_1, \hat{\gamma}_{2N}$ drop out from the Hamiltonian, and give rise to the unpaired Majorana zero modes. They follow non-Abelian statistics and provide a degenerate subspace where quantum operations can be implemented though braiding^[102,141]. Note

that such a topological protection is stabilized by the topological gap. In the presence of disorders, whose strengths are much larger than the gap, the emergence of the Majorana zero mode would be destroyed^[142].

The topological order of the p -wave superconductor is characterized by a topological invariant \mathbb{Z}_2 , which belongs to class D in the celebrated tenfold-way of Altland-Zirnbauer symmetry classes^[124-126,129,143], i.e. it only possesses particle-hole symmetry $\rho_x \mathcal{H}^\dagger \rho_x = -\mathcal{H}$, where ρ_x is a Pauli- X operator acting on the Nambu space. We remark that this kind of particle-hole symmetry stems from the redundancy of the Nambu spinor used to define the single-particle BdG Hamiltonian \mathcal{H} in Equation (1.17). For this reason, it has been suggested to be called as a Fermi constraint instead of a symmetry^[144].

1.3.3 Jordan-Wigner Transformation

To pave the way to the following sections, we provide a pedagogical introduction of the Jordan-Wigner transformation (JWT)^[106] with the generalized Hamiltonian in Equation (1.12). The crucial point is how to map the observation from the Hilbert space of a system with a spin-1/2 degree of freedom per site to that of spinless fermions jumping along a chain of single-orbital sites. We may suppose that the spin-up state of the chain $|\uparrow\rangle = |0\rangle_s$ can be associated with an occupied state $|1\rangle_f$ and the spin-down state $|\downarrow\rangle = |1\rangle_s$ with an hole state $|0\rangle_f$. That is to say we should find some transformations to connect operators from two representations:

$$\hat{\sigma}_i^+ \Leftrightarrow \hat{c}_i^\dagger, \quad \hat{\sigma}_i^- \Leftrightarrow \hat{c}_i, \quad \hat{\sigma}_i^z \Leftrightarrow \hat{n}_i, \quad (1.52)$$

where $\hat{n}_i \equiv \hat{c}_i^\dagger \hat{c}_i$ is the particle number, \hat{c}_i^\dagger is the creation operator, and \hat{c}_i is the annihilation operator for spinless fermion on site i . At first attempt we can fulfill the observation requirement on site i by following transformation:

$$\hat{\sigma}_i^+ = \hat{c}_i^\dagger, \quad \hat{\sigma}_i^- = \hat{c}_i, \quad \hat{\sigma}_i^z = 2\hat{n}_i - 1. \quad (1.53)$$

With these identifies, one can find that these operators partly resemble fermionic operators on the same single site i :

$$\{\hat{c}_i, \hat{c}_i^\dagger\} = 1, \quad (\hat{c}_i)^2 = (\hat{c}_i^\dagger)^2 = 0, \quad (1.54)$$

whereas they partly resemble bosonic operators on different sites i and j :

$$[\hat{c}_i, \hat{c}_j^\dagger] = [\hat{c}_i, \hat{c}_j] = [\hat{c}_i^\dagger, \hat{c}_j^\dagger] = 0, \quad i \neq j. \quad (1.55)$$

Since there contain different commutation rules, it is impossible to diagonalize the universal Hamiltonian in Equation (1.12) directly with the naive transformation (1.53).

Although transformation in Equation (1.53) fails to preserve the anti-commutation relations of fermions, it is possible to create a new transformation that strictly fulfills fermionic algebra simply by adding the Jordan-Wigner *string* $e^{i\pi \sum_{j<i} \hat{n}_j}$:

$$\hat{\sigma}_i^+ = e^{+i\pi \sum_{j<i} \hat{n}_j} \hat{c}_i^\dagger = \prod_{j<i} (1 - 2\hat{n}_j) \hat{c}_i^\dagger, \quad (1.56)$$

$$\hat{\sigma}_i^- = e^{-i\pi \sum_{j<i} \hat{n}_j} \hat{c}_i = \prod_{j<i} (1 - 2\hat{n}_j) \hat{c}_i, \quad (1.57)$$

$$\hat{\sigma}_i^z = 2\hat{n}_i - 1 = 2\hat{c}_i^\dagger \hat{c}_i - 1. \quad (1.58)$$

This is a highly nonlocal representation of the spins in terms of the fermionic operators, involving all the sites to the left of the i -th position. The inverse transformation is

$$\hat{c}_i^\dagger = e^{+i\pi \sum_{j<i} \hat{n}_j} \hat{\sigma}_i^+ = \prod_{j<i} (-\hat{\sigma}_j^z) \hat{\sigma}_i^+, \quad (1.59)$$

$$\hat{c}_i = e^{-i\pi \sum_{j<i} \hat{n}_j} \hat{\sigma}_i^- = \prod_{j<i} (-\hat{\sigma}_j^z) \hat{\sigma}_i^-, \quad (1.60)$$

$$\hat{n}_i = \hat{c}_i^\dagger \hat{c}_i = \frac{1 + \hat{\sigma}_i^z}{2}. \quad (1.61)$$

When $i = j$, we can see that \hat{c}_i and \hat{c}_j^\dagger follow the same relations as Equation (1.54). If $i \neq j$, without loss of generality assuming $i < j$, using the Pauli matrices relations in Section 1.3.1.1, we obtain following relations:

$$\{\hat{c}_i, \hat{c}_j^\dagger\} = \left\{ \prod_{m<i} (-\hat{\sigma}_m^z) \hat{\sigma}_i^-, \prod_{n<j} (-\hat{\sigma}_n^z) \hat{\sigma}_j^+ \right\} = \{\hat{\sigma}_i^-, -\hat{\sigma}_i^z\} \prod_{i<n<j} (-\hat{\sigma}_n^z) \hat{\sigma}_j^+ = 0, \quad (1.62)$$

$$\{\hat{c}_i, \hat{c}_j\} = \left\{ \prod_{m<i} (-\hat{\sigma}_m^z) \hat{\sigma}_i^-, \prod_{n<j} (-\hat{\sigma}_n^z) \hat{\sigma}_j^- \right\} = \{\hat{\sigma}_i^-, -\hat{\sigma}_i^z\} \prod_{i<n<j} (-\hat{\sigma}_n^z) \hat{\sigma}_j^- = 0, \quad (1.63)$$

$$\{\hat{c}_i^\dagger, \hat{c}_j^\dagger\} = \left\{ \prod_{m<i} (-\hat{\sigma}_m^z) \hat{\sigma}_i^+, \prod_{n<j} (-\hat{\sigma}_n^z) \hat{\sigma}_j^+ \right\} = \{\hat{\sigma}_i^+, -\hat{\sigma}_i^z\} \prod_{i<n<j} (-\hat{\sigma}_n^z) \hat{\sigma}_j^+ = 0. \quad (1.64)$$

Therefore, they are consistent with anti-commutation relations for spinless fermions:

$$\{\hat{c}_i, \hat{c}_j^\dagger\} = \delta_{ij}, \quad \{\hat{c}_i, \hat{c}_j\} = \{\hat{c}_i^\dagger, \hat{c}_j^\dagger\} = 0. \quad (1.65)$$

Using transformation (1.56), together with the Pauli matrices relations

$$\hat{\sigma}_i^x = \hat{\sigma}_i^+ + \hat{\sigma}_i^-, \quad \hat{\sigma}_i^y = (\hat{\sigma}_i^+ - \hat{\sigma}_i^-)/i, \quad (1.66)$$

we can transform $\hat{\sigma}_i^x \hat{\sigma}_{i+1}^x$ into

$$\begin{aligned}
 \hat{\sigma}_i^x \hat{\sigma}_{i+1}^x &= (\hat{\sigma}_i^+ + \hat{\sigma}_i^-)(\hat{\sigma}_{i+1}^+ + \hat{\sigma}_{i+1}^-) \\
 &= \prod_{j<i} (1 - 2\hat{n}_j)(\hat{c}_i^\dagger + \hat{c}_i) \prod_{j<i+1} (1 - 2\hat{n}_j)(\hat{c}_{i+1}^\dagger + \hat{c}_{i+1}) \\
 &= \prod_{j<i} \hat{\sigma}_j^z (\hat{c}_i^\dagger + \hat{c}_i) \prod_{j<i} \hat{\sigma}_j^z (1 - 2\hat{n}_j)(\hat{c}_{i+1}^\dagger + \hat{c}_{i+1}) \\
 &= (\hat{c}_i^\dagger + \hat{c}_i)(1 - 2\hat{c}_i^\dagger \hat{c}_i)(\hat{c}_{i+1}^\dagger + \hat{c}_{i+1}) \\
 &= (\hat{c}_i^\dagger + \hat{c}_i - 2\hat{c}_i^\dagger \hat{c}_i \hat{c}_i - 2\hat{c}_i \hat{c}_i^\dagger \hat{c}_i)(\hat{c}_{i+1}^\dagger + \hat{c}_{i+1}) \\
 &= (\hat{c}_i^\dagger - \hat{c}_i)(\hat{c}_{i+1}^\dagger + \hat{c}_{i+1}).
 \end{aligned} \tag{1.67}$$

Similarly, $\hat{\sigma}_i^y \hat{\sigma}_{i+1}^y$ is transformed into

$$\begin{aligned}
 \hat{\sigma}_i^y \hat{\sigma}_{i+1}^y &= -(\hat{\sigma}_i^+ - \hat{\sigma}_i^-)(\hat{\sigma}_{i+1}^+ - \hat{\sigma}_{i+1}^-) \\
 &= -\prod_{j<i} (1 - 2\hat{n}_j)(\hat{c}_i^\dagger - \hat{c}_i) \prod_{j<i+1} (1 - 2\hat{n}_j)(\hat{c}_{i+1}^\dagger - \hat{c}_{i+1}) \\
 &= -\prod_{j<i} \hat{\sigma}_j^z (\hat{c}_i^\dagger - \hat{c}_i) \prod_{j<i} \hat{\sigma}_j^z (1 - 2\hat{n}_j)(\hat{c}_{i+1}^\dagger - \hat{c}_{i+1}) \\
 &= -(\hat{c}_i^\dagger - \hat{c}_i)(1 - 2\hat{c}_i^\dagger \hat{c}_i)(\hat{c}_{i+1}^\dagger - \hat{c}_{i+1}) \\
 &= -(\hat{c}_i^\dagger - \hat{c}_i - 2\hat{c}_i^\dagger \hat{c}_i \hat{c}_i + 2\hat{c}_i \hat{c}_i^\dagger \hat{c}_i)(\hat{c}_{i+1}^\dagger - \hat{c}_{i+1}) \\
 &= -(\hat{c}_i^\dagger + \hat{c}_i)(\hat{c}_{i+1}^\dagger - \hat{c}_{i+1}).
 \end{aligned} \tag{1.68}$$

Also, $\hat{\sigma}_i^z \hat{\sigma}_{i+1}^z$ is transformed into

$$\hat{\sigma}_i^z \hat{\sigma}_{i+1}^z = (2\hat{c}_i^\dagger \hat{c}_i - 1)(2\hat{c}_{i+1}^\dagger \hat{c}_{i+1} - 1). \tag{1.69}$$

With the results from Equation (1.67) and Equation (1.68), we can transform the universal Hamiltonian in Equation (1.12) into the Fermionic representation:

$$\begin{aligned}
 \frac{\hat{H}}{J} &= -\sum_{i=1}^{N-1} [(\hat{c}_i^\dagger - \hat{c}_i)(\hat{c}_{i+1}^\dagger + \hat{c}_{i+1}) - \alpha(\hat{c}_i^\dagger + \hat{c}_i)(\hat{c}_{i+1}^\dagger - \hat{c}_{i+1})] \\
 &\quad - \beta \sum_{i=1}^{N-1} (2\hat{n}_i - 1)(2\hat{n}_{i+1} - 1) - g \sum_{i=1}^N (2\hat{n}_i - 1).
 \end{aligned} \tag{1.70}$$

When $\beta = 0$, the Hamiltonian describes a free fermion model, which is exactly solvable.

We note that in the quantum chemistry community^[145-148], another definition of Jordan-Wigner transformation is to map the spin-up state $|\uparrow\rangle = |0\rangle_s$ to the fermionic hole state $|0\rangle_f$ and the spin-down state to $|\downarrow\rangle = |1\rangle_s$ to the fermionic occupied state $|1\rangle_f$. In such a setting, the transformation becomes $\hat{c}_i^\dagger = \prod_{j<i} \hat{\sigma}_j^z \hat{\sigma}_i^-$.

1.3.4 Exactly Solvable Models

The one-dimensional XY quantum spin chains without the ZZ-type couplings can be exactly solved by the way of transforming into the spinless free fermionic systems through the aforementioned Jordan-Wigner transformation. Apart from this technique, the exact eigenvalues and eigenvectors of the one-dimensional quantum Heisenberg spin chain with the nearest interactions has been solved by Bethe^[149] in 1931. The generic form of the Bethe ansatz for a many-body wave function is^[150],

$$|\psi\rangle = \sum_{1 \leq n_1 < \dots < n_r \leq N} a(n_1, \dots, n_r) |n_1, \dots, n_r\rangle, \quad (1.71)$$

$$a(n_1, \dots, n_r) = \sum_{\mathcal{P} \in S_r} \exp \left(i \sum_{j=1}^r k_{\mathcal{P}_j} n_j + \frac{i}{2} \sum_{i < j} \theta_{\mathcal{P}_i \mathcal{P}_j} \right), \quad (1.72)$$

where N is the sizes of the spin chain, r is the number of down spins, $|n_1, \dots, n_r\rangle$ is the spin configuration under the computational basis, the summation $\mathcal{P} \in S_r$ is over all $r!$ permutations of the labels $\{1, 2, \dots, r\}$, k_i is the momentum of the i -th particle, $\theta_{ij} = -\theta_{ji}$ is the scattering phase shift function for each (k_i, k_j) pair. The momentum k_i and the scattering phase θ_{ij} are subjected to the following Bethe ansatz equations^[111],

$$2 \cot \frac{\theta_{ij}}{2} = \cot \frac{k_i}{2} - \cot \frac{k_j}{2}, \quad i, j = 1, \dots, r, \quad (1.73)$$

$$N k_i = 2\pi \lambda_i + \sum_{j \neq i} \theta_{ij}, \quad i = 1, \dots, r, \quad (1.74)$$

where the integers $\lambda_i \in \{0, 1, \dots, N-1\}$ are the Bethe quantum numbers. Different from the free fermion case, models solvable by the Bethe ansatz are not free. The interaction of two magnons k_i and k_j is reflected on the two-body scattering phase θ_{ij} . Their values can be analytically or numerically solved by iterating all combinations of λ_i , and thus determine the eigenvalues of the system,

$$E - E_0 = J \sum_{j=1}^r (1 - \cos k_j), \quad (1.75)$$

where E_0 is the energy of the reference state $|0, 0, \dots, 0\rangle$. We supplement an explicit solution of $N = 5$ Heisenberg spin chain in the *Mathematica* notebook^[70,151].

Another useful tool for analytically computing the partition function is the transfer matrix technique^[152-155]. This method was used by Onsager^[156] and Kaufman^[157] to exactly solve the two-dimensional *classical* Ising model in a $m \times n$ rectangular lattice in

the absence of external magnetic fields, whose partition function is shown as

$$\begin{aligned}
 Z = & \sum_{\{s_i = \pm 1\}_{i=1}^{m \times n}} \exp \left(\beta \sum_{\langle ij \rangle} J s_i s_j \right) = \frac{1}{2} [2 \sinh(2\phi)]^{mn/2} \\
 & \times \left\{ \prod_{j=1}^n \left[2 \cosh \left(\frac{m}{2} \epsilon_{2j-1} \right) \right] + \prod_{j=1}^n \left[2 \sinh \left(\frac{m}{2} \epsilon_{2j-1} \right) \right] \right. \\
 & \left. + \prod_{j=1}^n \left[2 \cosh \left(\frac{m}{2} \epsilon_{2j-2} \right) \right] - \prod_{j=1}^n \left[2 \sinh \left(\frac{m}{2} \epsilon_{2j-2} \right) \right] \right\}, \quad (1.76)
 \end{aligned}$$

where $\beta \equiv k_B T$, $\phi \equiv \beta J$, $s_i \in \{-1, 1\}$ is the i -th classical spin variable, k_B is the Boltzmann constant, T is the temperature for the canonical ensemble, J is the exchange coupling strength, and $\langle ij \rangle$ denotes the summation is over the nearest-neighbor sites. The variable ϵ_k is determined by the following transcendental equation:

$$\cosh \epsilon_k = \cosh(2\theta) \cosh(2\phi) - \cos(\pi k/n) \sinh(2\theta) \sinh(2\phi), \quad (1.77)$$

where $k \in \{0, 1, \dots, 2n-1\}$, and θ is the dual of ϕ which fulfills $\tanh(\theta) = \exp(-2\phi)$. By the Kramers-Wannier duality, the phase transition takes at $\theta = \phi = 1/2 \sinh^{-1}(1) = 1/2 \ln(\sqrt{2} + 1)$, which gives the critical temperature at $k_B T_c / J = 2 / \sinh^{-1}(1) = 2 / \ln(1 + \sqrt{2}) \approx 2.26919$. For the full procedure, we refer to Chapter 15 in Huang^[154] and the online *Mathematica* notebook^[70], here we sketch the essential steps:

- (i) Write down the transfer matrix under the basis of the spin configuration between two adjacent rows;
- (ii) Convert the above transfer matrix into the form of Pauli matrices appeared in the exponents;
- (iii) Use the Jordan-Wigner transformation to transform the transfer matrix into the representation of Majorana operators;
- (iv) Since Majorana operators follow Clifford algebra (see Appendix A.1.4 for the mathematical background), the $2^n \times 2^n$ transfer matrix are reduced into $\text{SO}(2n)$ rotations under the Majorana basis;
- (v) The eigenvalues of $\text{SO}(2n)$ rotations are found to be ϵ_k , whose combinations build up the final partition function in Equation (1.76).

In Appendix B, we give an analytical solution of the honeycomb Ising model via the transfer matrix technique, as it was shown that its partition function could be used to prove the barren plateau problem in quantum machine learning^[158] (see Section 2.3.2 for a detailed discussion). We remark in passing that, however, neither the two dimensional

classical Ising model in the presence of a field nor the three dimensional one has been exact solved hitherto^[159].

1.3.5 Cavity Quantum Electrodynamics

Cavity quantum electrodynamics (QED) studies the interaction of light and matter at the fundamental level: the coherent interaction of single atoms with single photons^[160-161]. Compared with the conventional electronic transport that has been widely adopted to investigate Majorana fermions physics, setups build upon cavity QED can non-invasively detect equilibrium and out-of-equilibrium electronic and spin systems. It has been proposed to use cavity QED setup to detect the topological features of the p -wave superconductor^[162], the braiding of Majorana zero mode^[163], constructing the quantum internet^[11], etc.

The basic idea behind the cavity QED detection scheme is to couple the interested system \hat{H}_s (e.g., quantum spin chains, topological insulators and superconductors) to a microwave cavity $\hat{H}_c = \omega_0 \hat{a}^\dagger \hat{a}$ by the coupling Hamiltonian $\hat{H}_{s-c} = \beta \hat{O}(\hat{a}^\dagger + \hat{a})$, as shown schematically in Figure 1.3, where $\hat{a}(\hat{a}^\dagger)$ is the photon annihilation (creation) operator, ω_0 is the frequency of the cavity and β is the electron-photon coupling strength. This setup allows us to extract various properties of the interested observables \hat{O} of the system, such as its spectrum and its electronic distribution function through photonic transport measurements. The whole Hamiltonian of the cavity and the detected system reads

$$\hat{H}_{\text{sys}} = \hat{H}_s + \hat{H}_{s-c} + \hat{H}_c. \quad (1.78)$$

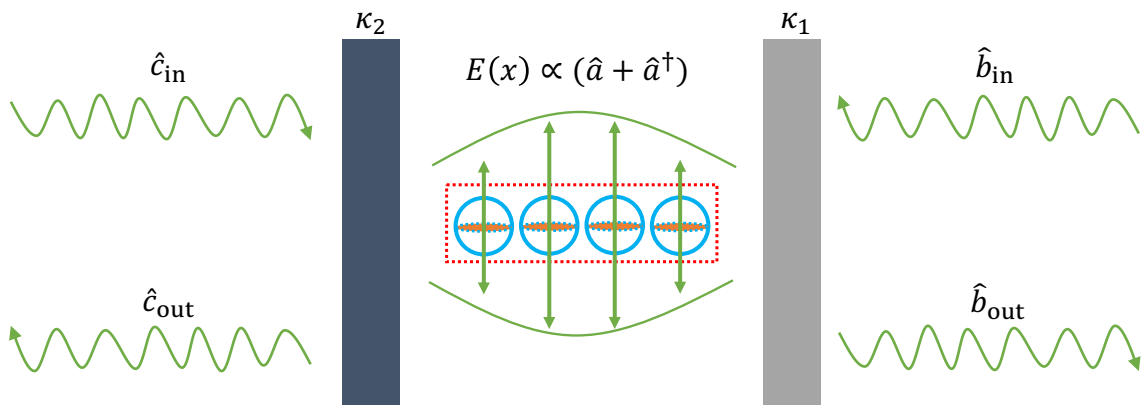


Figure 1.3 A cavity QED setup for detecting observables in quantum spin chains.

The cavity field $E(x)$ is described by the bosonic operators \hat{a} and \hat{a}^\dagger . For a two-sided cavity, there could be two input/output fields $\hat{b}_{\text{in,out}}$ and $\hat{c}_{\text{in,out}}$ sent from the right and left mirrors. For a one-sided cavity, one can set the decay rate $\kappa_1 = \kappa$ and $\kappa_2 = 0$ for simplicity.

Now we probe the whole system by photons injected from the bath,

$$\hat{H}_b = \sum_q \omega_q \hat{b}_q^\dagger \hat{b}_q, \quad (1.79)$$

$$\hat{H}_{c-b} = -i \sum_q (f_q \hat{a}^\dagger \hat{b}_q - f_q^* \hat{b}_q^\dagger \hat{a}), \quad (1.80)$$

$$\hat{H} = \hat{H}_{\text{sys}} + \hat{H}_{c-b} + \hat{H}_b, \quad (1.81)$$

where the rotating wave approximation is applied to the coupling Hamiltonian in Equation (1.80). Additionally, $\hat{b}_q(\hat{b}_q^\dagger)$ are the annihilation (creation) operators for the bath modes with energy ω_q , with q labeling their quantum numbers, and the complex coefficients f_q are coupling strengths between the cavity and the external bath. Under the Markovian approximation (see Appendix E2 in Clerk et al.^[164] for a detailed calculation), one can find the equation of motion for the cavity field,

$$\dot{\hat{a}} = i[\hat{H}, \hat{a}] = -i(\omega_0 \hat{a} + \beta \hat{O}) - \frac{\kappa}{2} \hat{a} - \sqrt{\kappa} \hat{b}_{\text{in}}, \quad (1.82)$$

where we denote $\kappa = 2\pi\rho|f|^2$ to be the cavity decay rate, with ρ the bath density of states and f the average coupling between the cavity and the bath modes. The relationship between the output field and the input one satisfies $\hat{b}_{\text{out}} = \hat{b}_{\text{in}} + \sqrt{\kappa} \hat{a}$.

For the two-sided cavity investigated in Dmytruk et al.^[162], the transport property can be captured by the complex transmission coefficient $\tau = Ae^{i\phi}$ that connects both the output and input photonic field. In the weakly coupled limit, they find

$$\tau(\omega) = \frac{\kappa}{-i(\omega - \omega_0) + \kappa - i\Pi(\omega)}, \quad (1.83)$$

where $\Pi(\omega)$ is the correlation function (susceptibility) which contains information about the spectrum of the detected system. When the probing field is close to the resonance frequency $\omega \approx \omega_0$, the phase and amplitude response of the cavity hold the following identities with the susceptibility $\Pi(\omega)$:

$$\delta\phi = \Pi'(\omega)/\kappa, \quad \delta A/A_{\text{in}} = \Pi''(\omega)/\kappa, \quad (1.84)$$

$$\delta\phi = \phi_{\text{out}} - \phi_{\text{in}}, \quad \delta A = A_{\text{in}} - A_{\text{out}}, \quad (1.85)$$

$$\Pi'(\omega) = \text{Re}[\Pi(\omega)], \quad \Pi''(\omega) = \text{Im}[\Pi(\omega)]. \quad (1.86)$$

We note in passing that the cavity QED has been also introduced into superconducting circuits, which is now known as the circuit QED. This approach has significantly improved the controllability of superconducting qubits, and has already been used to operate tens of superconducting qubits with high fidelity^[161,165].

1.3.6 Open Quantum Systems

For any physical system, however, the exchange of energy with the environment is inevitable, whereby the non-Hermitian Hamiltonians are more appropriate to describe open quantum systems. For example, wave systems with gain and loss (e.g., photonic and acoustic)^[166-168], and solid-state systems where electron-electron interactions or disorders introduce a non-Hermitian self-energy into the effective Hamiltonian of quasi-particle^[169-171]. In such situations, the dynamics of a system connected to several baths can be modeled by a Markovian interaction. The relevant equation of motion for the reduced density matrix ρ of the open system is the Lindblad master equation^[172-173]

$$\frac{d\rho}{dt} = i[\rho, \hat{H}] + \sum_n \left(\hat{L}_n \rho \hat{L}_n^\dagger - \frac{1}{2} \left\{ \hat{L}_n^\dagger \hat{L}_n, \rho \right\} \right), \quad (1.87)$$

where the jump operators L_n account for the dissipations. We can rewrite the Lindblad equation as^[174]

$$\frac{d\rho}{dt} = i \left(\rho \hat{H}_{\text{eff}}^\dagger - \hat{H}_{\text{eff}} \rho \right) + \sum_n \hat{L}_n \rho \hat{L}_n^\dagger, \quad (1.88)$$

where the effective non-Hermitian Hamiltonian

$$\hat{H}_{\text{eff}} = H - \frac{i}{2} \sum_n \hat{L}_n^\dagger \hat{L}_n, \quad (1.89)$$

describes the dynamics at short times.

In addition, the well-established theory of quantum transport that has been exploiting the non-Hermitian physics over decades^[61]. Generally, one will consider a junction to be a thermal reservoir (lead), which induces a self-energy on the surface of the system, thus leads to the effective non-Hermitian system Hamiltonian

$$\hat{H}_{\text{NH}} = \hat{H} + \Sigma_L^r(\omega), \quad (1.90)$$

where \hat{H} is the bare (isolated) Hermitian Hamiltonian, and $\Sigma_L^r(\omega)$ refers to the retarded self-energy at energies (frequencies) ω close to the chemical potential, accounting for the coupling to the lead. Note that, such non-Hermitian Hamiltonian is very sensitive around some exceptional points. The emergence of exceptional points in quasi-particle band structures can dramatically enrich their topological classification in crystalline materials^[175].

1.4 Machine Learning

The field of machine learning is extremely broad and versatile, as we can have a glimpse from the definition given by Mitchell^[176],

Definition 1.1: A computer program is said to learn from experience E with respect to some class of tasks T and performance measure P , if its performance at tasks in T , as measured by P , improves with experience E .

In the last decades, owing to the increased computational power and the availability of vast amounts of data, machine learning, or more broadly, artificial intelligence^[23,26-29], has achieved remarkable successes in tasks ranging from natural language processing^[177] to astronomical data mining^[178-179]. In particular, machine learning plays an essential role in the growing field of data science. For instance, apart from building up an accretion disk model for both the black hole and neutron star X-ray binaries (see Appendix C for a brief introduction)^[180], one can also utilize machine learning tools to classify the central accretor directly based on the observational data^[181]. In the following subsections, we will introduce three main learning paradigms of machine learning, supervised learning, unsupervised learning, and reinforcement learning,.

1.4.1 Supervised Learning

Supervised learning is a paradigm of machine learning that requires the training set to be pre-labeled by a knowledgeable supervisor. In the training process, the model is fed with a training set of N input-output pairs $\{(x_1, y_1), (x_2, y_2), \dots, (x_N, y_N)\}$ that generated by an unknown function $y = f(x)$, where x_i is the feature vector of the i -th example and y_i is its label. The goal of the machine learning model is to find a hypothesis function h that approximates the true function f . The closeness between h and f is quantified by a loss function L . By use of suitable optimization methods (e.g., gradient descent), the model can find a function h^* in the hypothesis space that minimizes the loss function L as much as possible. The accuracy of a hypothesis is measured by a test set that contains different examples from the training set. After training, if the model could correctly predict the label of unseen dataset, then we say the hypothesis h^* generalizes well. Representative algorithms include artificial neural networks, support vector machine, naive Bayes, linear discriminant analysis, decision trees^[29].

1.4.2 Unsupervised Learning

Unsupervised learning is another framework for machine learning, whose training set does not include any labels. The learning model can identify patterns and relationships within the data without a supervisor. Typical tasks for unsupervised learning include k -mean clustering, principal component analysis (PCA), expectation-maximization algorithm, etc. The k -means clustering algorithm divides the training set into k different clusters of examples by iteratively refining the overall Euclidean distance with respect to their corresponding centroids. The PCA algorithm learns a low-dimensional representation of the input dataset via a singular value decomposition of its covariance matrix^[26].

We give some additional remarks of the semi-supervised learning, which takes a middle-ground approach. The learning model is provided with relatively small set of labeled training data, together with a larger amount of unlabeled data. The combination of the two data types allows machine learning model to label the untagged data from the experience learning from the labeled data^[26].

1.4.3 Reinforcement Learning

Reinforcement learning (RL) is a separate paradigm of machine learning which does not require a pre-labelled dataset. Different from unsupervised learning, reinforcement learning is trying to maximize a reward signal instead of trying to find a hidden structure. It enables an agent A to learn in an interactive environment E , by use of rewards and punishments as signals for positive and negative behaviors. Such an interactive mode of learning is typically formulated in the mathematical framework of a Markov decision process (MDP), which is an extension of Markov chain (see Appendix A.6.2). A Markov decision process is a 3-tuple $M = (S, \mathcal{A}, \mathcal{R})$, where

- S is a set of states called the state space;
- \mathcal{A} is a set of actions called the action space;
- \mathcal{R} is a set of rewards called the reward space.

The agent and environment interact at each of a sequence of discrete time steps. At each time step, the agent receives some representation of the environment's state, $S_t \in S$, and the agent may choose any action $A_t \in \mathcal{A}(s)$ that is available in state s . The process responds at the next time step by randomly moving into a new state S_{t+1} , and giving the agent a corresponding reward $R_{t+1} \in \mathcal{R} \subset \mathbb{R}$. The MDP and agent together thereby give

rise to a sequence,

$$\{S_0, A_0, R_1, S_1, A_1, R_2, S_2, A_2, R_3 \dots\}. \quad (1.91)$$

For a particular realization of these random variables, $s \in \mathcal{S}$ and $r \in \mathcal{R}$, there is a probability of those values occurring at time t , given particular values of the preceding state and action^[182], $\forall s', s \in \mathcal{S}, r \in \mathcal{R}, a \in \mathcal{A}(s)$,

$$p(s', r | s, a) = \Pr\{S_t = s', R_t = r | S_{t-1} = s, A_{t-1} = a\}. \quad (1.92)$$

In a Markov decision process, the probabilities given by $p : \mathcal{S} \times \mathcal{R} \times \mathcal{S} \times \mathcal{A} \rightarrow [0, 1]$ completely characterize the environment's dynamics. A policy is a function π that specifies the actions a that the decision maker will choose when in state s :

$$\pi : \mathcal{A} \times \mathcal{S} \rightarrow [0, 1]; \quad \pi(a|s) = \Pr\{A_t = a | S_t = s\}. \quad (1.93)$$

The goal of reinforcement learning is to find an optimal policy $\pi_s^* = \arg \max_{\pi} v_{\pi}(s)$, that would maximize the total cumulative reward of the agent:

$$v_{\pi}(s) = \mathbb{E}_{\pi} \left[\sum_{k=0}^{\infty} \gamma^k R_{t+k+1} | S_t = s \right], \quad \forall s \in \mathcal{S}, \quad (1.94)$$

where the discount factor $\gamma \in [0, 1]$. Using a recursive relation described by the Bellman equation, the value function can be estimated. The Bellman optimality equation requires $v_*(s)$ must equal the expected return for the best action from that state:

$$v_*(s) = \max_a \sum_{s', r} p(s', r | s, a) [r + \gamma v_*(s')]. \quad (1.95)$$

We will reach an equilibrium if we iteratively follow the iteration step,

$$v_{i+1}(s) \leftarrow \max_a \sum_{s', r} p(s', r | s, a) [r + \gamma v_i(s')]. \quad (1.96)$$

In the end, the optimal policy is given by

$$\pi^*(a|s) = \arg \max_{a \in \mathcal{A}(s)} q_*(s, a) = \arg \max_{a \in \mathcal{A}(s)} \sum_{s', r} p(s', r | s, a) [r + \gamma v_*(s')]. \quad (1.97)$$

We implement the above algorithm to solve the Grid-World Problem (see Page 60 in Sutton et al.^[182] for a brief introduction) in the *Mathematica* notebook^[70]. For more sophisticated tasks in the real world, however, the agent often faces the dilemma of exploring new states while maximizing its overall reward at the same time, which is known a trade-off between exploration and exploitation. Several algorithms (e.g, proximal policy optimization^[183], Q-learning^[184]) has been proposed to alleviate this dilemma. Combined with deep neural networks, nowadays deep reinforcement learning has achieve the

Table 1.1 Comparisons for different types of neural networks

Here we only summarize the properties of the most commonly used architecture. For some specific variants, their connections and parameter settings can be different.

	FNN	CNN	RNN	CapsNets	Transformer
Prevalent dataset	Tabular data	Images	Corpus	Images	Corpus/Images
Recurrent connections	No	No	Yes	No	No
Residual connections	No	No	No	No	Yes
Parameter sharing	No	Yes	Yes	Yes	Yes
Spatial relationship	No	Yes	No	Yes	Yes

state-of-the-art performance in the fields of robotics^[185], Go game^[30-31], autonomous driving^[186], etc.

1.4.4 Artificial Neural Networks

The artificial neural network is a computational tool whose architecture is loosely inspired by the human brain^[24-26]. Like the way that biological neurons signal to one another, the artificial neural network is typically constructed by multiple layers of connected artificial neurons, or perceptrons, which carry out calculations. As shown in Figure 1.4, artificial neural networks consist of an input layer, one or more hidden layers, and an output layer. Neural networks contain multiple hidden layers is commonly called deep neural networks. In most cases, deep neural networks are trained using the backpropagation method. There are numerous types of neural networks, such as Hopfield network^[187], Boltzmann machine^[188], restricted Boltzmann machine^[189], generative adversarial networks^[190], auto encoders^[191], etc. In the following contexts, we will focus on the representative ones^[26], i.e., the feedforward neural networks, convolutional neural networks, recurrent neural networks, capsule networks^[192-193] and the Transformer^[194]. We summarized their basic properties in Table 1.1.

1.4.4.1 Feedforward Neural Networks

The feedforward neural network is one of the simplest artificial neural networks, also known as the multi-layer perceptrons, which generally follows the following rules:

- (i) All nodes are fully connected;
- (ii) Activation flows from input layer to output, without back loops;
- (iii) There are multiple hidden layers between input and output.

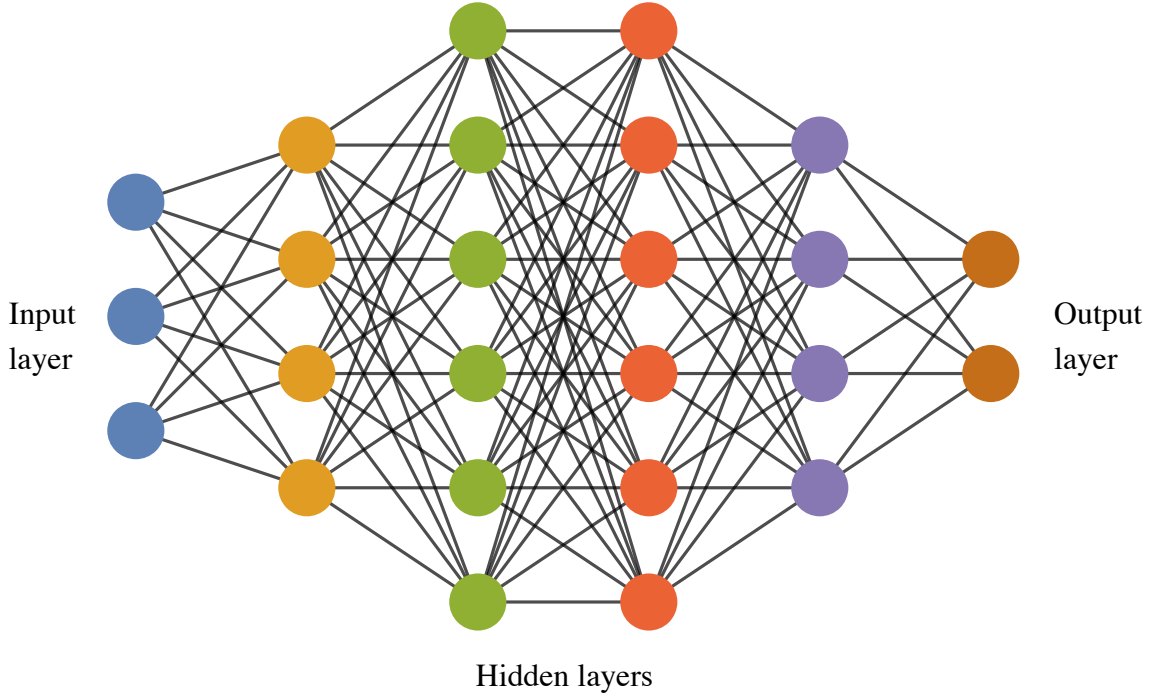


Figure 1.4 A feedforward neural network.

A simple fully connected feedforward neural network with six layers, comprised of one input layer, four hidden layers and one output layer.

Each neuron has an associated weight and bias. Those weights w_i and biases b_i form the trainable parameters of the network, which can number in the millions to billions. The input data can be represented as a vector $\vec{x} = \{x_i\}_{i=1}^n$, whose specific element x_i is fed into one corresponding neuron. The input layer processes the data as $a(\sum_{i=1}^n w_i x_i + b_i)$ with an activation function a , and sends this result into the next layer. There are numerous choices of activation functions^[26], such as step function, sigmoid function, Tanh function, rectified linear unit (ReLU), etc.

1.4.4.2 Convolutional Neural Networks

Convolutional neural networks (CNNs) are nowadays all the rage in the deep learning community. They are especially prevalent in image recognition tasks, e.g., classifying the handwritten digits in the MNIST dataset^[195] (see Figure 1.7). A simple CNN architecture for the MNIST classification is illustrated in Figure 1.5. The basic functionality of CNNs can be broken down into four key ingredients:

- (i) The input layer will be fed with the 28×28 pixel values of the image.
- (ii) The essence of the convolutional layer is filter, or kernel, which is a $w \times w$ -dimensional matrix. They can extract abstract information about the local structure

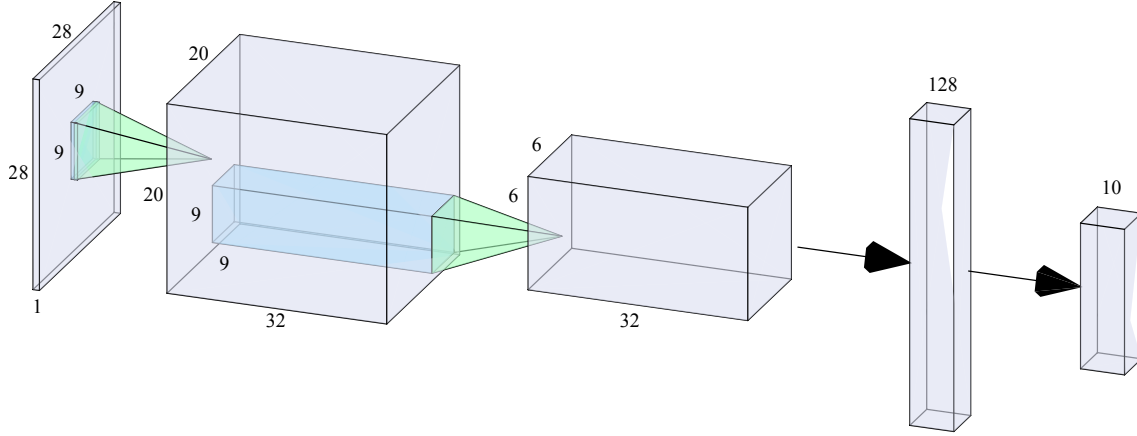


Figure 1.5 A convolutional neural network for classifying the MNIST dataset.

The MNIST handwritten data are processed through two convolutional layers with two 9×9 kernels (green polyhedra), $[28, 28, 1] \xrightarrow{\text{kernel: } 9 \times 9, \text{ stride: } 1} [20, 20, 32] \xrightarrow{\text{kernel: } 9 \times 9, \text{ stride: } 2} [6, 6, 32]$, and then passed through two fully connected feedforward neural networks (black arrows).

of the input data into feature maps using the convolution operation. Namely, the convolution layers compute new pixel values $x_{i,j}^l$ in the l -th layer from a linear combination of nearby ones in the preceding $(l-1)$ -th layer: $x_{i,j}^l = \sum_{a,b=1}^w w_{a,b} x_{i+a,j+b}^{l-1}$.

(iii) Between two convolutional layers, there could be an optional pooling layer reducing the unnecessary features. For example, the pooling layer scales down the feature map size by taking the maximum value from a few contiguous pixels, and is often followed by a nonlinear (activation) function.

(iv) These feature maps are then reshaped and processed through a fully connected layer. The classification results can be inferred from the output of the network.

1.4.4.3 Recurrent Neural Networks

Recurrent neural networks (RNNs) introduce a different type of cells—recurrent cells. Each recurrent cell takes one input data x^t and one hidden state h^t which is passed from a one-time step to the next. The complete formulation of a recurrent cell is,

$$h^t = g(W_{hh}h^{t-1} + W_{hx}x^t + b_h), \quad y^t = h^t, \quad (1.98)$$

which is illustrated in Figure 1.6. The sequential stack of these cells creates a complete RNN layer. We remark that the weight matrices W_{hh} , W_{hx} and bias b_h are shared across these recurrent cells. Such a looping constraint ensures that sequential information is captured in the input data. This type of neural networks is typically good at processing temporal data for predictions. The most common dataset is corpus, i.e., a collection of texts, since a word can be analyzed only in the context of sentences.

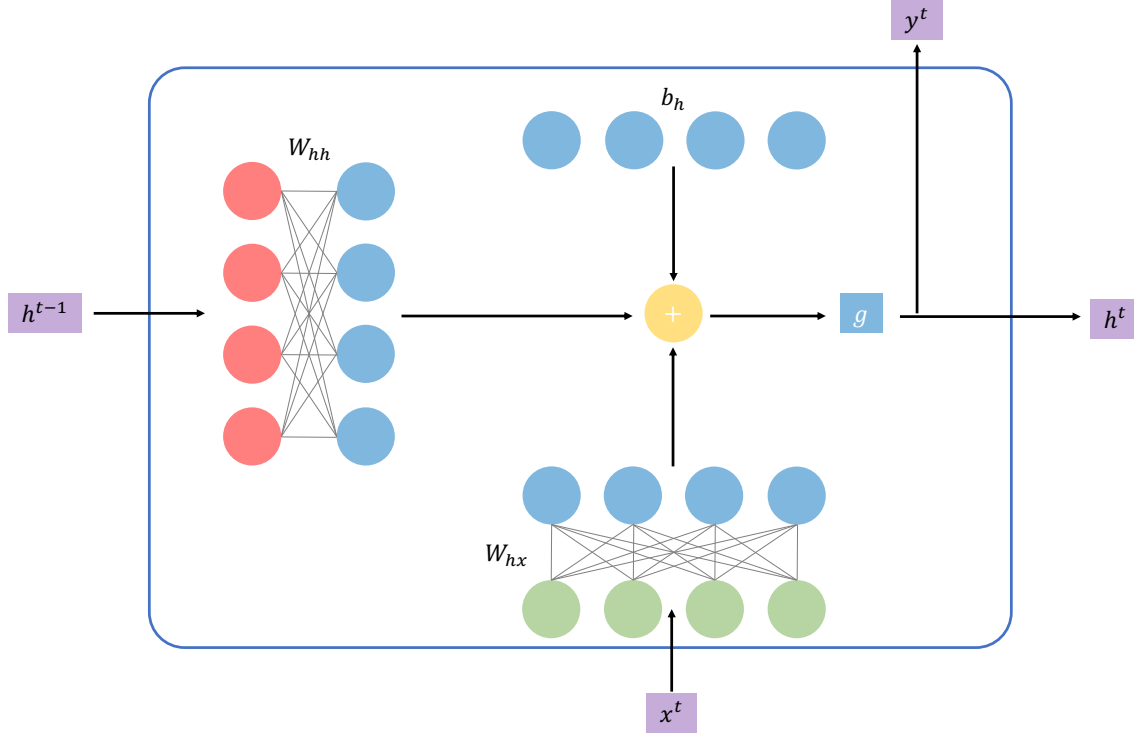


Figure 1.6 The flow of data and hidden state inside the RNN cell.

Here h^t and h^{t-1} are the hidden states from the time t and $t - 1$. x^t is the input at time t and y^t is the output at time t . There are two weight matrices W_{hh} and W_{hx} and one bias term b_h . In this simple illustration y^t is a copy of h_t .

There are many variations, such as the gate recurrent unit (GRU)^[196] and the long short-term memory (LSTM)^[197]. Specifically, LSTM networks introduce a memory cell that is able to process data with time gaps. Owing to such a special cell, LSTM networks could handle the problem of long-term dependencies much better than the conventional RNNs. Nowadays, LSTM networks allow machines to perform translations, classification and intent detection with the state-of-the-art accuracy until the advent of the Transformer network.

1.4.4.4 The Transformer

It is generally difficult to realize parallelization for the recurrent connections in recurrent neural networks, which hinders the performance of recurrent neural networks in processing temporal dataset. Yet in recent years, a novel neural network architecture—Transformer^[194]—has revolutionized the fields of both the natural language processing^[198] and the visual recognition^[199]. Different from recurrent neural networks, the Transformer networks do not have memory cells but are still able to process sequential data through a combination of two tricks:

- (i) Self-attention: The ability to focus on different positions of the input sequence to compute a representation of that sequence;
- (ii) Position-dependent embeddings: The word embeddings are supplemented by another set of vectors that indicate the position of the word in the sentence.

We can interpret the self-attention mechanism at the following high-level way. Suppose we would like to translate the following sentence:

The PhD student didn't want to write the thesis since he was too tired. The self-attention allows the machine learning model to associate “he” with “the PhD student” rather than “thesis”. More specifically, the idea is to apply three different linear transformations W_Q , W_K and W_V to each element of the input sequence to transform each word embedding into some other internal representation states called query (Q), key (K) and value (V). These states are then passed to the function that calculates the attention weights as follows (d_k is the embedding dimension of keys),

$$\text{Attention}(Q, K, V) = \text{softmax} \left(\frac{QK^T}{\sqrt{d_k}} \right) V, \quad (1.99)$$

which is known as the scaled-dot product attention. We note that in order to accomplish a natural language processing task in real life, one should equip the Transformer with more sophisticated structures, e.g., the encoder and decoder stacks, residual connections^[200], multi-head attention, and masked operation, etc. We would not elaborate on these technical details in this thesis but defer to the original paper—*Attention is All You Need*^[194].

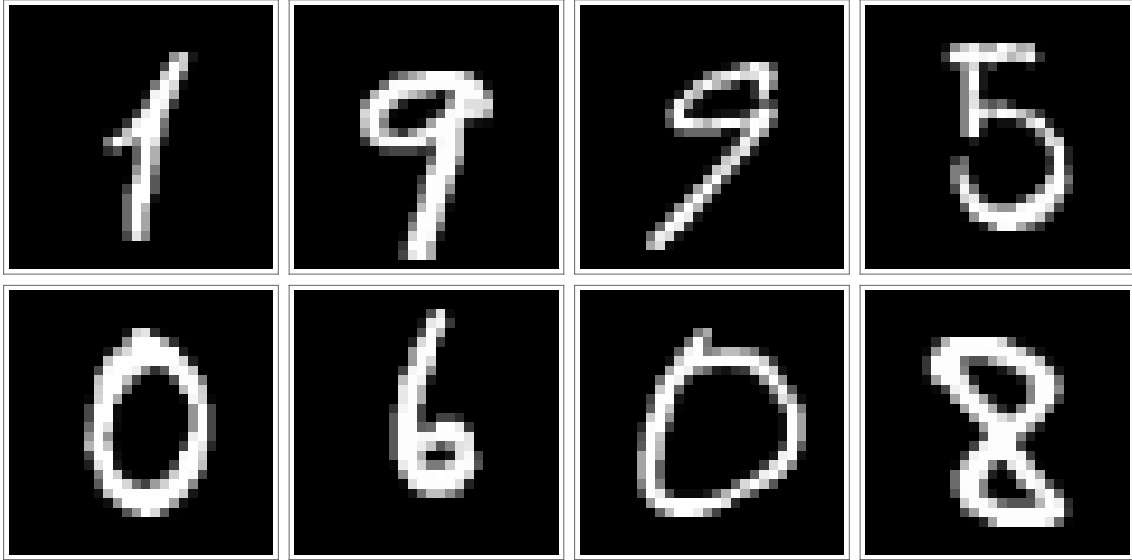


Figure 1.7 Samples of handwritten digits in the MNIST dataset.

There are 60000 training images and 10000 testing images in the MNIST database.^[195]

We remark that the Transformer architecture also contains some downsides. First, the self-attention weights are calculated from the entire history instead of only the inputs and the current hidden-state, which may be less efficient. Second, this architecture requires an appalling size of parameters. For instance, the number of parameters in the GPT-3 model is in the order of hundreds of billions^[198]. Furthermore, one usually requires a training dataset of a huge dimension and a massive computer network to carry out the training. An estimation of the training cost in terms of the electricity bill is in the order of \$4,600,000 for GPT-3, and it would take more than 350 years if only one single GPU was being used.

1.4.4.5 Capsule networks

Having learned the above commonly used neural network architectures, we specifically introduce technical details of the capsule network (CapsNet), as this novel architecture has been recently extended to the quantum domain and shows a potential exponential quantum speedup^[201]. The classical capsule network was first introduced in Hinton et al.^[192], and then equipped with a dynamic routing algorithm in Sabour et al.^[193] and an expectation-maximization routing algorithm in Hinton et al.^[202]. CapsNets are multi-layered networks, whose building block is a capsule that represented by a *vector*, instead of a *scalar* in Vanilla neural networks^[203]. The norm (length) of the vector reflects the probability of an *entity* being present, while the components (orientations) of the vector indicate the *features* of the entity. In computer graphics^[204], features refer to different types of instantiation parameters of an entity, such as its rotation, pose, hue, texture, deformation, etc. The capsule can learn to detect an entity in an object, together with its corresponding features.

The structure of CapsNets generally consist of three parts (see Figure 1.8). The first part is the convolutional layer that used in CNNs. In this layer, the model detects the basic local features of the input data. For the specific task demonstrated in Sabour et al.^[193], the MNIST handwritten data are processed through two convolutional layers:

$$[28, 28, 1] \xrightarrow[\text{kernel: } 9 \times 9, \text{ stride: } 1]{\text{ReLU Conv2d}} [20, 20, 256] \xrightarrow[\text{kernel: } 9 \times 9, \text{ stride: } 2]{\text{ReLU Conv2d}} [6, 6, 256] = [6, 6, 32 \times 8].$$

The second part is the PrimaryCaps layer, which not only captures the features of data, but also generates their combinations. In this layer, the above feature map is reshaped into $[n^p, v^p] = [6 \times 6 \times 32, 8]$, corresponding to 1152 capsule vectors living in the 8-dimensional Euclidean space. These capsule vectors are then fed into the third part — the DigitCaps layer. Therein, via dynamic routing between the PrimaryCaps layer and the DigitCaps

layer, the shape of the final output vector is $[n^D, v^D] = [10, 16]$, where n^D is equal to the number of categories for classification. The probability can be read from the norm of the vector, while its components represent the features of the entity, which can be further used to unbox the learning model and seek for its explainability.

The key feature of CapsNets is the dynamic routing algorithm^[193], whose pseudocode is presented in Algorithm 1.1. Consider the dynamic routing algorithm between the l -th and the $(l + 1)$ -th capsule layer in the classical CapsNets (as shown in Figure 1.9). Given the i -th capsule \mathbf{v}_i^l in the l -th layer, we first calculate the prediction vector $\mathbf{u}_{j|i}^{l+1}$ of the j -th capsule in the $(l + 1)$ -th layer by multiplying a weight matrix $\mathbf{W}_{ij} \in \mathbb{R}^{v_d \times v_p}$ (trained by backpropagation),

$$\mathbf{u}_{j|i}^{l+1} = \mathbf{W}_{ij} \mathbf{v}_i^l, \quad \forall i \in \mathcal{L}_l, j \in \mathcal{L}_{l+1}. \quad (1.100)$$

Then we sum over all the prediction vectors $\mathbf{u}_{j|i}^{l+1}$ in the l -th layer with routing coefficients r_{ij} to generate the pre-squashed vector \mathbf{s}_j^{l+1} of the j -th capsule in the $(l + 1)$ -th layer,

$$\mathbf{s}_j^{l+1} = \sum_i r_{ij} \mathbf{u}_{j|i}^{l+1}, \quad (1.101)$$

where r_{ij} quantifies the probability that the capsule vector i may affect the capsule vector j . Finding groups of similar $\mathbf{u}_{j|i}^{l+1}$ can be seen as a clustering problem, thus we can interpret r_{ij} as the probability that capsule i is grouped to cluster j , which requires $\sum_j r_{ij} = 1$. To this end, we introduce a set of digits (unnormalized routing coefficients) b_{ij} , which is

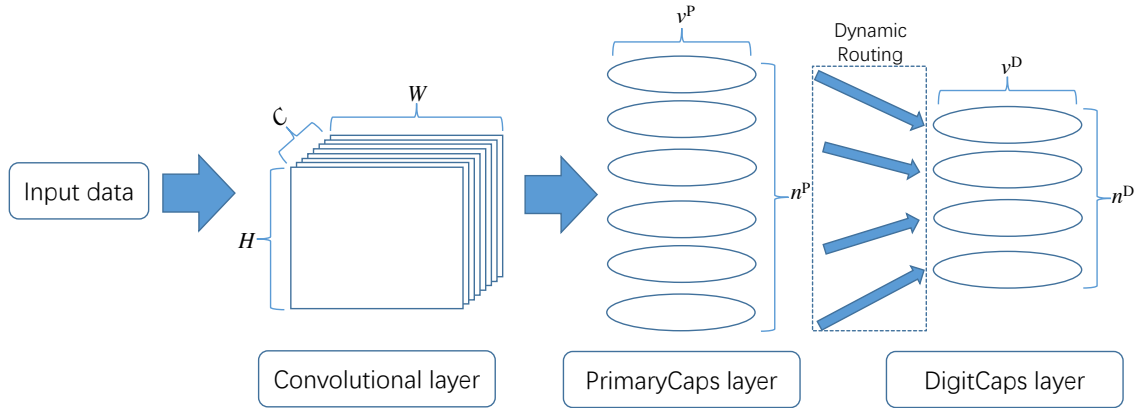


Figure 1.8 The structure of capsule networks with three essential layers.

The input data are first processed through the convolutional layer. Then the corresponding feature maps $[H, W, C]$ are fed into the PrimaryCaps layer and reshaped into n^p capsules living in a v^p -dimensional Euclidean space. Owing to the dynamic routing algorithm, the DigitCaps layer (n^D capsules in a v^D -dimensional space) is able to extract features of entities from lower-level capsules and capture their geometric relationships. The norm of the active capsule in the DigitCaps layer indicates the probability of a specific class being detected^[201].

Algorithm 1.1 Dynamic routing for classical capsule networks

Require: the index of layer l , the number of iteration e , the prediction vector $\mathbf{u}_{j|i}^{l+1} = \mathbf{W}_{ij}\mathbf{v}_i^l$

Ensure: the capsule vector \mathbf{v}_j^{l+1} in the $(l+1)$ -th layer

$\forall i \in \mathcal{L}_l, j \in \mathcal{L}_{l+1} : b_{ij} \leftarrow 0$

for e iterations **do**

$\forall i \in \mathcal{L}_l, j \in \mathcal{L}_{l+1} : r_{ij} \leftarrow \text{softmax}_j(b_{ij})$

$\forall j \in \mathcal{L}_{l+1} : \mathbf{s}_j^{l+1} \leftarrow \sum_i r_{ij} \mathbf{u}_{j|i}^{l+1}$

$\forall j \in \mathcal{L}_{l+1} : \mathbf{v}_j^{l+1} \leftarrow \text{squash}(\mathbf{s}_j^{l+1})$

$\forall i \in \mathcal{L}_l, j \in \mathcal{L}_{l+1} : b_{ij} \leftarrow b_{ij} + \mathbf{u}_{j|i}^{l+1} \cdot \mathbf{v}_j^{l+1}$.

end for

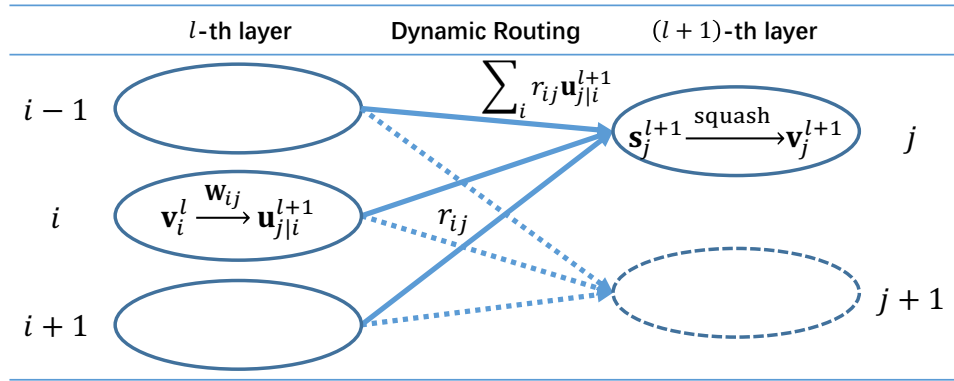


Figure 1.9 An illustration of the classical dynamic routing.

The prediction vector $\mathbf{u}_{j|i}^{l+1}$ of the j -th capsule in the $(l+1)$ -th layer is calculated by $\mathbf{u}_{j|i}^{l+1} = \mathbf{W}_{ij}\mathbf{v}_i^l$, where \mathbf{W}_{ij} is a weight matrix and \mathbf{v}_i^l is the i -th capsule in the l -th layer. The unnormalized capsule \mathbf{s}_j^{l+1} is given by $\mathbf{s}_j^{l+1} = \sum_i r_{ij} \mathbf{u}_{j|i}^{l+1}$ with routing coefficients r_{ij} . The output capsule is obtained by $\mathbf{v}_j^{l+1} = \text{squash}(\mathbf{s}_j^{l+1})$ with a nonlinear function $\text{squash}^{[201]}$.

related to the routing coefficient r_{ij} by a softmax function:

$$r_{ij} = \text{softmax}_j(b_{ij}) \equiv \frac{\exp(b_{ij})}{\sum_j \exp(b_{ij})}. \quad (1.102)$$

We remark that the nonlinearity of the classical CapsNets is contributed by the so-called “squashing” operation:

$$\mathbf{v}_j^{l+1} = \text{squash}(\mathbf{s}_j^{l+1}) \equiv \frac{\|\mathbf{s}_j^{l+1}\|^2}{1 + \|\mathbf{s}_j^{l+1}\|^2} \frac{\mathbf{s}_j^{l+1}}{\|\mathbf{s}_j^{l+1}\|}. \quad (1.103)$$

The squash function forces short vectors to get shrunk to almost zero length, and long vectors to get shrunk to a length slightly below one, which is analogous to $\text{sigmoid}(x) \equiv 1/(1 + e^{-x})$ in the classical neural networks. The essence of the dynamic routing algorithm is the so-called routing-by-agreement mechanism, which is able to exact the geometric relationship g_{ij} between prediction vectors $\mathbf{u}_{j|i}^{l+1}$ and the possible output vector \mathbf{v}_j^{l+1} . Note

that capsules vectors are living in the Euclidean space, the geometric relationship can be characterized by the dot product between them:

$$g_{ij} = \mathbf{u}_{j|i}^{l+1} \cdot \mathbf{v}_j^{l+1}. \quad (1.104)$$

At the beginning of the routing algorithm, all the routing digits b_{ij} are initialized to zero, which leads to a uniformly routing path between layers. During iterations, the routing digits are then iteratively refined by the agreement g_{ij} between the current output capsule \mathbf{v}_j^{l+1} and the prediction vector $\mathbf{u}_{j|i}^{l+1}$,

$$b_{ij} \leftarrow b_{ij} + g_{ij}. \quad (1.105)$$

Such a routing-by-agreement mechanism has been demonstrated far more effective than the max-pooling method used in CNNs^[193,202]. In short, CapsNet is a neural network which replaces scalar-output neurons with vector-output capsules and max-pooling with routing-by-agreement.

In order to detect possibly multiple handwritten digits in an image, the classical CapsNets use a separate margin loss L_c for each class c digit present in the image^[193]:

$$L_c = T_c \max(0, m^+ - \|\mathbf{v}_c^D\|)^2 + \lambda(1 - T_c) \max(0, \|\mathbf{v}_c^D\| - m^-)^2, \quad (1.106)$$

where \mathbf{v}_c^D is the c -th capsule in the DigitCaps layer, T_c is a indicator function for a specific class c , i.e., $T_c = 1$ if and only if an object of class c is present. The margins are set as $m^+ = 0.9$ and $m^- = 0.1$. Here, λ is a down-weighting term that prevents the initial learning from shrinking the activity vectors of all classes. The total margin loss $L_M = \sum_c L_c$ is just the sum of the losses of all classes. With such a loss function at hand, one can routinely utilize the backpropagation algorithm to train the parameters in the weight matrices \mathbf{W}_{ij} . We remark that the routing coefficients r_{ij} are not trainable parameters, but values determined by the dynamic routing algorithm.

Apart from the aforementioned three layers for classification, one can add additional reconstruction layers to enable capsules to encode the corresponding features of input data. Specifically, the most active capsule in the DigitCaps layer can be fed into a decoder which consist of three fully connected layers. After minimizing the mean square error L_{MSE} between the outputs of the logistic units and the original pixel intensities, one can use initiation parameters in the most active capsule to reconstruct the input image. In this vein, both the margin loss and the MSE loss should be optimized simultaneously, $L = L_M + \gamma L_{\text{MSE}}$, where γ is a small regularization term that scales down L_{MSE} so that it does not dominate L_M during training.

1.4.5 Towards Explainability

While neural networks can learn to solve enormously diverse tasks, the inner workings of these models remain elusive and are often considered to be a black box. There is a recent and ongoing high demand for understanding the way a specific model processes information and the underlying reasons for the decisions made by the model, which leads to emergence of field of explainable AI^[205].

There are many attribution techniques in the body of literature on machine learning and statistics, including stepwise forward feature selection, feature occlusion, attention weights and saliency maps^[33]. Some recent efforts have been initiated to interpret behavior of AI in physics^[206-208]. For instance, through adapting the disentanglement of variables and comes from the field of computer vision, SciNet can learn a heliocentric worldview^[206] directly based on astronomical data, without any prior information.

Switching to the quantum domain, however, a generally explainable quantum AI is still in its infancy. Recently, Liu, Shen, Li, Duan, and Deng^[201] adopts the classical capsule network into the field of quantum machine learning, which showcases a quantum speedup and indicates a potential explainability, i.e., a particular subspace of the capsule may corresponds to a human-understandable feature of the input data. In addition, the quantum neural tangent kernel is a useful tool to provide a rigorous guarantee on the convergence of quantum machine learning model, which enables us to understand the training dynamics in the limit of lazy training^[209].

CHAPTER 2 QUANTUM MACHINE LEARNING IN THE NISQ ERA

Quantum machine learning studies the interplay between machine learning and quantum physics^[36-37,39,210]. Depending on whether the data or the algorithm are class (C) or quantum (Q), we can classify quantum machine learning into four general settings^[37,54]: CC, CQ, QC and QQ. The classical machine learning introduced in Chapter 1 belongs to CC, i.e., using classical algorithms for classical data. Over the past two decades, machine learning has achieved dramatic success^[25,211]. Many problems that were notoriously challenging for artificial intelligence, such as playing the game of Go^[30-31] or predicting protein structures^[212], have been cracked recently. This gives rise to opportunities for using machine-learning techniques to solve difficult problems in quantum science, namely, the CQ approach. Indeed, machine-learning ideas and tools have been invoked in various applications in quantum physics, including representing quantum many-body states^[41,48], quantum-state tomography^[42,213], nonlocality detection^[46], topological quantum compiling^[214], etc. In particular, a number of supervised and unsupervised learning methods has been used to classify phases of matter and identify phase transitions^[50-51,215-223], albeit some adversarial issues (a tiny adversarial perturbation may lead to a wrong classification result) need to be addressed^[224-225]. Furthermore, several classical machine learning algorithms (e.g., reinforcement learning and genetic algorithms) have been exploited to search a well-performing quantum circuit with a smaller depth^[226-228]. This task is of crucial importance for the experimental demonstration of quantum machine learning on the noisy intermediate-scale quantum (NISQ) devices^[60], as the depth of the quantum circuits would be limited due to undesirable noises.

On the other hand, the idea of quantum computing has revolutionized the theories and implementations of computation^[1], which brings in the QC setting where one can use quantum computers to process classical data. In particular, quantum algorithms may offer unprecedented prospects to enhance, speed up, or innovate machine learning^[52-59]. Moreover, in the QQ framework, quantum dataset can be directly processed in the quantum device. Without a doubt, the studies of the interplay between machine learning and quantum physics will benefit both fields, and the emerging research frontier of quantum machine learning has become one of today's most rapidly growing interdisciplinary

fields^[36-37,39,210]. Yet we should keep in mind that the above data-algorithm classification is very rough. Usually there are hybrid algorithms that combine the quantum and classical approach. For instance, a hybrid quantum-classical framework—variational quantum eigensolver—has been proposed to find the ground state of a quantum Hamiltonian^[229-231]. Therein, the parameterized quantum circuits use the classical stochastic gradient descent algorithm to optimize the parameters of quantum circuits.

In this Chapter, we will first introduce the NISQ era and the near term progress for quantum simulation. We will also review some popular quantum linear algebra algorithms and variation quantum algorithms for machine learning. Along this way, we will specifically study the general framework of quantum artificial neural networks, or quantum classifiers. Therein, I will examine their expressibility, together with potential challenges, e.g., vanishing gradient and adversarial samples. We defer to Chapter 3 for a thorough discussion about quantum architecture search for NISQ devices.

2.1 Quantum Simulation in the NISQ Era

In recent years, many scientific disciplines have come together towards the development of quantum algorithms and their experimental realization. Most of the originally proposed quantum algorithms assume ideal logic qubits, which should be supplemented with quantum error correction techniques in real experimental implementations^[232-234]. There are many protocols for quantum error correction, amongst which the surface code is widely adopted in the superconducting setups^[235-236]. Assuming an error rate is one-tenth of the threshold rate 0.75%, a fault-tolerant logical qubit engineered in a surface code requires 10^3 – 10^4 physical qubits. Under this circumstance, if we want to factor a 2000-bits integer by the Shor’s algorithm^[5], the number of physical qubits we needed is about 220×10^6 physical qubits, operating for about one day^[237]. However, this is extremely impractical for currently realized quantum computers, which are dubbed noisy intermediate-scale quantum (NISQ) devices^[60]. Neither the fidelity nor the number of physics qubits is within current experimental capabilities of one specific platform. One of the goals in the NISQ era is to extract the maximum quantum computational power based on a few hundred noisy qubits^[238-239]. In the regard, quantum simulation provides a proof-of-principle demonstration of quantum primacy in the near term^[240].

2.1.1 Analog Quantum Simulation

As the Hilbert space increases exponentially with the size of the system, simulating a quantum system is a notoriously hard problem for classical computers. To tackle this long-standing problem, Feynman^[4] proposed to manipulate and probe the dynamics of a well-controlled quantum system \hat{H}_{sim} to learn about features of another one \hat{H}_{sys} which we do not have direct access to. This groundbreaking idea has spurred the field of analog quantum simulation^[9-10,241]. The core idea is establish a mapping between these two systems $\hat{H}_{\text{sim}} \leftrightarrow \hat{H}_{\text{sys}}$. There are many experimental platform for analog simulation, e.g., trapped ions^[80-84], nitrogen-vacancies in diamonds^[88,98], ultracold atoms^[94-97]. An important advantage of analog quantum simulation in the NISQ era is that, the noisy measurement results could still be useful to obtain some qualitative conclusions, up to a certain tolerance level^[10].

Here we briefly introduce adiabatic quantum computation, as it can be regarded as a special case of quantum simulation^[10]. Adiabatic quantum computation is another paradigm of quantum computing that goes beyond the description of quantum circuit model. The adiabatic theorem of quantum mechanics ensures that the system will always remain at the instantaneous ground state, if the tuning parameter $0 \leq t \leq T$ of the system Hamiltonian $\hat{H}(t)$ varies slowly enough. Based on this theorem, the computation can be achieved by a slow continuous transformation of an initial Hamiltonian $\hat{H}(0)$ into a final Hamiltonian $\hat{H}(T)$, whose ground state encodes the solution. The runtime for the entire algorithm is bounded by $T = \mathcal{O}(1/g_{\text{min}}^2)$, where g_{min}^2 is the minimum spectral gap for $\hat{H}(t)$ ^[242]. On the other hand, we can slightly relax the requirement of adiabatic evolution and exploit quantum fluctuations to explore solution space, which is known as the quantum annealing. Nowadays, adiabatic quantum computation and quantum annealing have been broadly used for solving hard optimization problems, e.g., the NP-complete combinatorial problems: 3SAT and maximum cut^[243].

2.1.2 Digital Quantum Simulation

In contrast to analog quantum simulation, digital quantum simulators decompose the unitary operator to be simulated into a temporal sequence of gates that are implemented on a quantum processor^[238]. In generally, the digital quantum simulator is engineered to be able to efficiently apply a universal gate set. For a concrete example, the simulation scheme of a fermionic system on a quantum computer consists of the following steps^[148]:

- (i) Hamiltonian mapping: In order to represent the fermionic creation and annihilation operators in terms of operations on qubits, we must map the fermionic occupation number basis vectors into the states of qubits. The common choice of such mappings are the Jordan-Wigner transformation introduced in Section 1.3.3 and the Bravyi-Kitaev transformation^[145].
- (ii) Unitary decomposition: To realize the unitary evolution,

$$U = \exp(-i\hat{H}t) = \exp\left(-i \sum_l \hat{H}_l t\right), \quad (2.1)$$

we should apply Suzuki-Trotter decomposition^[244],

$$U = [\exp(-i\hat{H}\Delta t)]^{t/\Delta t} \equiv [U(\Delta t)]^{t/\Delta t}, \quad (2.2)$$

$$U(\Delta t) = \exp\left(-i \sum_l \hat{H}_l \Delta t\right) \approx \prod_l \exp(-i\hat{H}_l \Delta t), \quad \Delta t \rightarrow 0, \quad (2.3)$$

such that $\exp(-i\hat{H}_l \Delta t)$ can be realized by a sequence of local gates.

- (iii) Quantum compiling^[214,245-246]: We should further map the above decomposed quantum circuit to more elementary gates pertaining to a specific device architecture. One should generally consider the available quantum gates, the connectivity of qubits, experimental limitations, etc.

In 1996, Lloyd^[247] had proved that any many-body quantum Hamiltonian containing local interactions can be efficiently simulated under the framework of digital quantum simulation. We remark that, however, at a price of the universality, digital quantum simulators generally require more quantum resources than the analog quantum simulation^[10]. To take advantage from these two approaches, there are a handful of digital-analog quantum simulation schemes being proposed^[248].

2.2 Quantum Algorithms for Machine Learning

Most quantum algorithms showing speedups over their classical counterparts are generally based on the three subroutines: quantum phase estimation, amplitude amplification, and Hamiltonian simulation^[249]. Despite the linearity of quantum mechanics is well known since its birth in the mid-1920s, it wasn't until last decade that the quantum computing community realized quantum algorithms can offer speedups for linear algebra or machine learning^[52-53,250-251]. In addition, variational quantum algorithms are widely believed to showcase quantum advantages for practical problems under the hybrid quantum-classical scheme in the NISQ era. In the follow subsections, we will investigate quantum algorithms for machine learning from the above two perspectives.

Table 2.1 Elementary operations for quantum algorithms.

Operations	Initial State	Final State
General oracle O	$ x\rangle y\rangle$	$ x\rangle y \oplus f(x)\rangle$
Hadamard gate $H^{\otimes n}$	$ j\rangle$	$\frac{1}{\sqrt{N}} \sum_{k=0}^{N-1} (-1)^{j \cdot k} k\rangle$
Quantum Fourier transform	$ j\rangle$	$\frac{1}{\sqrt{N}} \sum_{k=0}^{N-1} e^{2\pi i j k / N} k\rangle$
Successive controlled- U^{2^j}	$\frac{1}{\sqrt{N}} \sum_{k=0}^{N-1} k\rangle$	$\frac{1}{\sqrt{N}} \sum_{k=0}^{N-1} U^k k\rangle$

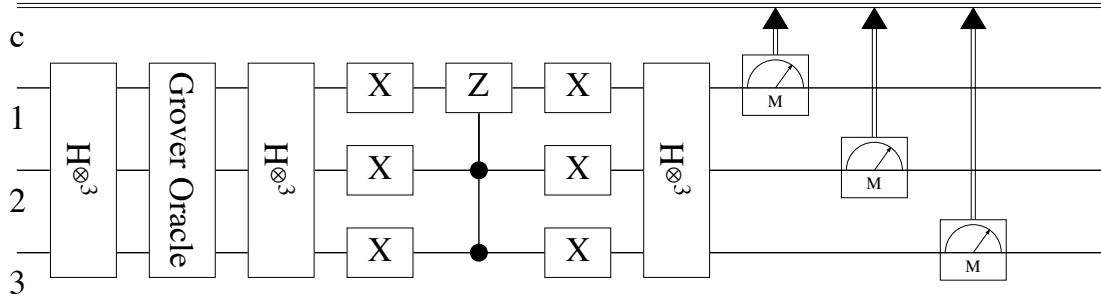


Figure 2.1 The quantum circuit for Grover's algorithm.

2.2.1 Quantum Algorithms for Linear Algebra

Before investigating quantum algorithms for linear algebra, we first recap some useful elementary operations for quantum algorithms^[1], which are listed in Table 2.1. To parallel evaluate a function $f(x)$ for different values of x , one usually assume there is a general oracle O transforming $|x\rangle|y\rangle$ to $|x\rangle|y \oplus f(x)\rangle$. In addition, we often apply $H^{\otimes n}$ to convert

Table 2.2 Subroutines for quantum algorithms.

Algorithms	Procedure
Quantum phase estimation	$ 0\rangle^{\otimes n} u\rangle \xrightarrow{H^{\otimes n}} \frac{1}{\sqrt{N}} \sum_{j=0}^{N-1} j\rangle u\rangle \xrightarrow{c-U^j} \frac{1}{\sqrt{N}} \sum_{j=0}^{N-1} e^{2\pi i j \varphi_u} j\rangle u\rangle \xrightarrow{\text{QFT}^\dagger} \varphi\rangle u\rangle$
Shor's algorithm order/period finding	$\frac{1}{\sqrt{N}} \sum_{x=0}^{N-1} x\rangle 0\rangle \xrightarrow{\text{Oracle}} \frac{1}{\sqrt{N}} \sum_{x=0}^{N-1} x\rangle f(x)\rangle \xrightarrow{\text{QFT}^\dagger} \frac{1}{\sqrt{r}} \sum_{l=0}^{r-1} lr\rangle \hat{f}(l)\rangle$
Grover's algorithm amplitude amplification	$ 0\rangle^{\otimes n} 1\rangle \xrightarrow{H^{\otimes n+1}} \frac{1}{\sqrt{N}} \sum_{x=0}^{N-1} x\rangle -\rangle \xrightarrow{\text{Rotate with Oracle}} x_0\rangle -\rangle$
Density matrix exponentiation	$\text{Tr}_B [\exp(-i\Delta t S) (\sigma_A \otimes \rho_B) \exp(i\Delta t S)]$

a computational basis $|j\rangle$ into a superposition state $\frac{1}{\sqrt{N}} \sum_{k=0}^{N-1} (-1)^{j \cdot k} |k\rangle$. Combining these two elementary operations can generate a phase kickback for the quantum state at which the function $f(x)$ targets. This trick is very important and is used in almost every quantum algorithm, e.g., the Grover's algorithm, whose example quantum circuit is shown in Figure 2.1. Indeed, the Shor's algorithm, or the more general hidden subgroup algorithm, is implemented by combining the general oracle for certain function f and the quantum Fourier transform. Furthermore, the combination of the successive controlled- U^{2^j} and the inverse quantum Fourier transform gives birth to an essential build-block for quantum algorithms—quantum phase estimation, whose example quantum circuit is illustrated in Figure 2.2.

Arguably, the Harrow-Hassidim-Lloyd (HHL) algorithm is the foundation of quantum algorithms for linear algebra, which combines the quantum phase estimation, quantum simulation and post-selection^[52]. Specifically, given an $N \times N$ Hermitian matrix A (if not, it can be embedded into an enlarged space and become Hermitian), and a vector \mathbf{b} , the HHL algorithm aims to extract information about the solution of a linear equation $A\mathbf{x} = \mathbf{b}$. At first glance, with respect to the query complexity shown in Table 2.3, the HHL algorithm shows an exponential speedup over its classical counterpart. However, to make this conclusion valid, one should address the following caveats^[252]:

- (i) The classical vector $\mathbf{b} = (b_1, \dots, b_N)$ should be prepared in a quantum state $|\mathbf{b}\rangle = \sum_{i=1}^N b_i |i\rangle$ in advance. This can be achieved by a quantum random access memory (QRAM). This is a device that, given a superposition of addresses i , returns a correlated set of data D_i : $\sum_i \alpha_i |i\rangle |0\rangle \xrightarrow{\text{qRAM}} \sum_i \alpha_i |i\rangle |D_i\rangle$ ^[253].
- (ii) The sparsity s of the matrix A should be much smaller than N such that the unitary operator e^{-iAt} can be efficiently simulated^[254].

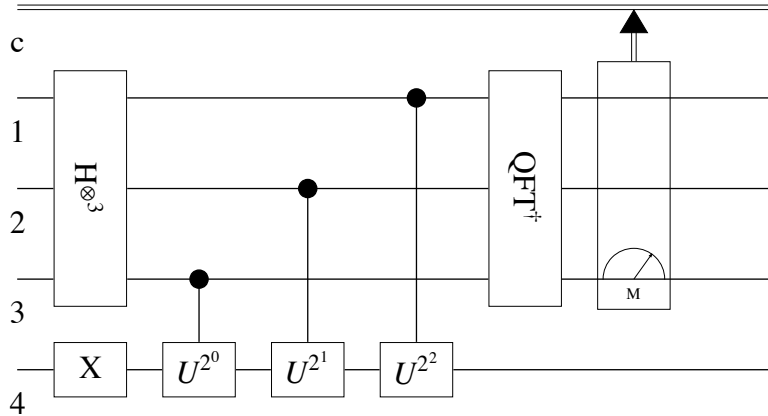


Figure 2.2 The quantum circuit for quantum phase estimation.

Table 2.3 The complexity of quantum algorithms and subroutines.

$\tilde{\mathcal{O}}$ suppresses more slowly growing factors, N is the vector dimension and M is the number of data, s, κ, r refer to the sparsity, the condition number and the rank of a matrix, ϵ is the accuracy.

Algorithms	Quantum Complexity	Classical Complexity
Quantum Fourier transform ^[1]	$\mathcal{O}(\log^2 N)$	$\mathcal{O}(N \log N)$
Quantum phase estimation ^[1]	$\mathcal{O}(\log^2 N)$	-
Shor's algorithm ^[5]	$\mathcal{O}(\log^3 N)$	$\mathcal{O}(N)$
Grover's algorithm ^[6]	$\mathcal{O}(\sqrt{N})$	$\mathcal{O}(N)$
Harrow-Hassidim-Lloyd algorithm ^[52]	$\tilde{\mathcal{O}}(s^4 \kappa^2 \log(N)/\epsilon)$	$\mathcal{O}(Ns\sqrt{\kappa} \log(1/\epsilon))$
Density matrix exponentiation ^[53]	$\mathcal{O}(t^2/\epsilon)$ copies	-
Quantum principal component analysis ^[53]	$\mathcal{O}(r \log N)$	$\mathcal{O}(\min(M^3, N^3))$
Quantum support vector machine ^[251]	$\tilde{\mathcal{O}}(\log(MN)\kappa^3/\epsilon^3)$	$\mathcal{O}((M+N)M^2 \log(1/\epsilon))$

- (iii) The condition number $\kappa = |\lambda_{\max}/\lambda_{\min}|$ of A should be not too large, where λ_{\max} and λ_{\min} are the largest and smallest eigenvalues of A .
- (iv) As retrieving the full information of the solution $|\mathbf{x}\rangle$ requires $\mathcal{O}(N)$ measurements, in order to maintain the quantum speedup, we can only reveal some limited statistical information about $|\mathbf{x}\rangle$.

Based on the matrix inversion technique provided by the HHL algorithm, there are numerous quantum algorithms for linear algebra being proposed in the last decade^[255]. The most representative one may be the quantum principal component analysis (QPCA) algorithm^[53], which is able to extract the largest eigenvalues of a non-sparse but low-rank matrix, together with their corresponding eigenvectors. It shows an exponential speed-up over any existing algorithm and can be applied to deal with large amounts of high-dimensional data for quantum machine learning problems, such as clustering and pattern recognition^[23]. In particular, the QPCA algorithm proposed a novel subroutine—density matrix exponentiation (see Table 2.2), which was later found to be extremely useful and now has been adopted as a subroutine in other quantum algorithms, e.g., quantum support vector machine (QSVM)^[251].

2.2.2 Variational Quantum Algorithms

In the NISQ era, in addition to the aforementioned linear-algebra-based quantum algorithms, an intriguing approach widely studied in quantum machine learning is to exploit the hybrid quantum-classical scheme, where parameterized quan-

tum circuits are optimized with classical methods (such as stochastic gradient descent) to satisfy certain objective functions. Notable examples in this category include various quantum classifiers^[59,251,256-268], variational quantum eigensolvers^[229,269-271], quantum Born machines^[272-273], and quantum approximation optimization algorithms (QAOA)^[231,274-275]. In this hybrid quantum-classical scheme, one typically chooses a variational ansatz circuit with a fixed structure and then optimizes its tunable parameters to tackle the given problem. Yet, different families of parameterized quantum circuits may bear distinct entangling capabilities and representation power, and thus are suitable for different tasks. For a given learning task, how to obtain a well-performing ansatz circuit as short as possible is extremely useful, especially for quantum learning with NISQ devices, where the depth of the quantum circuits would be limited due to undesirable noises carried by such a device.

We defer the general framework of variational quantum algorithms to the next section, since most of their ansatz are based on parameterized quantum circuits, which are intimately similar to quantum artificial neural networks. In the following we give a brief introduction to the QAOA ansatz^[231,274-275], which is an approach to approximately solve combinatorial optimization problems such as maximum cut. The near-term advantage of the QAOA is that, unlike quantum algorithm for linear algebra, it can be amenably implemented on NISQ device^[276]. Specifically, the shallowest depth version of the QAOA consists of the application of two unitary operators^[277]:

(i) The problem unitary:

$$U_C(\gamma) = e^{-i\gamma C}, \quad C = \sum_{j < k} w_{jk} Z_j Z_k.$$

(ii) The mixing unitary:

$$U_B(\beta) = e^{-i\beta B}, \quad B = \sum_j X_j.$$

(iii) The final evaluated state:

$$F_p(\gamma, \beta) = \langle \gamma, \beta | C | \gamma, \beta \rangle, \quad |\gamma, \beta\rangle = U_B(\beta_p) U_C(\gamma_p) \cdots U_B(\beta_1) U_C(\gamma_1) |+\rangle^{\otimes n}.$$

As the length of alternating sequence p increases, the performance of QAOA generally improves. Indeed, one can regard QAOA as a Trotterized version of quantum annealing^[238]. It is recently reported that QAOA has been implemented on trapped-ion-based analog quantum simulators^[278].

2.3 Quantum Artificial Neural Networks

Quantum neural networks, or variational quantum classifiers under the context of classification, has attracted tremendous attention in the last few years, which hold the appealing promise to achieve a quantum learning advantage with NISQ devices^[239,279]. Nowadays, the field of quantum neural network mainly focuses on two directions: the optimization strategies and the architecture search. We will elucidate the latter one in Chapter 3. As for the optimization strategies, quantum neural networks share many similarities with the classical neural networks, whose general framework contains three parts:

- (i) Cost function, which quantifies the deviation between the current output from the network and the target output. The forms of function depend on the specific task to be solved. For example, we can set the cost function as the expectation value of the Hamiltonian in the task of finding the ground state;
- (ii) Ansatz for quantum neural networks. The quantum structure ansatz is usually fixed at the beginning stage. Except for the hardware efficient ansatz widely adopted in parameterized quantum circuits^[280] as shown in Figure 2.3, several quantum neural network architectures have been proposed: the perceptron-based quantum neural networks (each node represents a qubit and their connections are given by parameterized unitary gates)^[257,281], quantum convolutional neural networks^[262], quantum capsule networks^[201], the tree tensor network classifier^[264], continuous-variable quantum neural networks^[282];
- (iii) Parameter optimization. Similar to the classical case, the variational parameters are iteratively adjusted via a classical optimizer so as to minimize an cost function. The essential step is to calculate the gradients of the cost functions with respect to the circuit parameters. A plethora of techniques have been investigated, including the well-known parameter shift rules^[259,283-285] and quantum natural gradient^[286].

Quantum neural networks have now been exploited to solve many tasks that are considered hard for classical computers, such as simulating (open) quantum system dynamics^[287-288], quantum compiling^[289-290], integer factoring^[291], solving linear or differential equations^[292-294], etc. In the following sections, we will examine their expressibility. Some potential challenges, e.g., barren plateau and adversarial learning are also discussed.

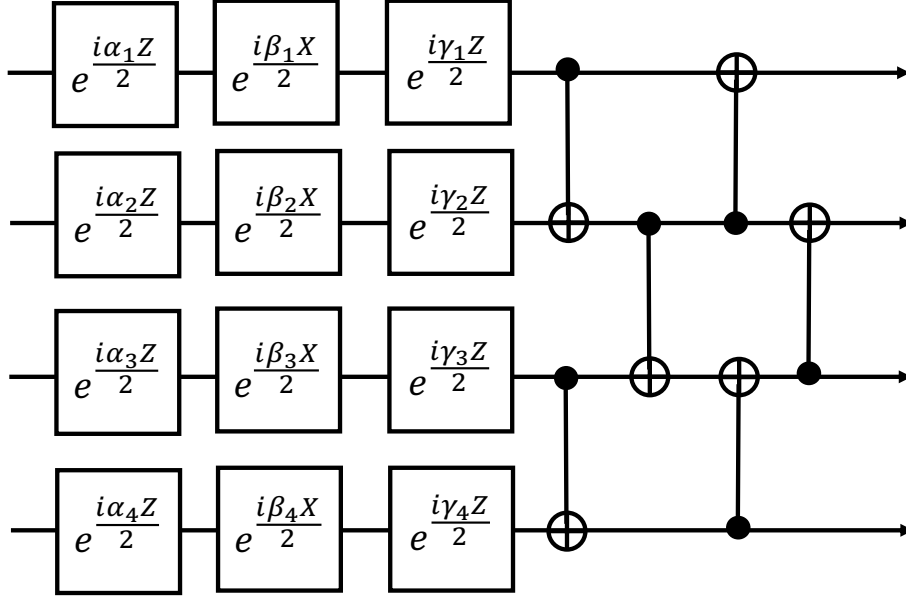


Figure 2.3 The structure of parametrized quantum circuits.

This architecture is also known as the hardware efficient ansatz^[280], which contains a set of parameterized gates with Euler rotation angles (α, β, γ) along the X, Y, Z axis, and CNOT gates between the nearest qubits.

2.3.1 The Expressibility

The expressibility or capacity of a machine learning model can be roughly inferred from its empirical performance. Yet such an approach is not rigorous for theoretical studies. The power of a machine learning model usually refers to its capacity to express various relationships between multiple variables^[295]. A popular way to quantify the capacity is to use the Vapnik-Chervonenkis (VC) dimension—the cardinality of the largest set of points that the model can shatter^[296]. However, many modern machine learning models (e.g., deep neural networks) are heavily over-parameterized. Thereby it's not practical to calculate the VC dimension in such a complex model with numerous parameters, as one needs to consider the whole parameter space. On the other hand, the measurement using VC dimension will ignore the data distribution, which is not suitable for a fairly finite dataset. Besides the VC dimension, there are also some methods like Gardner phase-space approach^[297], or the rank of the Jacobian matrix representing a transformation between the network and the observable variables^[298-299]. However, none of these take into account the fact that, only a finite-size sample of data is available in a real training process.

To tackle this problem, an effective dimension method is proposed which depends on the Fisher information and takes the distribution of input data into consideration^[300-302]. It should be noted that the Fisher information is an important quantity in a variety of

fields including physics and biology^[303]. It's of great significance for both the computational and statistical researches^[304]. According to the computational learning theory, the Fisher information is used to measure the complexity according to the principle of minimum description length^[305]. For the first step, viewing the neural network as a statistical model, the joint relationship between data pairs (x, y) can be expressed as $p(x, y; \theta) = p(y|x; \theta)p(x)$ for $x \in \mathcal{X} \subset \mathbb{R}^{s_{\text{in}}}$, $y \in \mathcal{Y} \subset \mathbb{R}^{s_{\text{out}}}$, and $\theta \in \Theta \subset [-1, 1]^d$, where d is the number of trainable parameters. Then the Fisher information matrix $F(\theta) \in \mathbb{R}^{d \times d}$ is defined as

$$F(\theta) = \mathbb{E}_{(x,y) \sim p} \left[\frac{\partial}{\partial \theta} \log p(x, y; \theta) \frac{\partial}{\partial \theta} \log p(x, y; \theta)^\top \right]. \quad (2.4)$$

Under some circumstances with limited samples, the above matrix can be approximated by the empirical one

$$\tilde{F}_k(\theta) = \frac{1}{k} \sum_{j=1}^k \frac{\partial}{\partial \theta} \log p(x_j, y_j; \theta) \frac{\partial}{\partial \theta} \log p(x_j, y_j; \theta)^\top. \quad (2.5)$$

The Fisher information can capture the sensitivity of a neural network's output relative to movements in the parameter space, which is useful for the analysis in natural gradient optimization—a method that uses the Fisher information as a guide to optimally navigate through the parameter space such that a model's loss declines^[306].

Recall that the goal of the effective dimension is to estimate the size that a model occupies in model space, and there are different choices for the definition of effective dimension. Here, we briefly introduce the definition proposed by Abbas et al.^[300-301], as it can be applied to both classical and quantum models. The size of data size determines a natural scale or resolution used to observe the model space. This is beneficial for practical reasons where training data is often limited, and can help us understand how data availability influences the accurate measure of the model complexity. With the Fisher information matrix in hand, the effective dimension of a statistical model $\mathcal{M}_\Theta := \{p(\cdot, \cdot; \theta) : \theta \in \Theta \subset \mathbb{R}^d\}$ can be defined as

$$\dim_{\gamma, n}(\mathcal{M}_\Theta) \equiv 2 \frac{\log \left(\frac{1}{V_\Theta} \int_\Theta \sqrt{\det \left(\text{id}_d + \frac{\gamma n}{2\pi \log n} \hat{F}(\theta) \right)} d\theta \right)}{\log \left(\frac{\gamma n}{2\pi \log n} \right)}, \quad (2.6)$$

where $\gamma \in (0, 1]$ is a constant, $n \in \mathbb{N}$, $n > 1$ is the number of data samples, $V_\Theta \equiv \int_\Theta d\theta \in \mathbb{R}_+$ is the volume of the parameter space, and id_d is a $d \times d$ -dimensional identity matrix.

In the above expression, $\hat{F}(\theta) \in \mathbb{R}^{d \times d}$ is a normalized Fisher information matrix

$$\hat{F}_{ij}(\theta) \equiv d \frac{V_{\Theta}}{\int_{\Theta} \text{tr}(F(\theta)) d\theta} F_{ij}(\theta), \quad (2.7)$$

where the normalization ensures that $\frac{1}{V_{\Theta}} \int_{\Theta} \text{tr}(\hat{F}(\theta)) d\theta = d$.

The definition of the effective dimension incorporates the Fisher information spectrum by integrating over its determinant. By comparing Equation (2.6) with the original expression from Berezniuk et al.^[302]:

$$\dim_n(\mathcal{M}_{\Theta}) \equiv 2 \frac{\log \left(\frac{1}{V_{\Theta}} \int_{\Theta} \sqrt{\det \left(\text{Id}_d + \frac{n}{2\pi} \hat{F}(\theta) \right)} d\theta \right)}{\log \frac{n}{2\pi}}, \quad (2.8)$$

we can find some minor differences: the constant γ and the $\log(n)$ term. These modifications are adopted since they are helpful for us to prove a generalization bound. In this regard, the effective dimension can be interpreted as a bounded capacity measure that serves as a useful tool to analyze the power of statistical models for both the classical and quantum ones.

Except for the effective dimension, it has been shown that the Fisher information matrix is connected to the phenomenon of barren plateaus^[266,307-311]. The distortions of parameter space are captured by a few very large eigenvalues of the Fisher information matrix, while the flatness corresponds to eigenvalues being close to zero. Specifically, a model suffering from a barren plateau will have a Fisher information spectrum with a concentration of zero eigenvalues. Conversely, a model with a Fisher information spectrum that is not concentrated around zero is unlikely to experience a barren plateau.

We note in passing that quantum neural networks may also suffer the catastrophic forgetting issue as the classical neural networks. Yet, Jiang et al.^[312] recently shown that this issue can be alleviated by adding the Fisher information matrix into the cost function as a regularization term, which opens a new avenue for exploring potential quantum advantages towards continual learning.

2.3.2 Barren Plateau

In classical machine learning, a notorious obstacle for training artificial neural networks concerns the barren plateau phenomenon, where the gradient of the loss function along any direction vanishes exponentially with the problem size^[313]. Under the assumption that the variational quantum circuits are unitary 2-designs, the barren plateaus phenomena have also been shown to exist for many quantum learning models^[307-308].

A measure of the unitary group dU is called the unitary t -design if the t -th moment with respect to dU equals to the t -th moment with respect to the Haar measure (see Appendix A.5 for a brief introduction). Based on this mathematical assumption, the average and variance of the loss functions with respect to the whole parameter space can be simply computed by the first moment and second moment of the random unitary matrices. Recently, Liu et al.^[158] has rigorously proved that barren plateaus is present in the training process of the matrix product state with global loss functions, which, however, is absent for local loss functions. This conclusion can also be generalized to high-dimensional tensor networks through analyzing the partition function of the honeycomb Ising model introduced in Appendix B. In addition, it has been shown that QCNs and QNNs with tree tensor network architectures do not exhibit barren plateau^[314].

There are already some potential solutions to avoid this challenge. First, we should prefer to use a local loss function rather than a global one. Second, we can smartly choose the initial training parameters based on one specific task. For example the Hartree-Fock assumption is widely adopted in variational quantum eigensolvers. Third, we can find a better circuit ansatz using some machine learning algorithms. In this regard, we will elucidate the quantum architecture search in the Chapter 3. All of these solutions will essentially reduce the randomness and depth of the circuit and thus break the assumption that the circuit approximates a unitary 2-design.

2.3.3 Adversarial Learning

Another challenge of quantum machine learning is the vulnerability of quantum algorithms under the adversarial attacks^[315-316], which has attracted extensive concerns among in recent years^[317-319]. To be more precise, a well-trained quantum machine learning model can make incorrect prediction at a high confidence level if we add a tiny amount of carefully crafted noise to the original legitimate input data. Here, the crafted input data is dubbed the adversarial sample, which is even undistinguishable with the original data for human eyes.

For the classical neural network used in classifying phases of matter in the many-body quantum physics^[216], Jiang et al.^[224] showed that in some specific cases, flipping one spin is already able to cause the classifier to make incorrect predictions with high level confidence. Moreover, after adding some perturbations to the time-flight images of cold atoms, the neural network will yield wrong Chern numbers, which cannot reflect the real topological order of the physical system.

On the quantum domain, the vulnerability of quantum machine learning algorithms has been investigated by Lu et al.^[317] on various adversarial attacks using the variational quantum circuits. Theoretically, it has been demonstrated that the vulnerability of the quantum classifiers is related to the quantum version no free lunch theorem and the measure concentration^[318,320-321]. Furthermore, Gong et al.^[319] has proved that there exist universal adversarial examples that could attack several quantum classifiers, and universal adversarial perturbations that could make different legitimate inputs become adversarial examples for a given quantum classifier. The understandings of the vulnerability of quantum machine learning can help us protect quantum classifiers against adversarial attacks.

CHAPTER 3 QUANTUM ARCHITECTURE SEARCH

Current NISQ devices only have hundreds of noisy qubits available. Due to their noisy nature, there are three main limitations to be addressed: the short coherence time, the long measurement time, and the less controllable environment. In addition to the challenges (expressibility, barren plateau and adversarial learning) that we mentioned in Chapter 2, the accuracy and the efficiency of experimental measurements also remain to be improved. From the operational point of view, there are two approaches to optimize the utility of the NISQ devices: bottom-up and top-down. The bottom-up approach refers to the scheme where one improve the gate fidelity and coherence life time for given hardware design. In this Chapter we will focus on the latter one—top-down approach and utilize some machine learning technique to algorithmically boost the performance of near-term quantum devices.

In this respect, quantum architecture search is a collection of methods devised to systematically engineer the architecture of quantum classifiers. Specifically, we introduce a quantum neuroevolution algorithm that autonomously finds near-optimal quantum neural networks for different machine-learning tasks. In particular, we establish a one-to-one mapping between quantum circuits and directed graphs, and reduce the problem of finding the appropriate gate sequences to a task of searching suitable paths in the corresponding graph as a Markovian process. We benchmark the effectiveness of the introduced algorithm through concrete examples including classifications of real-life images and symmetry-protected topological states. Our results showcase the vast potential of neuroevolution algorithms in quantum architecture search, which would boost the exploration towards quantum-learning advantage with noisy intermediate-scale quantum devices.

3.1 Neuroevolution of Augmenting Topologies Algorithm

Neuroevolution, a field that draws inspiration from the evolution of brains in nature, harnesses evolutionary algorithms to construct artificial neural networks. It bears a number of intriguing capabilities that are typically inaccessible to gradient-based approaches, including optimizing neural-network architectures, hyperparameters, and even learning the training rules. In designing classical neural networks, a renowned neuroevolution algorithm is the NEAT (NeuroEvolution of Augmenting Topologies) algorithm^[322], which

exploits concepts (e.g., genome, crossover, speciation, and mutation) from biology to evolve neural-network topologies along with weights. It has been recently adopted to optimize *classical* neural networks for quantum error decoding on the toric code^[323]. To demonstrate the performance of the genetic algorithm in *quantum* neural networks, we explicitly implement the NEAT algorithm in searching quantum circuits, which could be regarded as a naive generalization of the NEAT algorithm.

In conventional evolutionary algorithms, we evolve the population to create the next generation by applying genetic operators on individuals to generate offspring. Two important genetic operators are mutation and crossover^[322,324], where crossover produce new offspring by recombining two selected individuals (parents), and mutation generate new offspring by randomly mutating a selected individual. Applying them in searching quantum circuits, crossover is defined to divide each of two parent quantum circuits into two parts respectively and exchange their divided parts to create two offspring, mutation is defined to randomly generate some positions in circuits and then replace quantum gates in these positions with other different gates.

We design the genetic algorithm as shown in Algorithm 3.1 to search for optimal quantum classifier architectures (9-qubit circuits) for the MNIST handwritten digit dataset. The major hyperparameters (n_i, t_i) are set as (9, 3). Figure 3.1 displays the fitness of 86 quantum circuits totally evaluated in running the genetic algorithm. We find a circuit structure with fitness 92% at the third generation, whose number of quantum gates is more than 100. In Figure 3.2, we plot the average accuracy and loss for both the training and validation datasets as a function of the number of epochs during the training process. We see from Figure 3.1 that the local convergence appears at the third generation and the

Algorithm 3.1 The genetic algorithm^[66,322]

Require: Hyperparameters n_i, t_i, g_c, f_c , etc

Ensure: The optimal quantum circuit architecture

Initialization:: randomly generate n_1 quantum circuits, and compute their fitness

for $i = 1$ to g_c **do**

Choose the best t_i ($t_i < n_i$) circuits with highest fitness

Apply the crossover and mutation operator

Compute the fitness of individuals in the $(i + 1)$ -th generation

if $\max[\text{fitness}(\text{circuits})] \geq f_c$ **then**

Terminate the iteration

end if

end for

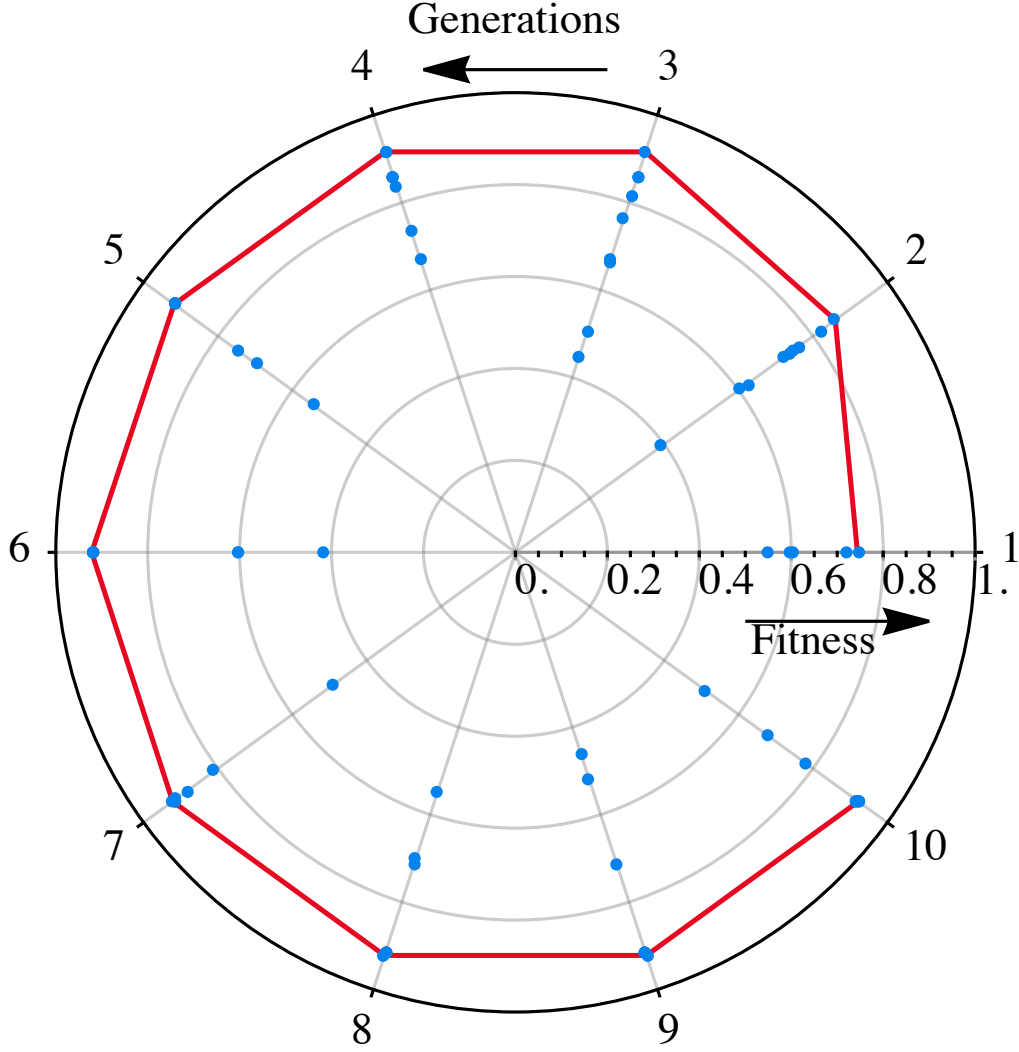


Figure 3.1 The performance of the genetic algorithm in the MNIST dataset.

We apply the genetic algorithm in the task of classifying handwritten-digit images in the MNIST dataset. The blue dots denote all the populations, while the red line refers to the highest fitness^[66].

fitness does not increase for later generations. The performance of the genetic algorithm is ineffective when directly applying these two operators in designing quantum classifiers.

Therefore, a straightforward adoption of NEAT in the quantum domain would not work since quantum neural networks differ substantially from classical ones. This may be due to the fact that, the quantum neurons (qubits) are connected by multi-qubit unitaries rather than weight parameters. As a result, certain techniques, such as explicit fitness sharing and matching up genomes^[322], used in NEAT become invalid or ambiguous in the quantum scenario.

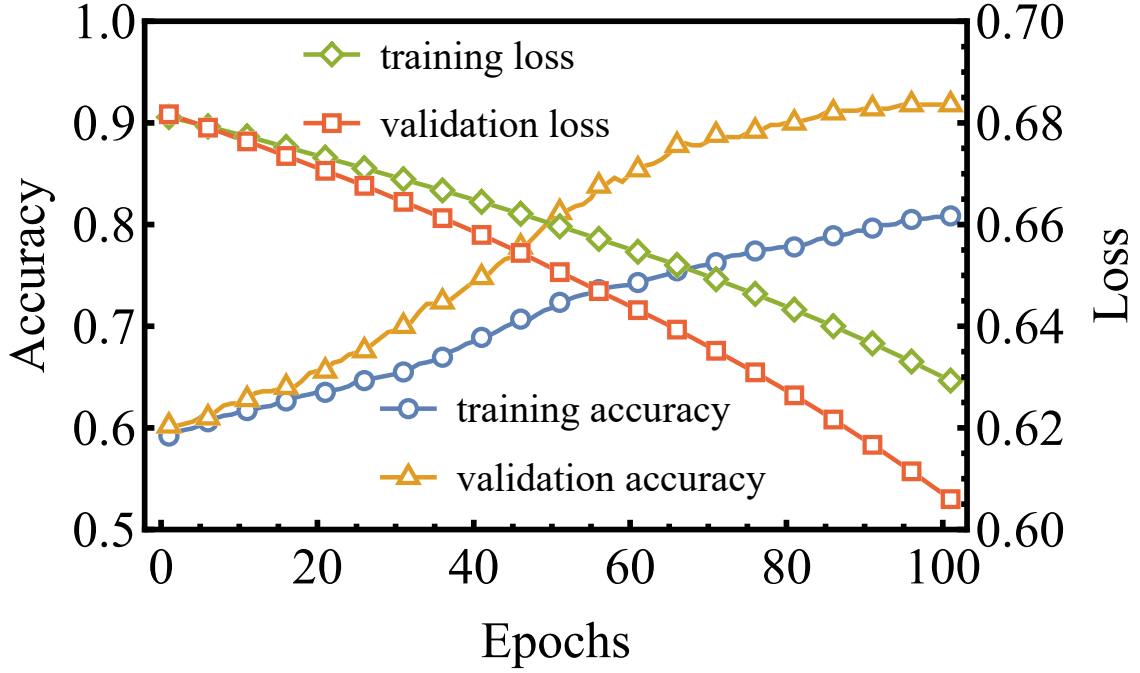


Figure 3.2 The loss and accuracy of the genetic algorithm for the tenth-generation.

The loss and accuracy as a function of training epochs for the tenth-generation quantum classifier with the highest fitness, in classifying handwritten-digit images in the MNIST dataset. Here, we use the genetic algorithm to construct quantum circuits^[66].

3.2 The Quantum Neuroevolution Algorithm

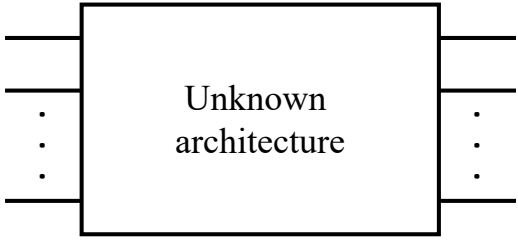
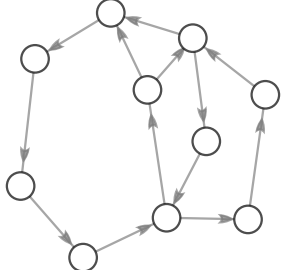
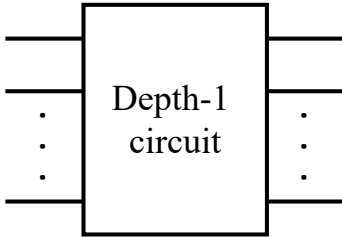
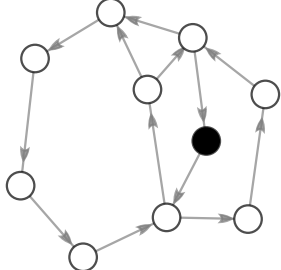
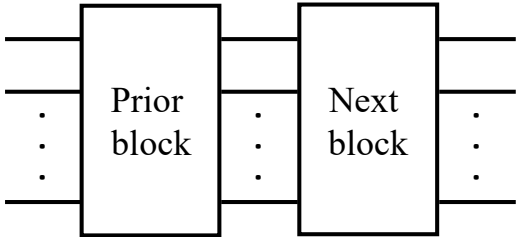
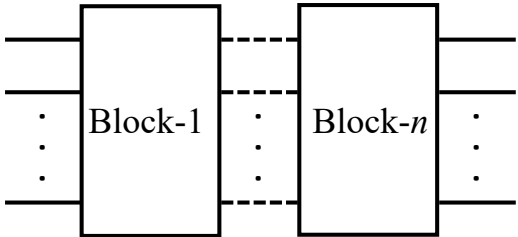
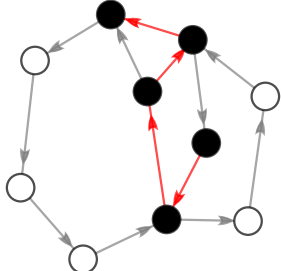
As shown in the last section, the simple genetic algorithm for designing quantum classifiers, which uses crossover and mutation directly, performs poorly in classifying the handwritten images in the MNIST dataset. The ineffectiveness of this algorithm is due to the following:

- (i) The encoding of the quantum circuits into bit strings is not a bijection, which increases the search space and slows down the searching process;
- (ii) The performance of the offspring generated from crossover and mutation is not guaranteed to be better than that of their parents, since crossover and mutation of unitaries may result in meaningless structures.

In this section, we introduce a quantum neuroevolution algorithm, which we call the Markovian quantum neuroevolution (MQNE) algorithm, to search for optimal ansatz quantum circuits for different machine-learning tasks. Our MQNE algorithm overcomes the shortcomings of naive generalization of the NEAT algorithm in Section 3.1. We propose a graph-encoding method (see Table 3.1), where the nodes of the graph correspond to the elementary gate blocks and the directed edges represent the allowed connection between gate blocks, to injectively map quantum circuits to directed graphs. Consequently,

Table 3.1 An illustration of the graph-encoding method.

The encoding method is based on which the problem of searching the optimal quantum circuits is reduced to a task of finding paths in the corresponding directed graphs. Each node represents one gate-block, and each path (red arrows) represents a sequence of gate-blocks. The nodes that the path passes through are solid, while other nodes are empty^[66].

System		
Gate block		
Relation between blocks		$\begin{pmatrix} 0 & 1 & \dots & 0 \\ 0 & 0 & \dots & 1 \\ \vdots & \vdots & \ddots & \vdots \\ 1 & 0 & \dots & 0 \end{pmatrix}$
Circuit sequence		

we recast the problem to a task of searching an appropriate directed path of the graph in a Markovian fashion. To illustrate the effectiveness of the MQNE algorithm, we apply it to a variety of quantum-learning tasks, including classifications of handwritten digit images in the MNIST dataset^[195], symmetry-protected topological (SPT) states, and the Breast Cancer Wisconsin Diagnostic dataset^[325]. We find that our algorithm yields ansatz quantum circuits with notably smaller depths, while maintaining a comparable classification accuracy.

3.2.1 Algorithm Overview

Now we introduce the technical details of our MQNE algorithm, which implemented by the `Yao.jl` open source package in the Julia language^[327-328]. The pseudocode for the MQNE algorithm is provided in Algorithm 3.2. First, we introduce a graph-encoding method, which maps quantum circuits to directed paths in the corresponding graph. Suppose we need to design a k -qubit quantum circuit to solve a given quantum machine-learning problem, and for simplicity we restrict our discussion to the case that the circuits are composed with only single-qubit rotations R and two-qubit controlled- R_x gates. The universal single-qubit rotation gate R is defined as the gate composed of $R_z R_x R_z$, i.e., the Z-X decomposition for a single-qubit rotation, where R_z and R_x denote rotations along z and x axis, respectively^[1]. We choose the controlled- R_x gate, rather than the controlled NOT gate typically used in designing quantum neural networks, to guarantee that the circuits from later generations cover these from earlier generations, so as to ensure improved performance of the offsprings. This can be easily deduced from the fact that the controlled- R_x gate reduces to identity when setting the controlled rotation angle to 0. To avoid ambiguity and duplication of successive rotations, we invoke some connection rules for arranging gate blocks (a gate block is a depth-1 quantum circuit) in sequential order to form the desired circuits (see Table 3.2):

- (i) The latter gate-block should not include any gate which can be operated in parallel with the former one;
- (ii) The latter gate block should not include the same gates as the former one on the same qubits.

Algorithm 3.2 Markovian quantum neuroevolution algorithm^[66]

Require: The directed graph, hyperparameters n_i , t_i , l , l' , f_c , and g_c

Ensure: The optimal quantum circuit architecture

Initialization: start from a fixed node and uniformly sample n_1 paths with length- l , and compute their fitness

for $i = 1$ to g_c **do**

Choose the t_i ($t_i < n_i$) paths with highest fitness

Evolution: produce paths in the $(i+1)$ -th generation by concatenating n_{i+1} segments of length l' to each of the t_i paths, and compute their fitness

if $\max [\text{fitness}(\text{paths})] \geq f_c$ **then**

Terminate the iteration

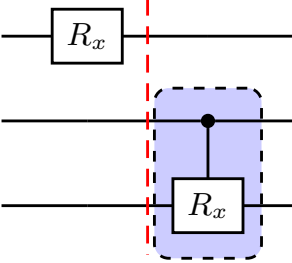
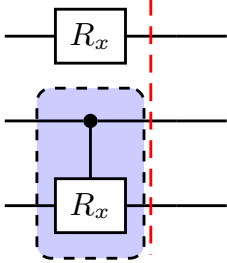
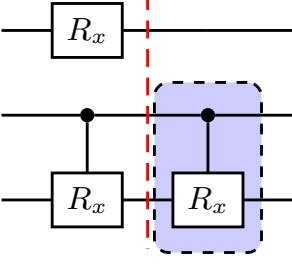
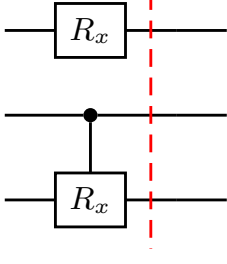
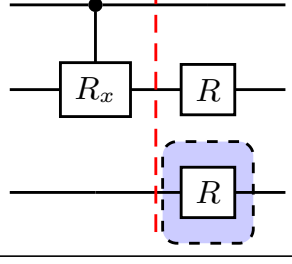
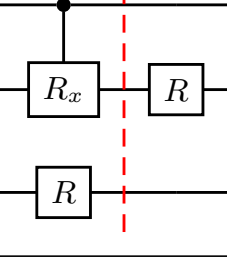
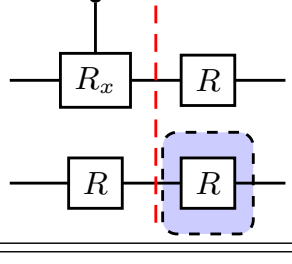
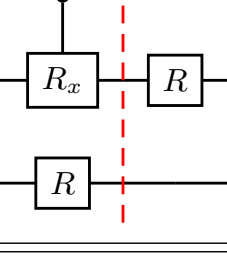
end if

end for

Output the optimal quantum circuit

Table 3.2 The connection rules for gate blocks.

The quantum circuits are drawn using Quantikz^[326]. The left column shows the forbidden connection configurations, which should be replaced by the corresponding permitted ones in the right column. Here, only two-qubit controlled- R_x gate and single-qubit rotation gate R are used in constructing various quantum circuits^[66].

Forbidden	Permitted
	
	
	
	

Such connection rules restrict the process of searching the optimal circuit structure in a Markovian fashion. We suppose that the qubits are arranged in a one-dimensional geometry and the controlled- R_x gates act only on adjacent qubits. We use a length- $(k + 2\lfloor k/2 \rfloor)$ vector to represent a quantum gate block. The first $2\lfloor k/2 \rfloor$ numbers encode controlled- R_x gates in a gate block. Here, two adjacent nonzero numbers represent a controlled- R_x gate acting on these two qubits labeled by them, and two adjacent 0 numbers mean that

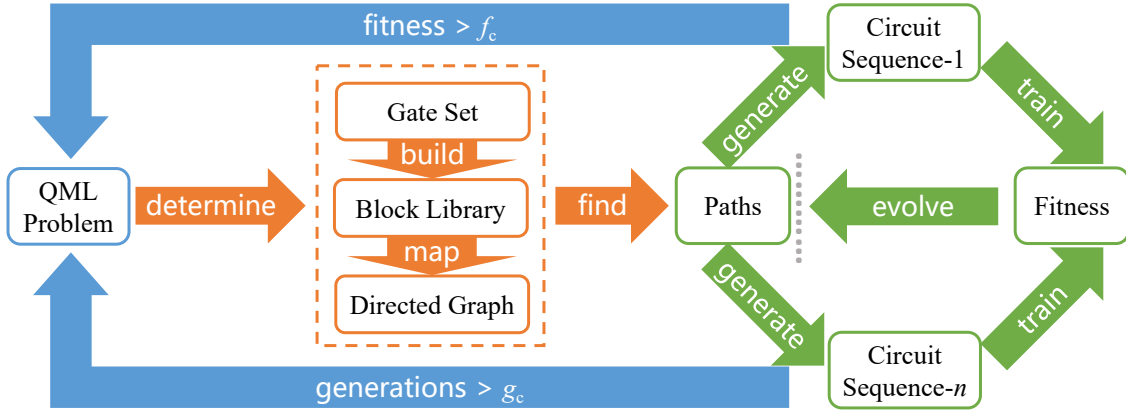


Figure 3.3 A schematic illustration of the MQNE algorithm.

For a given quantum machine-learning (QML) problem and experimental setup, we first determine the allowed gate blocks and the corresponding directed graph, and iteratively generate quantum circuits in a Markovian fashion. The algorithm terminates when the highest fitness of the generated circuits becomes larger than a certain threshold value f_c or the number of generations exceeds a given number g_c [66].

there is no controlled- R_x gate acting on the remaining qubits. The next k numbers encode the single-qubit rotation gates in a gate block, where we use 0 to denote the absence of rotation for the corresponding qubit.

Without further restrictions, it is straightforward to obtain that the number of possible gate-blocks is

$$f_1(k) = \frac{(1 + \sqrt{3})^{k+1} - (1 - \sqrt{3})^{k+1}}{2\sqrt{3}}. \quad (3.1)$$

These gate-blocks form a gate-block library and we use a directed graph to represent this library. Each node of the graph corresponds to a gate block, and each directed edge represents a legitimate connection of gate blocks according to the connection rules: there is an edge pointing from node x to y if and only if the gate block y is allowed to be put next to gate block x . For convenience, we use an adjacency matrix to denote the directed graph as in graph theory [329]. Noting that a quantum circuit is just a sequence of gate blocks in the corresponding library, hence the task of designing a well-performing quantum circuit is reduced to finding an optimal path in the directed graph. This can be solved with the following procedure:

- (i) Initialization: We start from a fixed node and uniformly sample n_1 paths with length l based on the directed graph, and compute the fitness (classification accuracy) of the corresponding variational quantum circuits. These n_1 paths form the first generation;

- (ii) Iteration in a Markovian fashion: From the i -th generation, we choose t_i paths with the largest fitness.

For each of the selected paths, we uniformly sample n_{i+1} segments of length l' , and then add these segments to the end of the path. Here we remark that one segment refers to a sequence of l' gate blocks. Due to the connection rules, not all possible segments can be added at will to the existed paths. Whether a new segment is allowed to be added depends on the last gate block of the given paths, which is similar to a Markovian process. In this way, we obtain the paths of the $(i + 1)$ -th generation. We then parallel evaluate the fitness of all $(i + 1)$ -th generation quantum circuits. whose running time is independent of the number of paths at each generation. If the fitness of a circuit is larger than a certain given threshold value f_c (or the number of iteration exceeds a given number g_c), we terminate the iteration and output the corresponding path and quantum circuit. If none of the circuits has a fitness larger than f_c , we repeat this step to generate paths and circuits for the next generation. A schematic illustration for our MQNE algorithm is given in Figure 3.3.

In the above discussion, we restrict our discussion to the case that the circuits are composed with only single-qubit rotation gates R (composed of $R_z R_x R_z$, where R_x and R_z denote rotations along x and z axes, respectively) and two-qubit controlled- R_x gates, and the controlled- R_x gates only act on adjacent qubits. We note that the number of nodes of the directed graph scales exponentially with the number of qubits involved $f_1(k) = \Theta(2^k)$. For large k , the size of the graph might exceed the capacity of any classical computer, rendering our MQNE algorithm infeasible in practice. To reduce the size of the graph, we can impose some further restrictions on building possible gate blocks. For instance, we may require that for each gate block there are at most c (a cutoff constant number) controlled- R_x gates, and the rest qubits all undergo single-qubit rotations. With these restrictions, the number of possible gate blocks reduces to a polynomial function of k . Accordingly, the size of the directed graph is also reduced. However, it is worthwhile to mention that the reduction of the graph may also bring up a problem: we may not be able to find the optimal ansatz circuits since the searching space is reduced too much by the restrictions.

3.2.2 The Scaling of the Gate-Block Library

For a k -qubit quantum gate-block library, we can sort all quantum gate-blocks into the ones containing 0 controlled- R_x gate, 1 controlled- R_x gate, until $\lfloor k/2 \rfloor$ controlled- R_x gates. For quantum gate-blocks containing 0 controlled- R_x gate, each of k qubits can be acted on by a single-qubit rotation gate R or an identity gate, corresponding to 2^k

quantum gate-blocks of this type totally. Likewise, for quantum gate-blocks containing 1 controlled- R_x gate, each of the remaining $k - 2$ qubits can be acted on by rotation gate R or identity gate pertaining to 2^{k-2} possibilities. Through some combinatorial calculations, we can obtain the total number of 1 controlled- R_x blocks:

$$N_1(1) = 2^{k-2} \times \binom{k-1}{1} \times 2^1. \quad (3.2)$$

Similarly, for quantum gate-blocks containing i controlled- R_x gate, where $i \leq \lfloor k/2 \rfloor$, each of the remaining $k - 2i$ qubits can be acted on by gate R or the identity gate, we obtain

$$N_1(i) = 2^{k-2i} \times \binom{k-i}{i} \times 2^i. \quad (3.3)$$

Then the total number of quantum gate-blocks is:

$$f_1(k) = \sum_{i=0}^{\lfloor k/2 \rfloor} N_1(i) = \frac{(1 + \sqrt{3})^{k+1} - (1 - \sqrt{3})^{k+1}}{2\sqrt{3}}. \quad (3.4)$$

In this way, we have calculated there are $f_1(k) = \Theta[(1 + \sqrt{3})^k]$ quantum gate-blocks in the gate-block library. To analyze the complexity of the searching space in the MQNE algorithm, we also numerically study how the outdegree (for a node, its outdegree is the number of other nodes it is allowed to point to) of nodes scale with respect to qubit number and show numerical results in Figure 3.4, from which it is evident that the maximum (average) value of the outdegree has the same growing trend as the library size, which will climb exponentially as qubit number increases.

In some realistic problems, considering limited classical computational power or other realistic reasons, especially for large qubit number case, it is necessary to impose further restrictions to reduce the size of the library, from the exponential scaling $f_1(k)$ to a polynomial scaling $f_2(k)$. In our proposal, We plus three more restrictions. Firstly, for quantum gate-blocks containing i controlled- R_x gate, we assume the remaining $k - 2i$ qubits are acted on *simultaneously* by either gate R or the identity gates. Secondly, for each controlled- R_x gate acting on two neighboring qubits i and $i + 1$, we assume that the i -th qubit is the controlling qubit. Thirdly, we restrict each quantum gate-block contains at most c (a cut-off constant) controlled- R_x gates. With these further restrictions, there are $N_2(i) = \binom{k-i}{i}$ gate-blocks containing i controlled- R_x gates, and consequently the total number of gate-blocks $f_2(k)$ in the library is given by

$$f_2(k) = \sum_{i=0}^c N_2(i) = \sum_{i=0}^c \binom{k-i}{i} = O(k^c). \quad (3.5)$$

We also numerically explore how the outdegree scale with respect to qubit number with

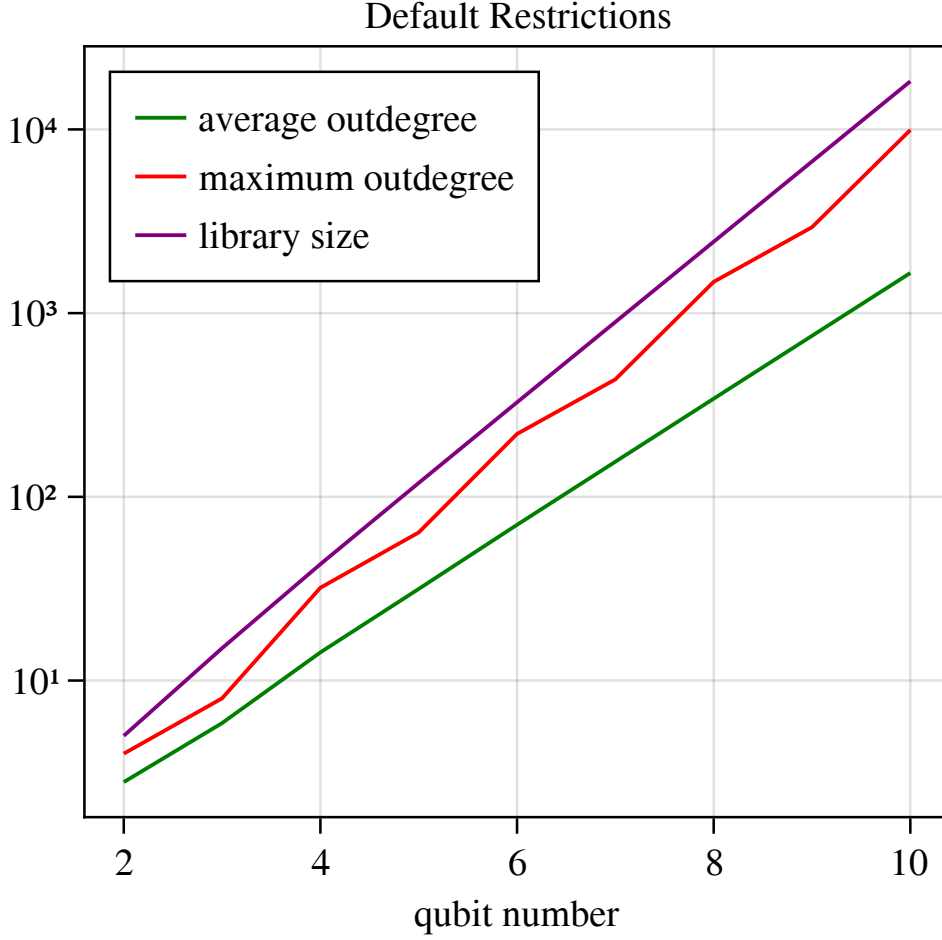


Figure 3.4 The size of the gate-block library under default restrictions.

Except for the size of the gate-block library, we also plot the maximum (average) outdegree of all nodes in the directed graph as functions of qubit number^[66].

numerical results shown in Figure 3.5, which reflects that the maximum (average) value of the outdegree which will rise polynomially with respect to qubit number. Similarly, adding more restrictions can even reduce the size of the library to a constant f_3 , independent of k . For instance, a gate-block library containing only three gate-blocks can be constructed to obtained a quantum classifier architecture as shown in Figure 3.6. We mention that, the gate-block marked yellow corresponds to the rotation layer, the gate-blocks marked orange and green correspond to the entanglement layer respectively, in the Figure 2 of Lu, Duan, and Deng^[317].

On the contrary, in order to improve the possibility of finding the optimal quantum circuits, we can enlarge the searching space by releasing some restrictions. For example, we may remove the restriction that the controlled- R_x gates only act on adjacent qubits.

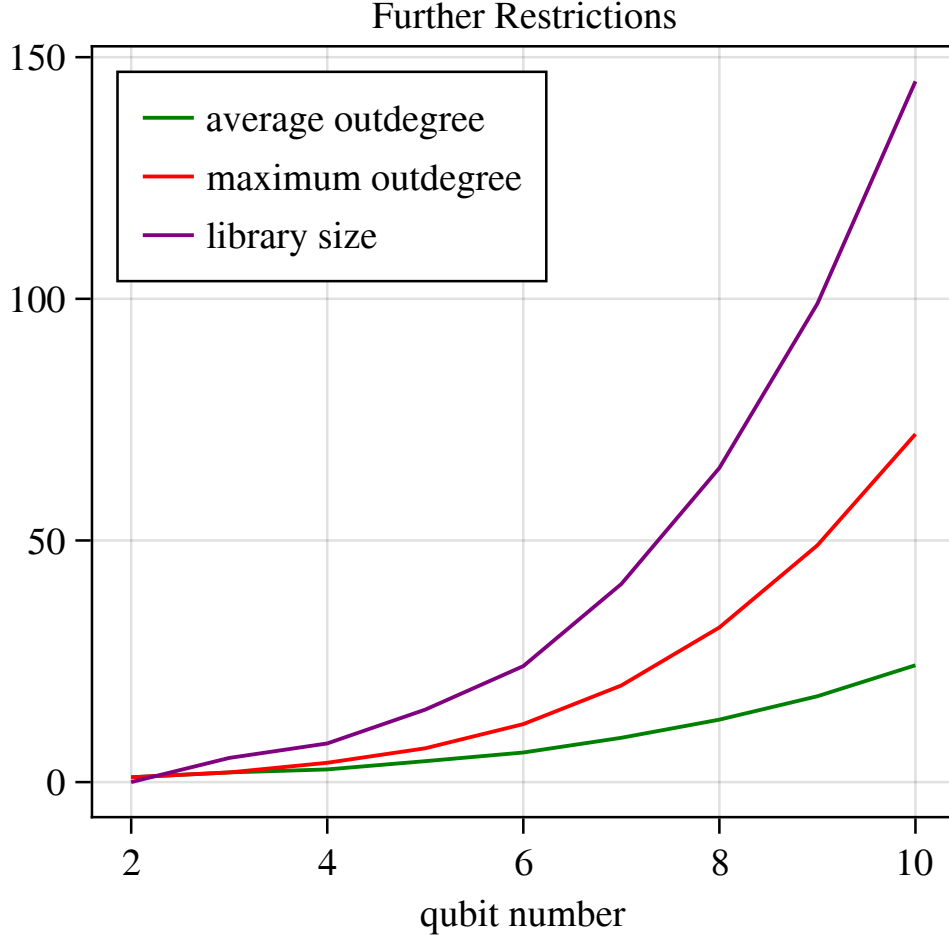


Figure 3.5 The size of the gate-block library under further restrictions.

Except for the size of the gate-block library, we also plot the maximum (average) outdegree of all nodes in the directed graph as functions of qubit number^[66].

We obtain the total number of quantum gate-blocks containing 1 controlled- R_x gate:

$$N_0(1) = 2^{k-2} \times A_k^2. \quad (3.6)$$

Likewise, for quantum gate-blocks containing i controlled- R_x gates, where $i \leq \lfloor k/2 \rfloor$, with each of the remaining $k - 2i$ qubits being acted on by gate R or identity gate, we obtain

$$N_0(i) = 2^{k-2i} \times A_k^{2i} / A_i^i. \quad (3.7)$$

Then the total number of gate-blocks is

$$f_0(k) = \sum_{i=0}^{\lfloor k/2 \rfloor} N_0(i). \quad (3.8)$$

In this way, the size of the quantum gate-block library is enlarged to $\Omega(\lfloor k/2 \rfloor!)$.

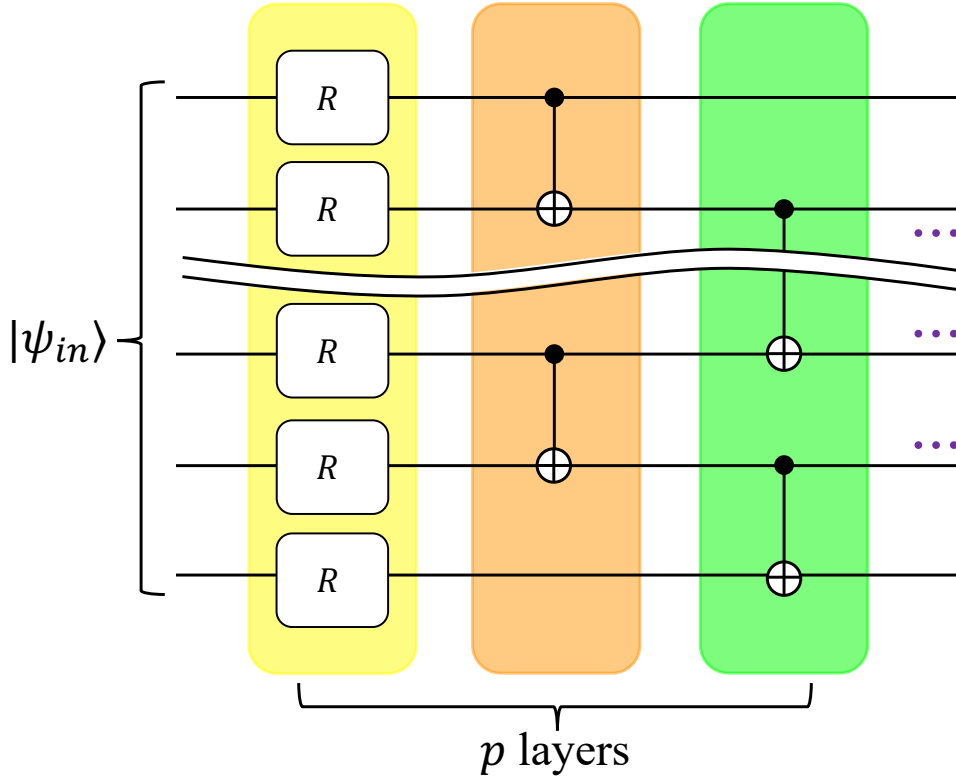


Figure 3.6 The architecture of quantum classifiers.

It consists of p same layers, each layer has three gate-blocks, the gate-block marked yellow is the rotation unit, the gate-blocks marked orange and green are in the entanglement unit^[66,317].

In practical applications, we can directly construct the gate-block library for $(k + 1)$ -qubit circuits based on existed libraries for $(k - 1)$ - and k -qubit circuits. Firstly, the operations on the top k qubits can be adopted entirely from the gate-block library of k -qubit circuits when the last qubit is acted on by gate R or identity gate. Secondly, the operations on the top $(k - 1)$ qubits can be adopted entirely from the gate-block library of $(k - 1)$ -qubit circuits when the last two qubits is acted on by a controlled- R_x gate. In this way, we can readily scale up the gate-block library of $(k - 1)$ -qubit and k -qubit circuits to the gate-block library of $(k + 1)$ -qubit circuits.

3.2.3 Towards the High-Order Markovian Process

In the above discussion, we only consider the rules between adjacent gate-blocks with the help of the single-qubit rotation gate R . We also assume that the transition probability is uniformly distributed on all states that the present state can transit to. We could regard finding paths in the directed graph as a Markovian process, in which the future state only depends on the current state of the system, but not on the previous ones. All paths of the graph correspond to the discrete state space, and the adjacency matrix of the graph

corresponds to the transition matrix describing the probabilities of transitions between states.

For the high-order Markovian process, we could directly use R_z and R_x gates, instead of the composed R gate, to construct quantum gate-blocks. Consequently, we need to invoke new rules between adjacent four gate-blocks to avoid ambiguity and duplication of successive rotations. For example, when three consecutive quantum gate-blocks contain R_z, R_x, R_z on the same qubit respectively, then the fourth gate-block should not have R_z or R_x on this qubit. So the future state depends on the previous three states of the system, which is a third-order Markovian process.

3.3 Performance Benchmark

In the following subsections, we give a couple of concrete examples to benchmark the effectiveness of our MQNE algorithm, including classifications of real-life images, symmetry-protected topological states and cancer dataset.

3.3.1 Classification of Handwritten-Digit Images

The first example we consider is the classification of handwritten-digit images in the MNIST dataset. This is a prototypical machine-learning task for benchmarking the effectiveness of various learning approaches. The MNIST dataset consists of gray-scale images for handwritten digits from 0 through 9. Each image is two dimensional, and contains 28×28 pixels (see Figure 1.7). For our purpose, we choose only a subset of MNIST consisting of images for digits 1 and 9 and reduce the size of the images to 16×16 pixels, so that we can run our MQNE algorithm and simulate the quantum classifiers generated with moderate classical computational resources. We use amplitude encoding to map the input images into quantum states and define the following loss function based on cross entropy for a single data sample encoded as $|\psi\rangle_{\text{in}}$:

$$L(h(|\psi\rangle_{\text{in}}; \Theta), \mathbf{a}) = -a_1 \log g_1 - a_2 \log g_2, \quad (3.9)$$

where $\mathbf{a} = (a_1, a_2) = (1, 0)$ or $(0, 1)$ denotes the one-hot encoding^[26] of the label of $|\psi\rangle_{\text{in}}$, $h(|\psi\rangle_{\text{in}}; \Theta)$ represents the output of the quantum classifier with its parameters denoted by Θ collectively, and $g_{1,2}$ denote the output probabilities of digits 1 and 9. For training the quantum classifier, we use a classical optimizer to search the optimal parameters Θ^* that minimize the averaged loss over the training dataset (see Lu et al.^[317] for more details).

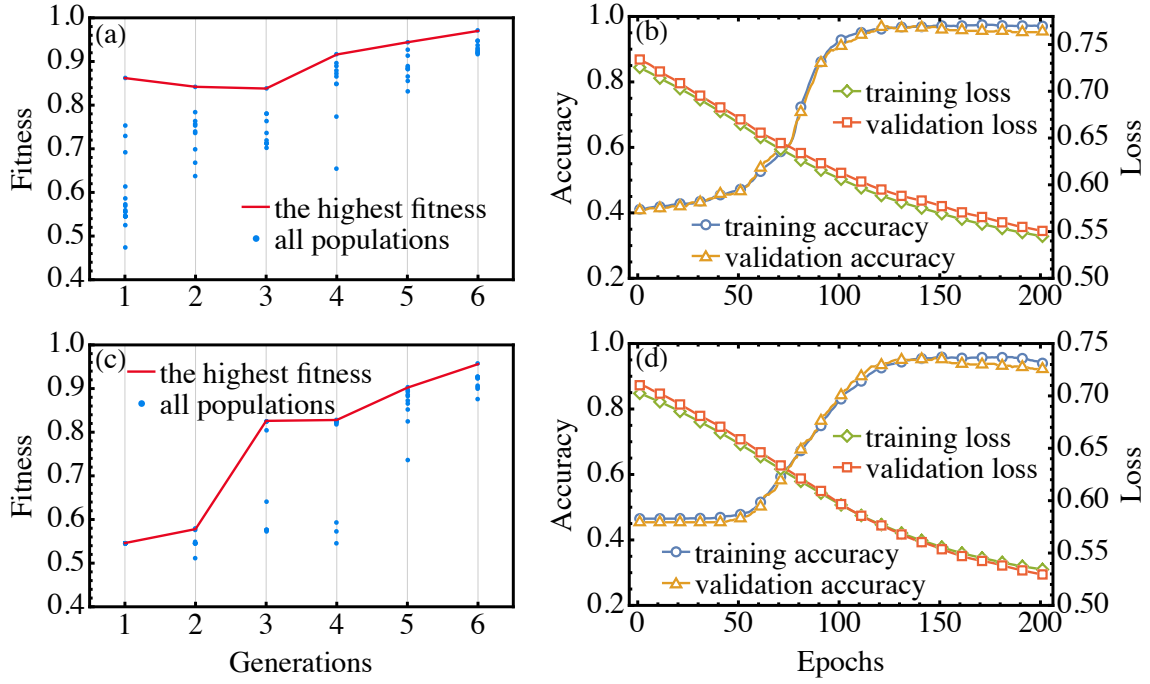


Figure 3.7 Numerical results of handwritten-digit images by the MQNE algorithm.

The image dataset are selected from the MNIST dataset. In (a), the initial variational parameters of single-qubit rotation gates are randomly chosen during the training process. In (b), we plot the loss and accuracy as a function of training epochs for the sixth-generation quantum circuit with the highest fitness. (c) shows the fitness of generated circuits for each generation with fixed initial variational parameters and (d) plots the loss and accuracy for the sixth-generation circuit that has largest fitness^[66].

For images with 16×16 pixels, we need eight qubits to encode each input sample, and for convenience, we also use an additional qubit to output the results of the binary classification. Thus, the ansatz circuit we aim to design is a nine-qubit variation circuit. Applying the graph-encoding method and supposing that controlled- R_x gates act only on adjacent qubits, we obtain 6688 gate blocks and the corresponding directed graph has 6688 nodes. Based on the connection rules, we compute the adjacency matrix and apply the MQNE algorithm with hyperparameters set as $(n_i, t_i, l, l') = (10, 1, 5, 2)$. Our results are summarized in Figure 3.7. In Figure 3.7(a), we randomly choose the initial variational parameters for single-qubit rotation gates when training the generated quantum classifiers at each generation. The MQNE algorithm outputs a quantum circuit with fitness (accuracy) 97% at the sixth generation, whose circuit structure is explicitly shown in Figure 3.8. The corresponding path for this circuit on the directed graph reads $[6687 \rightarrow 3969 \rightarrow 4418 \rightarrow 1321 \rightarrow 6319 \rightarrow 2817 \rightarrow 5933 \rightarrow 859 \rightarrow 2183 \rightarrow 5160 \rightarrow 4641 \rightarrow 4097 \rightarrow 4388 \rightarrow 2305 \rightarrow 4388]$, where the numbers denote the labels of the nodes of the graph. In Figure 3.7(b), we plot the average accuracy and loss for both the

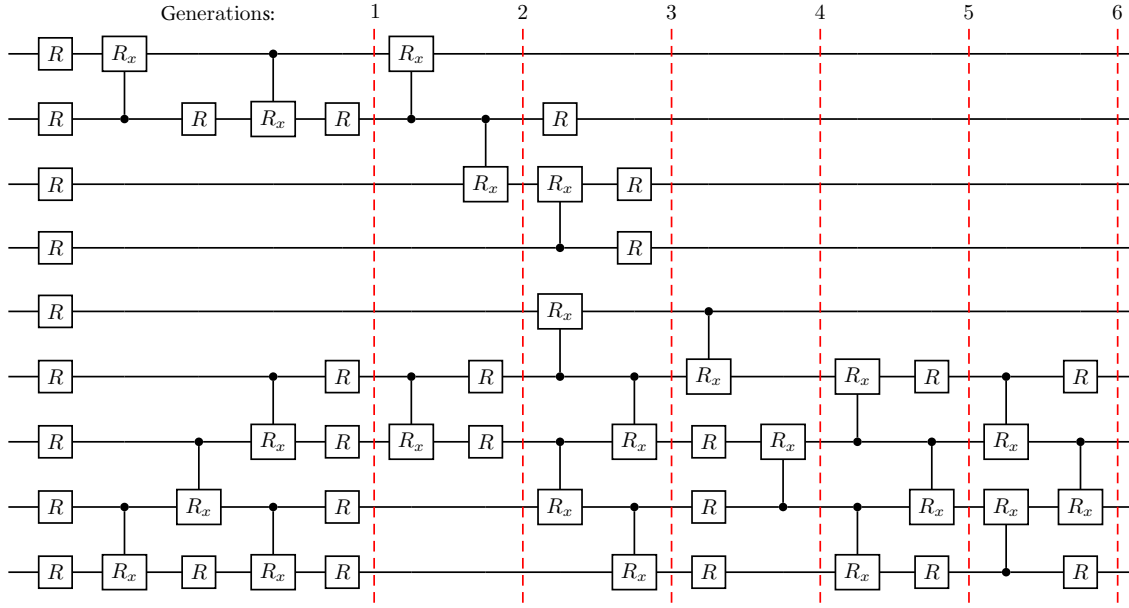


Figure 3.8 The optimal quantum circuit generated by the MQNE algorithm.

This circuit is trained by the MNIST dataset, and the numbers in the top denote the generations^[66].

training and validation datasets as a function of epochs during the training process. After training, the performance of this quantum classifier is also tested on the testing dataset and an accuracy of 97% is obtained. Figure 3.7 (c) and (d) are analogous to Figure 3.7 (a) and (b), respectively, but with fixed initial parameters for single-qubit rotation gates during the training process. We find that fixing the initial parameters would lead to a more stable improvement of the performance for next-generation classifiers.

3.3.2 Classification of Symmetry-Protected Topological States

Unlike classical classifiers, quantum classifiers may also be used to directly classify quantum states produced by quantum devices. To show the power of our MQNE algorithm in this scenario, we consider a quantum machine-learning task of classifying SPT states. For simplicity and concreteness, we consider the following cluster-Ising model, whose Hamiltonian reads^[330]

$$H(\lambda) = - \sum_{j=1}^N \sigma_{j-1}^x \sigma_j^z \sigma_{j+1}^x + \lambda \sum_{j=1}^N \sigma_j^y \sigma_{j+1}^y, \quad (3.10)$$

where σ_i^α , $\alpha = x, y, z$, are Pauli matrices acting on the i -th spin and λ is a parameter describing the strength of the nearest-neighbor interaction, and N denotes the number of spins. This model is exactly solvable and features a well-understood quantum phase transition at $\lambda = 1$, between a $\mathbb{Z}_2 \times \mathbb{Z}_2$ SPT cluster phase characterized by a string order

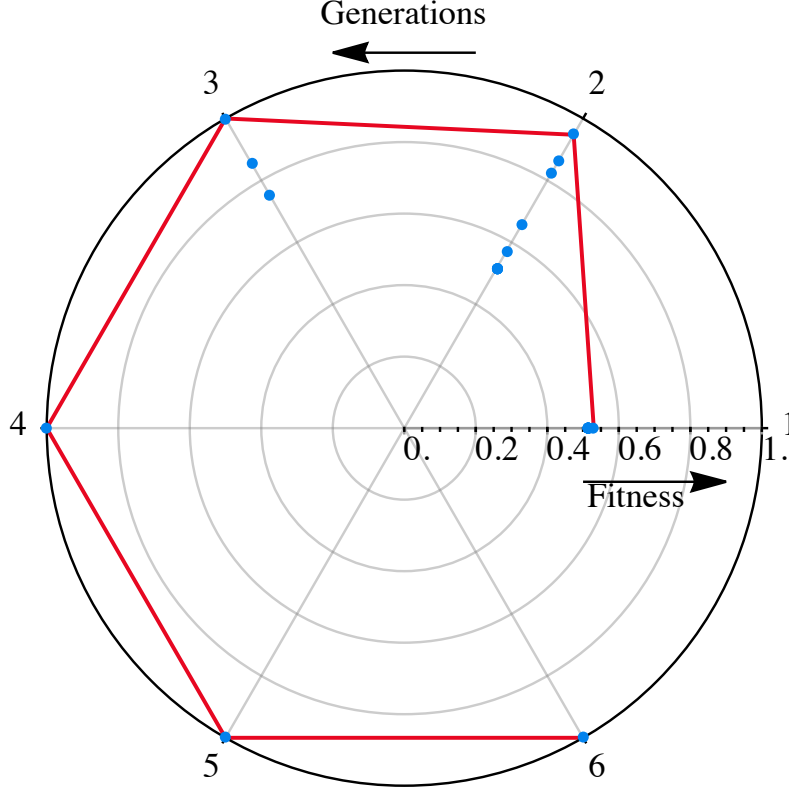


Figure 3.9 The performance of the MQNE algorithm for classifying SPT states.

The initial variational parameters are randomly chosen at the beginning of the training process^[66].

for $\lambda < 1$ and an antiferromagnetic phase with long-range order for $\lambda > 1$. Here, we apply the MQNE algorithm to obtain an optimal ansatz variational circuit, which serves as a quantum classifier for classifying these two distinct phases. To this end, we set $N = 8$ and uniformly sample 2000 Hamiltonians with varying λ from 0 to 2 under the periodic boundary condition. We compute their corresponding ground states, which are the input data to the classifier, and randomly choose 1600 of them for training and the remaining ones for testing. Our results are plotted in Figure 3.9, from which it is evident that the largest fitness increases at the first several generations and then saturates. We find a circuit at the third generation, which involves only 36 single-qubit and 10 two-qubit gates but has a fitness equals 100%.

More specifically, we use two strategies to train the generated quantum classifiers at each generation. Firstly, we randomly choose the initial variational parameters for single-qubit rotation gates when training the generated quantum classifiers at each generation, whose results are plotted in the Figure 3.9. The MQNE algorithm outputs a quantum circuit (with 46 variational parameters) with fitness 100% at the third generation. The corresponding path for this circuit on the directed graph reads $[6687 \rightarrow 1665 \rightarrow 2177 \rightarrow$

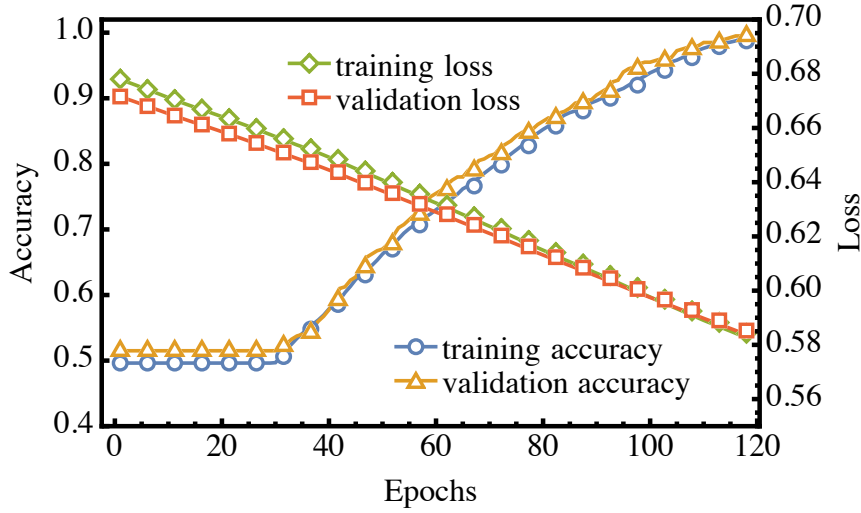


Figure 3.10 Numerical results of SPT states by the MQNE algorithm.

These SPT states are the ground states of the cluster-Ising model. The initial variational parameters of single-qubit rotation gates are randomly chosen during the training process, we plot the loss and accuracy as a function of training epochs for the sixth-generation quantum circuit with the highest fitness^[66].

2401 \rightarrow 4899 \rightarrow 3042 \rightarrow 4901]. In Figure 3.10, we plot the average accuracy and loss for both the training and validation datasets as a function of the number of epochs during the training process.

Secondly, we fix initial parameters for single-qubit rotation gates during the training process, the results are shown in Figure 3.11. The MQNE algorithm outputs a quantum circuit (bearing 54 variational parameters) with fitness 100% at the fourth generation. The corresponding path for this circuit on the directed graph reads [6687 \rightarrow 3649 \rightarrow 3173 \rightarrow 737 \rightarrow 1798 \rightarrow 60 \rightarrow 1217 \rightarrow 4905 \rightarrow 1826], In Figure 3.12, we plot the average accuracy and loss for both the training and validation datasets as a function of the number of epochs during the training process.

We stress that, in comparison with the typical variational circuits used in previous works^[317], the ansatz circuits found by the MQNE algorithm involve much fewer gates and variational parameters, while maintaining a comparable classification accuracy. For instance, for the example of classification of handwritten-digit images, the classifier used in Lu et al.^[317] uses more than 90 single-qubit and 80 two-qubit gates with circuit depth larger than 30 and the number of variational parameters larger than 270, whereas the circuit found by the MQNE algorithm at the sixth generation contains only 28 single-qubit rotation gates and 22 two-qubit gates with 106 variational parameters and circuit depth 15.

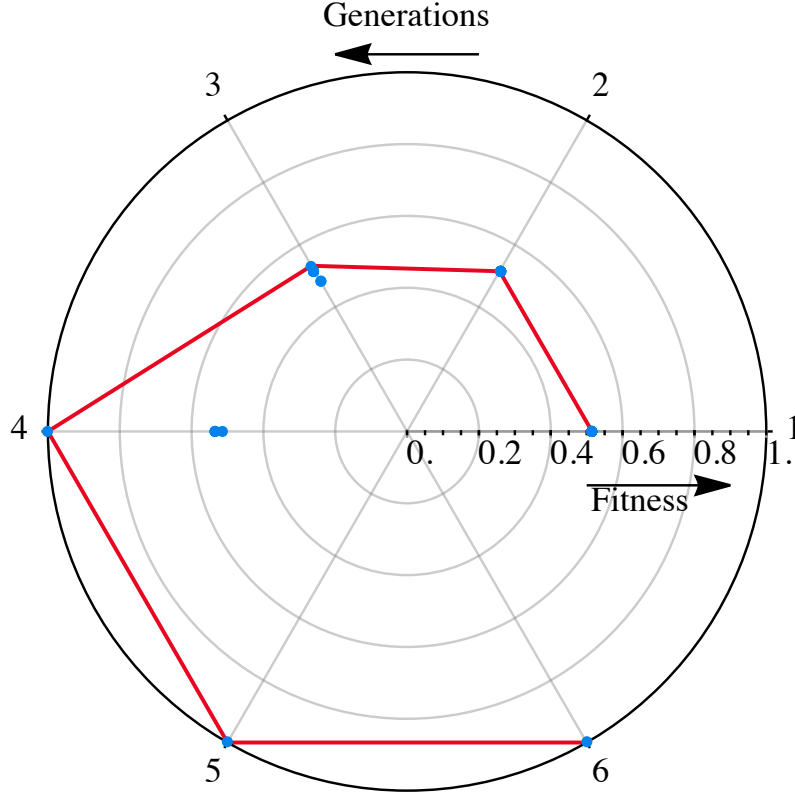


Figure 3.11 The performance of the MQNE algorithm with fixed initial parameters.

We apply the MQNE algorithm in the task of classifying symmetry-protected topological states. The initial variational parameters are fixed at the beginning of the training process^[66].

This significant reduction of the circuit depth and number of gates (up to a constant factor) is crucial for experimental demonstration of quantum learning with NISQ devices, as the depth of the quantum circuits would be limited due to undesirable noises carried by such devices. It not only simplifies the implementation of quantum classifiers substantially from the practical perspective, but also would mitigate the possible barren plateau problem (i.e., vanishing gradient)^[307-308,331] in training deep networks. We also mention that the performance of the MQNE may be improved further by choosing the hyperparameters judiciously according to different learning problems and experimental setups.

3.3.3 Classification of Cancer Diagnostic Data

In this subsection, we tested the MQNE algorithm in the task of classification of Breast Cancer Wisconsin Diagnostic dataset^[325], which may have useful application in medical machine learning^[332]. We need six qubits to encode each input sample and use an additional qubit to output the results of the binary classification (whether the label is cancer or not). Thus, the ansatz circuit we aim to design is a seven-qubit variational circuit. Applying the graph-encoding method for seven-qubit circuits and suppos-

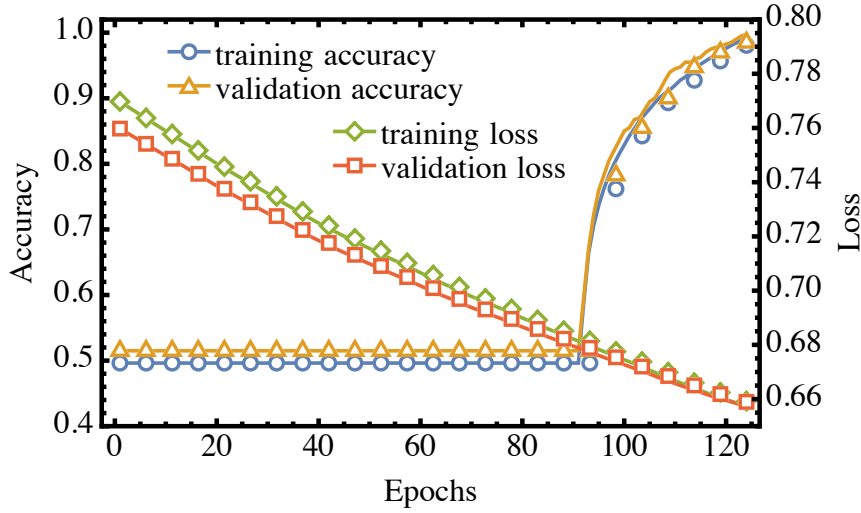


Figure 3.12 The loss and accuracy of the MQNE algorithm for the sixth-generation.

The loss and accuracy as a function of training epochs for the sixth-generation circuit with the highest fitness (see Figure 3.11), for the task of classifying symmetry-protected topological states of the cluster-Ising model^[66].

ing that controlled- R_x gates act only on adjacent qubits, we obtain 896 gate-blocks and the corresponding directed graph has 896 nodes. Based on the connection rules, we compute the adjacency matrix and apply the MQNE algorithm with hyperparameters set as $(n_i, t_i, l, l') = (10, 1, 3, 2)$.

Our results are summarized in Figure 3.13. In Figure 3.13(a), we randomly choose the initial variational parameters for single-qubit rotation gates when training the generated quantum classifiers at each generation. The MQNE algorithm outputs a quantum circuit (with 68 variational parameters) with fitness 94.6% at the sixth generation. The corresponding path for this circuit on the directed graph reads $[895 \rightarrow 31 \rightarrow 801 \rightarrow 273 \rightarrow 404 \rightarrow 643 \rightarrow 423 \rightarrow 593 \rightarrow 225 \rightarrow 481 \rightarrow 673 \rightarrow 792 \rightarrow 609]$, where the numbers denotes the labels of the nodes of the graph.

In Figure 3.13(b), we plot the average accuracy and loss for both the training and validation datasets as a function of the number of epochs during the training process. After training, the performance of this quantum classifier is also tested on the testing dataset and an accuracy of 94.6% is obtained. We mention that the numerical simulations of training the quantum classifiers are based on the Julia language^[327] and the Yao.jl^[328] framework. Figure 3.13 (c) and (d) are analogous to Figure 3.13 (a) and (b) respectively, but with fixed initial parameters during the training process.

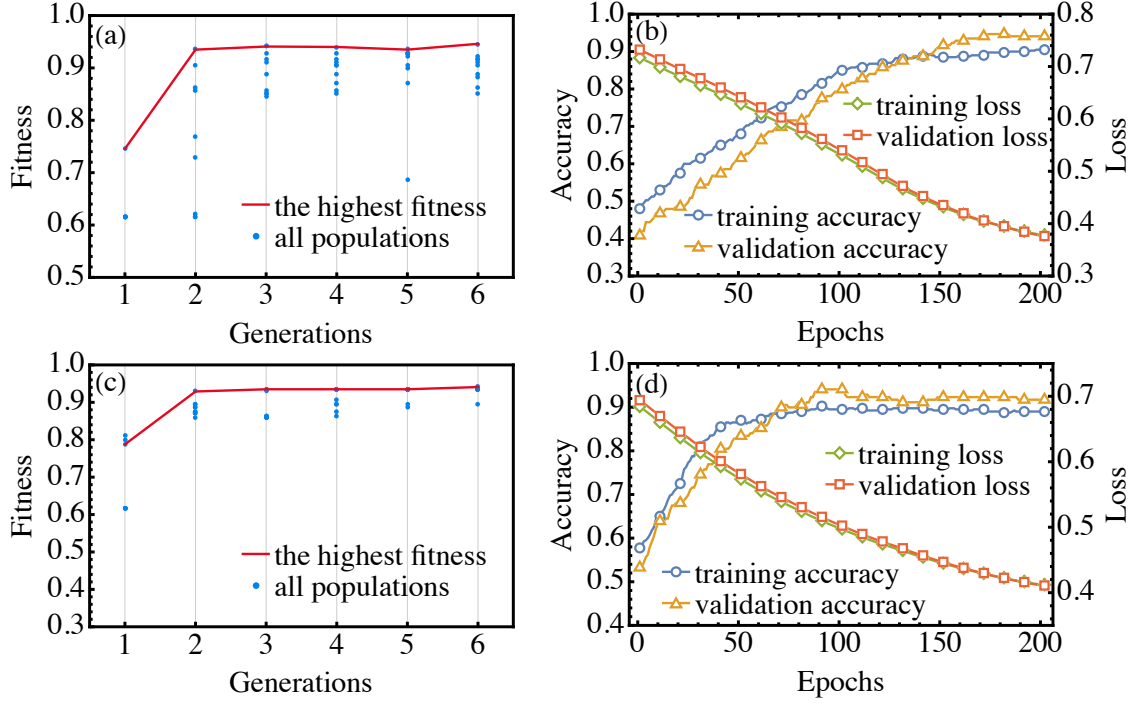


Figure 3.13 Numerical results of the cancer dataset by the MQNE algorithm.

We apply the MQNE algorithm to the task of classifying samples in the cancer dataset. In (a), we randomly choose the initial variational parameters of single-qubit rotation gates at the beginning of the training process. In (b), the loss and accuracy are plotted as functions of training epochs for the sixth-generation quantum circuit with the highest fitness. (c) and (d) are similar to (a) and (b), but with fixed initial variation parameters^[66].

3.3.4 Parameter Settings

In the task for classification of handwritten-digit images in the MNIST dataset (see Figure 3.7), we use the Adam optimizer with a batch size of 30 and a learning rate of 0.0015 to minimize the loss function. The training step is 200. The fitness is averaged on 2000 training samples and 500 validation samples which are not contained in the training dataset.

In the task for classifying symmetry-protected topological states (see Figure 3.9, Figure 3.11, 3.12 and 3.10), we use the Adam optimizer with a batch size of 20 and a learning rate of 0.0015 to minimize the loss function. The training step is 150. The fitness is averaged on 1600 training samples and 400 validation samples which are not contained in the training dataset.

In the task for classification of samples in the cancer dataset (see Figure 3.13), we use the Adam optimizer with a batch size of 20 and a learning rate of 0.0015 to minimize the loss function. The training step is 150. The fitness is averaged on 400 training samples and 169 validation samples which are not contained in the training dataset.

3.4 Discussion and Summary

Recent advances in quantum machine learning have revealed that quantum classifiers are highly vulnerable to adversarial attacks—adding a tiny amount of carefully crafted perturbations into the original legitimate data will cause the quantum classifiers to make incorrect predictions^[317-318]. Thus, how to enhance the robustness of quantum classifiers to adversarial perturbations is a problem for practical applications of quantum learning in the future. With the MQNE algorithm, a possible solution to this problem is to design ansatz circuits that are more robust to the given type of adversarial attack. This could be achieved by replacing the original loss function [e.g., Equation (3.9)] with a modified one that incorporates the adversarial perturbations^[315]. In addition, the graph-encoding method would also be combined with other evolution or genetic algorithms to construct optimal circuit structures for different quantum-learning problems. In the future, it would be interesting to consider some symmetries in the data as prior knowledge to enhance our algorithm by restricting the searching space into a smaller subspace.

In summary, we introduce a quantum neuroevolution algorithm, named the MQNE algorithm, to design optimal variational ansatz quantum circuits for different quantum-learning tasks. Through concrete examples involving classifications of real-life images and SPT quantum states, we demonstrate that the MQNE algorithm performs excellently in searching appropriate quantum classifiers. It finds ansatz circuits with notably smaller depths and number of gates, while maintaining a comparable classification accuracy. Our results provide a valuable guide for experimental implementations of quantum machine learning with NISQ devices. For instance, an experimentally suitable variational circuit architecture was found with our MQNE algorithm, which is further used to carry out the Floquet SPT phase experiment with superconducting qubits^[333].

CHAPTER 4 INFORMATION PROCESSING IN QUANTUM SPIN LINKS

In this Chapter, we investigate the quantum information processing in quantum spin chains. We first review some general properties of the quantum spin chain in Section 4.1. In Section 4.2, we introduce the spin system and the model Hamiltonian. There we perform the mapping from spins to fermions via the Jordan-Wigner transformation. In Section 4.3, we analyze the symmetries of the two representations appearing at the lattice level. In Section 4.4, we focus on the low-energy sector using both a continuum theory as well as the full lattice diagonalization, to solve for the Andreev bound states analytically, and compare to those found numerically. In Section 4.5, we discuss different scenarios of fractional Josephson effects regarding an effective time-reversal symmetry in the continuum limit and an inversion time-reversal symmetry at the lattice level, respectively. In Section 4.6, we calculate the texture of the spin entanglement in the presence of a spin supercurrent in the XY sector. In Section 4.7, we propose and analyze the coupling of the spin chain to a microwave cavity for readout of the spin current and the periodicities of the Josephson effects, along with examining the robustness of the fractional Josephson effects under perturbations of the in-plane magnetic fields. We summarize our results in Section 4.8.

4.1 General Properties of the Quantum Spin Chain

The generalized one-dimensional anisotropic spin chain Hamiltonian in a transverse field is given by

$$\hat{H}_G^s = -J \sum_i [(t_i + \gamma_i) \hat{\sigma}_i^m \hat{\sigma}_{i+1}^m + (t_i - \gamma_i) \hat{\sigma}_i^n \hat{\sigma}_{i+1}^n + \delta_i \hat{\sigma}_i^z \hat{\sigma}_{i+1}^z + g_i \hat{\sigma}_i^z], \quad (4.1)$$

where $\hat{\sigma}_i^{m(n)} = \hat{\sigma}_i \cdot \mathbf{m}_i(\mathbf{n}_i)$, $\hat{\sigma}_i = (\hat{\sigma}_i^x, \hat{\sigma}_i^y, \hat{\sigma}_i^z)$ is a spin vector constructed by Pauli matrices at site i , $\mathbf{m}_i = (\cos \phi_i, \sin \phi_i, 0)$, $\mathbf{n}_i = (-\sin \phi_i, \cos \phi_i, 0)$, ϕ_i is the spin anisotropic angle with respect to the z axis, $J > 0$ is the spin exchange constant, $0 \leq t_i \leq 1$ is the coupling strength on the xy -plane, $0 \leq \gamma_i \leq 1$ marks their degree of anisotropy, δ_i is the spin coupling strength along the z -direction, $g_i = g$ is the relative magnitude of the global transverse field along the z axis. Lengths are measured in units of the lattice spacing a .

After the JWT, we obtain the generalized Hamiltonian in the fermionic representation:

$$\begin{aligned} \hat{H}_G^F = & -2J \sum_i [(t_i \hat{c}_i^\dagger \hat{c}_{i+1} + \gamma_i e^{-2i\phi} \hat{c}_i^\dagger \hat{c}_{i+1}^\dagger + \text{H.c.}) \\ & + \delta_i (1/2 - \hat{c}_i^\dagger \hat{c}_i - \hat{c}_{i+1}^\dagger \hat{c}_{i+1} + 2\hat{n}_i \hat{n}_{i+1}) + g_i (\hat{c}_i^\dagger \hat{c}_i - 1/2)], \end{aligned} \quad (4.2)$$

where the global spin anisotropic angle ϕ generating a global gauge transformation $\hat{c}_i \rightarrow \hat{c}_i e^{i\phi}$. Starting from the non-interacting case $\delta_i = 0$, if all the parameters in Equation (4.2) are invariant at every site, we can impose periodic boundary conditions to yield translation symmetry, which does not affect bulk properties. Through applying the Fourier transformation $\hat{c}_k = \sum_j \hat{c}_j e^{-ikaj}/\sqrt{N}$, the Hamiltonian in the momentum space reads:

$$\hat{H}_G^k = -2J \sum_k [(2t \cos ka + g) \hat{c}_k^\dagger \hat{c}_k + \gamma \sin ka (ie^{-2i\phi} \hat{c}_k^\dagger \hat{c}_{-k}^\dagger + \text{H.c.}) - g/2], \quad (4.3)$$

where $k = 2\pi n/(Na)$ is the wave number with n taking in the range of $([-N/2], [+N/2])$. Defining a momentum spinor $\hat{C}_k = [\hat{c}_k, \hat{c}_{-k}^\dagger]^\top$, we write down the Hamiltonian $\hat{H}_G^k = \frac{1}{2} \sum_k \hat{C}_k^\dagger \mathcal{H}_G^k \hat{C}_k$ in the BdG form with the matrix

$$\mathcal{H}_G^k/2J = -(2t \cos ka + g) \rho_z + 2\gamma \sin ka e^{-2i\phi} \rho_y, \quad (4.4)$$

where $\rho_{x,y,z}$ are Pauli matrices acting on the Nambu particle-hole space. Now Equation (4.3) can be readily diagonalized into

$$\hat{H}_G^k = \frac{1}{2} \sum_k \hat{D}_k^\dagger \epsilon_k \rho_z \hat{D}_k = \sum_k \epsilon_k (\hat{d}_k^\dagger \hat{d}_k - \frac{1}{2}), \quad (4.5)$$

$$\epsilon_k = 2J \sqrt{(2t \cos ka + g)^2 + 4\gamma^2 \sin^2 ka}, \quad (4.6)$$

by introducing the Bogoliubov quasi-particle $\hat{D}_k = [\hat{d}_k, \hat{d}_{-k}^\dagger]^\top$ as

$$\hat{d}_k = e^{+i\phi} \sin(\theta_k/2) \hat{c}_k - i e^{-i\phi} \cos(\theta_k/2) \hat{c}_{-k}^\dagger, \quad (4.7)$$

$$\theta_k = \arctan[2\gamma \sin ka / (2t \cos ka + g)]. \quad (4.8)$$

We can use θ_k to define the topological invariant by the winding number

$$\mathcal{W} = \frac{1}{2\pi} \oint d\theta_k = \frac{1}{2\pi} \int_{\text{BZ}} \frac{d\theta_k}{dk} dk = \Theta(2t - |g|), \quad (4.9)$$

where Θ is the Heaviside step function. When $g < |2t|$ the bulk is in the topological phase with $\mathcal{W} = 1$, which means if the chain was cut at a point, two unpaired Majorana modes would appear at the ends of it. However, if $\mathcal{W} = 0$ the bulk will lie in the trivial phase and the edge modes disappear, which is known as the bulk-edge correspondence.

When the spin chain consists of different parametric parts, k is not a good quantum number anymore, we should come back to the real space. Especially for the non-interacting case $\delta_i = 0$, Equation (4.2) is reduced into the single-particle form \mathcal{H}_G^F shown

in Equation (4.23). By use of the PHS as $\{\mathcal{H}_G^F, C_F\} = 0$, $C_F = \rho_x \mathcal{K}$, for every eigenvector

$$\Phi_n^+ = [u_n(1), \dots, u_n(N), v_n(1), \dots, v_n(N)]^T \quad (4.10)$$

with positive energy $+\epsilon_n$, there is a corresponding eigenvector

$$\Phi_n^- = C_F \Phi_n^+ = [v_n^*(1), \dots, v_n^*(N), u_n^*(1), \dots, u_n^*(N)]^T \quad (4.11)$$

for the negative energy $-\epsilon_n$. Therefore, \mathcal{H}_G^F can be diagonalized as

$$\hat{H}_G^F = \frac{1}{2} \hat{C}^\dagger \mathcal{H}_G^F \hat{C} = \frac{1}{2} \hat{C}^\dagger \mathcal{P} \mathcal{E} \mathcal{P}^\dagger \hat{C} = \frac{1}{2} \hat{D}^\dagger \mathcal{E} \hat{D} = \sum_n \epsilon_n (\hat{d}_n^\dagger \hat{d}_n - \frac{1}{2}), \quad (4.12)$$

by the Bogoliubov quasi-particle $\hat{D} = (\hat{d}_1, \hat{d}_2, \dots, \hat{d}_N, \hat{d}_1^\dagger, \hat{d}_2^\dagger, \dots, \hat{d}_N^\dagger)^T$, where

$$\mathcal{E} = \sum_n \rho_z \otimes \epsilon_n |n\rangle \langle n| = \begin{bmatrix} +\epsilon_1 & 0 & 0 & & & \\ 0 & \ddots & 0 & & & \\ 0 & 0 & +\epsilon_N & & & \\ & & & -\epsilon_1 & 0 & 0 \\ & 0 & & 0 & \ddots & 0 \\ & & & 0 & 0 & -\epsilon_N \end{bmatrix}, \quad (4.13)$$

and $\mathcal{P} \equiv [\Phi_1^+, \dots, \Phi_N^+, \dots, \Phi_1^-, \dots, \Phi_N^-]$ is constructed by their eigenvectors,

$$\mathcal{P} = \begin{bmatrix} u_1(1) & \cdots & u_N(1) & v_1^*(1) & \cdots & v_N^*(1) \\ \vdots & \ddots & \vdots & \vdots & \ddots & \vdots \\ u_1(N) & \cdots & u_N(N) & v_1^*(N) & \cdots & v_N^*(N) \\ v_1(1) & \cdots & v_N(1) & u_1^*(1) & \cdots & u_N^*(1) \\ \vdots & \ddots & \vdots & \vdots & \ddots & \vdots \\ v_1(N) & \cdots & v_N(N) & u_1^*(N) & \cdots & u_N^*(N) \end{bmatrix}. \quad (4.14)$$

whose column vectors and row vectors should be orthonormal:

$$\sum_i [u_m^*(i) u_n(i) + v_m^*(i) v_n(i)] = \delta_{m,n}, \quad (4.15)$$

$$\sum_n [u_n^*(i) u_n(j) + v_n(i) v_n^*(j)] = \delta_{i,j}. \quad (4.16)$$

$$\sum_i [u_m^*(i) v_n^*(i) + v_m^*(i) u_n^*(i)] = 0 \quad (4.17)$$

$$\sum_n [u_n^*(i) v_n(j) + v_n(i) u_n^*(j)] = 0. \quad (4.18)$$

Since $\hat{D} = \mathcal{P}^\dagger \hat{C}$, $\hat{C} = \mathcal{P} \hat{D}$, the transformation between quasi-particles and fermions is

$$\hat{d}_n = \sum_i [u_n^*(i) \hat{c}_i + v_n^*(i) \hat{c}_i^\dagger], \quad (4.19)$$

$$\hat{c}_i = \sum_n [u_n(i) \hat{d}_n + v_n(i) \hat{d}_n^\dagger]. \quad (4.20)$$

If there are interacting terms $\delta_i \neq 0$ in Equation (4.2), above single-particle method fails since the Hamiltonian will not be quadratic anymore. Under this circumstance, we have to stay in the spin space and apply brute-force diagonalization on a $2^N \times 2^N$ matrix of Equation (4.1) to extract the many-body spectrum directly.

4.2 The Ising-XY-Ising Spin Link

In Section 1.3.2.1, we have demonstrated that the p -wave superconductor offers a platform for topological quantum computation. Unfortunately, compounds hosting topological superconductivity are rare, for example, Sr_2RuO_4 is believed to be one^[334]. However, material engineering of heterostructures composed of semiconducting and superconducting materials can lead to such special superconductors, i.e., 1D nanowires and 2D topological insulators with strong spin-orbit interaction (SOI) proximitized with the conventional s -wave superconductor^[335-337]. On the other hand, quantum magnets can mimic electronic systems without the proximity requirements^[338-340]. Specifically, a 1D quantum Ising model can emulate a Kitaev p -wave superconductor, via the renowned JWT^[106,136,341-342]. In particular, the topological phase transition and the occurrence of Majorana fermions as low-energy modes are all mapped into the spin system when the applied transverse magnetic field is varied, where the ferromagnetic (paramagnetic) phase in the spin chain corresponds to the topologically nontrivial (trivial) phase of the fermionic system^[69].

However, one should not be misled: Although there are some analogies of low-energy excitations between fermionic system and spin space, some topological properties will be lost after transformation^[108,343-344]. In the spin space, Majorana fermions are not localized objects anymore, and they can be mixed simply by a magnetic field along the Ising axis, i.e. the parity of the ground state is fragile. Nevertheless, it is of crucial importance to investigate which of the topological properties associated with Majorana fermions can survive in the spin chain and provide experimental witnesses of their manifestations. To achieve that, in this dissertation we propose and study the spin transport through an Ising-XY-Ising (IXI) inhomogeneous spin chain in which the Ising axes are misaligned. Borrowing from the electronic description, such a spin chain system emulates a phase-biased topological superconducting-normal-superconducting (SNS) junction that hosts Andreev bound states (ABSs), with a supercurrent flowing through the normal part^[62,345-347].

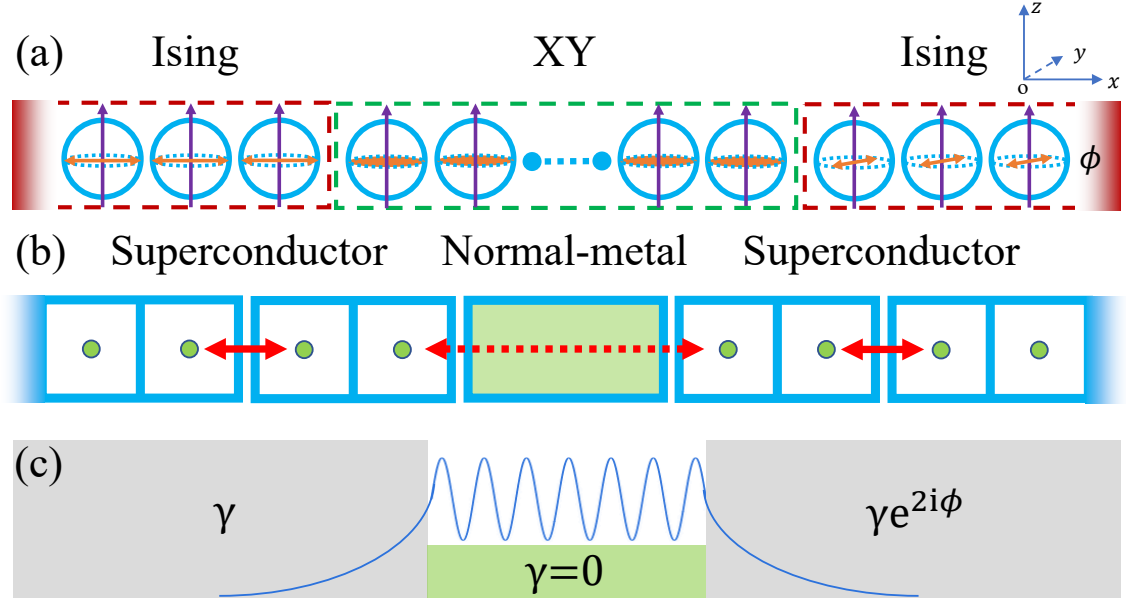


Figure 4.1 The mapping between the IXI spin chain and the SNS structure.

(a) Schematic of the IXI spin (blue ball) chain in the transverse field (purple arrow): the middle part (green dashed box) is the isotropic XY model, the left and right parts (red dashed boxes) are the quasi-Ising model with the same anisotropy γ , whereas the right part contains a different spin anisotropic angle ϕ (the orientation of the orange arrow) from the left part. (b) After the JWT, the IXI emulates a topological SNS structure, every fermion (blue box) is split into two Majoranas (green dots). There can host Majorana couplings (red dashed arrow) between the left and right p -wave superconductors. (c) The wave function (blue curve) of the JW Majorana bound state lies in the gapped-gapless-gapped topological SNS structure^[67].

4.2.1 Model Hamiltonian

The N -site anisotropic XY spin chain in a transverse magnetic field, presented schematically in Figure 4.1(a) with open boundary conditions, is governed by the following Hamiltonian

$$\hat{H}_G^S = -J \sum_i (t_i + \gamma_i) \hat{\sigma}_i^m \hat{\sigma}_{i+1}^m + (t_i - \gamma_i) \hat{\sigma}_i^n \hat{\sigma}_{i+1}^n + g_i \hat{\sigma}_i^z. \quad (4.21)$$

By tuning the value of parameters, the chain is split into three regions: Ising-XY-Ising, pertaining to the spin Josephson junctions (JJs). The number of sites in the left, middle, and right parts is N_L , N_M , N_R , respectively. The middle chain and the left and right interfaces ($x_L = N_L$, $x_R = N_L + N_M$, respectively) are described by the isotropic XY model by setting $\gamma_i = \phi_i = 0$, $\forall i \in [x_L, x_R]$. The left and right parts are misaligned, i.e., $\phi_i = \phi$ in the right part and $\phi_i = 0$ in the left part, quasi-Ising (anisotropic XY) spin chains such that $\gamma_i = \gamma \neq 0$. Although the coupling strength is set as $t_i = t$ in the bulk regions of the spin chain, the parameters at the two interfaces are different: $t_{x_L} = t_{x_R} = \mathbb{t}$. When $\mathbb{t} = t$, the connection between different regions are perfect, while if $\mathbb{t} = 0$ they are decoupled from each other.

We perform the Jordan-Wigner transformation $\hat{c}_i^\dagger = \prod_{j=1}^{i-1} (-\hat{\sigma}_j^z) \hat{\sigma}_i^+$, $\hat{\sigma}_i^\pm = (\hat{\sigma}_i^x \pm i\hat{\sigma}_i^y)/2$ on Equation (4.21), and obtain the fermionic Hamiltonian

$$\hat{H}_G^F = -2J \sum_i \left[(t_i \hat{c}_i^\dagger \hat{c}_{i+1} + \gamma_i e^{-2i\phi_i} \hat{c}_i^\dagger \hat{c}_{i+1}^\dagger + \text{H.c.}) + g_i (\hat{c}_i^\dagger \hat{c}_i - 1/2) \right], \quad (4.22)$$

where \hat{c}_i^\dagger (\hat{c}_i) is the creation (annihilation) operator of the JW electron at site i . It turns out the IXI emulates a topological superconducting-normal-superconducting (SNS) junction [Figure 4.1(b)]. Since Equation (4.22) is quadratic, it can be expressed in Bogoliubov-de Gennes (BdG) form $\hat{H}_G^F = \hat{C}^\dagger \mathcal{H}_G^F \hat{C}/2$ with

$$\mathcal{H}_G^F = -2J \sum_i \left\{ [(t_i \rho_z + i\gamma_i e^{-2i\phi_i} \rho_y) \otimes |i\rangle \langle i+1| + \text{H.c.}] + g_i \rho_z \otimes |i\rangle \langle i| \right\}, \quad (4.23)$$

where $\hat{C} = (\hat{c}_1, \hat{c}_2, \dots, \hat{c}_N, \hat{c}_1^\dagger, \hat{c}_2^\dagger, \dots, \hat{c}_N^\dagger)^\top$ is a $2N$ -dimensional spinor and $|i\rangle = (0, \dots, 1, 0, \dots)^\top$ is an N -dimensional basis vector corresponding to the i th site of the chain. By use of the Bogoliubov quasi-particle $\hat{D} = (\hat{d}_1, \hat{d}_2, \dots, \hat{d}_N, \hat{d}_1^\dagger, \hat{d}_2^\dagger, \dots, \hat{d}_N^\dagger)^\top$ basis, \hat{H}_G^F is diagonalized into $\sum_n \epsilon_n (\hat{d}_n^\dagger \hat{d}_n - 1/2)$ with a set of single-particle energy ϵ_n .

4.2.2 The Spin Current Operator

When the twisting angle ϕ of the right Ising part is nonzero, there is a spin supercurrent flowing through the middle sector, whose coupling Hamiltonian is XY-type, $\hat{H}_{\text{xy}} = -Jt(\hat{\sigma}_i^x \hat{\sigma}_{i+1}^x + \hat{\sigma}_i^y \hat{\sigma}_{i+1}^y)$. In the Heisenberg picture the general spin current operator follows the conservation condition equation

$$\Delta \hat{J} \equiv -\dot{\hat{\sigma}}_i(t) = i[\hat{\sigma}_i(t), \hat{H}_{\text{xy}}]. \quad (4.24)$$

Expand the equation in the x, y, z axis (we hide time-dependent index for simplicity),

$$\begin{aligned} \Delta \hat{J}_x &= -iJt \left(\hat{\sigma}_{i-1}^x [\hat{\sigma}_i^x, \hat{\sigma}_i^x] + \hat{\sigma}_{i-1}^y [\hat{\sigma}_i^x, \hat{\sigma}_i^y] + [\hat{\sigma}_i^x, \hat{\sigma}_i^x] \hat{\sigma}_{i+1}^x + [\hat{\sigma}_i^x, \hat{\sigma}_i^y] \hat{\sigma}_{i+1}^y \right) \\ &= +2Jt \left(\hat{\sigma}_{i-1}^y \hat{\sigma}_i^z + \hat{\sigma}_i^z \hat{\sigma}_{i+1}^y \right) = 0, \end{aligned} \quad (4.25)$$

$$\begin{aligned} \Delta \hat{J}_y &= -iJt \left(\hat{\sigma}_{i-1}^x [\hat{\sigma}_i^y, \hat{\sigma}_i^x] + \hat{\sigma}_{i-1}^y [\hat{\sigma}_i^y, \hat{\sigma}_i^y] + [\hat{\sigma}_i^y, \hat{\sigma}_i^x] \hat{\sigma}_{i+1}^x + [\hat{\sigma}_i^y, \hat{\sigma}_i^y] \hat{\sigma}_{i+1}^y \right) \\ &= -2Jt \left(\hat{\sigma}_{i-1}^x \hat{\sigma}_i^z + \hat{\sigma}_i^z \hat{\sigma}_{i+1}^x \right) = 0, \end{aligned} \quad (4.26)$$

$$\begin{aligned} \Delta \hat{J}_z &= -iJt \left(\hat{\sigma}_{i-1}^x [\hat{\sigma}_i^z, \hat{\sigma}_i^x] + \hat{\sigma}_{i-1}^y [\hat{\sigma}_i^z, \hat{\sigma}_i^y] + [\hat{\sigma}_i^z, \hat{\sigma}_i^x] \hat{\sigma}_{i+1}^x + [\hat{\sigma}_i^z, \hat{\sigma}_i^y] \hat{\sigma}_{i+1}^y \right) \\ &= +2Jt \left(\hat{\sigma}_{i-1}^x \hat{\sigma}_i^y - \hat{\sigma}_{i-1}^y \hat{\sigma}_i^x + \hat{\sigma}_i^y \hat{\sigma}_{i+1}^x - \hat{\sigma}_i^x \hat{\sigma}_{i+1}^y \right). \end{aligned} \quad (4.27)$$

Thus we have

$$\Delta \hat{J} = \hat{J}^{\text{out}} - \hat{J}^{\text{in}} = -2Jt [(\hat{\sigma}_i^x \hat{\sigma}_{i+1}^y - \hat{\sigma}_i^y \hat{\sigma}_{i+1}^x) - (\hat{\sigma}_{i-1}^x \hat{\sigma}_i^y - \hat{\sigma}_{i-1}^y \hat{\sigma}_i^x)] \mathbf{e}_z, \quad (4.28)$$

and define a z-component spin current operator as $\hat{J}_z \equiv \hat{J}_z^{\text{out}} [348-349]$, more explicitly ^①,

$$\hat{J}_z / (-2Jt) = \hat{\sigma}_i^x \hat{\sigma}_{i+1}^y - \hat{\sigma}_i^y \hat{\sigma}_{i+1}^x = 2i(\hat{c}_i^\dagger \hat{c}_{i+1} - \hat{c}_{i+1}^\dagger \hat{c}_i). \quad (4.29)$$

In this dissertation, we only focus on \hat{J}_z , since the expectation values of \hat{J}_x and \hat{J}_y vanish, while \hat{J}_z remains a constant $\forall i \in (x_L, x_R)$ in the middle part due to current conservation. With the help of quasi-particle in fermionic space in Equation (4.20), the expectation value of the spin current is calculated as

$$\begin{aligned} \langle \hat{J}_z \rangle &= -4iJt \sum_{m,n} \left[\langle [u_m^*(i) \hat{d}_m^\dagger + v_m(i) \hat{d}_m] [u_n(i+1) \hat{d}_n + v_n^*(i+1) \hat{d}_n^\dagger] \right. \\ &\quad \left. - \langle [u_m^*(i+1) \hat{d}_m^\dagger + v_m(i+1) \hat{d}_m] [u_n(i) \hat{d}_n + v_n^*(i) \hat{d}_n^\dagger] \rangle \right] \\ &= -4iJt \sum_n \left[\{ [u_n^*(i) u_n(i+1) \langle \hat{d}_n^\dagger \hat{d}_n \rangle + v_n(i) v_n^*(i+1) \langle \hat{d}_n \hat{d}_n^\dagger \rangle] \right. \\ &\quad \left. - [u_n^*(i+1) u_n(i) \langle \hat{d}_n^\dagger \hat{d}_n \rangle + v_n(i+1) v_n^*(i) \langle \hat{d}_n \hat{d}_n^\dagger \rangle] \} \right] \\ &= -4iJt \sum_n \left[\{ [u_n^*(i) u_n(i+1) - v_n(i) v_n^*(i+1)] \right. \\ &\quad \left. - [u_n^*(i+1) u_n(i) - v_n(i+1) v_n^*(i)] \} f_n + [v_n(i) v_n^*(i+1) - v_n(i+1) v_n^*(i)] \right] \\ &= -4Jt \sum_n \left[\{ i[u_n^*(i) u_n(i+1) - v_n(i) v_n^*(i+1)] + \text{c.c.} \} f_n \right. \\ &\quad \left. + [iv_n(i) v_n^*(i+1) + \text{c.c.}] \right] \\ &= -8Jt \sum_n \text{Re} \left\{ i[u_n^*(i) u_n(i+1) - v_n(i) v_n^*(i+1)] f_n + iv_n(i) v_n^*(i+1) \right\} \\ &= +8Jt \sum_n \text{Im} \left\{ [u_n^*(i) u_n(i+1) - v_n(i) v_n^*(i+1)] f_n + v_n(i) v_n^*(i+1) \right\} \\ &= +8Jt \sum_n \text{Im} \left\{ [u_n^*(i) u_n(i+1) + v_n^*(i) v_n(i+1)] f_n + u_n(i) u_n^*(i+1) \right\}, \quad (4.30) \end{aligned}$$

where Equation (4.16) is used to simplify the last line.

Such a spin superfluidity is analogous to the superconductivity in the presence of a phase bias. Note that, however, in order to fulfill the charge conservation at the mean field level, the superconducting gap has to be self-consistently take a certain value. Yet, the anisotropy degree of the IXI spin link allows \hat{J}_z to be not conserved in the Ising portions. Therefore, the lattice, whose dynamics are neglected in this dissertation, effectively acts as a source and drain of spin.

^① Alternatively, one can define $\hat{J}_z \equiv \hat{J}_z^{\text{in}} = 2Jt(\hat{\sigma}_{i-1}^y \hat{\sigma}_i^x - \hat{\sigma}_{i-1}^x \hat{\sigma}_i^y) = 4iJt(\hat{c}_i^\dagger \hat{c}_{i-1} - \hat{c}_{i-1}^\dagger \hat{c}_i)$, whose expectation value is the same as \hat{J}_z^{out} , since $\Delta \hat{J}_z = 0$ for a stationary state.

4.3 Symmetry Analysis

The symmetries of a system play an essential role in the topological phase classification. Nowadays, non-interacting fermionic systems are classified into ten classes by means of three fundamental symmetries: time-reversal symmetry (TRS), particle-hole symmetry (PHS), and sublattice symmetry^[124,129,350-351]. In addition, crystalline symmetries (e.g., inversion symmetry)^[352-355], as well as many-body interactions^[356-357], can also lead to different topological classes, which, combined with magnetic impurities^[358-360], may result in various types of Josephson effects (JEs) in superconducting junctions. Roughly speaking, periodicities of JEs are 2π in the trivial phase, 4π in the topological phase, and 8π in the topological phase with many-body interactions or impurities. The latter two cases are known as \mathbb{Z}_2 and \mathbb{Z}_4 fractional JEs pertaining to contributions from Majoranas and parafermions, respectively^[360-362]. We note that, for more general parafermionic systems, the periodicity can be further fractionalized^[343]. In this Chapter, we realize the spin chain-analogs of these JEs and unveil an exotic dependence of the \mathbb{Z}_2 and \mathbb{Z}_4 fractional spin JEs on the parity of the number of sites. We go on to find several symmetries in the spin chain that protect the associated spin current from various types of spin-spin interactions and demonstrate their robustness against fluctuating magnetic fields. The symmetries of a system are independent of representations, although they can be interpreted differently in the spin and fermionic pictures. In the following subsections, we will identify the symmetries occurring in the spin system and find out their fermionic counterparts through the JWT. To be more general, we introduce two types of interacting Hamiltonians: the spin-spin interactions in the z direction (ZZ-type),

$$\hat{H}_I^S = -J \sum_i \delta_i \hat{\sigma}_i^z \hat{\sigma}_{i+1}^z, \quad (4.31)$$

acting on the spin space, and the Coulomb interactions (NN-type),

$$\hat{H}_I^F = -4J \sum_i \chi_i \hat{n}_i \hat{n}_{i+1}. \quad (4.32)$$

Equations (4.31) and (4.32) are connected by the JWT up to global renormalization of the magnetic field $4\hat{n}_i \hat{n}_{i+1} \Leftrightarrow 1 + \hat{\sigma}_i^z + \hat{\sigma}_{i+1}^z + \hat{\sigma}_i^z \hat{\sigma}_{i+1}^z$ which, as we see below, will have significant implications. To begin with, we first introduce a theorem for time-reversal invariant systems.

Theorem 4.1 (Kramers Theorem^[363]): Given a time-reversal invariant system described by the Hamiltonian H , if the time reversal operator Θ follows $\Theta^2 = -1$, all energy levels of the system are at least two-fold degenerate.

Proof Suppose such a system has a non-degenerate energy eigenstate $|\psi\rangle$ with eigenvalue E , the time reversal operator commute with the Hamiltonian $[\Theta, H] = 0$. Applying Θ to such a state gives $\Theta|\psi\rangle = \exp(i\alpha)|\psi\rangle$, where α is a constant. Since Θ is anti-unitary,

$$\Theta^2|\psi\rangle = \Theta e^{i\alpha}|\psi\rangle = e^{-i\alpha}\Theta|\psi\rangle = |\psi\rangle, \quad (4.33)$$

which contradicts to the prerequisite $\Theta^2 = -1$ and implies the energy eigenstate $|\psi\rangle$ must be degenerate. ■

4.3.1 Spin \mathbb{Z}_2 Symmetry

The spin chain has a \mathbb{Z}_2 symmetry since $[\hat{H}_G^s, \hat{P}_s] = 0$ with $\hat{P}_s = \prod_i \hat{\sigma}_i^z$, $\hat{P}_s^2 = +1$, which acts on Pauli operators as

$$\hat{P}_s \hat{\sigma}_i^{m(n)} \hat{P}_s^{-1} = -\hat{\sigma}_i^{m(n)}, \quad \hat{P}_s \hat{\sigma}_i^z \hat{P}_s^{-1} = +\hat{\sigma}_i^z. \quad (4.34)$$

By the JWT, the corresponding operator in the fermionic system is identified as a parity operator $\hat{P}_f = \prod_i (2\hat{n}_i - 1)$, which transforms fermionic operators as

$$\hat{P}_f \hat{c}_i^\dagger \hat{P}_f^{-1} = -\hat{c}_i^\dagger, \quad \hat{P}_f \hat{c}_i \hat{P}_f^{-1} = -\hat{c}_i. \quad (4.35)$$

Since Equation (4.22) is a sum of terms containing an even number of fermionic creation and annihilation operators, the system is required to preserve the parity as $[\hat{H}_G^f, \hat{P}_f] = 0$ at any time, although the number of fermions is not conserved. One can easily verify that \mathbb{Z}_2 symmetry holds for the aforementioned two types of interacting Hamiltonians in Equations (4.31)-(4.32). Considering the pure Ising chain with $\delta_i = g_i = 0$ and $\gamma_i = t_i$, the spin ground states will simultaneously break above \mathbb{Z}_2 symmetry, which in turn gives two degenerate ground states in the Kitaev model characterized by Majorana zero modes.

4.3.2 Real Time-Reversal Symmetry

If $g_i = 0$ globally, Equation (4.21) contains *real* TRS (rTRS) with $[\hat{H}_G^s, \hat{T}_s] = 0$ by the operator $\hat{T}_s = \prod_i i\hat{\sigma}_i^y \mathcal{K}$ acting on the Pauli operators as

$$\hat{T}_s \hat{\sigma}_i^\alpha \hat{T}_s^{-1} = -\hat{\sigma}_i^\alpha, \quad \alpha = m, n, z. \quad (4.36)$$

where \mathcal{K} is an anti-unitary complex conjugate operator. Since $\hat{T}_s^2 = (-1)^N$, according to the Kramers theorem, all many-body spectra must be degenerate when N is odd. Through the JWT, Equation (4.22) fulfills $[\hat{H}_G^f, \hat{T}_f] = 0$ inherited from the spin space,

$$\hat{T}_f = \prod_i [\hat{c}_i^\dagger + (-1)^{N+1+i} \hat{c}_i] \mathcal{K} \quad (4.37)$$

is a *second-quantized* operator acting on Fock space as $\hat{T}_F \hat{T}_F^{-1} = -i$,

$$\hat{T}_F \hat{c}_i^\dagger \hat{T}_F^{-1} = (-1)^i \hat{c}_i, \quad \hat{T}_F \hat{c}_i \hat{T}_F^{-1} = (-1)^i \hat{c}_i^\dagger. \quad (4.38)$$

These identities can be immediately verified as

$$\begin{aligned} \hat{T}_F \hat{c}_i &= [\hat{c}_1^\dagger - (-1)^{N+1} \hat{c}_1] \cdots [\hat{c}_i^\dagger - (-1)^{N+i} \hat{c}_i] \cdots [\hat{c}_N^\dagger - \hat{c}_N] \mathcal{K} \hat{c}_i \\ &= (-1)^{N-i} [\hat{c}_1^\dagger - (-1)^{N+1} \hat{c}_1] \cdots [\hat{c}_i^\dagger - (-1)^{N+i} \hat{c}_i] \hat{c}_i \cdots [\hat{c}_N^\dagger - \hat{c}_N] \mathcal{K} \\ &= (-1)^{N-i} [\hat{c}_1^\dagger - (-1)^{N+1} \hat{c}_1] \cdots (-1)^{N+i+1} \hat{c}_i^\dagger [\hat{c}_i^\dagger - (-1)^{N+i} \hat{c}_i] \cdots [\hat{c}_N^\dagger - \hat{c}_N] \mathcal{K} \\ &= (-1)^{N-i} (-1)^{N+i+1} (-1)^{i-1} \hat{c}_i^\dagger [\hat{c}_1^\dagger - (-1)^{N+1} \hat{c}_1] \cdots [\hat{c}_i^\dagger - (-1)^{N+i} \hat{c}_i] \cdots [\hat{c}_N^\dagger - \hat{c}_N] \mathcal{K} \\ &= (-1)^i \hat{c}_i^\dagger [\hat{c}_1^\dagger - (-1)^{N+1} \hat{c}_1] \cdots [\hat{c}_i^\dagger - (-1)^{N+i} \hat{c}_i] \cdots [\hat{c}_N^\dagger - \hat{c}_N] \mathcal{K} \\ &= (-1)^i \hat{c}_i^\dagger \hat{T}_F \quad \Leftrightarrow \quad \hat{T}_F \hat{c}_i \hat{T}_F^{-1} = (-1)^i \hat{c}_i^\dagger, \\ \hat{T}_F \hat{c}_i^\dagger &= [\hat{c}_1^\dagger - (-1)^{N+1} \hat{c}_1] \cdots [\hat{c}_i^\dagger - (-1)^{N+i} \hat{c}_i] \cdots [\hat{c}_N^\dagger - \hat{c}_N] \mathcal{K} \hat{c}_i^\dagger \\ &= (-1)^{N-i} [\hat{c}_1^\dagger - (-1)^{N+1} \hat{c}_1] \cdots [\hat{c}_i^\dagger - (-1)^{N+i} \hat{c}_i] \hat{c}_i^\dagger \cdots [\hat{c}_N^\dagger - \hat{c}_N] \mathcal{K} \\ &= (-1)^{N-i} [\hat{c}_1^\dagger - (-1)^{N+1} \hat{c}_1] \cdots (-1)^{N+i+1} \hat{c}_i [\hat{c}_i^\dagger - (-1)^{N+i} \hat{c}_i] \cdots [\hat{c}_N^\dagger - \hat{c}_N] \mathcal{K} \\ &= (-1)^{N-i} (-1)^{N+i+1} (-1)^{i-1} \hat{c}_i [\hat{c}_1^\dagger - (-1)^{N+1} \hat{c}_1] \cdots [\hat{c}_i^\dagger - (-1)^{N+i} \hat{c}_i] \cdots [\hat{c}_N^\dagger - \hat{c}_N] \mathcal{K} \\ &= (-1)^i \hat{c}_i [\hat{c}_1^\dagger - (-1)^{N+1} \hat{c}_1] \cdots [\hat{c}_i^\dagger - (-1)^{N+i} \hat{c}_i] \cdots [\hat{c}_N^\dagger - \hat{c}_N] \mathcal{K} \\ &= (-1)^i \hat{c}_i \hat{T}_F \quad \Leftrightarrow \quad \hat{T}_F \hat{c}_i^\dagger \hat{T}_F^{-1} = (-1)^i \hat{c}_i, \\ \hat{T}_F^2 &= \prod_{i=1}^{N-1} (-1)^i \prod_{i=1}^N [\hat{c}_i^\dagger - (-1)^{N+i} \hat{c}_i] \prod_{i=N}^1 [\hat{c}_i^\dagger - (-1)^{N+i} \hat{c}_i] = \prod_{i=1}^{N-1} (-1)^i \prod_{i=1}^N (-1)^{N+1+i} \\ &= (-1)^{N(N-1)/2} \times (-1)^{3(N+1)N/2} = (-1)^{2N^2+N} = (-1)^N. \end{aligned}$$

This can be interpreted as the charge conjugation in the fermionic language. Based on non-interacting Equation (4.23), we can rewrite \hat{T}_F in a *first-quantized* form

$$\mathcal{T}_F = \rho_x \mathcal{K} \otimes \sum_i (-1)^i |i\rangle \langle i|, \quad \mathcal{T}_F^2 = +1, \quad (4.39)$$

which renders $[\mathcal{H}_G^F, \mathcal{T}_F] = 0$. Note Equations (4.38) are more general than Equations (4.39) since they can accommodate interactions, i.e., Equation (4.32). We find $[\hat{H}_1^F, \hat{T}_F] \neq 0$, yet the ZZ-type interactions in Equation (4.31) retain rTRS due to $[\hat{H}_1^S, \hat{T}_S] = 0$.

When N is odd, the twofold degeneracies in the many-body spectrum are protected by the second-quantized rTRS operator with $\hat{T}_F^2 = -1$, which enforces intrinsic zero modes in the single-particle spectrum. Under the fermionic picture, as the coupling strength \mathfrak{t} increases, amplitudes of the intrinsic zero modes in the middle part will exponentially leak into the superconducting parts, and fully merge with Majorana zero modes in the thermodynamic limit, whose wave functions are well localized at the edges of the chain

and cause no effect on the in-gap spectrum.

4.3.3 Inversion Time-Reversal Symmetry

Although the first-quantized rTRS operator $\mathcal{T}_F^2 = +1$ cannot reflect any degenerate properties in the single-particle spectrum, it gives us a hint to find out a hidden *inversion* TRS (iTRS) which leads to an odd-even effect (see discussions in Section. 4.5.3). We first introduce a lattice inversion operator,

$$\mathcal{I} = \sum_i (-1)^i (|i\rangle \langle N+1-i|), \quad \mathcal{I}^2 = (-1)^{N+1}, \quad (4.40)$$

which will transform matrix elements of the nearest-neighboring sites with an additional minus sign after applying on the lattice space, e.g., $\tilde{t}_i \equiv t_{N-i} \rightarrow -t_i$ whereas $\tilde{g}_i \equiv g_{N+1-i} \rightarrow g_i$, where we denote parameters with tilde are elements inverted from original position. With the help of \mathcal{I} , we can define the iTRS operator

$$\mathcal{T}_1 = \begin{cases} i\rho_y \mathcal{K} \otimes \mathcal{I}, & \text{for odd } N, \\ \rho_x \mathcal{K} \otimes \mathcal{I}, & \text{for even } N. \end{cases} \quad (4.41)$$

Applying \mathcal{T}_1 to Equation (4.23), we obtain

$$\begin{aligned} \mathcal{T}_1 \mathcal{H}_G^F \mathcal{T}_1^{-1} = & -2J \sum_i \left\{ [(\tilde{t}_i \rho_z - (-1)^N i\tilde{\gamma}_i e^{-2i\tilde{\phi}_i \rho_z} \rho_y) \otimes |i\rangle \langle i+1| + \text{H.c.}] \right. \\ & \left. - \tilde{g}_i \rho_z \otimes |i\rangle \langle i| \right\}. \end{aligned} \quad (4.42)$$

By comparing Equations (4.23) and (4.42), it turns out that to retain iTRS as $[\mathcal{H}_G^F(\phi), \mathcal{T}_1] = 0$ in the IXI chain, not only should we set $\tilde{g}_i = g_i = 0$, $\tilde{t}_i = t_i$, $\tilde{\gamma}_i = \gamma_i$, but also ϕ is restricted to the following values:

$$e^{-2i\phi} = (-1)^{N+1} \Leftrightarrow \phi = \begin{cases} l\pi, & \text{for odd } N, \\ \pi/2 + l\pi, & \text{for even } N, \end{cases} \quad (4.43)$$

with $l \in \mathbb{Z}$. Note that $\mathcal{T}_1^2 = -1$ in both odd-even cases, according to Kramers theorem, all *single-particle* states at above specific ϕ should contain twofold degeneracy.

More generally, we rewrite Equations (4.40) in a second-quantized form acting on fermions as $\hat{T}_1 \hat{T}_1^{-1} = -i$,

$$\hat{T}_1 \hat{c}_i^\dagger \hat{T}_1^{-1} = \begin{cases} +i(-1)^i \hat{c}_{N+1-i}, & \text{for odd } N, \\ (-1)^i \hat{c}_{N+1-i}, & \text{for even } N, \end{cases} \quad (4.44)$$

and its actions on spins are $\hat{T}_1 \hat{\sigma}_i^z \hat{T}_1^{-1} = -\hat{\sigma}_{N+1-i}^z$,

$$\hat{T}_1 \hat{\sigma}_i^{m(n)} \hat{T}_1^{-1} = \begin{cases} +i\hat{P}_s \hat{\sigma}_{N+1-i}^{m(n)}, & \text{for odd } N, \\ \pm i\hat{P}_s \hat{\sigma}_{N+1-i}^{n(m)}, & \text{for even } N, \end{cases} \quad (4.45)$$

which can be understood as the charge-parity symmetry. It is straightforward to verify that $[\hat{H}_G^F, \hat{T}_1] = 0$ in the non-interacting case $\delta_i = 0$, the tricky parts are superconducting terms $\hat{T}_1(\gamma_i e^{-2i\phi_i} \hat{c}_i^\dagger \hat{c}_{i+1}^\dagger + \text{H.c.}) \hat{T}_1^{-1}$

$$\begin{cases} +\gamma_i e^{+2i\phi_i} \hat{c}_{N+1-i} \hat{c}_{N-i} + \gamma_i e^{-2i\phi_i} \hat{c}_{N-i}^\dagger \hat{c}_{N+1-i}^\dagger \equiv +(\tilde{\gamma}_{N-i} \hat{c}_{N-i}^\dagger \hat{c}_{N+1-i}^\dagger + \text{h.c.}), & N \text{ is odd;} \\ -\gamma_i e^{+2i\phi_i} \hat{c}_{N+1-i} \hat{c}_{N-i} - \gamma_i e^{-2i\phi_i} \hat{c}_{N-i}^\dagger \hat{c}_{N+1-i}^\dagger \equiv -(\tilde{\gamma}_{N-i} \hat{c}_{N-i}^\dagger \hat{c}_{N+1-i}^\dagger + \text{h.c.}), & N \text{ is even;} \end{cases}$$

which meets requirements of *first-quantized* in Equation(4.43). Applying the rTRS operator to the ZZ-type interactions of Equation (4.31), we get

$$\begin{aligned} \delta_i \hat{\sigma}_i^z \hat{\sigma}_{i+1}^z &\xrightarrow{\text{JWT}} \delta_i (2\hat{c}_i^\dagger \hat{c}_i - 1)(2\hat{c}_{i+1}^\dagger \hat{c}_{i+1} - 1) \\ &\xrightarrow{\hat{T}_1} \delta_i (2\hat{c}_{N+1-i} \hat{c}_{N+1-i}^\dagger - 1)(2\hat{c}_{N-i} \hat{c}_{N-i}^\dagger - 1) \\ &= \delta_i (2\hat{c}_{N-i}^\dagger \hat{c}_{N-i} - 1)(2\hat{c}_{N+1-i}^\dagger \hat{c}_{N+1-i} - 1) \\ &\xrightarrow{\text{JWT}} \delta_i \hat{\sigma}_{N-i}^z \hat{\sigma}_{N+1-i}^z \equiv \tilde{\delta}_{N-i} \hat{\sigma}_{N-i}^z \hat{\sigma}_{N+1-i}^z. \end{aligned} \quad (4.46)$$

Once $\delta_i = \tilde{\delta}_i$ are set symmetrically, the system Hamiltonian always commutes with iTRS operator at specific ϕ illustrated in Equation (4.43), which ensures twofold degeneracies of many-body states in the interacting case. As for the NN-type interactions in Equation (4.32), we obtain

$$\hat{T}_1(-\hat{H}_1^F/4J)\hat{T}_1^{-1} = \sum_i \tilde{\chi}_i \hat{c}_i \hat{c}_i^\dagger \hat{c}_{i+1} \hat{c}_{i+1}^\dagger, \quad (4.47)$$

and expand to $\sum_i \tilde{\chi}_i (\hat{n}_i \hat{n}_{i+1} + 1 - \hat{c}_i^\dagger \hat{c}_i - \hat{c}_{i+1}^\dagger \hat{c}_{i+1})$, whose last three terms will break iTRS at any ϕ , even if we set $\chi_i = \tilde{\chi}_i$ symmetrically. Such seemingly trivial local terms will dramatically alter the periodicities of the spin JEs (see Figure 4.3 and further discussions in Section 4.5).

Note that in the above proof all parameters are required to hold strict inversion symmetry under $N_L = N_R$, thus the odd-even effect only depends on N_M . However, by the fact that the ABSs decay exponentially in the two superconducting parts, as long as their lengths are much larger than superconducting coherence length, the degenerate properties are still robust within the energy gap regardless of the parity and the equality of N_L and N_R , which in turn underscores the dominance of N_M .

4.4 Low-Energy Theory

In the following subsections, we will focus on the low-energy sectors under the fermionic description, utilizing both a continuum theory and a full lattice diagonalization. Given translation symmetry under periodic boundary conditions, similar to Equation (1.47) in Section 1.3.2, the bulk spectrum of the isolated anisotropic XY spin chain reads^[341]

$$\epsilon_k = 2J \sqrt{(2t \cos ka + g)^2 + 4\gamma^2 \sin^2 ka}, \quad (4.48)$$

where k is the wave number after the Fourier transformation. When $\gamma \neq 0$, the spectrum is always gapped except at $|g| = 2t$ where the system undergoes a quantum phase transition. In the case of $|g| < 2t$, the fermionic chain will be in a topological phase where Majorana fermions appear at the edges if we cut off the chain, and the corresponding topological invariant is characterized by the topological winding number $\mathcal{W} = 1$. However, if $|g| > 2t$ such edge modes will disappear, the chain enters the trivial phase, and the value of the topological winding number goes to zero. Figure 4.1(c) depicts the wave function of the JW Majorana bound state (MBS) in the presence of a phase bias between two superconducting parts. Note that the middle sector is gapped in the trivial regime $|g| > 2t$, which hinders the occurrence of the supercurrent and makes the chain insulating. Since we are interested in the JEs pertaining to the supercurrent, we will only focus on the topological regime in the whole dissertation. Since the analytical expressions of the low-energy wave functions and the scattering matrices are rather complicated, we supplement the code for the verification of solutions in the *Mathematica* notebook^[70].

4.4.1 Spectra Near the Critical Point

On account of the long wavelength excitations dominating the low-energy properties near the critical point^①, we can replace the fermionic operators in Equation (4.22) by a continuous Fermi field operator $\hat{c}_i = \sqrt{a}\hat{\psi}(x)$. In the continuum limit $a \rightarrow 0$, the anti-commutation relations are transformed from Kronecker delta to a Dirac delta:

$$\{\hat{\psi}(x), \hat{\psi}^\dagger(x')\} = \delta(x - x'). \quad (4.49)$$

① Strictly speaking, the energy gap occurs at $k = 0$ when $g \rightarrow -2t$, while if $g \rightarrow +2t$, the energy gap takes at $k = \pm\pi/a$. The sign of g only depends on the direction of the z axis in the spin Hamiltonian and does not cause any different observational effect. When $g > 0$, we can define $k' = k + \pi/a$ to translate the momentum in the Brillouin zone and come back to the case of $g < 0$, hence in the whole dissertation we only investigate the negative regime.

Substituting the continuum Fermi field operators back into the Hamiltonian in Equation (4.22) and expanding it to second order in the spatial gradients, we obtain:

$$\begin{aligned}
 \frac{\hat{H}_G^c}{2J} &= - \sum_i \left(t \hat{c}_i^\dagger \hat{c}_{i+1} + t \hat{c}_{i+1}^\dagger \hat{c}_i + \gamma_i e^{-2i\phi_i} \hat{c}_i^\dagger \hat{c}_{i+1}^\dagger + \gamma_i e^{+2i\phi_i} \hat{c}_{i+1} \hat{c}_i + \frac{g}{2} \hat{c}_i^\dagger \hat{c}_i - \frac{g}{2} \hat{c}_i \hat{c}_i^\dagger \right) \\
 &= - \sum_i a \left[t \hat{\psi}^\dagger(x_i) \hat{\psi}(x_{i+1}) + t \hat{\psi}^\dagger(x_{i+1}) \hat{\psi}(x_i) + \gamma_i e^{-2i\phi_i} \hat{\psi}^\dagger(x_i) \hat{\psi}^\dagger(x_{i+1}) \right. \\
 &\quad \left. + \gamma_i e^{+2i\phi_i} \hat{\psi}(x_{i+1}) \hat{\psi}(x_i) + \frac{g}{2} \hat{\psi}^\dagger(x_i) \hat{\psi}(x_i) - \frac{g}{2} \hat{\psi}(x_i) \hat{\psi}^\dagger(x_i) \right] \\
 &= - \int dx \left[t \hat{\psi}^\dagger(x) \hat{\psi}(x+a) + t \hat{\psi}^\dagger(x+a) \hat{\psi}(x) + \gamma_i e^{-2i\phi_i} \hat{\psi}^\dagger(x) \hat{\psi}^\dagger(x+a) \right. \\
 &\quad \left. + \gamma_i e^{+2i\phi_i} \hat{\psi}(x+a) \hat{\psi}(x) + \frac{g}{2} \hat{\psi}^\dagger(x) \hat{\psi}(x) - \frac{g}{2} \hat{\psi}(x) \hat{\psi}^\dagger(x) \right] \\
 &= - \int dx \left[t \left(\hat{\psi}^\dagger(x) \hat{\psi}(x) + \hat{\psi}^\dagger(x) \frac{d\hat{\psi}(x)}{dx} a + \hat{\psi}^\dagger(x) \frac{d^2\hat{\psi}(x)}{dx^2} \frac{a^2}{2} \right) \right. \\
 &\quad \left. + t \left(\hat{\psi}^\dagger(x) \hat{\psi}(x) + a \frac{d\hat{\psi}^\dagger(x)}{dx} \hat{\psi}(x) + \frac{a^2}{2} \frac{d^2\hat{\psi}^\dagger(x)}{dx^2} \hat{\psi}(x) \right) \right. \\
 &\quad \left. + \gamma_i e^{-2i\phi_i} \left(\hat{\psi}^\dagger(x) \hat{\psi}^\dagger(x) + \hat{\psi}^\dagger(x) \frac{d\hat{\psi}^\dagger(x)}{dx} a + \hat{\psi}^\dagger(x) \frac{d^2\hat{\psi}^\dagger(x)}{dx^2} \frac{a^2}{2} \right) \right. \\
 &\quad \left. + \gamma_i e^{+2i\phi_i} \left(\hat{\psi}(x) \hat{\psi}(x) + a \frac{d\hat{\psi}(x)}{dx} \hat{\psi}(x) + \frac{a^2}{2} \frac{d^2\hat{\psi}(x)}{dx^2} \hat{\psi}(x) \right) \right. \\
 &\quad \left. + \frac{g}{2} \hat{\psi}^\dagger(x) \hat{\psi}(x) - \frac{g}{2} \hat{\psi}(x) \hat{\psi}^\dagger(x) \right] + O(a^3) \\
 &= - \int dx \frac{d}{dx} \left(t a \hat{\psi}^\dagger(x) \hat{\psi}(x) \right) - \int dx \left[\left(t + \frac{g}{2} \right) \hat{\psi}^\dagger(x) \hat{\psi}(x) - \left(t + \frac{g}{2} \right) \hat{\psi}(x) \hat{\psi}^\dagger(x) \right. \\
 &\quad \left. + \gamma_i a \left(e^{-2i\phi_i} \hat{\psi}^\dagger(x) \frac{d\hat{\psi}^\dagger(x)}{dx} - e^{+2i\phi_i} \hat{\psi}(x) \frac{d\hat{\psi}(x)}{dx} \right) \right. \\
 &\quad \left. + \frac{a^2}{2} \left(t \hat{\psi}^\dagger(x) \frac{d^2\hat{\psi}(x)}{dx^2} - t \hat{\psi}(x) \frac{d^2\hat{\psi}^\dagger(x)}{dx^2} \right) \right. \\
 &\quad \left. + \gamma_i e^{-2i\phi_i} \hat{\psi}^\dagger(x) \frac{d^2\hat{\psi}^\dagger(x)}{dx^2} + \gamma_i e^{+2i\phi_i} \hat{\psi}(x) \frac{d^2\hat{\psi}(x)}{dx^2} \right] + O(a^3) \\
 &= \text{Constant} - \frac{1}{2} \int dx [\hat{\psi}^\dagger(x), \hat{\psi}(x)] \\
 &\quad \times \begin{bmatrix} 2t + g + t a^2 \partial_x^2 & \gamma_i e^{-2i\phi_i} (2a \partial_x + a^2 \partial_x^2) \\ \gamma_i e^{+2i\phi_i} (-2a \partial_x + a^2 \partial_x^2) & -2t - g - t a^2 \partial_x^2 \end{bmatrix} \begin{bmatrix} \hat{\psi}(x) \\ \hat{\psi}^\dagger(x) \end{bmatrix} + O(a^3).
 \end{aligned}$$

Thus we can rewrite

$$\hat{H}_G^c = \text{Constant} + \frac{1}{2} \int dx \hat{\Psi}(x)^\dagger \mathcal{H}_G^c \hat{\Psi}(x) + O(a^3), \quad (4.50)$$

where \mathcal{H}_G^c is a single-particle continuous BdG Hamiltonian under the field spinor $\hat{\Psi}(x) = [\hat{\psi}(x), \hat{\psi}^\dagger(x)]^T$ basis:

$$\begin{aligned} \mathcal{H}_G^c/2J &= - (2t + g + ta^2\partial_x^2) \rho_z - 2i\gamma_i a e^{-2i\phi_i \rho_z} \rho_y \partial_x - \underbrace{\gamma_i a^2 e^{-2i\phi_i \rho_z} \rho_x \partial_x^2}_{\text{neglected for simplicity}} \\ &\approx - (2t + g + ta^2\partial_x^2) \rho_z - 2i\gamma_i a e^{-2i\phi_i \rho_z} \rho_y \partial_x. \end{aligned} \quad (4.51)$$

The coefficient in front of the second and first derivative indicates the effective mass, $m_i^* = \hbar^2/(4Jta^2)$, and velocity, respectively^[69]. To mimic the imperfect connections between different parts, we introduce a fictitious potential $\lambda a \delta(x - x_{L,R})$ at two interfaces, $x = x_{L,R}$, with barrier strength λ . When $\lambda \rightarrow \infty$, the three parts of the chain are decoupled from each other. Through the S-matrix approach^[62,364], we obtain the solvability equation for the ABSs spectrum,

$$\text{Re} \left[S_0^2 e^{i(K_M^+ - K_M^-)L} - S_1^2 e^{i(K_M^+ + K_M^-)L} \right] = S_2^2 \cos(2\phi), \quad (4.52)$$

where $K_M^\pm = \sqrt{\Omega \pm \Xi}/ta$ are the middle wave numbers with $\Omega = t(2t + g)$, $\Xi = t\epsilon/2J$, and $L = (N_M + 1)a$ is the length of the middle part, $S_{0,1,2}$ are the entries of the S matrix, whose explicit expressions are given in Section 4.4.2, together with the wave functions and the technical details. In the leading order series expansion around zero energy, the spectrum $E = \Xi/t$ is given by

$$E = 2\sqrt{\Omega} \left(\frac{\pi}{2} \mp \phi + n\pi \right) / \left[\frac{L}{a} + \frac{t(\lambda - \gamma)^2 + 2t\Omega}{2\gamma\Omega} \right], \quad (4.53)$$

which is plotted in Figure 4.2(a) against the spectra from the exact continuum theory and the lattice model.

4.4.2 Wave Functions Near the Critical Point

We can diagonalize the low-energy continuous Equation (4.51) as $\mathcal{H}_G^c \Phi(x) = \epsilon \Phi(x)$ by solving out differential equations of the two-component wave function $\Phi(x) = [u(x), v(x)]^T$, whose generalized expressions are shown as

$$\begin{aligned} u(x) &= e^{-i\phi} (C_1 \cos U e^{+K^+x} + C_2 \sin V e^{+K^-x} \\ &\quad + C_3 \cos U e^{-K^+x} + C_4 \sin V e^{-K^-x}), \end{aligned} \quad (4.54)$$

$$\begin{aligned} v(x) &= e^{+i\phi} (-C_1 \cos V e^{+K^+x} - C_2 \sin U e^{+K^-x} \\ &\quad + C_3 \cos V e^{-K^+x} + C_4 \sin U e^{-K^-x}), \end{aligned} \quad (4.55)$$

where $K^\pm = \sqrt{\Gamma - \Omega \pm \Lambda}/ta$, $U = \arccos[(\Lambda - \Xi)/\Gamma]/2$, $V = \arccos[(\Lambda + \Xi)/\Gamma]/2$, $\Lambda = \sqrt{\Gamma^2 + \Xi^2 - 2\Gamma\Omega}$, $\Gamma = 2\gamma^2$, $\Omega = t(2t + g)$, $\Xi = t\epsilon/2J$ are introduced for simplicity. Additionally, $K^+ = 2\gamma \cos U \cos V/ta$, $K^- = 2\gamma \sin U \sin V/ta$. Applying infinite boundary conditions on Equations (4.54), the right part wave functions are defined by setting $C_1 = C_2 = 0$, and the left part of the wave functions are obtained by setting $C_3 = C_4 = \phi = 0$. The middle part is a special case of $\phi = \gamma = 0$; one could reduce $K^\pm \rightarrow i\sqrt{\Omega \mp \Xi}/ta \equiv iK_M^\mp$ and find $K_M^+ = 2\gamma \sin U \cos V/ta$, $K_M^- = 2\gamma \cos U \sin V/ta$ after taking the limit $\gamma \rightarrow 0$. We are only interested in the ABSs, whose eigenvalues lie within the gap, i.e. $|\epsilon| < 2J(2t + g) \Leftrightarrow |\Xi| < \Omega$, which ensures K_M^\pm to be real. By introducing a new set of coefficients C_5, C_6, C_7, C_8 in the middle region, the explicit wave functions are shown as

$$u_M(x) = 1/\sqrt{K_M^+} \times (C_5 e^{+iK_M^+ x} + C_6 e^{-iK_M^+ x}), \quad (4.56)$$

$$v_M(x) = 1/\sqrt{K_M^-} \times (C_7 e^{+iK_M^- x} + C_8 e^{-iK_M^- x}). \quad (4.57)$$

The above wave functions have been normalized by the square root of wave numbers to maintain the quasi-particle current^[345]. Through imposing continuity and current conservation conditions at two interfaces presented in Section 4.4.3, we obtain the left- and right-scattering matrices $S_L^c = S(-1, 0)$, $S_R^c = S(+1, \phi)$ with

$$S(\tau, \phi) = \frac{1}{S_0^*} \begin{bmatrix} S_1 & i\tau e^{-2i\phi} S_2 \\ i\tau e^{+2i\phi} S_2 & S_1^* \end{bmatrix}, \quad (4.58)$$

and the entries are defined as

$$S_0 = \sin \beta (1 + \zeta^2 - 2\zeta e^{i\beta}) - 2ie^{i\beta} (\sin^2 \alpha - \sin^2 \beta), \quad (4.59)$$

$$S_1 = -\sin \beta [1 + \zeta^2 - 2\zeta (\cos \beta + i \sin \alpha)], \quad (4.60)$$

$$S_2 = 2 \sin \alpha \sqrt{\sin^2 \alpha - \sin^2 \beta}, \quad (4.61)$$

where $\alpha = U + V$, $\beta = U - V$, $\zeta = \lambda/\gamma$. The waves at the two interfaces only contain different factors caused by the middle wave number $K_M^\pm = \sqrt{\Omega \pm \Xi}/ta$, which is described by scattering matrix $S_M^c = \exp(i\rho_z K_M^{\rho_z} L)$. Notice that such a wave function factor will be canceled out due to Andreev reflection after traveling for one loop, which enforces,

$$\det(1 - S_M^c S_R^c S_M^c S_L^c) = 0, \quad (4.62)$$

and gives the energy transcendental Equation (4.52) for the ABSs. The wave-function coefficients are then determined by normalization condition $\int |u_n(x)|^2 + |v_n(x)|^2 dx = 1$.

After solving out the wave functions, the Hamiltonian is diagonalized into

$$\begin{aligned}
 \hat{H}_G^C &= \text{Constant} + \frac{1}{2} \int dx \hat{\Psi}(x)^\dagger \mathcal{H}_G^C \hat{\Psi}(x) \\
 &= \text{Constant} + \frac{1}{2} \int dx [\hat{\Psi}^\dagger(x), \hat{\Psi}(x)] \\
 &\quad \left(\sum_n \begin{bmatrix} u_n(x) & v_n^*(x) \\ v_n(x) & u_n^*(x) \end{bmatrix} \begin{bmatrix} +\epsilon_n & 0 \\ 0 & -\epsilon_n \end{bmatrix} \begin{bmatrix} u_n^*(x) & v_n^*(x) \\ v_n(x) & u_n(x) \end{bmatrix} \right) \begin{bmatrix} \hat{\Psi}(x) \\ \hat{\Psi}^\dagger(x) \end{bmatrix} \\
 &= \text{Constant} + \frac{1}{2} \sum_n \left(\int dx [\hat{\Psi}^\dagger(x), \hat{\Psi}(x)] \begin{bmatrix} u_n(x) & v_n^*(x) \\ v_n(x) & u_n^*(x) \end{bmatrix} \right) \\
 &\quad \times \begin{bmatrix} +\epsilon_n & 0 \\ 0 & -\epsilon_n \end{bmatrix} \left(\int dx \begin{bmatrix} u_n^*(x) & v_n^*(x) \\ v_n(x) & u_n(x) \end{bmatrix} \begin{bmatrix} \hat{\Psi}(x) \\ \hat{\Psi}^\dagger(x) \end{bmatrix} \right) \\
 &= \text{Constant} + \frac{1}{2} \sum_n [\hat{d}_n^\dagger, \hat{d}_n] \begin{bmatrix} +\epsilon_n & 0 \\ 0 & -\epsilon_n \end{bmatrix} \begin{bmatrix} \hat{d}_n \\ \hat{d}_n^\dagger \end{bmatrix} \\
 &= \text{Constant} + \sum_n \epsilon_n \left(\hat{d}_n^\dagger \hat{d}_n - \frac{1}{2} \right).
 \end{aligned}$$

by Bogoliubon \hat{d}_n , whose transformation with field operator is given by

$$\hat{d}_n = \int dx \Phi_n^\dagger(x) \hat{\Psi}(x), \quad \hat{\Psi}(x) = \sum_n \Phi_n(x) \hat{d}_n. \quad (4.63)$$

Recall Equation (4.51) holds the PHS as $\{\mathcal{H}_G^C, C_c\} = 0$ by the operator $C_c = \rho_x \mathcal{K}$, thus $C_c \Phi_n(x) = [v_n^*(x), u_n^*(x)]^T \equiv \Phi_{-n}(x)$ is the wave function for $-\epsilon_n \equiv \epsilon_{-n}$. It is worthwhile to point out that it is the branch cut of V on the Riemann surface that takes great effect on the quantum phase transition, i.e., $V \rightarrow -\arccos[(\Lambda + \Xi)/\Gamma]/2$ with an additional minus sign across the critical point, which prohibits the zero-mode solution of Majoranas.

4.4.3 Boundary Conditions Near the Critical Point

Recall that in the lattice model we introduce $0 \leq t \leq 1$ at junction sites to tune the coupling strength of different parts, whereas in the continuum theory wave functions are quite nonlocal around the critical point and thus we cannot separate different parts by specific junction sites. However, we can add a fictitious barrier potential $\lambda a \delta(x - x_\pm)$ into Equation (4.51) to emulate the imperfect connections between different parts (we denote $+$, $-$ for R, L respectively to generalize the expressions of two junction sites in the following statements). Around two interfaces, the Schrödinger equation requires:

$$\begin{aligned}
 \mathcal{H}_G^C \Phi(x) &= -2J \{ [2t + g + \lambda a \delta(x - x_\pm) + t a^2 \partial_x^2] \rho_z \\
 &\quad + i \gamma a [\Theta(\pm x \mp x_\pm), \partial_x]_+ \rho_y \} \Phi(x) = \epsilon \Phi(x), \quad (4.64)
 \end{aligned}$$

where the phase ϕ is absorbed in γ temperately, and the anti-commutator

$$[\Theta(\pm x \mp x_{\pm}), \partial_x]_{+} = 2\Theta(\pm x \mp x_{\pm})\partial_x \pm \delta(x - x_{\pm}). \quad (4.65)$$

Moving the second-order derivative term to the left-hand side and integrating the whole equation around the junction sites by an infinitesimal parameter η , we find

$$\begin{aligned} \text{L.H.S.} &= \int_{x_{\pm}-\eta}^{x_{\pm}+\eta} ta^2 \partial_x^2 \rho_z \Phi(x) dx \\ &= \pm ta^2 [\partial_x \rho_z \Phi_{\pm}(x_{\pm}) - \partial_x \rho_z \Phi_M(x_{\pm})] \\ &= \pm ta^2 \begin{bmatrix} +u'_{\pm}(x_{\pm}) - u'_M(x_{\pm}) \\ -v'_{\pm}(x_{\pm}) + v'_M(x_{\pm}) \end{bmatrix}, \\ \text{R.H.S.} &= - \int_{x_{\pm}-\eta}^{x_{\pm}+\eta} \left\{ \epsilon/2J + [2t + g + \lambda a \delta(x - x_{\pm})] \rho_z \right. \\ &\quad \left. + i\gamma a [\Theta(\pm x \mp x_{\pm})\partial_x \pm \delta(x - x_{\pm})] \rho_y \right\} \Phi(x) dx \\ &= -a [\lambda \rho_z \Phi_M(x_{\pm}) \pm i\gamma \rho_y \Phi_{\pm}(x_{\pm})] \\ &= \pm a [\mp \lambda \rho_z \Phi_M(x_{\pm}) - i\gamma \rho_y \Phi_{\pm}(x_{\pm})] \\ &= \pm a \begin{bmatrix} \mp \lambda u_M(x_{\pm}) - \gamma u_{\pm}(x_{\pm}) \\ \pm \lambda v_M(x_{\pm}) + \gamma v_{\pm}(x_{\pm}) \end{bmatrix}. \end{aligned}$$

Replacing subscript $+$, $-$ back into R, L and specifying the value of γ , ϕ in different parts (releasing ϕ from γ), we obtain the current conservation conditions:

$$ta u'_M(x_L) + \lambda u_M(x_L) = ta u'_L(x_L) + \gamma v_L(x_L), \quad (4.66)$$

$$ta v'_M(x_L) + \lambda v_M(x_L) = ta v'_L(x_L) + \gamma u_L(x_L), \quad (4.67)$$

$$ta u'_M(x_R) - \lambda u_M(x_R) = ta u'_R(x_R) + \gamma e^{-2i\phi} v_R(x_R), \quad (4.68)$$

$$ta v'_M(x_R) - \lambda v_M(x_R) = ta v'_R(x_R) + \gamma e^{+2i\phi} u_R(x_R), \quad (4.69)$$

together with four trivial wave function continuity conditions

$$u_L(x_L) = u_M(x_L), v_L(x_L) = v_M(x_L), u_R(x_R) = u_M(x_R), v_R(x_R) = v_M(x_R). \quad (4.70)$$

When $\lambda = 0$, Equations (4.66)–(4.69) impose perfect coupling boundary conditions while if $\lambda \rightarrow \infty$ the three parts in our chain system are independent, and the ϕ dependence will be suppressed. One could use $\lambda \sim (t - \mathbb{t})/\mathbb{t}$ as a fitting function for the mapping between the lattice and the continuum model, while the explicit formula is varied with different parameter ranges, which is beyond the scope of this dissertation.

4.4.4 Spectra in the Deep Topological Regime

In the deep topological regime $g \rightarrow 0$, the energy gap $\epsilon_{\text{gap}} = 2J\gamma\sqrt{4 - g^2/(t^2 - \gamma^2)} \rightarrow 4J\gamma$ occurs around

$$\pm k_F = \pm \frac{1}{a} \arccos(-\frac{g}{2t}) \approx \pm \frac{\pi}{2a}, \quad (4.71)$$

with the proviso of $\gamma \ll t$. Accordingly, we can expand the lattice fermionic operator around two Fermi points as

$$\frac{\hat{c}_i}{\sqrt{a}} = e^{+ik_F x} \hat{\psi}_R(x) + e^{-ik_F x} \hat{\psi}_L(x), \quad (4.72)$$

where $\hat{\psi}_{R,L}$ are right and left mover field operators. Substituting above transformation back into Equation (4.22) and expanding it to the leading order in the spatial gradients:

$$\begin{aligned} \frac{\hat{H}_G^D}{2J} &= - \sum_i \left[\left(t \hat{c}_i^\dagger \hat{c}_{i+1} + \gamma_i e^{-2i\phi_i} \hat{c}_i^\dagger \hat{c}_{i+1}^\dagger + \text{H.c.} \right) + g \hat{c}_i^\dagger \hat{c}_i \right] - \frac{gN}{2} \\ &= - \int dx \left\{ \left[t \left(e^{-ik_F x} \hat{\psi}_R^\dagger(x) + e^{+ik_F x} \hat{\psi}_L^\dagger(x) \right) \left(e^{+ik_F(x+a)} \hat{\psi}_R(x+a) + e^{-ik_F(x+a)} \hat{\psi}_L(x+a) \right) \right. \right. \\ &\quad \left. \left. + \gamma_i e^{-2i\phi_i} \left(e^{-ik_F x} \hat{\psi}_R^\dagger(x) + e^{+ik_F x} \hat{\psi}_L^\dagger(x) \right) \right. \right. \\ &\quad \left. \left. \times \left(e^{-ik_F(x+a)} \hat{\psi}_R^\dagger(x+a) + e^{+ik_F(x+a)} \hat{\psi}_L^\dagger(x+a) \right) + \text{H.c.} \right] \right. \\ &\quad \left. + g \left(e^{-ik_F x} \hat{\psi}_R^\dagger(x) + e^{+ik_F x} \hat{\psi}_L^\dagger(x) \right) \left(e^{+ik_F x} \hat{\psi}_R(x) + e^{-ik_F x} \hat{\psi}_L(x) \right) \right\} + \text{Constant} \\ &= - \int dx \left\{ \left[t \left(e^{+ik_F a} \hat{\psi}_R^\dagger(x) \hat{\psi}_R(x+a) + e^{-ik_F a} \hat{\psi}_L^\dagger(x) \hat{\psi}_L(x+a) \right) \right. \right. \\ &\quad \left. \left. + \gamma_i e^{-2i\phi_i} \left(e^{+ik_F a} \hat{\psi}_R^\dagger(x) \hat{\psi}_L^\dagger(x+a) + e^{-ik_F a} \hat{\psi}_L^\dagger(x) \hat{\psi}_R^\dagger(x+a) \right) + \text{H.c.} \right] \right. \\ &\quad \left. + g \left(\hat{\psi}_R^\dagger(x) \hat{\psi}_R(x) + \hat{\psi}_L^\dagger(x) \hat{\psi}_L(x) \right) \right\} + \text{Constant} \\ &= - \int dx \left\{ \left[t \left(e^{+ik_F a} \hat{\psi}_R^\dagger(x) \hat{\psi}_R(x) + a e^{+ik_F a} \hat{\psi}_R^\dagger(x) \partial_x \hat{\psi}_R(x) \right. \right. \right. \\ &\quad \left. \left. + e^{-ik_F a} \hat{\psi}_L^\dagger(x) \hat{\psi}_L(x) + a e^{-ik_F a} \hat{\psi}_L^\dagger(x) \partial_x \hat{\psi}_L(x) \right) \right. \\ &\quad \left. \left. + \gamma_i e^{-2i\phi_i} \left(e^{+ik_F a} \hat{\psi}_R^\dagger(x) \hat{\psi}_L^\dagger(x) + \cancel{a e^{+ik_F a} \hat{\psi}_R^\dagger(x) \partial_x \hat{\psi}_L^\dagger(x)} \right. \right. \right. \\ &\quad \left. \left. + e^{-ik_F a} \hat{\psi}_L^\dagger(x) \hat{\psi}_R^\dagger(x) + \cancel{a e^{-ik_F a} \hat{\psi}_L^\dagger(x) \partial_x \hat{\psi}_R^\dagger(x)} \right) + \text{H.c.} \right] \\ &\quad \left. + g \left(\hat{\psi}_R^\dagger(x) \hat{\psi}_R(x) + \hat{\psi}_L^\dagger(x) \hat{\psi}_L(x) \right) \right\} + \text{Constant} + O(a^2) \\ &= - \int dx \left\{ \left[2t \left(\cos(k_F a) \hat{\psi}_R^\dagger(x) \hat{\psi}_R(x) + ia \sin(k_F a) \hat{\psi}_R^\dagger(x) \partial_x \hat{\psi}_R(x) \right. \right. \right. \\ &\quad \left. \left. + \cos(k_F a) \hat{\psi}_L^\dagger(x) \hat{\psi}_L(x) - ia \sin(k_F a) \hat{\psi}_L^\dagger(x) \partial_x \hat{\psi}_L(x) \right) \right. \\ &\quad \left. \left. + 2i\gamma_i \sin(k_F a) e^{-2i\phi_i} \hat{\psi}_R^\dagger(x) \hat{\psi}_L^\dagger(x) - 2i\gamma_i \sin(k_F a) e^{+2i\phi_i} \hat{\psi}_L^\dagger(x) \hat{\psi}_R^\dagger(x) \right] \right\} \end{aligned}$$

$$\begin{aligned}
 & \underbrace{-2t \cos(k_F a)}_{\text{by Equation. (4.71)}} \left(\hat{\psi}_R^\dagger(x) \hat{\psi}_R(x) + \hat{\psi}_L^\dagger(x) \hat{\psi}_L(x) \right) \Big\} + \text{Constant} + O(a^2) \\
 &= \int dx \left\{ 2ta \sin(k_F a) \left[\hat{\psi}_R^\dagger(x) (-i\partial_x) \hat{\psi}_R(x) - \hat{\psi}_L^\dagger(x) (-i\partial_x) \hat{\psi}_L(x) \right] \right. \\
 &\quad \left. + 2\gamma_i \sin(k_F a) \left[-ie^{-2i\phi_i} \hat{\psi}_R^\dagger(x) \hat{\psi}_L^\dagger(x) + ie^{+2i\phi_i} \hat{\psi}_L(x) \hat{\psi}_R(x) \right] \right\} + \text{Constant} + O(a^2) \\
 &= \int dx \left\{ \Upsilon \left[\hat{\psi}_R^\dagger(x) (-i\partial_x) \hat{\psi}_R(x) - \hat{\psi}_L^\dagger(x) (-i\partial_x) \hat{\psi}_L(x) \right] + \right. \\
 &\quad \left. \underbrace{\Delta_i \left[e^{-2i(\phi_i + \pi/4)} \hat{\psi}_R^\dagger(x) \hat{\psi}_L^\dagger(x) + e^{+2i(\phi_i + \pi/4)} \hat{\psi}_L(x) \hat{\psi}_R(x) \right]}_{\text{globally redefine } \phi_i + \pi/4 \rightarrow \phi_i} \right\} + \underbrace{\text{Constant} + O(a^2)}_{\text{neglected for simplicity}} \\
 &= \frac{1}{2} \int dx \left\{ \Upsilon \left[\hat{\psi}_R^\dagger(x) (-i\partial_x) \hat{\psi}_R(x) - \hat{\psi}_L^\dagger(x) (-i\partial_x) \hat{\psi}_L(x) \right. \right. \\
 &\quad \left. \left. - \hat{\psi}_L(x) (-i\partial_x) \hat{\psi}_L^\dagger(x) + \hat{\psi}_R(x) (-i\partial_x) \hat{\psi}_R^\dagger(x) \right] \right. \\
 &\quad \left. + \Delta_i \left[e^{+2i\phi_i} \hat{\psi}_L(x) \hat{\psi}_R(x) - e^{+2i\phi_i} \hat{\psi}_R(x) \hat{\psi}_L(x) \right. \right. \\
 &\quad \left. \left. + e^{-2i\phi_i} \hat{\psi}_R^\dagger(x) \hat{\psi}_L^\dagger(x) - e^{-2i\phi_i} \hat{\psi}_L^\dagger(x) \hat{\psi}_R^\dagger(x) \right] \right\} \\
 &= \frac{1}{2} \int dx \left[\hat{\psi}_R^\dagger(x), \hat{\psi}_L^\dagger(x), \hat{\psi}_L(x), -\hat{\psi}_R(x) \right] \\
 &\quad \times \begin{bmatrix} \Upsilon(-i\partial_x) & 0 & \Delta_i e^{-2i\phi_i} & 0 \\ 0 & -\Upsilon(-i\partial_x) & 0 & \Delta_i e^{-2i\phi_i} \\ \Delta_i e^{+2i\phi_i} & 0 & -\Upsilon(-i\partial_x) & 0 \\ 0 & \Delta_i e^{+2i\phi_i} & 0 & \Upsilon(-i\partial_x) \end{bmatrix} \begin{bmatrix} \hat{\psi}_R(x) \\ \hat{\psi}_L(x) \\ \hat{\psi}_L^\dagger(x) \\ -\hat{\psi}_R^\dagger(x) \end{bmatrix} \\
 &= \frac{1}{2} \int dx \hat{\Psi}(x)^\dagger \mathcal{H}_G^D \hat{\Psi}(x)
 \end{aligned}$$

where \mathcal{H}_G^D is a single-particle continuous BdG Hamiltonian under the continuous Fermi field spinor $\hat{\Psi}(x) = [\hat{\psi}_R(x), \hat{\psi}_L(x), \hat{\psi}_L^\dagger(x), -\hat{\psi}_R^\dagger(x)]^T$,

$$\mathcal{H}_G^D/2J = \Upsilon(-i\partial_x) \rho_z \tau_z + \Delta_i e^{-2i\phi_i} \rho_z \rho_x. \quad (4.73)$$

Here, $\Upsilon = 2ta \sin(k_F a)$ is the effective velocity, $\Delta_i = 2\gamma_i \sin(k_F a)$ is the effective pairing potential^[62], $\tau_{x,y,z}$ are Pauli matrices acting on the mover space. Note that the phase is globally shifted by $\pi/4$ in order to keep Δ_i a real number. The above Hamiltonian shares the same form with JJs created at the edge of a quantum spin Hall (QSH) insulator^[365-367]: our movers $\hat{\psi}_{R,L}$ in $\vec{\tau}$ space correspond to their two edge states living in the spin space. Hence, the IXI chain emulates the QSH JJs at low energies. The rTRS in the QSH JJ equates to an *effective* TRS (eTRS) in the IXI chain with $[\mathcal{H}_G^D(\phi), \mathcal{T}_e] = 0$, $\mathcal{T}_e = i\tau_y \mathcal{K}$ at $\phi = l\pi/2, l \in \mathbb{Z}$ ^[368]. Since $\mathcal{T}_e^2 = -1$, there must be spectrum degeneracies at those

specific phases due to Kramers theorem. With the help of the S-matrix technique, we obtain the transcendental equation for the ABSs in the deep topological regime:

$$E L/\Upsilon + \tau\phi = \arccos(E/\Delta) + n\pi, \quad n \in \mathbb{Z}. \quad (4.74)$$

Under the low-energy leading approximation, the energy can be expressed explicitly as

$$E = (\pi/2 - \tau\phi + n\pi)/(L/\Upsilon + 1/\Delta), \quad n \in \mathbb{Z}, \quad (4.75)$$

which is plotted in Figure 4.2(b) against the exact continuum spectrum and the full lattice spectrum. The index τ indicates the slope of the spectrum as a function of ϕ : $\tau = \pm 1$ for the downward (upward) branches respectively. In the case of the point contact limit $L \rightarrow 0$, Equation (4.74) is reduced to $E \rightarrow \tau\Delta \cos \phi$ ^[346]. In Section 4.4.5, we present the explicit wave functions and the technical details of the S matrix.

4.4.5 Wave Functions in the Deep Topological Regime

Owing to $[\mathcal{H}_G^D, \tau_z] = 0$, it is more convenient for us to decompose the Hilbert space in two τ_z eigen-sectors $\tau = \pm 1$ and solve out Equation (4.73) as $\mathcal{H}_G^D \Phi^\tau(x) = \epsilon^\tau \Phi^\tau(x)$ with their corresponding eigenfunctions $\Phi^+(x) = [u^+(x), 0, v^+(x), 0]^T$, $\Phi^-(x) = [0, u^-(x), 0, v^-(x)]^T$, whose explicit expressions are shown as

$$u^\tau(x) = e^{-i\phi} (C_1 e^{-iW} e^{+\tau Kx} + C_2 e^{+iW} e^{-\tau Kx}), \quad (4.76)$$

$$v^\tau(x) = e^{+i\phi} (C_1 e^{+iW} e^{+\tau Kx} + C_2 e^{-iW} e^{-\tau Kx}), \quad (4.77)$$

where $K = \sqrt{\Delta^2 - E^2}/\Upsilon$, $W = \arccos(E/\Delta)/2$, $E = \epsilon/2J$ are introduced for simplicity. The wave functions of left and right parts only contain the exponential decaying branches due to infinite boundary conditions, while the middle part is the case of $\phi = \gamma = 0$ where $K = iE/\Upsilon \equiv iK_M$. Since $\epsilon_{\text{gap}} \rightarrow 4J\gamma$, $\Delta \rightarrow 2\gamma$ in the deep topological regime, $|E| < \Delta$ will be always valid for the ABSs. The explicit middle wave functions are shown as $u_M^\tau(x) = C_3 \exp(+i\tau K_M x)$, $v_M^\tau(x) = C_4 \exp(-i\tau K_M x)$ with two new coefficients. Applying continuity conditions at two interfaces $x_{L,R}$ on the wave functions of each eigen-sector, we can obtain the left- and right-scattering matrices $S_L^D = \exp(-2iW)\rho_x$, $S_R^D = \exp(-2iW)e^{-2i\phi\rho_z}\rho_x$, where we denote $W = \arccos(E/\Delta)/2$, $E = \epsilon/2J$. The scattering matrix of the middle part is only determined by the middle wave number $K_M = E/\Upsilon$ as $S_M^D = \exp(iK_M L)e^{ik_F\rho_z}$. The solvability equation

$$\det(\mathbb{1} - S_M^D S_R^D S_M^D S_L^D) = 0 \quad (4.78)$$

of the Andreev reflection gives the energy transcendental Equation (4.74) for the ABSs. By use of the normalization condition, the full normalized wave functions for the whole chain are expressed as

$$u_n^\tau(x) = \mathcal{A}_n (-1)^n e^{-K|x-l(x)|} e^{+i\tau K_M l(x)}, \quad (4.79)$$

$$v_n^\tau(x) = \mathcal{A}_n e^{+i\phi} \times e^{-K|x-l(x)|} e^{-i\tau K_M l(x)}, \quad (4.80)$$

where $\mathcal{A}_n = 1/\sqrt{2(L+1/K)}$ is the normalization factor, $l(x) = x$ for $x \leq |L/2|$ and $\text{sgn}(x)L/2$ for $x > |L/2|$. Using the PHS as $\{\mathcal{H}_G^D, C_D\} = 0, C_D = \rho_y \tau_y \mathcal{K}$, Equation (4.73) is diagonalized into $\sum_{n,\tau} \epsilon_n^\tau (\hat{d}_n^{\tau\dagger} \hat{d}_n^\tau - \frac{1}{2})$ with:

$$\hat{d}_n^\tau = \int dx \Phi_n^{\tau\dagger}(x) \hat{\Psi}(x), \quad \hat{\Psi}(x) = \sum_{n,\tau} \Phi_n^\tau(x) \hat{d}_n^\tau. \quad (4.81)$$

4.4.6 Lattice Diagonalization

With the single-particle spectrum ϵ_n solved exactly from the numerical lattice diagonalization, we can construct the many-body spectrum E_n : The ground state is built with all the negative-energy single-particles filled, the following excited states are obtained by adding the corresponding quasi-particles to the ground state, whose total number characterizes the parity of the system. Note, however, we could only utilize a few ABSs to create the many-body spectra from the continuum theory.

Figure 4.2 displays the exact numerical single-particle and the many-body spectra near the critical point and in the deep topological regime, compared with results from two low-energy continuum models, respectively. It is clear that both continuum theories show great agreement with solutions from the numerical lattice model in the single-particle spectrum [Figures 4.2(a) and (b)], which can be interpreted as follows: When the spin chain is near the critical point $\Omega \rightarrow 0$ with $\Gamma \gtrsim \Omega$, the energy gap $2J|2t - |g||$ will always happen around $k = 0$, where the long wavelength continuum theory dominates. While, if the chain is in a deep topological regime with $\Gamma \ll \Omega$, the spectrum is gapped with $\epsilon_{\text{gap}} \approx 4J\gamma$ near the two Fermi points $\pm k_F$ which is in agreement with the deep topological continuum theory. From the perspective of fermionic language, the superconducting coherence length is defined as $\xi = Y/\Delta = ta/\gamma^{[62]}$, while the continuum theory requires the coherence length to be much larger than the wave length, i.e., $\xi \gg 2\pi/k_F$, which also leads to the validity condition $\gamma \ll t$.

In spite of the excellent agreement between the numerical and analytical results in the single-particle spectra [Figures 4.2(a) and (b)], there is only fair agreement between the

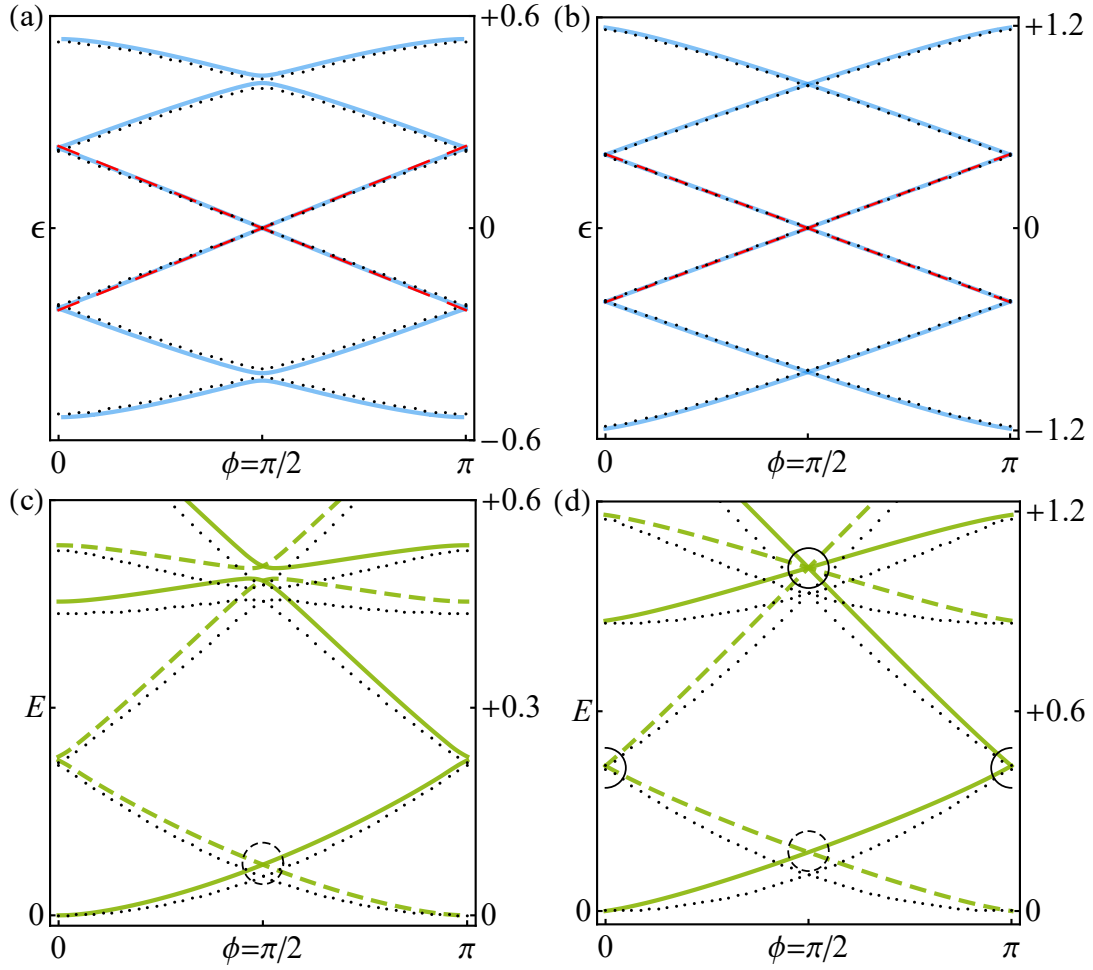


Figure 4.2 The spectra of the IXI spin chain as a function of the twisting angle.

The parameters are set as $J = a = t = \mathfrak{t} = 1$, $\gamma = 0.3$, $\lambda = 0$, $N_L = N_R = 100$, $N_M = 10$ in two regimes. (a) and (b) are the single-particle spectra near the critical point $g = -1.7$ and in the deep topological regime $g = 0$, respectively. (c) and (d) are their corresponding many-body spectra. Black dots are solved numerically by the lattice model, blue lines are obtained by solving the transcendental Equations (4.52) and (4.74) of the low-energy continuum theory in two regimes, red dashed lines are Majorana solutions calculated by the explicit Equations (4.53) and (4.75) by setting $n = -1$ ($n = 0$) for upward (downward) branch, green (dashed) lines are many-body spectra with even (odd) parity constructed by the single-particle energies, solid (dashed) circles are crossings protected by the eTRS (PHS)^[67].

numerical and analytical results in the many-body spectra [Figures 4.2(c) and (d)], where we have globally shifted the energies to make the ground-state energy zero at $\phi = 0$. Since the many-body spectra of the low-energy continuum theory can only be constructed by a few single-particle energies of the ABSs in the gap, the contributions from the propagating states outside the gap will not be captured in the analytical continuum theory, which could also lead to small discontinuities in slope at $\phi = l\pi$, $l \in \mathbb{Z}$. Yet, we note that the spectra near the critical point match better than that in the deep topological regime due to the weaker ϕ -dependence of the propagating state energies.

4.5 The Spin Josephson Effect

4.5.1 Fractional Spin Josephson Effect

Historically, the original Josephson effect was used to describe the supercurrent through a weak link between the conventional s -wave superconductors, following 2π periodicity of the system Hamiltonian^[347]. Nevertheless, JJs between topological p -wave superconductors are predicted to exhibit a 4π -periodic supercurrent, a hallmark manifestation for the existence of MBSs^[369-371]. Notably, a variety of JEs can be identified by coupling the edges of QSH insulators to s -wave superconductors. Under the TRS and parity conservation, a dc voltage bias gradually connects the in-gap states to the bulk of scattering states, generating a 2π -periodic dissipative current. Once the TRS is broken, the current becomes dissipationless and evolves as 4π periodicity, as protected by the PHS stemming from the MBSs^[367]. Furthermore, given the TRS with the Coulomb interactions^[361] or the impurities^[358-360], the current can even be dissipationless with 8π periodicity, while the s_z -conserving interactions will lead to dissipation with the original 2π periodicity (note that s_z refers to the electron spin at the QSH edge, instead of the spin in the IXI chain, see Hui et al.^[359]). Such 4π (8π) periodicity is called \mathbb{Z}_2 (\mathbb{Z}_4) fractional JE for the sake of e ($e/2$) electron charge being transferred in 2π period of the system Hamiltonian, instead of Cooper pairs $2e$ in the conventional superconductors. However, in Laflamme et al.^[68] it was shown that such 8π periodicity can be achieved *without* Coulomb interactions, based on a p -wave superconductor lattice ring interrupted by one weakly coupled normal site.

Before analyzing the spin JEs in our setup, we want to make a key observation: The spin twisting angle ϕ has been mapped into the superconducting phase 2ϕ , i.e., it was doubled, which makes all periodicities of the fermionic JEs twice as large as the spin JEs. Explicitly, the periodicities of trivial, \mathbb{Z}_2 , \mathbb{Z}_4 JEs become π , 2π , 4π in the spin chain, respectively, compared with 2π , 4π , 8π in the fermionic systems. To avoid confusion, in the following discussions, we will use trivial, \mathbb{Z}_2 , \mathbb{Z}_4 terms to illustrate various JEs in the two representations.

Although the properties of fractional JEs in the fermionic systems are well-studied, a question naturally arises: Except for the alteration at the phase ϕ by a factor of 2, what are the similarities and differences between fermionic JEs and spin JEs? In the following subsections, we will investigate various spin JEs from two perspectives: the continuum theory and the lattice model. Moreover, to reveal the influence of the many-body in-

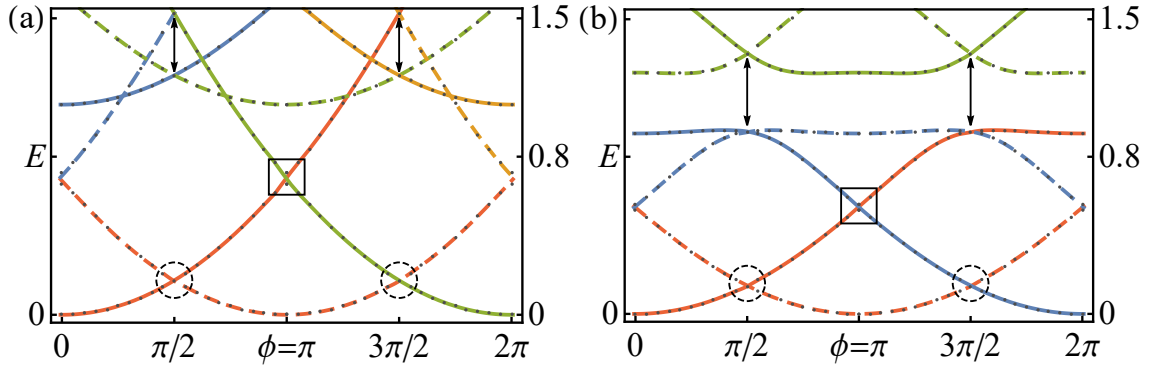


Figure 4.3 The spectra of the IXI spin chain under two types of interactions.

The plots are calculated by the exact diagonalization under $J = t = \uparrow = 1$, $\gamma = 0.6$, $g = 0$, $N_L = N_R = 9$, $N_M = 6$ after adding two types of interactions. (a) is under ZZ-type (spin) interactions [Equation (4.31)] with $\delta = 0.4$, while (b) includes NN-type (fermionic) interactions [Equation (4.32)] with $\chi = 0.4$. Solid (dashed) lines indicate even (odd) parity supplemented with original data (black dots), dashed circles are crossings protected by the PHS, rectangles refer to crossings protected by the eTRS in the continuum limit while broken by finite-size effects, gaps at the arrows are lifted by interactions^[67].

interactions on the spin fractional JEs, we will add ZZ-type interactions [Equation (4.31)] and NN-type interactions [Equation (4.32)] into Equations (4.21) and (4.22), respectively, both of which act only within the middle sector. We note that these interactions, which are quartic in fermionic operators, force us to apply a brute-force diagonalization on a $2^N \times 2^N$ matrix in spin space, effectively limiting the number of sites, N , of the chain.

4.5.2 Continuum Scenarios

In the low-energy continuum limit, both Equations (4.51) and (4.73) obey PHS: $\{\mathcal{H}_G^C, C_c\} = 0$, $C_c = \rho_x \mathcal{K}$ near the critical point and $\{\mathcal{H}_G^D, C_d\} = 0$, $C_d = \rho_y \tau_y \mathcal{K}$ in the deep topological regime, which guarantees the crossings of MBSs and switches the parity of the ground state at $\phi = \pi/2 + l\pi$. Additionally, as we have shown in Section 4.4, crossings at $\phi = l\pi/2$ are protected by the eTRS of Equation (4.73) in the deep topological regime, which is indeed equivalent to JJs attached to the edge of QSH insulators. Therefore, adiabatically advancing the spin twisting angle ϕ will pump each ABS into the bulk and lead to dissipative current with trivial periodicity, as displayed in Figures 4.2(b) and 4.2(d). Nonetheless, when the system is tuned close to the critical point where the eTRS is broken, there are anti-crossings at $\phi = l\pi/2$ in Figures 4.2(a) and 4.2(c), with the exception of the low-energy crossings (dashed circles) at $\phi = \pi/2 + l\pi$ that are still protected by the Majorana PHS. Under this circumstance, every ABS is detached from the bulk and give rise to dissipationless spin current with \mathbb{Z}_2 periodicity.

In Figure 4.3, we show the many-body spectra in the deep topological regime, taking into account interactions of ZZ type [Equation (4.31)] and NN type [Equation (4.32)], respectively, both still with the eTRS maintained. Compared with Figure 4.2(d), prior fourfold degeneracy at $\phi = \pi/2$ is lifted via the Coulomb interactions [indicated by the vertical arrows in Figure 4.3(b)], a dissipationless \mathbb{Z}_4 spin current occurs as expected^[361]. Conversely, ZZ-type interactions only shift crossings [indicated by the vertical arrows in Figure 4.3(a)]. Because the energy levels move into the bulk as ϕ is increased, the spin current remains dissipative with trivial periodicity as in the aforementioned non-interacting case. This phenomenon basically resembles QSH JJs accompanied with s_z -conserving interactions in Hui et al.^[359]. Although there are small gaps at $\phi = \pi$ caused by finite-size effects (e.g., slowly oscillatory umklapp or Friedel terms), they can be fairly suppressed under the continuum limit^[368].

4.5.3 Lattice Odd-Even Effect

The eTRS in the continuum limit requires the transport through JJs to be highly transparent, any imperfect connections $\mathbb{t} \neq t$ are able to break such symmetry and open gaps at the lattice level, which leads to the following odd-even effects. As we have proven in Section 4.3., there is an iTRS appearing at the lattice level when all parameters are set inverted symmetrically, bringing about different crossing properties for odd-even sites. In particular, for all single-particle states illustrated in Figures 4.4(a) and 4.4(b), there must be Kramers pairs at $\phi = l\pi$ for odd N and $\phi = \pi/2 + l\pi$ for even N , according to the conclusions of Equation (4.43). By changing the parity of the sites, crossings and anti-crossings can be created or destroyed at specific ϕ in the spectra, shown in Figure 4.4. As a consequence, adiabatically following the ground states will eventually lead to \mathbb{Z}_2 (\mathbb{Z}_4) spin current for the even (odd) sites, pumping different amounts of net spin between the left and the right Ising parts, as displayed in Figures 4.4(e) and 4.4(f) calculated by Equation (4.29) [or Equation (4.94), see Section 4.6.3 for details]. Alternatively, because there are no many-body interactions, the spin current can be analytically computed using $\langle \hat{J}_z \rangle_n = -2\partial E_n / \partial \phi$, upon applying a phase-shifted JWT $\hat{c}_i^\dagger = e^{-i\phi} \prod_{j=1}^{i-1} (-\hat{\sigma}_j^z) \hat{\sigma}_i^+$ on the right part and transforming ϕ into the right interface^[108], which gets along with conventional results for the fermionic Josephson current^[347]. To evaluate the full adiabatic spin current in the presence of a time-dependent angle twist $\phi(t)$, one needs to account for the possible Berry phase contributions to the current stemming from the velocity of the twist, $\dot{\phi}(t)$ which, however, is beyond the scope of this dissertation^[372].

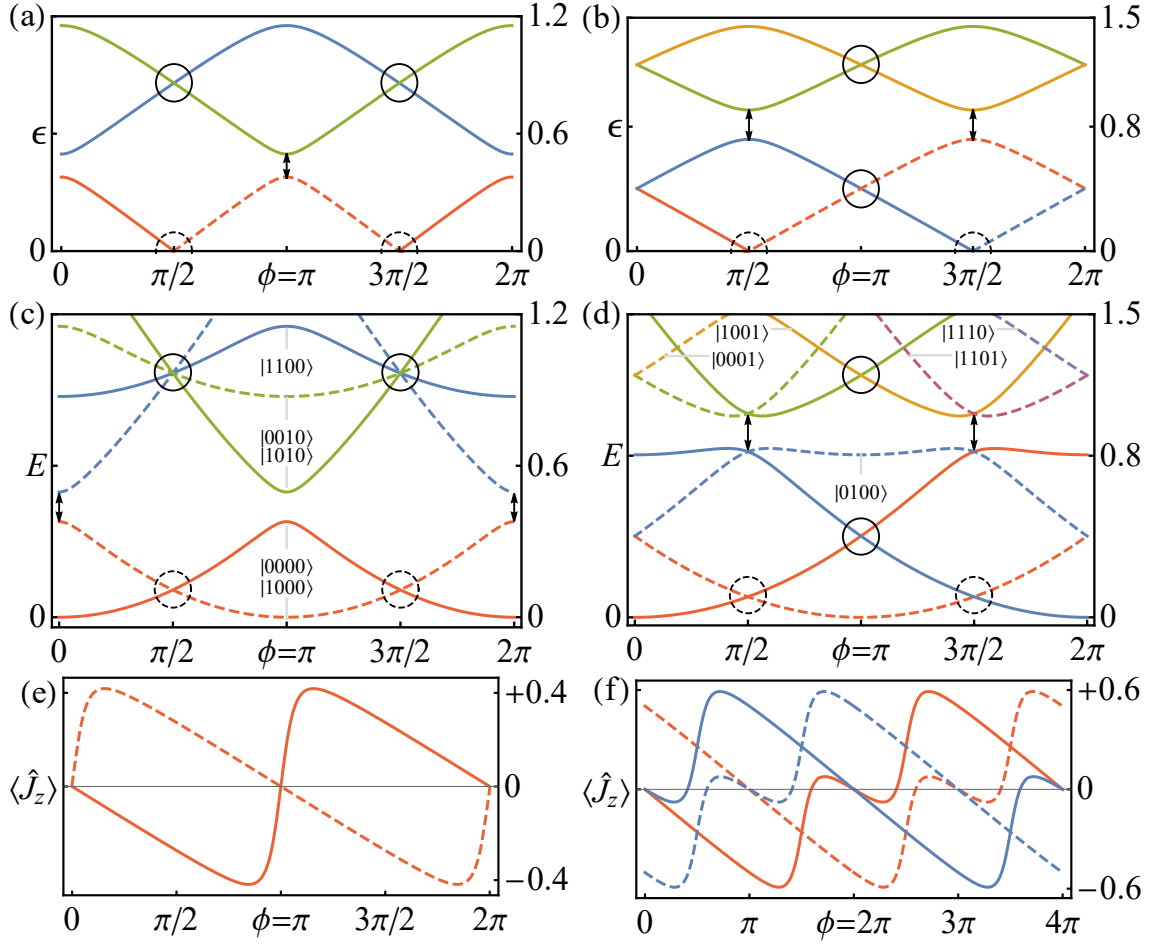


Figure 4.4 The odd-even effect in the IXI spin chain.

The spectra and spin supercurrent of the IXI as a function of ϕ are solved numerically by the BdG matrix diagonalization under $J = t = 1$, $\mathfrak{t} = 0.8$, $\gamma = 0.4$, $g = 0$, $N_L = N_R = 100$ in both odd-even cases. (a) and (b) are the single-particle spectra for $N_M = 10$ and $N_M = 11$, respectively. (c) and (d) are their corresponding many-body spectra, whose single-particle occupations are shown in plot labels. (e) and (f) are spin current of their lowest two and four states evaluated from Equation (4.29), where the variation of ϕ is extended to full 4π period in (f), showing \mathbb{Z}_2 and \mathbb{Z}_4 periodicities respectively. Solid (dashed) lines in the single-particle spectra are the energies of the particles (holes), solid (dashed) lines in the many-body spectra refer to the even (odd) parity, solid (dashed) circles are crossings protected by the iTRS (PHS), the gaps specified by the arrows are lifted by the imperfect couplings $\mathfrak{t} < t$ ^[67].

In addition, our conclusion reveals the unusual \mathbb{Z}_4 fractional JE in Laflamme et al.^[68] is actually protected by the iTRS. In fact, their model Hamiltonian is equivalent to ours for $N_M = 1$ after applying the phase-shifted JWT^①. The reason why in their case the \mathbb{Z}_4 periodicity cannot survive under the Coulomb interactions is that NN-type interactions do not commute with iTRS, whereas ZZ-type interactions do, as it happens in spin chains^[111]. Namely, the spectra may be shifted under ZZ-type interactions while crossings are still

① Although periodic boundary conditions are imposed in their p -wave superconducting parts to form a ring geometry, degenerate properties within the gap are still well established.

protected. Therefore, \mathbb{Z}_4 spin current originating from iTRS does not depend on whether there are ZZ-type interactions or not.

4.6 The Spin Entanglement

One of the most counterintuitive characteristics in the quantum world is entanglement whose non-locality provides another instructive insight to understand topological phases^[373]. Nowadays, there is still no universal way to quantify the entanglement of a mixed state shared by arbitrary subsystems^[374]. However, there are several metrics to measure entanglement between two qubits, such as concurrence^[375], entanglement entropy, negativity, etc. In the following section, we will explicit show how to calculate the spin entanglement by various metrics. Specifically, by using concurrence. we demonstrate the texture of spin entanglement of the Ising-XY-Ising spin chains.

4.6.1 Metrics for Entanglement

The amount of entanglement present in a quantum state can be quantified by the entanglement monotone, which is a nonnegative function whose value does not increase under local operations and classical communication^[374]. Generally, there are two choices of subsystems in which one can calculate the entanglement^[376]:

- (i) A single spin A and the rest of the chain B ;
- (ii) Two arbitrary spins i and j in the chain.

For the former case, we have two entanglement measures. The first one is given via the *von Neumann entropy*

$$S(\rho_A) = -\text{tr}[\rho_A \log_2 \rho_A] = -\text{tr}[\rho_B \log_2 \rho_B] = S(\rho_B), \quad (4.82)$$

assuming the whole chain in a pure state $\rho_{AB} = |\Psi\rangle\langle\Psi|_{AB}$. Another one is the logarithmic negativity calculated as

$$E_N(\rho) = \log_2 \|\rho^{\Gamma_A}\|_1, \quad (4.83)$$

where Γ_A is the partial transpose operation and $\|\cdot\|_1$ denotes the trace norm.

For the two sites case in a mixed state, the amount of entanglement shared between the spins is quantified by the concurrence C . In particular, for two arbitrary spin- $\frac{1}{2}$ sites at the positions i and j in the chain, the concurrence is given by^[375]

$$C(\rho_{ij}) = \max[0, \lambda_{ij}^1 - \lambda_{ij}^2 - \lambda_{ij}^3 - \lambda_{ij}^4], \quad (4.84)$$

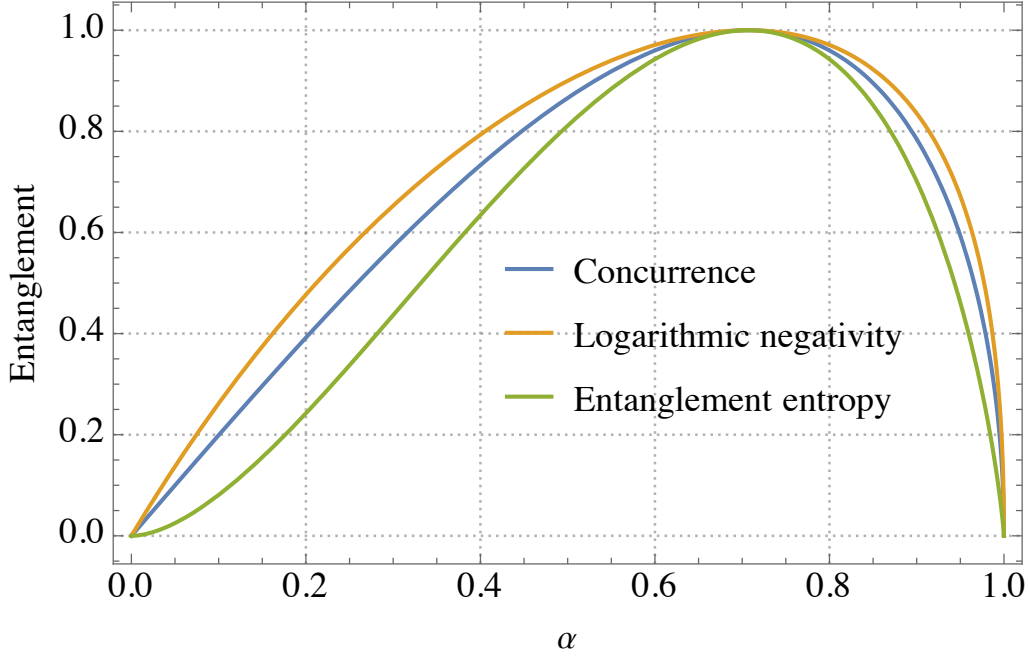


Figure 4.5 Comparisons of three quantum entanglement metrics.

where the λ_{ij}^k are the eigenvalues of the Hermitian matrix $R_{ij} = \sqrt{\sqrt{\rho_{ij}} \tilde{\rho}_{ij} \sqrt{\rho_{ij}}}$ sorted in descending order with $\tilde{\rho}_{ij} = (\hat{\sigma}_i^y \otimes \hat{\sigma}_j^y) \rho_{ij}^* (\hat{\sigma}_i^y \otimes \hat{\sigma}_j^y)$. The concurrence increases from $C = 0$ for a separable state to $C = 1$ for a maximally entangled state. In Figure 4.5, we plot three entanglement measure for the state $\alpha |00\rangle + \sqrt{1 - \alpha^2} |11\rangle$.

4.6.2 Texture of Spin Entanglement

The variation of the entanglement across the quantum phase transition point has been investigated in the anisotropic XY spin chain with periodic boundary conditions^[376]. Here, we evaluate the entanglement between spins and show that it can be enhanced in the presence of a spin current owing to the misaligned Ising axes. This effect, while present in the spin chain, does not have a fermionic counterpart in topological superconductors. Specifically, in this section, we evaluate various spin correlation functions in the presence of the spin supercurrent carried by JW Majoranas in the XY sector. We are interested in the single spin expectation value $p_i^\alpha \equiv p_i^\alpha(\phi) = \langle \hat{\sigma}_i^\alpha \rangle$, as well as the spin-spin correlation function $p_{ij}^{\alpha\beta} \equiv p_{ij}^{\alpha\beta}(\phi) = \langle \hat{\sigma}_i^\alpha \hat{\sigma}_j^\beta \rangle$ with $\alpha, \beta = x, y, z$. This allows us to derive the reduced density matrices for an arbitrary single and pair of spins,

$$\rho_i(\phi) = \frac{1}{2} \sum_{\alpha=0}^3 p_i^\alpha \hat{\sigma}_i^\alpha, \quad \rho_{ij}(\phi) = \frac{1}{4} \sum_{\alpha,\beta=0}^3 p_{\alpha\beta} \hat{\sigma}_i^\alpha \hat{\sigma}_j^\beta, \quad (4.85)$$

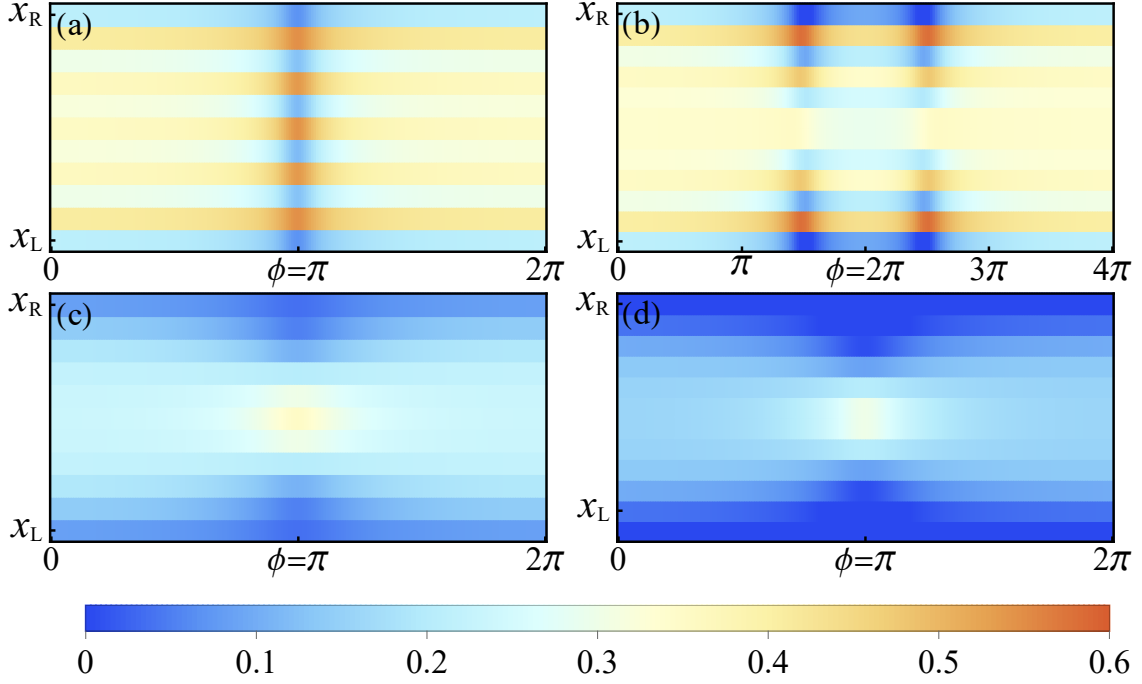


Figure 4.6 The concurrences in the XY sector for ground states.

The plots are computed from the Pfaffian of the correlation matrices under $J = t = 1$, $t = 0.8$, $\gamma = 0.4$, $N_L = N_R = 100$ in all sub-figures. (a) and (b) are nearest-neighbor concurrences in the deep topological regime $g = 0$ for $N_M = 10$ and $N_M = 11$ separately, where the variation of ϕ is extended to full 4π period in (b). While (c) and (d) are nearest-neighbor and next-nearest-neighbor concurrences for $N_M = 10$ near the critical point $g = -1.8$, respectively^[67].

respectively. Since the Hamiltonian conserves the parity of the system, we can readily infer that $p_i^x = p_i^y = 0$, thus the spin texture has only one non-zero component p_i^z , along the z -direction. Similarly for the two-spin correlators, several components vanish: $p_{ij}^{xz} = p_{ij}^{zx} = p_{ij}^{yz} = p_{ij}^{zy} = 0$. It is clear from the definition of spin current that when there is a finite spin supercurrent flowing through the middle part, p_{ij}^{xy} and p_{ij}^{yx} must be nonzero. In this case, regular determinant stratagems^[69,341,376] cannot be used to find the correlator between two arbitrary spins. However, such correlators, together with nonzero p_{ij}^{xx} and p_{ij}^{yy} , can be obtained by computing the Pfaffian of their corresponding $2k \times 2k$ skew-symmetric matrices^[377-378], where $k = |i - j|$ (see Section 4.6.3).

With all spin correlators at hand, we are able to establish the reduced density matrices, and then evaluate the degree of entanglement in the system. Although the single-site entropy and the concurrence between two arbitrary spins is known to peak at the quantum phase transition^[376], here we determine how the entanglement in the XY sector is affected by the presence of spin supercurrent due to a finite twist between the Ising directions.

In Figure 4.6 we plot the texture of the spin concurrences as a function of ϕ for odd-even cases in different regimes, following the ground states in Figure 4.4. It is apparent to

see that there are two different textures of spin entanglement for odd-even cases depicted in Figures 4.4(a) and 4.4(b), not only evolving with two kinds of periodicities, but also taking peaks (nadirs) at different ϕ . Such phenomena are due to the fact that through increasing ϕ , the many-body levels have been shifted to higher values, which makes them more susceptible to higher excited states. Owing to finite size effects with open boundary conditions, the entanglement also oscillates with frequency $\sim 2k_F$ as a function of site index^[379], which can be enhanced by larger susceptibilities close to anti-crossing points. Hence, one can strongly control the entanglement between the spins in the XY sector via the twisting angle, which could be utilized to process quantum information.

Furthermore, by comparing Figures 4.4(a) and 4.4(b) to 4.4(c) and 4.4(d), one might wonder why concurrences near the critical point are less than that in the deep topological regime, since the chain should be more entangled around quantum phase transition. The reason is as follows: In the deep topological regime, only nearest-neighbor concurrences are nonzero, which means the entanglement is well confined in nearest-neighbor spins; while as the system approaches the critical point, the entanglement will be spread out into next-nearest-neighbor (and so on) spins^[376], which makes the initial nearest-neighbor concurrence decrease.

4.6.3 Spin Correlation Functions

By use of transformation Equations (4.20) and orthonormality conditions of wave functions Equations (4.15), we define two operators,

$$\hat{A}_i = \hat{c}_i^\dagger + \hat{c}_i = \sum_n [a_n^*(i)\hat{d}_n^\dagger + a_n(i)\hat{d}_n], \quad (4.86)$$

$$\hat{B}_i = \hat{c}_i^\dagger - \hat{c}_i = \sum_n [b_n^*(i)\hat{d}_n^\dagger - b_n(i)\hat{d}_n], \quad (4.87)$$

with $a_n(i) = u_n(i) + v_n(i)$, $b_n(i) = u_n(i) - v_n(i)$. By using orthonormality conditions in Equation (4.15), we find following identities

$$\begin{aligned} \sum_n a_n(i)a_n^*(j) &= \sum_n [u_n(i)u_n^*(j) + v_n(i)v_n^*(j) + u_n(i)v_n^*(j) + v_n(i)u_n^*(j)] \\ &= +\delta_{ij} + \sum_n [u_n(i)u_n^*(j) - u_n^*(i)u_n(j) + u_n(i)v_n^*(j) - u_n^*(i)v_n(j)] \\ &= +\delta_{ij} + \sum_n [u_n(i)a_n^*(j) - u_n^*(i)a_n(j)] \\ &= +\delta_{ij} + 2i \operatorname{Im} \sum_n u_n(i)a_n^*(j), \end{aligned} \quad (4.88)$$

$$\begin{aligned} \sum_n b_n(i)b_n^*(j) &= \sum_n [u_n(i)u_n^*(j) + v_n(i)v_n^*(j) - u_n(i)v_n^*(j) - v_n(i)u_n^*(j)] \\ &= +\delta_{ij} + \sum_n [u_n(i)u_n^*(j) - u_n^*(i)u_n(j) - u_n(i)v_n^*(j) + u_n^*(i)v_n(j)] \end{aligned}$$

$$\begin{aligned}
 &= +\delta_{ij} + \sum_n [u_n(i)b_n^*(j) - u_n^*(i)b_n(j)] \\
 &= +\delta_{ij} + 2i \operatorname{Im} \sum_n u_n(i)b_n^*(j), \\
 \sum_n b_n(i)a_n^*(j) &= \sum_n [u_n(i)u_n^*(j) - v_n(i)v_n^*(j) + u_n(i)v_n^*(j) - v_n(i)u_n^*(j)] \\
 &= -\delta_{ij} + \sum_n [u_n(i)u_n^*(j) + u_n^*(i)u_n(j) + u_n(i)v_n^*(j) + u_n^*(i)v_n(j)] \\
 &= -\delta_{ij} + \sum_n [u_n(i)a_n^*(j) + u_n^*(i)a_n(j)] \\
 &= -\delta_{ij} + 2 \operatorname{Re} \sum_n u_n(i)a_n^*(j).
 \end{aligned} \tag{4.89}$$

Then, we calculate out the expectation values of \hat{A}_i, \hat{B}_i pairs, $M_{i,j} \equiv \langle \hat{A}_i \hat{A}_j \rangle$, $N_{i,j} \equiv \langle \hat{B}_i \hat{B}_j \rangle$, $G_{i,j} \equiv \langle \hat{B}_i \hat{A}_j \rangle$ as

$$\begin{aligned}
 M_{i,j} &= \sum_n [+a_n^*(i)a_n(j) \langle \hat{d}_n^\dagger \hat{d}_n \rangle + a_n(i)a_n^*(j) \langle \hat{d}_n \hat{d}_n^\dagger \rangle] \\
 &= +\delta_{ij} + 2i \operatorname{Im} \sum_n [u_n(i)a_n^*(j) + a_n^*(i)a_n(j)f_n],
 \end{aligned} \tag{4.91}$$

$$\begin{aligned}
 N_{i,j} &= \sum_n [-b_n^*(i)b_n(j) \langle \hat{d}_n^\dagger \hat{d}_n \rangle - b_n(i)b_n^*(j) \langle \hat{d}_n \hat{d}_n^\dagger \rangle] \\
 &= -\delta_{ij} - 2i \operatorname{Im} \sum_n [u_n(i)b_n^*(j) + b_n^*(i)b_n(j)f_n],
 \end{aligned} \tag{4.92}$$

$$\begin{aligned}
 G_{i,j} &= \sum_n [+b_n^*(i)a_n(j) \langle \hat{d}_n^\dagger \hat{d}_n \rangle - b_n(i)a_n^*(j) \langle \hat{d}_n \hat{d}_n^\dagger \rangle] \\
 &= +\delta_{ij} - 2 \operatorname{Re} \sum_n [u_n(i)a_n^*(j) - b_n^*(i)a_n(j)f_n],
 \end{aligned} \tag{4.93}$$

where $f_n \equiv \langle \hat{d}_n^\dagger \hat{d}_n \rangle$ is the occupation number of quasi-particles. These expressions are different from Sachdev^[69], Lieb et al.^[341], Osborne et al.^[376] as a result of the imaginary parts of the wave functions stemming from the spin supercurrent in Equation (4.29):

$$\langle \hat{J}_z \rangle / (-2Jt) = \operatorname{Im}[N_{i,i+1} - M_{i,i+1}]. \tag{4.94}$$

One can verify that the Equation. (4.94) is the same as Equation. (4.30). We also have

$$\langle \hat{B}_i \hat{A}_j \rangle = -\langle \hat{A}_j \hat{B}_i \rangle, \tag{4.95}$$

$$\langle \hat{A}_i \hat{A}_j \rangle = \langle \hat{A}_j \hat{A}_i \rangle^*, \tag{4.96}$$

$$\langle \hat{B}_i \hat{B}_j \rangle = \langle \hat{B}_j \hat{B}_i \rangle^*, \tag{4.97}$$

$$\langle \hat{\sigma}_i^z \rangle = \langle \hat{B}_i \hat{A}_i \rangle = G_{i,i} \tag{4.98}$$

$$\langle \hat{\sigma}_i^z \hat{\sigma}_j^z \rangle = \langle \hat{B}_i \hat{A}_i \hat{B}_j \hat{A}_j \rangle = G_{i,i} G_{j,j} - G_{i,j} G_{j,i} - N_{i,j} M_{i,j}. \tag{4.99}$$

However, it is not so straightforward to obtain the correlators at arbitrary length $k = |i-j|$:

$$\begin{aligned}
 \langle \hat{\sigma}_i^x \hat{\sigma}_j^x \rangle &= +\langle \hat{B}_i \hat{A}_{i+1} \hat{B}_{i+1} \cdots \hat{A}_{j-1} \hat{B}_{j-1} \hat{A}_j \rangle, \\
 \langle \hat{\sigma}_i^y \hat{\sigma}_j^y \rangle &= -\langle \hat{A}_i \hat{A}_{i+1} \hat{B}_{i+1} \cdots \hat{A}_{j-1} \hat{B}_{j-1} \hat{B}_j \rangle, \\
 \langle \hat{\sigma}_i^x \hat{\sigma}_j^y \rangle &= -i \langle \hat{B}_i \hat{A}_{i+1} \hat{B}_{i+1} \cdots \hat{A}_{j-1} \hat{B}_{j-1} \hat{B}_j \rangle,
 \end{aligned}$$

$$\langle \hat{\sigma}_i^y \hat{\sigma}_j^x \rangle = -i \langle \hat{A}_i \hat{A}_{i+1} \hat{B}_{i+1} \cdots \hat{A}_{j-1} \hat{B}_{j-1} \hat{A}_j \rangle, \quad (4.100)$$

which will be expanded into $(2k-1)!!$ terms according to Wick theorem. Those correlators are found to be systematically expressed as the Pfaffian

$$\begin{aligned} \langle \hat{\sigma}_i^x \hat{\sigma}_j^x \rangle &= +(-1)^{k(k-1)/2} \text{pf}(Q_{ij}^{xx}), \\ \langle \hat{\sigma}_i^y \hat{\sigma}_j^y \rangle &= +(-1)^{k(k-1)/2} \text{pf}(Q_{ij}^{yy}), \\ \langle \hat{\sigma}_i^x \hat{\sigma}_j^y \rangle &= -i(-1)^{k(k-1)/2} \text{pf}(Q_{ij}^{xy}), \\ \langle \hat{\sigma}_i^y \hat{\sigma}_j^x \rangle &= +i(-1)^{k(k-1)/2} \text{pf}(Q_{ij}^{yx}), \end{aligned} \quad (4.101)$$

of the following well-organized $2k \times 2k$ skew-symmetric matrices^[377-378]:

$$\begin{aligned} Q_{ij}^{xx} &= \begin{bmatrix} \mathcal{N}_{ij}^{xx} & \mathcal{G}_{ij}^{xx} \\ -\mathcal{G}_{ij}^{xxT} & \mathcal{M}_{ij}^{xx} \end{bmatrix}, \\ Q_{ij}^{yy} &= \begin{bmatrix} \mathcal{M}_{ij}^{yy} & \mathcal{G}_{ij}^{yy} \\ -\mathcal{G}_{ij}^{yyT} & \mathcal{N}_{ij}^{yy} \end{bmatrix}, \end{aligned}$$

with their corresponding blocks

$$\begin{aligned} \mathcal{G}_{ij}^{xx} &= \begin{bmatrix} G_{i,i+1} & \cdots & G_{i,j-1} & G_{i,j} \\ G_{i+1,i+1} & \cdots & G_{i+1,j-1} & G_{i+1,j} \\ \vdots & \ddots & \vdots & \vdots \\ G_{j-1,i+1} & \cdots & G_{j-1,j-1} & G_{j-1,j} \end{bmatrix}, \\ \mathcal{G}_{ij}^{yy} &= \begin{bmatrix} G_{i+1,i} & \cdots & G_{j-1,i} & G_{j,i} \\ G_{i+1,i+1} & \cdots & G_{j-1,i+1} & G_{j,i+1} \\ \vdots & \ddots & \vdots & \vdots \\ G_{i+1,j-1} & \cdots & G_{j-1,j-1} & G_{j,j-1} \end{bmatrix}, \\ \mathcal{M}_{ij}^{xx} &= \begin{bmatrix} 0 & M_{i+1,i+2} & \cdots & M_{i+1,j} \\ -M_{i+1,i+2} & 0 & \ddots & \vdots \\ \vdots & \ddots & 0 & M_{j-1,j} \\ -M_{i+1,j} & \cdots & M_{j-1,j} & 0 \end{bmatrix}, \\ \mathcal{M}_{ij}^{yy} &= \begin{bmatrix} 0 & M_{i,i+1} & \cdots & M_{i,j-1} \\ -M_{i,i+1} & 0 & \ddots & \vdots \\ \vdots & \ddots & 0 & M_{j-2,j-1} \\ -M_{i,j-1} & \cdots & M_{j-2,j-1} & 0 \end{bmatrix}, \end{aligned}$$

$$\mathcal{N}_{ij}^{xx} = \begin{bmatrix} 0 & N_{i,i+1} & \cdots & N_{i,j-1} \\ -N_{i,i+1} & 0 & \ddots & \vdots \\ \vdots & \ddots & 0 & N_{j-2,j-1} \\ -N_{i,j-1} & \cdots & N_{j-2,j-1} & 0 \end{bmatrix},$$

$$\mathcal{N}_{ij}^{yy} = \begin{bmatrix} 0 & N_{i+1,i+2} & \cdots & N_{i+1,j} \\ -N_{i+1,i+2} & 0 & \ddots & \vdots \\ \vdots & \ddots & 0 & N_{j-1,j} \\ -N_{i+1,j} & \cdots & N_{j-1,j} & 0 \end{bmatrix}.$$

Through observing Equation (4.100), the correlators of $\langle \hat{\sigma}_i^x \hat{\sigma}_j^y \rangle$, $\langle \hat{\sigma}_i^y \hat{\sigma}_j^x \rangle$ only differ on the last operator from $\langle \hat{\sigma}_i^x \hat{\sigma}_j^x \rangle$, $\langle \hat{\sigma}_i^y \hat{\sigma}_j^y \rangle$, hence we can calculate Q_{ij}^{xy} , Q_{ij}^{yx} by replacing the last column and its corresponding transpose row $\boxed{\cdots}$ of Q_{ij}^{xx} , Q_{ij}^{yy} , respectively:

$$Q_{ij}^{xx} = \begin{bmatrix} \cdots & G_{i,j} \\ \cdots & G_{i+1,j} \\ \cdots & \vdots \\ \cdots & G_{j-1,j} \\ \cdots & M_{i+1,j} \\ \cdots & \vdots \\ \cdots & M_{j-1,j} \\ \boxed{GM} & 0 \end{bmatrix} \Rightarrow \begin{bmatrix} \cdots & N_{i,j} \\ \cdots & N_{i+1,j} \\ \cdots & \vdots \\ \cdots & N_{j-1,j} \\ \cdots & -G_{j,i+1} \\ \cdots & \vdots \\ \cdots & -G_{j,j-1} \\ \boxed{NG} & 0 \end{bmatrix} \equiv Q_{ij}^{xy};$$

$$Q_{ij}^{yy} = \begin{bmatrix} \cdots & G_{j,i} \\ \cdots & G_{j,i+1} \\ \cdots & \vdots \\ \cdots & G_{j,j-1} \\ \cdots & N_{i+1,j} \\ \cdots & \vdots \\ \cdots & N_{j-1,j} \\ \boxed{GN} & 0 \end{bmatrix} \Rightarrow \begin{bmatrix} \cdots & M_{j,i} \\ \cdots & M_{j,i+1} \\ \cdots & \vdots \\ \cdots & M_{j,j-1} \\ \cdots & G_{i+1,j} \\ \cdots & \vdots \\ \cdots & G_{j-1,j} \\ \boxed{MG} & 0 \end{bmatrix} \equiv Q_{ij}^{yx}.$$

When the twisting angle is zero, the spin supercurrent vanishes with $\langle \hat{\sigma}_i^x \hat{\sigma}_j^y \rangle = \langle \hat{\sigma}_i^y \hat{\sigma}_j^x \rangle = 0$. Furthermore, block-diagonal terms in Q_{ij}^{xx} , Q_{ij}^{yy} are also found out to be zero. In this special case, $\langle \hat{\sigma}_i^x \hat{\sigma}_j^x \rangle$ and $\langle \hat{\sigma}_i^y \hat{\sigma}_j^y \rangle$ are reduced into $\det(\mathcal{G}_{ij}^{xx})$ and $\det(\mathcal{G}_{ij}^{yy})$, respectively, which agree with previous formulas used in Sachdev^[69], Lieb et al.^[341], Osborne et al.^[376].

4.7 Detection and Robustness

The experimental method of choice for detecting spin current in insulating (quantum) magnets is via the inverse spin-Hall effect in which a metal with strong SOI is coupled to the insulating magnet. Spin current is injected into the metal which is converted, via the SOI, into charge current and can be measured by usual means^[380]. While this method is effective for large spin systems, the signal might be too small for quantum spin chains. Thus, we propose detecting the spin current by embedding our system in a cavity QED setup wherein such a spin flow shifts both the cavity frequency and the Q factor, which can then be detected by measuring the spectral features of the cavity.

4.7.1 General Expression of the Susceptibility

In this section, we address the detection of the spin supercurrent pertaining to the JW Majoranas in the IXI spin junction. While the method of choice for measuring spin current is through the use of the spin Hall effect^[380], in which case a spin current is converted to a charge current that can be measured by usual techniques, via the SOI in the adjacent material, here we propose a less invasive method based on microwave detection. Such an approach has been found suitable for measuring both the statics and dynamics of ABSs in electronic systems^[381-383]. The idea is to couple the field of a nearby resonator to various observables of the system (see Figure 1.3 for a schematic of the cavity QED setup). The interaction between our chain and the resonator can be written as

$$\hat{V}(t) = \beta \hat{O}(a^\dagger + a), \quad (4.102)$$

where a (a^\dagger) is the annihilation (creation) operator for the photon in the resonator (assuming one mode only), while \hat{O} are the observables of the system, e.g., $\hat{O} = \hat{\sigma}_i^\alpha$ (or the sum of a string of spins), with coupling strength β . This coupling will alter the properties of the resonator, which in turn can be measured in a dispersive readout. Following Dmytruk et al.^[162], we can write the equation of motion for the cavity field in the Heisenberg picture as

$$\dot{a} = i[\hat{H}_{\text{ph}} + \hat{V}(t), a] - \frac{\kappa}{2}a - \sqrt{\kappa}b_{\text{in}}(t), \quad (4.103)$$

where $\hat{H}_{\text{ph}} = \omega_0 a^\dagger a$ is the cavity Hamiltonian, κ quantifies the decay rate of the cavity, and $b_{\text{in}}(t)$ is the input field sent to probe it. Note that the output field, exiting from the cavity $b_{\text{out}}(t)$, and the input one satisfy $b_{\text{out}}(t) = b_{\text{in}}(t) + \sqrt{\kappa}a(t)$, which is used to infer the cavity response. In leading order in the cavity-system coupling and in the frequency

space, we find^[162]

$$a(\omega) = -\frac{\sqrt{\kappa}b_{\text{in}}(\omega) + i\beta\langle\hat{O}_I(\omega)\rangle_0}{-i(\omega - \omega_0) + \kappa/2 - i\beta^2\Pi_{\hat{O}}(\omega_0)}, \quad (4.104)$$

where $a(\omega) = \int dt e^{-i\omega t} a(t)$ and

$$\begin{aligned} \Pi_{\hat{O}}(\omega) &= -i \int_0^\infty dt e^{-i\omega t} \langle [\hat{O}_I(t), \hat{O}_I(0)] \rangle_0 \\ &= \sum'_{m,n} \frac{|\langle m|\hat{O}|n\rangle|^2 (F_m - F_n)}{E_m - E_n - \omega - i\eta}, \end{aligned} \quad (4.105)$$

being the retarded correlation function associated with the observable \hat{O} over the stationary state of the system $\langle \dots \rangle_0$. Above, $|n\rangle$ and E_n are the many-body eigen-states and eigen-energies of the system, respectively, F_n is the many-body occupation, while the ' index selects only the states $n \neq m$ in the summation. Note that all quantities are expressed in the interaction picture, and $\langle \hat{O}_I(\omega) \rangle_0$ is the expectation value of the observable \hat{O} in the frequency space in the absence of the cavity. Since the energies E_n , as well as the matrix elements $\langle m|\hat{O}|n\rangle$ are functions of ϕ , the entire correlation function will carry such a dependence too. In typical spectroscopic experiments, the input field $b_{\text{in}}(\omega) \gg \langle \hat{O}_I(\omega) \rangle_0$ (large number of photons are sent into the cavity), and we can neglect this term in the following. Nevertheless, such contribution can become relevant in out-of-equilibrium situations, when it affects the photon number and photon statistics in the cavity. We will not discuss such regimes here, but refer to Aftergood et al.^[383] for some details. The effect of the spins on the cavity photons results in changes in both the resonance frequency ω_0 and the quality factor (or Q factor) of the cavity, which can be straightforwardly related to the correlation function as follows:

$$\delta\omega_0(\phi) = \beta^2 \text{Re } \Pi_{\hat{O}}(\omega_0, \phi), \quad (4.106)$$

$$\frac{\delta Q(\phi)}{Q} = \frac{\beta^2 \text{Im } \Pi_{\hat{O}}(\omega_0, \phi)}{\omega_0}, \quad (4.107)$$

implying quadratic dependence on the coupling strength β of these quantities. This coupling depends on the specific implementation of our model, ranging from a tens of Hz for electron spins coupled directly to the magnetic component of an electromagnetic cavity, to tens of MHz in the case of superconducting qubits (in which case the coupling occurs via the electrical field of the cavity instead).

In this dissertation, we consider a capacitive-like coupling between the spin chain and the cavity *magnetic* field (through the Zeeman coupling), following Aftergood et al.^[383].

Moreover, we assume the *magnetic* field of a microwave cavity couples to the spins in the XY part over a length $l < L$, or $\hat{O} = \hat{S}_l \cdot \mathbf{n}$, with $\hat{S}_l = \sum_{i \in l} \hat{\sigma}_i$. Here, \mathbf{n} is the direction of the cavity magnetic field at the position of the wire, which can be different from the z direction, and the coupling is assumed to take place from site l_0 to site $l_0 + l - 1$. The susceptibility can be written as $\Pi_s(\omega) = \Pi_s^z(\omega) + \Pi_s^\perp(\omega)$, where the first and second terms corresponding to the matrix element $\langle m | \hat{S}_l^z | n \rangle$ (longitudinal) and $\langle m | \hat{S}_l \cdot \mathbf{n}_\perp | n \rangle$ (transverse), respectively, with $\mathbf{n}_\perp = \mathbf{n} - \mathbf{e}_z$. There are no cross terms between the z (parity preserving) and x, y (parity flipping) spin components as all the states in the system have a definite parity. The above susceptibilities have a simple interpretation in the fermionic language: The first contribution stems from the cavity probing particle number operator over the length l , while the second one effectively represents electronic tunneling into the spin chain over the same distance, thus accessing the transport properties of the spin chain. However, as we see in the following discussions, the analogy is only partial for the second coupling because of the non-locality of the JW string.

4.7.2 Longitudinal Susceptibility

The longitudinal susceptibility can now be numerically evaluated from the lattice model by including all possible states. However, in order to understand the behavior, it is worth analyzing the limit of small $\omega \ll \Delta$ in which case the cavity probes mostly the low-energy ABSs (truncated up to the 12th state in calculation), including the MBSs. We transform the spins into fermions in the lattice \hat{c}_i , and eventually in terms of quasi-particles describing the Andreev states \hat{d}_n , with i and n specifying the lattice and eigen-energy index, respectively. By using $\hat{c}_i = \sum_n [u_n(i) \hat{d}_n + v_n^*(i) \hat{d}_n^\dagger]$ with coefficients $u_n(i)$ and $v_n(i)$ found from wave functions of numerical diagonalization, we write down \hat{S}_l^z in the form of quasi-particles,

$$\hat{S}_l^z = \sum_{i \in l} \sum_{r,s} [b_r^*(i) \hat{d}_r^\dagger - b_r(i) \hat{d}_r] [a_s^*(i) \hat{d}_s^\dagger + a_s(i) \hat{d}_s], \quad (4.108)$$

with $a_s(i) = u_s(i) + v_s(i)$, $b_s(i) = u_s(i) - v_s(i)$, where r, s are single-particle indices of their corresponding many-body states in Equation (4.105), given in the labels of Figures 4.4(c) and 4.4(d). The matrix elements of $\hat{O} = \hat{S}_l^z = \sum_{i \in l} \hat{\sigma}_i^z$ is calculated by

$$\begin{aligned} \langle m | \hat{S}_l^z | n \rangle &= \sum_{i \in l} \langle m | \hat{\sigma}_i^z | n \rangle = \sum_{i \in l} \langle m | (\hat{c}_i^\dagger - \hat{c}_i)(\hat{c}_i^\dagger + \hat{c}_i) | n \rangle \\ &= \sum_{i \in l} \sum_{r,s} \langle m | [b_r^*(i) \hat{d}_r^\dagger - b_r(i) \hat{d}_r] [a_s^*(i) \hat{d}_s^\dagger + a_s(i) \hat{d}_s] | n \rangle \end{aligned}$$

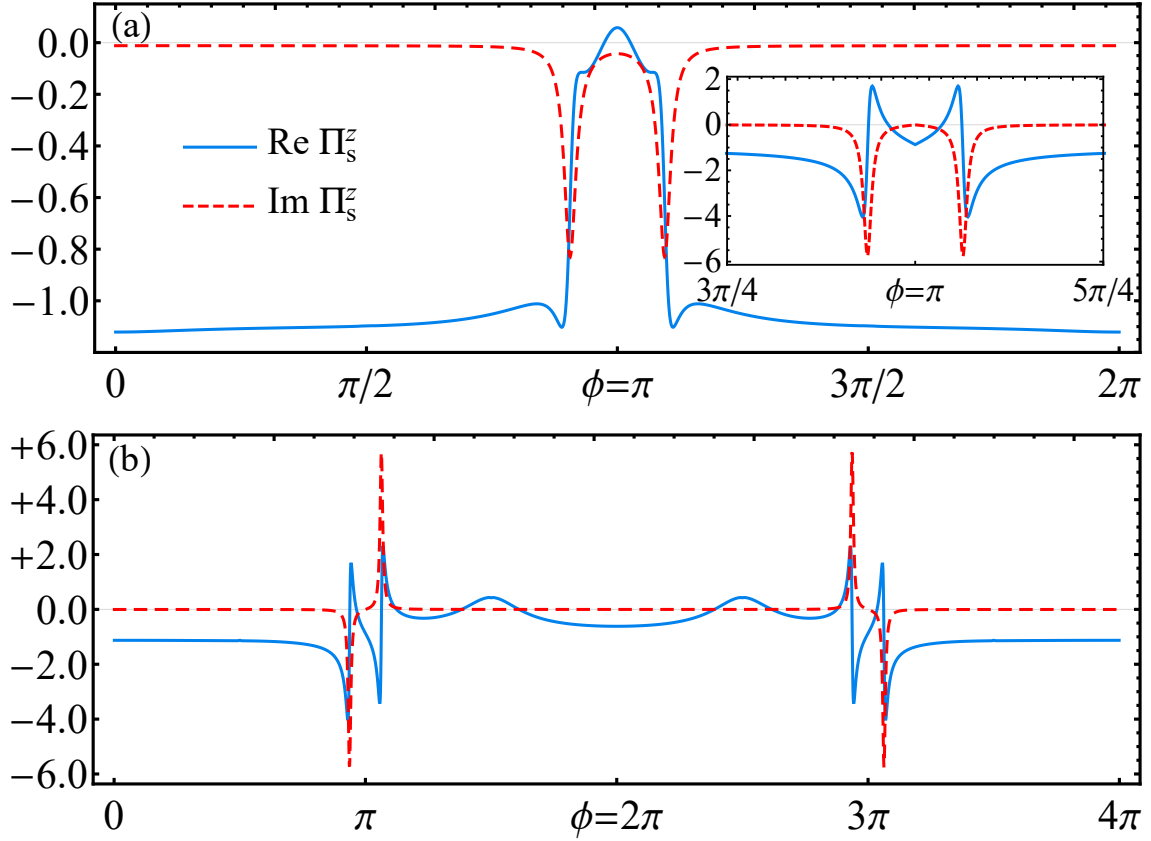


Figure 4.7 The longitudinal susceptibility as a function of the twisting angle.

The plots are calculated by Equation (4.112) with $J = t = 1$, $\mathbb{t} = 0.8$, $\gamma = 0.4$, $g = 0$, $\eta = 0.1\omega$, $N_L = N_R = 100$, whose real (imaginary) parts are represented by blue (red dashed) lines. In both (a) and (b), the cavity couples to five spins starting from $l_0 = N_L + 3$. More specifically, (a) is \mathbb{Z}_2 case with $N_M = 10$, $\omega = 0.2$, which shows negative peaks of the imaginary parts around $\phi = \pi$; (b) is \mathbb{Z}_4 case with $N_M = 11$, $\omega = 0.1$, which shows peaks of the imaginary parts around $\phi = \pi$ that have opposite signs. In the presence of relaxation, for odd number of sites, the susceptibility will return to \mathbb{Z}_2 periodicity as shown in the inset of (a), which exhibits a singularity in the real part at $\phi = \pi$ [67].

$$\begin{aligned}
 &= \sum_{i \in l} \sum_{r,s} [b_r^*(i) a_s^*(i) \langle m | \hat{d}_r^\dagger \hat{d}_s^\dagger | n \rangle + b_r^*(i) a_s(i) \langle m | \hat{d}_r^\dagger \hat{d}_s | n \rangle \\
 &\quad - b_r(i) a_s^*(i) \langle m | \hat{d}_r \hat{d}_s^\dagger | n \rangle - b_r(i) a_s(i) \langle m | \hat{d}_r \hat{d}_s | n \rangle].
 \end{aligned} \tag{4.109}$$

One can observe that there are two types of $\langle m | \hat{S}_l^z | n \rangle$: quasi-particle conserving type $\mathcal{S}_{r,s}^c$ and non-conserving type $\mathcal{S}_{r,s}^n$, which are shown explicitly as

$$\mathcal{S}_{r,s}^c = \sum_{i \in l} [b_r^*(i) a_s(i) + b_s(i) a_r^*(i)], \tag{4.110}$$

$$\mathcal{S}_{r,s}^n = \sum_{i \in l} [b_r(i) a_s(i) - b_s(i) a_r(i)]. \tag{4.111}$$

With single-particle occupation $f_s \equiv \langle \hat{d}_s^\dagger \hat{d}_s \rangle$, the longitudinal susceptibility is written in the single-particle form:

$$\begin{aligned} \Pi_s^z(\omega) = \sum_{r,s}' & \left[\frac{(f_r - f_s)|S_{r,s}^c|^2}{\epsilon_r - \epsilon_s - \omega - i\eta} + \frac{(f_r - f_s)|S_{r,s}^c|^2}{\epsilon_r - \epsilon_s + \omega + i\eta} \right. \\ & \left. + \frac{(f_r + f_s - 1)|S_{r,s}^n|^2}{\epsilon_r + \epsilon_s - \omega - i\eta} + \frac{(f_r + f_s - 1)|S_{r,s}^n|^2}{\epsilon_r + \epsilon_s + \omega + i\eta} \right], \end{aligned} \quad (4.112)$$

where the first (second) line accounts for the quasi-particle conserving (non-conserving) contributions. For the pedagogical purpose, we explicit calculate the transition between 4 lowest states in the \mathbb{Z}_4 -like case, which are constructed by following single-particle states

$$|0\rangle = |00\rangle, \quad |1\rangle = |10\rangle, \quad |2\rangle = |01\rangle, \quad |3\rangle = |11\rangle. \quad (4.113)$$

With the help of single-particle configuration, we can calculate the matrix elements between states with the same parity

$$\langle 3|\hat{S}_l^z|0\rangle = \sum_{i \in l} [b_1^*(i)a_2^*(i) - b_2^*(i)a_1^*(i)] = 2 \sum_{i \in l} [u_1^*(i)v_2^*(i) - u_2^*(i)v_1^*(i)], \quad (4.114)$$

$$\langle 0|\hat{S}_l^z|3\rangle = \sum_{i \in l} [b_1(i)a_2(i) - b_2(i)a_1(i)] = 2 \sum_{i \in l} [u_1(i)v_2(i) - u_2(i)v_1(i)], \quad (4.115)$$

$$\langle 2|\hat{S}_l^z|1\rangle = \sum_{i \in l} [b_1(i)a_2^*(i) + b_2^*(i)a_1(i)] = 2 \sum_{i \in l} [u_1(i)u_2^*(i) - v_2^*(i)v_1(i)], \quad (4.116)$$

$$\langle 1|\hat{S}_l^z|2\rangle = \sum_{i \in l} [b_1^*(i)a_2(i) + b_2(i)a_1^*(i)] = 2 \sum_{i \in l} [u_1^*(i)u_2(i) - v_2(i)v_1^*(i)], \quad (4.117)$$

Thus we obtain

$$\begin{aligned} \Pi_s^z(\omega) = & \frac{|\langle 2|\hat{S}_l^z|1\rangle|^2(F_2 - F_1)}{E_2 - E_1 - \omega - i\eta} + \frac{|\langle 1|\hat{S}_l^z|2\rangle|^2(F_1 - F_2)}{E_1 - E_2 - \omega - i\eta} + \\ & \frac{|\langle 3|\hat{S}_l^z|0\rangle|^2(F_3 - F_0)}{E_3 - E_0 - \omega - i\eta} + \frac{|\langle 0|\hat{S}_l^z|3\rangle|^2(F_0 - F_3)}{E_0 - E_3 - \omega - i\eta} \end{aligned} \quad (4.118)$$

$$\begin{aligned} = & \left(\frac{|\langle 2|\hat{S}_l^z|1\rangle|^2}{E_2 - E_1 - \omega - i\eta} + \frac{|\langle 1|\hat{S}_l^z|2\rangle|^2}{E_2 - E_1 + \omega + i\eta} \right) (F_2 - F_1) + \\ & \left(\frac{|\langle 3|\hat{S}_l^z|0\rangle|^2}{E_3 - E_0 - \omega - i\eta} + \frac{|\langle 0|\hat{S}_l^z|3\rangle|^2}{E_3 - E_0 + \omega + i\eta} \right) (F_3 - F_0) \end{aligned} \quad (4.119)$$

$$\begin{aligned} = & \left(\frac{|\langle 2|\hat{S}_l^z|1\rangle|^2}{\epsilon_2 - \epsilon_1 - \omega - i\eta} + \frac{|\langle 1|\hat{S}_l^z|2\rangle|^2}{\epsilon_2 - \epsilon_1 + \omega + i\eta} \right) (f_2 - f_1) + \\ & \left(\frac{|\langle 3|\hat{S}_l^z|0\rangle|^2}{\epsilon_2 + \epsilon_1 - \omega - i\eta} + \frac{|\langle 0|\hat{S}_l^z|3\rangle|^2}{\epsilon_2 + \epsilon_1 + \omega + i\eta} \right) (f_2 + f_1 - 1). \end{aligned} \quad (4.120)$$

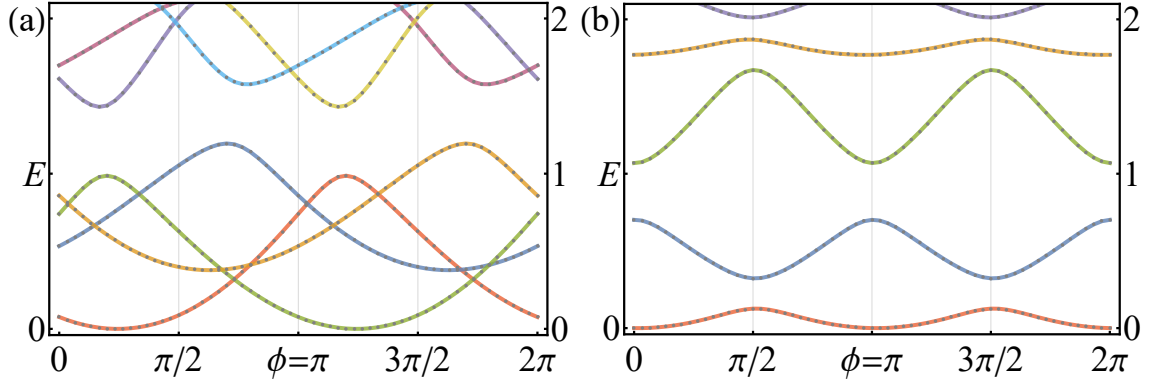


Figure 4.8 The spectra of the IXI spin chain under random perturbations.

The plots are computed by exact diagonalization with $J = t = \gamma = 1$, $\mathfrak{t} = 0.8$, $g = -0.2$, $N_L = N_M = N_R = 4$. (a) is under local spin perturbations [Equation (4.121)] from the in-plane magnetic fields, crossings are preserved albeit with lifted degeneracies. (b) suffers local fermionic perturbations [Equation (4.122)] from the quasi-particle poisoning, crossings are destroyed while each state still contains twofold degeneracy. All perturbation strengths η_i^x and η_i^y are set randomly site by site in the middle XY chain within the range of $(0, 0.2)^{[67]}$.

In Figures 4.7(a) and 4.7(b), we show the real and the imaginary parts of $\Pi_s^z(\omega)$ as a function of ϕ for odd and even cases, respectively, evolving adiabatically in their initial ground states at $\phi = 0$, whose peaks indicate the resonances between the cavity and the low-energy levels in Figures 4.4(c) and 4.4(d). They present different periodicities and reach peaks at different ϕ , as a result of the odd-even effect. Particularly, one can distinguish \mathbb{Z}_4 spin current from the \mathbb{Z}_2 case, by way of opposite signs near $\phi = \pi$ in the imaginary parts. Moreover, even taking into account the relaxation effects such that the system always follows the ground state, the real part still exhibits a singularity at $\phi = \pi$ in Figure 4.7(c), which is again a signature for \mathbb{Z}_4 crossing of the levels. We note that while the magnetic coupling to each individual spin is typically small (a few Hz in cavity QED setups), by coupling the cavity to many spins in the chains \hat{S}_I , the response function is enhanced by an order $\sim l^2$ as compared to the single spin scenario.

4.7.3 Transverse Susceptibility and Spin Noise

Borrowing from the fermionic parity-flipping picture due to the quasi-particle poisoning, one may conjecture that the transverse susceptibility $\Pi_s^\perp(\omega)$ has a nonzero value. Surprisingly, we find out numerically that the matrix elements of $\Pi_s^\perp(\omega)$ are exponentially reduced to *zero* as the length of the Ising part increases, which makes transitions between different parities *impossible* in the topological spin JJs. Such phenomenon is because the local in-plane spin operators $\hat{\sigma}_i^x, \hat{\sigma}_i^y$ become highly non-local objects with the additional JW string in the fermionic space — it is inevitable to alter the states of *external* JW Majorana

ranas, which in turn flips the parity back to itself and thus forbids the transitions between them. To verify this, we study the influences from two kinds of in-plane perturbations within the middle part (x_L, x_R) :

$$\hat{H}_P^S = \sum_{i \in M} [\eta_i^x \hat{\sigma}_i^x + \eta_i^y \hat{\sigma}_i^y], \quad (4.121)$$

$$\hat{H}_P^F = \sum_{i \in M} \left[\eta_i^x \prod_{j=1}^{i-1} (-\hat{\sigma}_j^z) \hat{\sigma}_i^x + \eta_i^y \prod_{j=1}^{i-1} (-\hat{\sigma}_j^z) \hat{\sigma}_i^y \right], \quad (4.122)$$

where η_i^x and η_i^y are perturbation strengths along x and y directions, respectively, both set randomly site by site. Equation (4.122) indeed emulates the conventional local fermionic perturbations from quasi-particle poisoning and breaks Majorana crossings in Figure 4.8(b) as expected. On the other hand, in Figure 4.8(a) we see that the local spin perturbations [Equation (4.121)] only shift twofold degeneracy (from external JW Majoranas) away and cannot destroy \mathbb{Z}_2 periodicity (even when we extend the random perturbations to the whole spin chain), in contrast to topological JJs in superconducting systems.

4.8 Discussion and Summary

Table 4.1 A summary of conclusions, contrasted with the electronic counterpart.

	Fractional Josephson effects		Entanglement	Detection	Robustness
	Continuum	Lattice			
SNS	\mathbb{Z}_2 or \mathbb{Z}_4	\mathbb{Z}_2 or \mathbb{Z}_4	No counterpart	Transport	No
IXI	\mathbb{Z}_2	\mathbb{Z}_2 or \mathbb{Z}_4	ϕ -dependence (\mathbb{Z}_2 or \mathbb{Z}_4)	Cavity QED	Yes

In this dissertation, we analyzed an Ising-XY-Ising spin link that emulates a topological superconducting-normal-superconducting structure, both analytically and numerically. Our results are summarized in Table 4.1 and as follows:

(i) Odd versus even. The iTRS gives rise to the odd-even effect at the lattice level and protects \mathbb{Z}_4 (\mathbb{Z}_2) fractional spin JE in chains with an odd (even) number of spins, irrespective of ZZ-type interactions. The resulting texture of spin entanglement highlights the effects of the spin current carried by JW Majoranas, whose periodicities can be detected by cavity QED setup through dispersive readout methods.

(ii) Lattice versus continuum. By use of the low-energy theory, we analytically solve out the spectra of ABSs and their fermionic wave functions. Yet, the aforementioned odd-even effect can only be observed in a discrete lattice but not in the continuum theory.

(iii) Spin versus fermion. At the lattice level, we identified various symmetries emerging from the spin chain and determine their electronic counterparts, demonstrating that ZZ-type interactions and NN-type interactions affect differently the many-body spectra. One remarkable result is that although \mathbb{Z}_2 -periodic current can be broken by local fermionic perturbations, spin \mathbb{Z}_2 JEs are robust to local spin perturbations.

Our proposal could be implemented in a plethora of spin systems, such as trapped ions^[384], photonic lattices^[385-386], electron spins in quantum dots^[387], and magnetic impurities on surfaces^[388-389]. In addition, the spin JEs should possibly be simulated and observed in the noisy intermediate-scale quantum computer (e.g. the IBM Q quantum machines) through measuring the correlation functions^[390-391]. Since \mathbb{Z}_2 fractional spin JEs are immune to any local perturbations from arbitrary directions of magnetic field (as long as the chain is still in the topological phase), the ground state can, together with the first excited state, be used to set up a logical qubit: advancing ϕ adiabatically by π realizes a quantum X gate^[108,392]. Alternatively, we can utilize such robustness for quantum memory. In addition, the middle XY chain will be gapped when $|g| > 2t$, which prohibits the transport of spin supercurrent. Hence, one may use this feature to engineer a quantum spin transistor based on the JEs^[393].

CHAPTER 5 CONCLUSION AND OUTLOOK

In this dissertation, we have discussed and investigated quantum machine learning and information processing. In particular, we have briefly reviewed the basic concepts of three closely related areas: condensed matter physics, quantum computation and AI. Specifically, we have introduced an efficient Markovian quantum neuro-evolution algorithm to search for optimal ansatz quantum circuits. Except for the high-level implementation of quantum machine learning tasks, we have also studied the low-level information processing in spin chains. We have shown that a specifically designed anisotropic spin chains offer a promising platform for quantum computation. Moreover, we have specifically investigated the spin transport through an Ising-XY-Ising spin link and revealed several type of spin Josephson effects.

Quantum machine learning is a fledging research field that is growing in a promising but also challenging way. To tackle these challenges, the quantum machine learning community has started to incorporate the techniques developed by classical machine learning, and extends the boundaries of conventional quantum information processing research. There is also a lively community developing powerful open-sources software libraries for quantum machine learning such as Qiskit^[394], Cirq^[395], OpenFermion^[148], Yao^[328], etc. These platforms provide a testbed to evaluate theoretical proposals before implementing them in real experimental setups. Undoubtedly, the marriage of machine learning and quantum physics would significantly boost information processing.

There are many interesting aspects of quantum machine learning that worth further investigation. Along the direction of AI for quantum physics, one important question is how to identify the topological phases for interacting fermions via machine learning techniques. For free-fermion systems, a complete classification for topological insulators and superconductors has been obtained via the renowned periodic table^[124]. Hence, it is straightforward to use supervised learning methods to capture the well-understood topological phases. Yet, for interacting fermion systems, a complete classification of topological phases still remains to be explored^[396]. We may exploit some unsupervised learning methods to unveil some new topological phases for interacting fermions.

Other future directions about quantum computation might involve developing more efficient strategies for quantum architecture search, as well as introducing some new quan-

tum neural networks and algorithms for machine learning. It has been shown that quantum circuits can be further simplified through the ZX-calculus (i.e., a graphical language for reasoning about linear maps between qubits)^[397]. We may combine this powerful tool with state-of-the-art machine learning techniques (e.g., dynamic neural networks^[398]) to construct optimal circuit structures for different quantum-learning problems. In the last few years, the Transformer network has demonstrated an exceptional performance in the fields of both computer vision and natural language processing^[194]. We conjecture that a quantum extension of the transformer would be proficient at learning the pattern of temporal data (e.g., quantum dynamics). Recently, we noticed a seminal paper by Martyn et al.^[399] which unifies phase estimation, unstructured search, and Hamiltonian simulation in a general framework of the quantum singular value transformation. We may exploit this powerful framework to develop some new quantum algorithms.

On the subject of condensed matter physics, there are several generalizations of the Ising-XY-Ising spin link. First, we can take into account the effect of dissipation (due to, for example, the presence of a magnetic substrate) and investigate spin Josephson effects in a non-equilibrium phase^[400] (e.g., owing to the driving of the spin bias). In addition, the cavity QED setup proposed here could serve as an engineered environment that can not only monitor the spin flow, but also affect and control it. Moreover, we can integrate out the self-energy of the environment and then obtain the non-Hermitian dynamics pertaining to such a spin chain^[61]. It has been shown that the non-Hermitian Hamiltonian is very sensitive around some exceptional points^[401]. In particular, the emergence of exceptional points in quasi-particle band structures can dramatically enrich their topological classification in crystalline materials^[175]. Hence it would be desirable to explore the properties of quantum spin current around the exceptional points^[402]. Second, generalization to multi-junction quantum spin chains, similar to superconducting systems^[403-404], which could result in emulating various higher dimensional topological structures. Third, generalization to more complex insulating quantum spin systems, such as 2D quantum (anti)ferromagnets insulators or even quantum spin liquids^[405], subject to dissipationless spin flows. With regard to the \mathbb{Z}_2 spin Josephson effect, there are two inspiring directions to explore: first, it is worthwhile to theoretically formalize its robustness against fluctuating magnetic fields; second, it would be valuable to simulate and examine its robustness on the NISQ devices.

REFERENCES

- [1] Nielsen M A, Chuang I L. Quantum Computation and Quantum Information[M/OL]. Cambridge: Cambridge University Press, 2010. DOI: 10.1017/CBO9780511976667.
- [2] Mermin N D. Quantum Computer Science: An Introduction[M]. 2007.
- [3] Wilde M M. Quantum Information Theory[M]. Second ed. Cambridge, UK: Cambridge University Press, 2017.
- [4] Feynman R P. Simulating physics with computers[J/OL]. International Journal of Theoretical Physics, 1982, 21(6): 467-488. DOI: 10.1007/BF02650179.
- [5] Shor P W. Algorithms for quantum computation: Discrete logarithms and factoring[C/OL]// Proceedings 35th Annual Symposium on Foundations of Computer Science. 1994: 124-134. DOI: 10.1109/SFCS.1994.365700.
- [6] Grover L K. Quantum Mechanics Helps in Searching for a Needle in a Haystack[J/OL]. Physical Review Letters, 1997, 79(2): 325-328. DOI: 10.1103/PhysRevLett.79.325.
- [7] Aaronson S, Arkhipov A. The computational complexity of linear optics[C/OL]//STOC '11: Proceedings of the Forty-Third Annual ACM Symposium on Theory of Computing. New York, NY, USA: Association for Computing Machinery, 2011: 333-342. DOI: 10.1145/1993636.1993682.
- [8] Harrow A W, Montanaro A. Quantum computational supremacy[J/OL]. Nature, 2017, 549 (7671): 203-209. DOI: 10.1038/nature23458.
- [9] Trabesinger A. Quantum simulation[J/OL]. Nature Physics, 2012, 8(4): 263-263. DOI: 10.1038/nphys2258.
- [10] Georgescu I M, Ashhab S, Nori F. Quantum simulation[J/OL]. Reviews of Modern Physics, 2014, 86(1): 153-185. DOI: 10.1103/RevModPhys.86.153.
- [11] Kimble H J. The quantum internet[J/OL]. Nature, 2008, 453(7198): 1023-1030. DOI: 10.1038/nature07127.
- [12] Arute F, Arya K, Babbush R, et al. Quantum supremacy using a programmable superconducting processor[J/OL]. Nature, 2019, 574(7779): 505-510. DOI: 10.1038/s41586-019-1666-5.
- [13] Wu Y, Bao W S, Cao S, et al. Strong Quantum Computational Advantage Using a Superconducting Quantum Processor[J/OL]. Physical Review Letters, 2021, 127(18): 180501. DOI: 10.1103/PhysRevLett.127.180501.
- [14] Zhong H S, Deng Y H, Qin J, et al. Phase-Programmable Gaussian Boson Sampling Using Stimulated Squeezed Light[J/OL]. Physical Review Letters, 2021, 127(18): 180502. DOI: 10.1103/PhysRevLett.127.180502.
- [15] Altland A, Simons B D. Condensed Matter Field Theory[M]. Second ed. New York: Cambridge University Press, 2010.
- [16] Fradkin E. Field Theories of Condensed Matter Physics[M]. Second ed. New York: Cambridge University Press, 2013.

REFERENCES

- [17] Ashcroft N W, Mermin N D. Solid State Physics[M]. First ed. New York: Cengage Learning, 1976.
- [18] Kittel C. Introduction to Solid State Physics[M]. Eighth ed. Hoboken, NJ: Wiley, 2004.
- [19] Burkard G, Loss D. Quantum Computing with Solid-State Systems[M/OL]//Quantum Information. John Wiley & Sons, Ltd, 2016: 553-585. DOI: 10.1002/9783527805785.ch25.
- [20] Loss D, DiVincenzo D P. Quantum computation with quantum dots[J/OL]. Physical Review A, 1998, 57(1): 120-126. DOI: 10.1103/PhysRevA.57.120.
- [21] Makhlin Y, Schön G, Shnirman A. Quantum-state engineering with Josephson-junction devices [J/OL]. Reviews of Modern Physics, 2001, 73(2): 357-400. DOI: 10.1103/RevModPhys.73.357.
- [22] Kitaev A Y. Fault-tolerant quantum computation by anyons[J/OL]. Annals of Physics, 2003, 303(1): 2-30. DOI: 10.1016/S0003-4916(02)00018-0.
- [23] Bishop C. Information Science and Statistics: Pattern Recognition and Machine Learning [M/OL]. New York: Springer-Verlag, 2006. <https://www.springer.com/gp/book/9780387310732>.
- [24] Nielsen M A. Neural networks and deep learning: volume 2018[M/OL]. Determination press San Francisco, CA, 2015. <http://neuralnetworksanddeeplearning.com/>.
- [25] LeCun Y, Bengio Y, Hinton G. Deep learning[J/OL]. Nature, 2015, 521(7553): 436-444. DOI: 10.1038/nature14539.
- [26] Goodfellow I, Bengio Y, Courville A. Deep Learning[M/OL]. Cambridge: The MIT Press, 2016. <https://www.deeplearningbook.org/>.
- [27] Mohri M, Rostamizadeh A, Talwalkar A. Foundations of Machine Learning[M]. Second ed. Cambridge, Massachusetts: The MIT Press, 2018.
- [28] Sewak M. Deep Reinforcement Learning: Frontiers of Artificial Intelligence[M/OL]. Springer Singapore, 2019. DOI: 10.1007/978-981-13-8285-7.
- [29] Russell S, Norvig P. Artificial Intelligence: A Modern Approach[M/OL]. Fourth ed. Hoboken: Pearson, 2020. <http://aima.cs.berkeley.edu/>.
- [30] Silver D, Huang A, Maddison C J, et al. Mastering the game of Go with deep neural networks and tree search[J/OL]. Nature, 2016, 529(7587): 484-489. DOI: 10.1038/nature16961.
- [31] Silver D, Schrittwieser J, Simonyan K, et al. Mastering the game of Go without human knowledge[J/OL]. Nature, 2017, 550(7676): 354-359. DOI: 10.1038/nature24270.
- [32] Jumper J, Evans R, Pritzel A, et al. Highly accurate protein structure prediction with AlphaFold [J/OL]. Nature, 2021: 1-11. DOI: 10.1038/s41586-021-03819-2.
- [33] Davies A, Veličković P, Buesing L, et al. Advancing mathematics by guiding human intuition with AI[J/OL]. Nature, 2021, 600(7887): 70-74. DOI: 10.1038/s41586-021-04086-x.
- [34] Degraeve J, Felici F, Buchli J, et al. Magnetic control of tokamak plasmas through deep reinforcement learning[J/OL]. Nature, 2022, 602(7897): 414-419. DOI: 10.1038/s41586-021-04301-9.
- [35] Wittek P. Quantum Machine Learning: What Quantum Computing Means to Data Mining[M]. Academic Press, 2014.

REFERENCES

- [36] Biamonte J, Wittek P, Pancotti N, et al. Quantum machine learning[J/OL]. *Nature*, 2017, 549 (7671): 195-202. DOI: 10.1038/nature23474.
- [37] Dunjko V, Briegel H J. Machine learning & artificial intelligence in the quantum domain: A review of recent progress[J/OL]. *Reports on Progress in Physics*, 2018, 81(7): 074001. DOI: 10.1088/1361-6633/aab406.
- [38] Ciliberto C, Herbster M, Ialongo A D, et al. Quantum machine learning: A classical perspective [J/OL]. *Proceedings of the Royal Society A: Mathematical, Physical and Engineering Sciences*, 2018, 474(2209): 20170551. DOI: 10.1098/rspa.2017.0551.
- [39] Das Sarma S, Deng D L, Duan L M. Machine learning meets quantum physics[J/OL]. *Physics Today*, 2019, 72(3): 48-54. DOI: 10.1063/PT.3.4164.
- [40] Schuld M, Petruccione F. *Machine Learning with Quantum Computers*[M]. Second ed. Switzerland: Springer, 2021.
- [41] Carleo G, Troyer M. Solving the quantum many-body problem with artificial neural networks [J/OL]. *Science*, 2017, 355(6325): 602-606. DOI: 10.1126/science.aag2302.
- [42] Torlai G, Mazzola G, Carrasquilla J, et al. Neural-network quantum state tomography[J/OL]. *Nature Physics*, 2018, 14(5): 447-450. DOI: 10.1038/s41567-018-0048-5.
- [43] Nomura Y, Darmawan A S, Yamaji Y, et al. Restricted Boltzmann machine learning for solving strongly correlated quantum systems[J/OL]. *Physical Review B*, 2017, 96(20): 205152. DOI: 10.1103/PhysRevB.96.205152.
- [44] You Y Z, Yang Z, Qi X L. Machine learning spatial geometry from entanglement features [J/OL]. *Physical Review B*, 2018, 97(4): 045153. DOI: 10.1103/PhysRevB.97.045153.
- [45] Deng D L, Li X, Das Sarma S. Machine learning topological states[J/OL]. *Physical Review B*, 2017, 96(19): 195145. DOI: 10.1103/PhysRevB.96.195145.
- [46] Deng D L. Machine Learning Detection of Bell Nonlocality in Quantum Many-Body Systems [J/OL]. *Physical Review Letters*, 2018, 120(24): 240402. DOI: 10.1103/PhysRevLett.120.240402.
- [47] Deng D L, Li X, Das Sarma S. Quantum Entanglement in Neural Network States[J/OL]. *Physical Review X*, 2017, 7(2): 021021. DOI: 10.1103/PhysRevX.7.021021.
- [48] Gao X, Duan L M. Efficient representation of quantum many-body states with deep neural networks[J/OL]. *Nature Communications*, 2017, 8(1): 1-6. DOI: 10.1038/s41467-017-00705-2.
- [49] Melko R G, Carleo G, Carrasquilla J, et al. Restricted Boltzmann machines in quantum physics [J/OL]. *Nature Physics*, 2019, 15(9): 887-892. DOI: 10.1038/s41567-019-0545-1.
- [50] Ch'ng K, Carrasquilla J, Melko R G, et al. Machine Learning Phases of Strongly Correlated Fermions[J/OL]. *Physical Review X*, 2017, 7(3): 031038. DOI: 10.1103/PhysRevX.7.031038.
- [51] Wang L. Discovering phase transitions with unsupervised learning[J/OL]. *Physical Review B*, 2016, 94(19): 195105. DOI: 10.1103/PhysRevB.94.195105.
- [52] Harrow A W, Hassidim A, Lloyd S. Quantum Algorithm for Linear Systems of Equations[J/OL]. *Physical Review Letters*, 2009, 103(15): 150502. DOI: 10.1103/PhysRevLett.103.150502.

REFERENCES

- [53] Lloyd S, Mohseni M, Rebentrost P. Quantum principal component analysis[J/OL]. *Nature Physics*, 2014, 10(9): 631-633. DOI: 10.1038/nphys3029.
- [54] Dunjko V, Taylor J M, Briegel H J. Quantum-Enhanced Machine Learning[J/OL]. *Physical Review Letters*, 2016, 117(13): 130501. DOI: 10.1103/PhysRevLett.117.130501.
- [55] Amin M H, Andriyash E, Rolfe J, et al. Quantum Boltzmann Machine[J/OL]. *Physical Review X*, 2018, 8(2): 021050. DOI: 10.1103/PhysRevX.8.021050.
- [56] Gao X, Zhang Z Y, Duan L M. A quantum machine learning algorithm based on generative models[J/OL]. *Science Advances*, 2018, 4(12): eaat9004. DOI: 10.1126/sciadv.aat9004.
- [57] Lloyd S, Weedbrook C. Quantum Generative Adversarial Learning[J/OL]. *Physical Review Letters*, 2018, 121(4): 040502. DOI: 10.1103/PhysRevLett.121.040502.
- [58] Hu L, Wu S H, Cai W, et al. Quantum generative adversarial learning in a superconducting quantum circuit[J/OL]. *Science Advances*, 2019, 5(1): eaav2761. DOI: 10.1126/sciadv.aav2761.
- [59] Schuld M, Killoran N. Quantum Machine Learning in Feature Hilbert Spaces[J/OL]. *Physical Review Letters*, 2019, 122(4): 040504. DOI: 10.1103/PhysRevLett.122.040504.
- [60] Preskill J. Quantum Computing in the NISQ era and beyond[J/OL]. *Quantum*, 2018, 2: 79. DOI: 10.22331/q-2018-08-06-79.
- [61] Datta S. Quantum Transport: Atom to Transistor[M]. Cambridge University Press, 2005.
- [62] Kopnin N. Theory of Nonequilibrium Superconductivity[M/OL]. Oxford: Oxford University Press, 2001. <https://doi.org/10.1093/acprof:oso/9780198507888.001.0001>.
- [63] Sonin E B. Spin currents and spin superfluidity[J/OL]. *Advances in Physics*, 2010, 59(3): 181-255. DOI: 10.1080/00018731003739943.
- [64] Awschalom D D, Bassett L C, Dzurak A S, et al. Quantum Spintronics: Engineering and Manipulating Atom-Like Spins in Semiconductors[J/OL]. *Science*, 2013. DOI: 10.1126/science.1231364.
- [65] Baltz V, Manchon A, Tsoi M, et al. Antiferromagnetic spintronics[J/OL]. *Reviews of Modern Physics*, 2018, 90(1): 015005. DOI: 10.1103/RevModPhys.90.015005.
- [66] Lu Z, Shen P X, Deng D L. Markovian Quantum Neuroevolution for Machine Learning[J/OL]. *Physical Review Applied*, 2021, 16(4): 044039. DOI: 10.1103/PhysRevApplied.16.044039.
- [67] Shen P X, Hoffman S, Trif M. Theory of topological spin Josephson junctions[J/OL]. *Physical Review Research*, 2021, 3(1): 013003. DOI: 10.1103/PhysRevResearch.3.013003.
- [68] Laflamme C, Budich J C, Zoller P, et al. Non-equilibrium 8π Josephson effect in atomic Kitaev wires[J/OL]. *Nature Communications*, 2016, 7(1): 1-7. DOI: 10.1038/ncomms12280.
- [69] Sachdev S. Quantum Phase Transitions[M/OL]. Second ed. Cambridge: Cambridge University Press, 2011. <https://doi.org/10.1017/CBO9780511973765>.
- [70] Shen P X. Quantum Machine Learning and Information Processing[EB/OL]. 2022. <https://github.com/peixinshen/PhD-Thesis-Source-Code>.
- [71] Benioff P. The computer as a physical system: A microscopic quantum mechanical Hamiltonian model of computers as represented by Turing machines[J/OL]. *Journal of Statistical Physics*, 1980, 22(5): 563-591. DOI: 10.1007/BF01011339.

REFERENCES

- [72] Farhi E, Goldstone J, Gutmann S, et al. A Quantum Adiabatic Evolution Algorithm Applied to Random Instances of an NP-Complete Problem[J/OL]. *Science*, 2001, 292(5516): 472-475. DOI: 10.1126/science.1057726.
- [73] Raussendorf R, Briegel H J. A One-Way Quantum Computer[J/OL]. *Physical Review Letters*, 2001, 86(22): 5188-5191. DOI: 10.1103/PhysRevLett.86.5188.
- [74] Watrous J. On one-dimensional quantum cellular automata[C/OL]//*Proceedings of IEEE 36th Annual Foundations of Computer Science*. 1995: 528-537. DOI: 10.1109/SFCS.1995.492583.
- [75] Boykin P, Mor T, Pulver M, et al. On universal and fault-tolerant quantum computing: A novel basis and a new constructive proof of universality for Shor's basis[C/OL]//*40th Annual Symposium on Foundations of Computer Science (Cat. No.99CB37039)*. 1999: 486-494. DOI: 10.1109/SFCS.1999.814621.
- [76] Gottesman D E. Stabilizer Codes and Quantum Error Correction[D/OL]. *California Institute of Technology*, 1997. DOI: 10.7907/rzr7-dt72.
- [77] DiVincenzo D P. The Physical Implementation of Quantum Computation[J/OL]. *Fortschritte der Physik*, 2000, 48(9-11): 771-783. <https://onlinelibrary.wiley.com/doi/abs/10.1002/1521-3978%28200009%2948%3A9%3C771%3A%3AAID-PROP771%3E3.0.CO%3B2-E>.
- [78] Houck A A, Koch J, Devoret M H, et al. Life after charge noise: Recent results with transmon qubits[J/OL]. *Quantum Information Processing*, 2009, 8(2): 105-115. DOI: 10.1007/s11128-009-0100-6.
- [79] Barends R, Kelly J, Megrant A, et al. Coherent Josephson Qubit Suitable for Scalable Quantum Integrated Circuits[J/OL]. *Physical Review Letters*, 2013, 111(8): 080502. DOI: 10.1103/PhysRevLett.111.080502.
- [80] Cirac J I, Zoller P. Quantum Computations with Cold Trapped Ions[J/OL]. *Physical Review Letters*, 1995, 74(20): 4091-4094. DOI: 10.1103/PhysRevLett.74.4091.
- [81] Leibfried D, Blatt R, Monroe C, et al. Quantum dynamics of single trapped ions[J/OL]. *Reviews of Modern Physics*, 2003, 75(1): 281-324. DOI: 10.1103/RevModPhys.75.281.
- [82] Blatt R, Wineland D. Entangled states of trapped atomic ions[J/OL]. *Nature*, 2008, 453(7198): 1008-1015. DOI: 10.1038/nature07125.
- [83] Häffner H, Roos C F, Blatt R. Quantum computing with trapped ions[J/OL]. *Physics Reports*, 2008, 469(4): 155-203. DOI: 10.1016/j.physrep.2008.09.003.
- [84] Blatt R, Roos C F. Quantum simulations with trapped ions[J/OL]. *Nature Physics*, 2012, 8(4): 277-284. DOI: 10.1038/nphys2252.
- [85] Imamoglu A, Awschalom D D, Burkard G, et al. Quantum Information Processing Using Quantum Dot Spins and Cavity QED[J/OL]. *Physical Review Letters*, 1999, 83(20): 4204-4207. DOI: 10.1103/PhysRevLett.83.4204.
- [86] Petta J R, Johnson A C, Taylor J M, et al. Coherent Manipulation of Coupled Electron Spins in Semiconductor Quantum Dots[J/OL]. *Science*, 2005. DOI: 10.1126/science.1116955.
- [87] Englund D, Fattal D, Waks E, et al. Controlling the Spontaneous Emission Rate of Single Quantum Dots in a Two-Dimensional Photonic Crystal[J/OL]. *Physical Review Letters*, 2005, 95(1): 013904. DOI: 10.1103/PhysRevLett.95.013904.

REFERENCES

- [88] Hanson R, Kouwenhoven L P, Petta J R, et al. Spins in few-electron quantum dots[J/OL]. *Reviews of Modern Physics*, 2007, 79(4): 1217-1265. DOI: 10.1103/RevModPhys.79.1217.
- [89] Kane B E. A silicon-based nuclear spin quantum computer[J/OL]. *Nature*, 1998, 393(6681): 133-137. DOI: 10.1038/30156.
- [90] Vrijen R, Yablonovitch E, Wang K, et al. Electron-spin-resonance transistors for quantum computing in silicon-germanium heterostructures[J/OL]. *Physical Review A*, 2000, 62(1): 012306. DOI: 10.1103/PhysRevA.62.012306.
- [91] de Sousa R, Delgado J D, Das Sarma S. Silicon quantum computation based on magnetic dipolar coupling[J/OL]. *Physical Review A*, 2004, 70(5): 052304. DOI: 10.1103/PhysRevA.70.052304.
- [92] Hollenberg L C L, Greentree A D, Fowler A G, et al. Two-dimensional architectures for donor-based quantum computing[J/OL]. *Physical Review B*, 2006, 74(4): 045311. DOI: 10.1103/PhysRevB.74.045311.
- [93] Morello A, Pla J J, Zwanenburg F A, et al. Single-shot readout of an electron spin in silicon[J/OL]. *Nature*, 2010, 467(7316): 687-691. DOI: 10.1038/nature09392.
- [94] Jaksch D, Zoller P. The cold atom Hubbard toolbox[J/OL]. *Annals of Physics*, 2005, 315(1): 52-79. DOI: 10.1016/j.aop.2004.09.010.
- [95] Lewenstein M, Sanpera A, Ahufinger V, et al. Ultracold atomic gases in optical lattices: Mimicking condensed matter physics and beyond[J/OL]. *Advances in Physics*, 2007, 56(2): 243-379. DOI: 10.1080/00018730701223200.
- [96] Bloch I, Dalibard J, Zwierger W. Many-body physics with ultracold gases[J/OL]. *Reviews of Modern Physics*, 2008, 80(3): 885-964. DOI: 10.1103/RevModPhys.80.885.
- [97] Gross C, Bloch I. Quantum simulations with ultracold atoms in optical lattices[J/OL]. *Science*, 2017. DOI: 10.1126/science.aal3837.
- [98] Dutt M V G, Childress L, Jiang L, et al. Quantum Register Based on Individual Electronic and Nuclear Spin Qubits in Diamond[J/OL]. *Science*, 2007. DOI: 10.1126/science.1139831.
- [99] Knill E, Laflamme R, Milburn G J. A scheme for efficient quantum computation with linear optics[J/OL]. *Nature*, 2001, 409(6816): 46-52. DOI: 10.1038/35051009.
- [100] Pittman T B, Jacobs B C, Franson J D. Probabilistic quantum logic operations using polarizing beam splitters[J/OL]. *Physical Review A*, 2001, 64(6): 062311. DOI: 10.1103/PhysRevA.64.062311.
- [101] Franson J D, Donegan M M, Fitch M J, et al. High-Fidelity Quantum Logic Operations Using Linear Optical Elements[J/OL]. *Physical Review Letters*, 2002, 89(13): 137901. DOI: 10.1103/PhysRevLett.89.137901.
- [102] Nayak C, Simon S H, Stern A, et al. Non-Abelian anyons and topological quantum computation[J/OL]. *Reviews of Modern Physics*, 2008, 80(3): 1083-1159. DOI: 10.1103/RevModPhys.80.1083.
- [103] Avella A, Mancini F. *Springer Series in Solid-State Sciences: Strongly Correlated Systems: Theoretical Methods*[M/OL]. Berlin Heidelberg: Springer-Verlag, 2012. DOI: 10.1007/978-3-642-21831-6.

REFERENCES

- [104] Bruus H, Flensberg K. Many-Body Quantum Theory in Condensed Matter Physics: An Introduction[M]. Oxford ; New York: Oxford University Press, 2004.
- [105] Avella A, Mancini F. Springer Series in Solid-State Sciences: Strongly Correlated Systems: Numerical Methods[M/OL]. Berlin Heidelberg: Springer-Verlag, 2013. DOI: 10.1007/978-3-642-35106-8.
- [106] Jordan P, Wigner E P. About the Pauli exclusion principle[J/OL]. Zeitschrift fUr Physik, 1928, 47: 631-651. DOI: 10.1007/978-3-662-02781-3_9.
- [107] Karbach M, Hu K, Müller G. Introduction to the Bethe Ansatz II[J/OL]. Computers in Physics, 1998, 12(6): 565-573. DOI: 10.1063/1.168740.
- [108] Tserkovnyak Y, Loss D. Universal quantum computation with ordered spin-chain networks [J/OL]. Physical Review A, 2011, 84(3): 032333. DOI: 10.1103/PhysRevA.84.032333.
- [109] IBM Research C. IBM Quantum[EB/OL]. 2021. <https://quantum-computing.ibm.com/>.
- [110] Stenger J P T, Bronn N T, Egger D J, et al. Simulating the dynamics of braiding of Majorana zero modes using an IBM quantum computer[J/OL]. Physical Review Research, 2021, 3(3): 033171. DOI: 10.1103/PhysRevResearch.3.033171.
- [111] Giamarchi T. Quantum Physics in One Dimension[M/OL]. Oxford: Oxford University Press, 2003. <https://oxford.universitypressscholarship.com/view/10.1093/acprof:oso/9780198525004.001.0001/acprof-9780198525004>.
- [112] Essler F H L. The One-Dimensional Hubbard Model[M]. First ed. Cambridge: Cambridge University Press, 2010.
- [113] Ginzburg V L, Landau L D. On the Theory of Superconductivity[M/OL]//Ginzburg V L. On Superconductivity and Superfluidity: A Scientific Autobiography. Berlin, Heidelberg: Springer, 2009: 113-137. DOI: 10.1007/978-3-540-68008-6_4.
- [114] Tsui D C, Stormer H L, Gossard A C. Two-Dimensional Magnetotransport in the Extreme Quantum Limit[J/OL]. Physical Review Letters, 1982, 48(22): 1559-1562. DOI: 10.1103/PhysRevLett.48.1559.
- [115] Bednorz J G, Müller K A. Possible highTc superconductivity in the Ba-La-Cu-O system[J/OL]. Zeitschrift für Physik B Condensed Matter, 1986, 64(2): 189-193. DOI: 10.1007/BF01303701.
- [116] Wen X G, Wilczek F, Zee A. Chiral spin states and superconductivity[J/OL]. Physical Review B, 1989, 39(16): 11413-11423. DOI: 10.1103/PhysRevB.39.11413.
- [117] Wen X G. Topological orders in rigid states[J/OL]. International Journal of Modern Physics B, 1990, 04(02): 239-271. DOI: 10.1142/S0217979290000139.
- [118] Armstrong M A. Basic Topology[M]. First ed. New York: Springer, 1983.
- [119] Hasan M Z, Kane C L. Colloquium: Topological insulators[J/OL]. Reviews of Modern Physics, 2010, 82(4): 3045-3067. DOI: 10.1103/RevModPhys.82.3045.
- [120] Qi X L, Zhang S C. Topological insulators and superconductors[J/OL]. Reviews of Modern Physics, 2011, 83(4): 1057-1110. DOI: 10.1103/RevModPhys.83.1057.
- [121] Chiu C K, Teo J C Y, Schnyder A P, et al. Classification of topological quantum matter with symmetries[J/OL]. Reviews of Modern Physics, 2016, 88(3): 035005. DOI: 10.1103/RevModPhys.88.035005.

REFERENCES

- [122] Wen X G. Colloquium: Zoo of quantum-topological phases of matter[J/OL]. *Reviews of Modern Physics*, 2017, 89(4): 041004. DOI: 10.1103/RevModPhys.89.041004.
- [123] Zeng B, Chen X, Zhou D L, et al. *Quantum Science and Technology: Quantum Information Meets Quantum Matter: From Quantum Entanglement to Topological Phases of Many-Body Systems*[M/OL]. New York: Springer-Verlag, 2019. DOI: 10.1007/978-1-4939-9084-9.
- [124] Kitaev A. Periodic table for topological insulators and superconductors[J/OL]. *AIP Conference Proceedings*, 2009, 1134(1): 22-30. DOI: 10.1063/1.3149495.
- [125] Schnyder A P, Ryu S, Furusaki A, et al. Classification of topological insulators and superconductors in three spatial dimensions[J/OL]. *Physical Review B*, 2008, 78(19): 195125. DOI: 10.1103/PhysRevB.78.195125.
- [126] Ryu S, Schnyder A P, Furusaki A, et al. Topological insulators and superconductors: Tenfold way and dimensional hierarchy[J/OL]. *New Journal of Physics*, 2010, 12(6): 065010. DOI: 10.1088/1367-2630/12/6/065010.
- [127] Chen X, Gu Z C, Liu Z X, et al. Symmetry-Protected Topological Orders in Interacting Bosonic Systems[J/OL]. *Science*, 2012, 338(6114): 1604-1606. DOI: 10.1126/science.1227224.
- [128] Chen X, Gu Z C, Liu Z X, et al. Symmetry protected topological orders and the group cohomology of their symmetry group[J/OL]. *Physical Review B*, 2013, 87(15): 155114. DOI: 10.1103/PhysRevB.87.155114.
- [129] Ludwig A W W. Topological phases: Classification of topological insulators and superconductors of non-interacting fermions, and beyond[J/OL]. *Physica Scripta*, 2015, T168: 014001. DOI: 10.1088/0031-8949/2015/T168/014001.
- [130] Kane C L. Topological Band Theory and the \mathbb{Z}_2 Invariant[M]//*Contemporary Concepts of Condensed Matter Science: volume 6*. Elsevier, 2013: 3-34.
- [131] Bernevig B A, Hughes T L. *Topological Insulators and Topological Superconductors*[M]. Princeton: Princeton University Press, 2013.
- [132] Asbóth J K, Oroszlány L, Pályi A. *Lecture Notes in Physics: A Short Course on Topological Insulators: Band Structure and Edge States in One and Two Dimensions*[M/OL]. Springer International Publishing, 2016. DOI: 10.1007/978-3-319-25607-8.
- [133] Beenakker C. Search for Majorana fermions in superconductors[J/OL]. *Annual Review of Condensed Matter Physics*, 2013, 4(1): 113-136. DOI: 10.1146/annurev-conmatphys-030212-184337.
- [134] Alicea J, Oreg Y, Refael G, et al. Non-Abelian statistics and topological quantum information processing in 1D wire networks[J/OL]. *Nature Physics*, 2011, 7(5): 412-417. DOI: 10.1038/nphys1915.
- [135] Leijnse M, Flensberg K. Introduction to topological superconductivity and Majorana fermions[J/OL]. *Semiconductor Science and Technology*, 2012, 27(12): 124003. DOI: 10.1088/0268-1242/27/12/124003.
- [136] Kitaev A Y. Unpaired Majorana fermions in quantum wires[J/OL]. *Physics-Uspekhi*, 2001, 44 (10S): 131-136. DOI: 10.1070/1063-7869/44/10S/S29.

REFERENCES

- [137] Oreg Y, Refael G, von Oppen F. Helical Liquids and Majorana Bound States in Quantum Wires [J/OL]. *Physical Review Letters*, 2010, 105(17): 177002. DOI: 10.1103/PhysRevLett.105.177002.
- [138] Lutchyn R M, Sau J D, Das Sarma S. Majorana Fermions and a Topological Phase Transition in Semiconductor-Superconductor Heterostructures[J/OL]. *Physical Review Letters*, 2010, 105(7): 077001. DOI: 10.1103/PhysRevLett.105.077001.
- [139] Mourik V, Zuo K, Frolov S M, et al. Signatures of Majorana Fermions in Hybrid Superconductor-Semiconductor Nanowire Devices[J/OL]. *Science*, 2012, 336(6084): 1003-1007. DOI: 10.1126/science.1222360.
- [140] Kauffman L H. Majorana Fermions and representations of the braid group[J/OL]. *International Journal of Modern Physics A*, 2018, 33(23): 1830023. DOI: 10.1142/S0217751X18300235.
- [141] Das Sarma S, Freedman M, Nayak C. Majorana zero modes and topological quantum computation[J/OL]. *npj Quantum Information*, 2015, 1(1): 1-13. DOI: 10.1038/npjqi.2015.1.
- [142] Pan H, Das Sarma S. Physical mechanisms for zero-bias conductance peaks in Majorana nanowires[J/OL]. *Physical Review Research*, 2020, 2(1): 013377. DOI: 10.1103/PhysRevResearch.2.013377.
- [143] Altland A, Zirnbauer M R. Nonstandard symmetry classes in mesoscopic normal-superconducting hybrid structures[J/OL]. *Physical Review B*, 1997, 55(2): 1142-1161. DOI: 10.1103/PhysRevB.55.1142.
- [144] Kennedy R, Zirnbauer M R. Bott Periodicity for \mathbb{Z}_2 Symmetric Ground States of Gapped Free-Fermion Systems[J/OL]. *Communications in Mathematical Physics*, 2016, 342(3): 909-963. DOI: 10.1007/s00220-015-2512-8.
- [145] Seeley J T, Richard M J, Love P J. The Bravyi-Kitaev transformation for quantum computation of electronic structure[J/OL]. *The Journal of Chemical Physics*, 2012, 137(22): 224109. DOI: 10.1063/1.4768229.
- [146] Tranter A, Love P J, Mintert F, et al. A Comparison of the Bravyi-Kitaev and Jordan-Wigner Transformations for the Quantum Simulation of Quantum Chemistry[J/OL]. *Journal of Chemical Theory and Computation*, 2018, 14(11): 5617-5630. DOI: 10.1021/acs.jctc.8b00450.
- [147] McArdle S, Endo S, Aspuru-Guzik A, et al. Quantum computational chemistry[J/OL]. *Reviews of Modern Physics*, 2020, 92(1): 015003. DOI: 10.1103/RevModPhys.92.015003.
- [148] McClean J R, Rubin N C, Sung K J, et al. OpenFermion: The electronic structure package for quantum computers[J/OL]. *Quantum Science and Technology*, 2020, 5(3): 034014. DOI: 10.1088/2058-9565/ab8ebc.
- [149] Bethe H. Zur Theorie der Metalle[J/OL]. *Zeitschrift für Physik*, 1931, 71(3): 205-226. DOI: 10.1007/BF01341708.
- [150] Karabach M, Müller G, Gould H, et al. Introduction to the Bethe Ansatz I[J/OL]. *Computers in Physics*, 1997, 11(1): 36-43. DOI: 10.1063/1.4822511.
- [151] Wolfram Research I. Mathematica, Version 13.0[EB/OL]. Champaign, Illinois, 2021. <https://www.wolfram.com/mathematica>.

REFERENCES

- [152] Kramers H A, Wannier G H. Statistics of the Two-Dimensional Ferromagnet. Part I[J/OL]. Physical Review, 1941, 60(3): 252-262. DOI: 10.1103/PhysRev.60.252.
- [153] Kramers H A, Wannier G H. Statistics of the Two-Dimensional Ferromagnet. Part II[J/OL]. Physical Review, 1941, 60(3): 263-276. DOI: 10.1103/PhysRev.60.263.
- [154] Huang K. Statistical Mechanics[M]. Second ed. New York: Wiley, 1987.
- [155] Yang C N. The Spontaneous Magnetization of a Two-Dimensional Ising Model[J/OL]. Physical Review, 1952, 85(5): 808-816. DOI: 10.1103/PhysRev.85.808.
- [156] Onsager L. Crystal Statistics. I. A Two-Dimensional Model with an Order-Disorder Transition [J/OL]. Physical Review, 1944, 65(3-4): 117-149. DOI: 10.1103/PhysRev.65.117.
- [157] Kaufman B. Crystal Statistics. II. Partition Function Evaluated by Spinor Analysis[J/OL]. Physical Review, 1949, 76(8): 1232-1243. DOI: 10.1103/PhysRev.76.1232.
- [158] Liu Z, Yu L W, Duan L M, et al. The Presence and Absence of Barren Plateaus in Tensor-network Based Machine Learning[EB/OL]. 2021. <http://arxiv.org/abs/2108.08312>.
- [159] Baxter R J. Exactly Solved Models in Statistical Mechanics[M]. Elsevier, 2016.
- [160] Scully M O, Zubairy M S. Quantum Optics[M]. First ed. Cambridge University Press, 1997.
- [161] Blais A, Huang R S, Wallraff A, et al. Cavity quantum electrodynamics for superconducting electrical circuits: An architecture for quantum computation[J/OL]. Physical Review A, 2004, 69(6): 062320. DOI: 10.1103/PhysRevA.69.062320.
- [162] Dmytruk O, Trif M, Simon P. Cavity quantum electrodynamics with mesoscopic topological superconductors[J/OL]. Physical Review B, 2015, 92(24): 245432. DOI: 10.1103/PhysRevB.92.245432.
- [163] Trif M, Simon P. Braiding of Majorana Fermions in a Cavity[J/OL]. Physical Review Letters, 2019, 122(23): 236803. DOI: 10.1103/PhysRevLett.122.236803.
- [164] Clerk A A, Devoret M H, Girvin S M, et al. Introduction to quantum noise, measurement, and amplification[J/OL]. Reviews of Modern Physics, 2010, 82(2): 1155-1208. DOI: 10.1103/RevModPhys.82.1155.
- [165] Kjaergaard M, Schwartz M E, Braumüller J, et al. Superconducting Qubits: Current State of Play[J/OL]. Annual Review of Condensed Matter Physics, 2020, 11(1): 369-395. DOI: 10.1146/annurev-conmatphys-031119-050605.
- [166] Zheng M C, Christodoulides D N, Fleischmann R, et al. \mathcal{PT} optical lattices and universality in beam dynamics[J/OL]. Physical Review A, 2010, 82(1): 010103. DOI: 10.1103/PhysRevA.82.010103.
- [167] Longhi S. \mathcal{PT} -symmetric laser absorber[J/OL]. Physical Review A, 2010, 82(3): 031801. DOI: 10.1103/PhysRevA.82.031801.
- [168] Chong Y D, Ge L, Cao H, et al. Coherent Perfect Absorbers: Time-Reversed Lasers[J/OL]. Physical Review Letters, 2010, 105(5): 053901. DOI: 10.1103/PhysRevLett.105.053901.
- [169] San-Jose P, Cayao J, Prada E, et al. Majorana bound states from exceptional points in non-topological superconductors[J/OL]. Scientific Reports, 2016, 6: 21427. DOI: 10.1038/srep21427.

REFERENCES

- [170] Denner M M, Skurativska A, Schindler F, et al. Exceptional topological insulators[J/OL]. *Nature Communications*, 2021, 12(1): 5681. DOI: 10.1038/s41467-021-25947-z.
- [171] Puel T O, Chesi S, Kirchner S, et al. Nonequilibrium phases and phase transitions of the XY model[J/OL]. *Physical Review B*, 2021, 103(3): 035108. DOI: 10.1103/PhysRevB.103.035108.
- [172] Lindblad G. On the generators of quantum dynamical semigroups[J/OL]. *Communications in Mathematical Physics*, 1976, 48(2): 119-130. DOI: 10.1007/BF01608499.
- [173] Manzano D. A short introduction to the Lindblad master equation[J/OL]. *AIP Advances*, 2020, 10(2): 025106. DOI: 10.1063/1.5115323.
- [174] Bergholtz E J, Budich J C, Kunst F K. Exceptional topology of non-Hermitian systems[J/OL]. *Reviews of Modern Physics*, 2021, 93(1): 015005. DOI: 10.1103/RevModPhys.93.015005.
- [175] Kawabata K, Shiozaki K, Ueda M, et al. Symmetry and Topology in Non-Hermitian Physics [J/OL]. *Physical Review X*, 2019, 9(4): 041015. DOI: 10.1103/PhysRevX.9.041015.
- [176] Mitchell T M. *Machine Learning*[M]. First ed. New York: McGraw-Hill Education, 1997.
- [177] Hinton G, Deng L, Yu D, et al. Deep Neural Networks for Acoustic Modeling in Speech Recognition: The Shared Views of Four Research Groups[J/OL]. *IEEE Signal Processing Magazine*, 2012, 29(6): 82-97. DOI: 10.1109/MSP.2012.2205597.
- [178] Ball N M, Brunner R J. Data Mining and Machine Learning in Astronomy[J/OL]. *International Journal of Modern Physics D*, 2012. DOI: 10.1142/S0218271810017160.
- [179] Graff P, Feroz F, Hobson M P, et al. SkyNet: An efficient and robust neural network training tool for machine learning in astronomy[J/OL]. *Monthly Notices of the Royal Astronomical Society*, 2014, 441(2): 1741-1759. DOI: 10.1093/mnras/stu642.
- [180] Shen P X, Gu W M. Accretion disc–jet couplings in X-ray binaries[J/OL]. *Monthly Notices of the Royal Astronomical Society*, 2020, 495(2): 2408-2415. DOI: 10.1093/mnras/staa1349.
- [181] Pattnaik R, Sharma K, Alabarta K, et al. A machine-learning approach for classifying low-mass X-ray binaries based on their compact object nature[J/OL]. *Monthly Notices of the Royal Astronomical Society*, 2021, 501(3): 3457-3471. DOI: 10.1093/mnras/staa3899.
- [182] Sutton R S, Barto A G. *Reinforcement Learning, An Introduction*[M]. Second ed. Cambridge, Massachusetts: Bradford Books, 2018.
- [183] Schulman J, Wolski F, Dhariwal P, et al. Proximal Policy Optimization Algorithms[EB/OL]. 2017. <http://arxiv.org/abs/1707.06347>.
- [184] Watkins C J C H, Dayan P. Q-learning[J/OL]. *Machine Learning*, 1992, 8(3): 279-292. DOI: 10.1007/BF00992698.
- [185] Kober J, Bagnell J A, Peters J. Reinforcement learning in robotics: A survey[J/OL]. *International Journal of Robotics Research*, 2013, 32(11): 1238-1274. DOI: 10.1177/0278364913495721.
- [186] Grigorescu S, Trasnea B, Cocias T, et al. A survey of deep learning techniques for autonomous driving[J/OL]. *Journal of Field Robotics*, 2020, 37(3): 362-386. DOI: 10.1002/rob.21918.
- [187] Hopfield J J. Neural networks and physical systems with emergent collective computational abilities[J]. *Proceedings of the National Academy of Sciences*, 1982, 79(8): 2554-2558.

REFERENCES

- [188] Ackley D H, Hinton G E, Sejnowski T J. A Learning Algorithm for Boltzmann Machines[J/OL]. *Cognitive Science*, 1985, 9(1): 147-169. DOI: 10.1207/s15516709cog0901_7.
- [189] Hinton G E. A Practical Guide to Training Restricted Boltzmann Machines[M/OL]//Montavon G, Orr G B, Müller K R. *Neural Networks: Tricks of the Trade: volume 7700*. Berlin, Heidelberg: Springer Berlin Heidelberg, 2012: 599-619. DOI: 10.1007/978-3-642-35289-8_32.
- [190] Goodfellow I, Pouget-Abadie J, Mirza M, et al. Generative Adversarial Nets[J/OL]. *Advances in Neural Information Processing Systems*, 2014, 27: 2672-2680. <https://proceedings.neurips.cc/paper/2014/hash/5ca3e9b122f61f8f06494c97b1afccf3-Abstract.html>.
- [191] Kramer M A. Nonlinear principal component analysis using autoassociative neural networks [J/OL]. *AICHE Journal*, 1991, 37(2): 233-243. DOI: 10.1002/aic.690370209.
- [192] Hinton G E, Krizhevsky A, Wang S D. Transforming Auto-Encoders[C/OL]//Honkela T, Duch W, Girolami M, et al. *Lecture Notes in Computer Science: Artificial Neural Networks and Machine Learning – ICANN 2011*. Berlin, Heidelberg: Springer, 2011: 44-51. DOI: 10.1007/978-3-642-21735-7_6.
- [193] Sabour S, Frosst N, Hinton G E. Dynamic Routing Between Capsules[EB/OL]. 2017. <http://arxiv.org/abs/1710.09829>.
- [194] Vaswani A, Shazeer N, Parmar N, et al. Attention Is All You Need[EB/OL]. 2017. <http://arxiv.org/abs/1706.03762>.
- [195] LeCun Y, Cortes C, Burges C. MNIST handwritten digit database[EB/OL]. 1998. <http://yann.lecun.com/exdb/mnist/>.
- [196] Cho K, van Merriënboer B, Bahdanau D, et al. On the Properties of Neural Machine Translation: Encoder-Decoder Approaches[EB/OL]. 2014. <http://arxiv.org/abs/1409.1259>.
- [197] Hochreiter S, Schmidhuber J. Long Short-Term Memory[J/OL]. *Neural Computation*, 1997, 9 (8): 1735-1780. DOI: 10.1162/neco.1997.9.8.1735.
- [198] Brown T B, Mann B, Ryder N, et al. Language Models are Few-Shot Learners[EB/OL]. 2020. <http://arxiv.org/abs/2005.14165>.
- [199] Dosovitskiy A, Beyer L, Kolesnikov A, et al. An Image is Worth 16x16 Words: Transformers for Image Recognition at Scale[EB/OL]. 2021. <http://arxiv.org/abs/2010.11929>.
- [200] He K, Zhang X, Ren S, et al. Deep Residual Learning for Image Recognition[C/OL]//2016 IEEE Conference on Computer Vision and Pattern Recognition (CVPR). 2016: 770-778. DOI: 10.1109/CVPR.2016.90.
- [201] Liu Z, Shen P X, Li W, et al. Quantum Capsule Networks[EB/OL]. 2022. <http://arxiv.org/abs/2201.01778>.
- [202] Hinton G E, Sabour S, Frosst N. Matrix capsules with EM routing[C/OL]//International Conference on Learning Representations. Vancouver, BC, Canada, 2018. <https://openreview.net/forum?id=HJWLfGWrb¬eId=rk5MadsMf¬eId=rk5MadsMf>.
- [203] Géron A. *Hands-On Machine Learning with Scikit-Learn and TensorFlow: Concepts, Tools, and Techniques to Build Intelligent Systems*[M]. First ed. Beijing ; Boston: O'Reilly Media, 2017.

REFERENCES

- [204] Hughes J, van Dam A, McGuire M, et al. Computer Graphics: Principles and Practice[M]. Third ed. Upper Saddle River, New Jersey: Addison-Wesley Professional, 2013.
- [205] Roscher R, Bohn B, Duarte M F, et al. Explainable Machine Learning for Scientific Insights and Discoveries[J/OL]. IEEE Access, 2020, 8: 42200-42216. DOI: 10.1109/ACCESS.2020.2976199.
- [206] Iten R, Metger T, Wilming H, et al. Discovering physical concepts with neural networks[J/OL]. Physical Review Letters, 2020, 124(1): 010508. DOI: 10.1103/PhysRevLett.124.010508.
- [207] Krenn M. Physics Insights from Neural Networks[J/OL]. Physics, 2020, 13: 2. DOI: 10.1103/Physics.13.2.
- [208] Krenn M, Kottmann J S, Tischler N, et al. Conceptual Understanding through Efficient Automated Design of Quantum Optical Experiments[J/OL]. Physical Review X, 2021, 11(3): 031044. DOI: 10.1103/PhysRevX.11.031044.
- [209] Liu J, Tacchino F, Glick J R, et al. Representation Learning via Quantum Neural Tangent Kernels [EB/OL]. 2021. <http://arxiv.org/abs/2111.04225>.
- [210] Carleo G, Cirac I, Cranmer K, et al. Machine learning and the physical sciences[J/OL]. Reviews of Modern Physics, 2019, 91(4): 045002. DOI: 10.1103/RevModPhys.91.045002.
- [211] Jordan M I, Mitchell T M. Machine learning: Trends, perspectives, and prospects[J/OL]. Science, 2015, 349(6245): 255-260. DOI: 10.1126/science.aaa8415.
- [212] Senior A W, Evans R, Jumper J, et al. Improved protein structure prediction using potentials from deep learning[J/OL]. Nature, 2020, 577(7792): 706-710. DOI: 10.1038/s41586-019-1923-7.
- [213] Carrasquilla J, Torlai G, Melko R G, et al. Reconstructing quantum states with generative models [J/OL]. Nature Machine Intelligence, 2019, 1(3): 155-161. DOI: 10.1038/s42256-019-0028-1.
- [214] Zhang Y H, Zheng P L, Zhang Y, et al. Topological Quantum Compiling with Reinforcement Learning[J/OL]. Physical Review Letters, 2020, 125(17): 170501. DOI: 10.1103/PhysRevLett.125.170501.
- [215] Zhang Y, Kim E A. Quantum Loop Topography for Machine Learning[J/OL]. Physical Review Letters, 2017, 118(21): 216401. DOI: 10.1103/PhysRevLett.118.216401.
- [216] Carrasquilla J, Melko R G. Machine learning phases of matter[J/OL]. Nature Physics, 2017, 13(5): 431-434. DOI: 10.1038/nphys4035.
- [217] van Nieuwenburg E P L, Liu Y H, Huber S D. Learning phase transitions by confusion[J/OL]. Nature Physics, 2017, 13(5): 435-439. DOI: 10.1038/nphys4037.
- [218] Broecker P, Carrasquilla J, Melko R G, et al. Machine learning quantum phases of matter beyond the fermion sign problem[J/OL]. Scientific Reports, 2017, 7(1): 8823. DOI: 10.1038/s41598-017-09098-0.
- [219] Zhang Y, Melko R G, Kim E A. Machine learning \mathbb{Z}_2 quantum spin liquids with quasiparticle statistics[J/OL]. Physical Review B, 2017, 96(24): 245119. DOI: 10.1103/PhysRevB.96.245119.

REFERENCES

- [220] Wetzel S J. Unsupervised learning of phase transitions: From principal component analysis to variational autoencoders[J/OL]. *Physical Review E*, 2017, 96(2): 022140. DOI: 10.1103/PhysRevE.96.022140.
- [221] Hu W, Singh R R P, Scalettar R T. Discovering phases, phase transitions, and crossovers through unsupervised machine learning: A critical examination[J/OL]. *Physical Review E*, 2017, 95(6): 062122. DOI: 10.1103/PhysRevE.95.062122.
- [222] Zhang Y, Mesaros A, Fujita K, et al. Machine learning in electronic-quantum-matter imaging experiments[J/OL]. *Nature*, 2019, 570(7762): 484-490. DOI: 10.1038/s41586-019-1319-8.
- [223] Lian W, Wang S T, Lu S, et al. Machine Learning Topological Phases with a Solid-State Quantum Simulator[J/OL]. *Physical Review Letters*, 2019, 122(21): 210503. DOI: 10.1103/PhysRevLett.122.210503.
- [224] Jiang S, Lu S, Deng D L. Adversarial Machine Learning Phases of Matter[EB/OL]. 2021. <http://arxiv.org/abs/1910.13453>.
- [225] Shen P X, Jiang W J, Li W K, et al. Adversarial learning in quantum artificial intelligence[J/OL]. *Acta Physica Sinica*, 2021, 70(14): 140302-140302-12. DOI: 10.7498/aps.70.20210789.
- [226] Zhang S X, Hsieh C Y, Zhang S, et al. Differentiable Quantum Architecture Search[EB/OL]. 2021. <http://arxiv.org/abs/2010.08561>.
- [227] Anand A, Degroote M, Aspuru-Guzik A. Natural evolutionary strategies for variational quantum computation[J/OL]. *Machine Learning: Science and Technology*, 2021, 2(4): 045012. DOI: 10.1088/2632-2153/abf3ac.
- [228] Wang H, Ding Y, Gu J, et al. QuantumNAS: Noise-Adaptive Search for Robust Quantum Circuits[EB/OL]. 2022. DOI: 10.48550/arXiv.2107.10845.
- [229] Peruzzo A, McClean J, Shadbolt P, et al. A variational eigenvalue solver on a photonic quantum processor[J/OL]. *Nature Communications*, 2014, 5(1): 4213. DOI: 10.1038/ncomms5213.
- [230] McClean J R, Romero J, Babbush R, et al. The theory of variational hybrid quantum-classical algorithms[J/OL]. *New Journal of Physics*, 2016, 18(2): 023023. DOI: 10.1088/1367-2630/18/2/023023.
- [231] Moll N, Barkoutsos P, Bishop L S, et al. Quantum optimization using variational algorithms on near-term quantum devices[J/OL]. *Quantum Science and Technology*, 2018, 3(3): 030503. DOI: 10.1088/2058-9565/aab822.
- [232] Shor P W. Scheme for reducing decoherence in quantum computer memory[J/OL]. *Physical Review A*, 1995, 52(4): R2493-R2496. DOI: 10.1103/PhysRevA.52.R2493.
- [233] Lidar D A. Quantum Error Correction[M]. First ed. Cambridge, United Kingdom ; New York: Cambridge University Press, 2013.
- [234] Terhal B M. Quantum error correction for quantum memories[J/OL]. *Reviews of Modern Physics*, 2015, 87(2): 307-346. DOI: 10.1103/RevModPhys.87.307.
- [235] Bravyi S B, Kitaev A Y. Quantum codes on a lattice with boundary[EB/OL]. 1998. <http://arxiv.org/abs/quant-ph/9811052>.
- [236] Dennis E, Kitaev A, Landahl A, et al. Topological quantum memory[J/OL]. *Journal of Mathematical Physics*, 2002, 43(9): 4452-4505. DOI: 10.1063/1.1499754.

REFERENCES

- [237] Fowler A G, Mariantoni M, Martinis J M, et al. Surface codes: Towards practical large-scale quantum computation[J/OL]. *Physical Review A*, 2012, 86(3): 032324. DOI: 10.1103/PhysRevA.86.032324.
- [238] Bharti K, Cervera-Lierta A, Kyaw T H, et al. Noisy intermediate-scale quantum algorithms [J/OL]. *Reviews of Modern Physics*, 2022, 94(1): 015004. DOI: 10.1103/RevModPhys.94.015004.
- [239] Cerezo M, Arrasmith A, Babbush R, et al. Variational quantum algorithms[J/OL]. *Nature Reviews Physics*, 2021, 3(9): 625-644. DOI: 10.1038/s42254-021-00348-9.
- [240] Cirac J I, Zoller P. Goals and opportunities in quantum simulation[J/OL]. *Nature Physics*, 2012, 8(4): 264-266. DOI: 10.1038/nphys2275.
- [241] Hangleiter D, Carolan J, Thébault K P Y. Analogue Quantum Simulation: A New Instrument for Scientific Understanding[M]. Springer International Publishing, 2022.
- [242] Farhi E, Goldstone J, Gutmann S, et al. Quantum Computation by Adiabatic Evolution[EB/OL]. 2000. <http://arxiv.org/abs/quant-ph/0001106>.
- [243] Das A, Chakrabarti B K. Colloquium: Quantum annealing and analog quantum computation [J/OL]. *Reviews of Modern Physics*, 2008, 80(3): 1061-1081. DOI: 10.1103/RevModPhys.80.1061.
- [244] Suzuki M. Generalized Trotter's formula and systematic approximants of exponential operators and inner derivations with applications to many-body problems[J/OL]. *Communications in Mathematical Physics*, 1976, 51(2): 183-190. DOI: 10.1007/BF01609348.
- [245] Chong F T, Franklin D, Martonosi M. Programming languages and compiler design for realistic quantum hardware[J/OL]. *Nature*, 2017, 549(7671): 180-187. DOI: 10.1038/nature23459.
- [246] Heim B, Soeken M, Marshall S, et al. Quantum programming languages[J/OL]. *Nature Reviews Physics*, 2020, 2(12): 709-722. DOI: 10.1038/s42254-020-00245-7.
- [247] Lloyd S. Universal Quantum Simulators[J/OL]. *Science*, 1996, 273(5278): 1073-1078. DOI: 10.1126/science.273.5278.1073.
- [248] Lamata L, Parra-Rodriguez A, Sanz M, et al. Digital-analog quantum simulations with superconducting circuits[J/OL]. *Advances in Physics: X*, 2018, 3(1): 1457981. DOI: 10.1080/23746149.2018.1457981.
- [249] Prakash A. Quantum algorithms for linear algebra and machine learning[D/OL]. UC Berkeley, 2014. <https://escholarship.org/uc/item/5v9535q4>.
- [250] Lloyd S, Mohseni M, Rebentrost P. Quantum algorithms for supervised and unsupervised machine learning[EB/OL]. 2013. <http://arxiv.org/abs/1307.0411>.
- [251] Rebentrost P, Mohseni M, Lloyd S. Quantum Support Vector Machine for Big Data Classification[J/OL]. *Physical Review Letters*, 2014, 113(13): 130503. DOI: 10.1103/PhysRevLett.113.130503.
- [252] Aaronson S. Read the fine print[J/OL]. *Nature Physics*, 2015, 11(4): 291-293. DOI: 10.1038/nphys3272.
- [253] Giovannetti V, Lloyd S, Maccone L. Quantum Random Access Memory[J/OL]. *Physical Review Letters*, 2008, 100(16): 160501. DOI: 10.1103/PhysRevLett.100.160501.

REFERENCES

- [254] Berry D W, Ahokas G, Cleve R, et al. Efficient Quantum Algorithms for Simulating Sparse Hamiltonians[J/OL]. *Communications in Mathematical Physics*, 2007, 270(2): 359-371. DOI: 10.1007/s00220-006-0150-x.
- [255] Duan B, Yuan J, Yu C H, et al. A survey on HHL algorithm: From theory to application in quantum machine learning[J/OL]. *Physics Letters A*, 2020, 384(24): 126595. DOI: 10.1016/j.physleta.2020.126595.
- [256] Schuld M, Bocharov A, Svore K M, et al. Circuit-centric quantum classifiers[J/OL]. *Physical Review A*, 2020, 101(3): 032308. DOI: 10.1103/PhysRevA.101.032308.
- [257] Farhi E, Neven H. Classification with Quantum Neural Networks on Near Term Processors [EB/OL]. 2018. <http://arxiv.org/abs/1802.06002>.
- [258] Schuld M, Fingerhuth M, Petruccione F. Implementing a distance-based classifier with a quantum interference circuit[J/OL]. *EPL (Europhysics Letters)*, 2017, 119(6): 60002. DOI: 10.1209/0295-5075/119/60002.
- [259] Mitarai K, Negoro M, Kitagawa M, et al. Quantum circuit learning[J/OL]. *Physical Review A*, 2018, 98(3): 032309. DOI: 10.1103/PhysRevA.98.032309.
- [260] Havlíček V, Córcoles A D, Temme K, et al. Supervised learning with quantum-enhanced feature spaces[J/OL]. *Nature*, 2019, 567(7747): 209-212. DOI: 10.1038/s41586-019-0980-2.
- [261] Zhu D, Linke N M, Benedetti M, et al. Training of quantum circuits on a hybrid quantum computer[J/OL]. *Science Advances*, 2019, 5(10): eaaw9918. DOI: 10.1126/sciadv.aaw9918.
- [262] Cong I, Choi S, Lukin M D. Quantum convolutional neural networks[J/OL]. *Nature Physics*, 2019, 15(12): 1273-1278. DOI: 10.1038/s41567-019-0648-8.
- [263] Wan K H, Dahlsten O, Kristjánsson H, et al. Quantum generalisation of feedforward neural networks[J/OL]. *npj Quantum Information*, 2017, 3(1): 1-8. DOI: 10.1038/s41534-017-0032-4.
- [264] Grant E, Benedetti M, Cao S, et al. Hierarchical quantum classifiers[J/OL]. *npj Quantum Information*, 2018, 4(1): 1-8. DOI: 10.1038/s41534-018-0116-9.
- [265] Du Y, Hsieh M H, Liu T, et al. Implementable Quantum Classifier for Nonlinear Data[EB/OL]. 2018. <http://arxiv.org/abs/1809.06056>.
- [266] Uvarov A V, Kardashin A S, Biamonte J D. Machine learning phase transitions with a quantum processor[J/OL]. *Physical Review A*, 2020, 102(1): 012415. DOI: 10.1103/PhysRevA.102.012415.
- [267] Blank C, Park D K, Rhee J K K, et al. Quantum classifier with tailored quantum kernel[J/OL]. *npj Quantum Information*, 2020, 6(1): 1-7. DOI: 10.1038/s41534-020-0272-6.
- [268] Tacchino F, Macchiavello C, Gerace D, et al. An artificial neuron implemented on an actual quantum processor[J/OL]. *npj Quantum Information*, 2019, 5(1): 1-8. DOI: 10.1038/s41534-019-0140-4.
- [269] Kokail C, Maier C, van Bijnen R, et al. Self-verifying variational quantum simulation of lattice models[J/OL]. *Nature*, 2019, 569(7756): 355-360. DOI: 10.1038/s41586-019-1177-4.
- [270] Liu J G, Zhang Y H, Wan Y, et al. Variational quantum eigensolver with fewer qubits[J/OL]. *Physical Review Research*, 2019, 1(2): 023025. DOI: 10.1103/PhysRevResearch.1.023025.

REFERENCES

- [271] Wang D, Higgott O, Brierley S. Accelerated Variational Quantum Eigensolver[J/OL]. Physical Review Letters, 2019, 122(14): 140504. DOI: 10.1103/PhysRevLett.122.140504.
- [272] Liu J G, Wang L. Differentiable learning of quantum circuit Born machines[J/OL]. Physical Review A, 2018, 98(6): 062324. DOI: 10.1103/PhysRevA.98.062324.
- [273] Coyle B, Mills D, Danos V, et al. The Born supremacy: Quantum advantage and training of an Ising Born machine[J/OL]. npj Quantum Information, 2020, 6(1): 1-11. DOI: 10.1038/s41534-020-00288-9.
- [274] Farhi E, Goldstone J, Gutmann S. A Quantum Approximate Optimization Algorithm[EB/OL]. 2014. <http://arxiv.org/abs/1411.4028>.
- [275] Zhou L, Wang S T, Choi S, et al. Quantum Approximate Optimization Algorithm: Performance, Mechanism, and Implementation on Near-Term Devices[J/OL]. Physical Review X, 2020, 10(2): 021067. DOI: 10.1103/PhysRevX.10.021067.
- [276] Barak B. Work with what you've got[J/OL]. Nature Physics, 2021: 1-2. DOI: 10.1038/s41567-020-01126-7.
- [277] Harrigan M P, Sung K J, Neeley M, et al. Quantum approximate optimization of non-planar graph problems on a planar superconducting processor[J/OL]. Nature Physics, 2021: 1-5. DOI: 10.1038/s41567-020-01105-y.
- [278] Pagano G, Bapat A, Becker P, et al. Quantum approximate optimization of the long-range Ising model with a trapped-ion quantum simulator[J/OL]. Proceedings of the National Academy of Sciences, 2020, 117(41): 25396-25401. DOI: 10.1073/pnas.2006373117.
- [279] Li W, Deng D L. Recent advances for quantum classifiers[J/OL]. SCIENCE CHINA Physics, Mechanics & Astronomy, 2021, 65(2): 220301. DOI: 10.1007/s11433-021-1793-6.
- [280] Kandala A, Mezzacapo A, Temme K, et al. Hardware-efficient variational quantum eigensolver for small molecules and quantum magnets[J/OL]. Nature, 2017, 549(7671): 242-246. DOI: 10.1038/nature23879.
- [281] Beer K, Bondarenko D, Farrelly T, et al. Training deep quantum neural networks[J/OL]. Nature Communications, 2020, 11(1): 808. DOI: 10.1038/s41467-020-14454-2.
- [282] Killoran N, Bromley T R, Arrazola J M, et al. Continuous-variable quantum neural networks [J/OL]. Physical Review Research, 2019, 1(3): 033063. DOI: 10.1103/PhysRevResearch.1.033063.
- [283] Li J, Yang X, Peng X, et al. Hybrid Quantum-Classical Approach to Quantum Optimal Control [J/OL]. Physical Review Letters, 2017, 118(15): 150503. DOI: 10.1103/PhysRevLett.118.150503.
- [284] Schuld M, Bergholm V, Gogolin C, et al. Evaluating analytic gradients on quantum hardware [J/OL]. Physical Review A, 2019, 99(3): 032331. DOI: 10.1103/PhysRevA.99.032331.
- [285] Mari A, Bromley T R, Killoran N. Estimating the gradient and higher-order derivatives on quantum hardware[J/OL]. Physical Review A, 2021, 103(1): 012405. DOI: 10.1103/PhysRevA.103.012405.
- [286] Stokes J, Izaac J, Killoran N, et al. Quantum Natural Gradient[J/OL]. Quantum, 2020, 4: 269. DOI: 10.22331/q-2020-05-25-269.

REFERENCES

- [287] Türkpençe D, Akıncı T Ç, Şeker S. A steady state quantum classifier[J/OL]. *Physics Letters A*, 2019, 383(13): 1410-1418. DOI: 10.1016/j.physleta.2019.01.063.
- [288] Liu Z, Duan L M, Deng D L. Solving quantum master equations with deep quantum neural networks[J/OL]. *Physical Review Research*, 2022, 4(1): 013097. DOI: 10.1103/PhysRevResearch.4.013097.
- [289] Cheng S, Chen J, Wang L. Information Perspective to Probabilistic Modeling: Boltzmann Machines versus Born Machines[J/OL]. *Entropy*, 2018, 20(8): 583. DOI: 10.3390/e20080583.
- [290] Benedetti M, Garcia-Pintos D, Perdomo O, et al. A generative modeling approach for benchmarking and training shallow quantum circuits[J/OL]. *npj Quantum Information*, 2019, 5(1): 1-9. DOI: 10.1038/s41534-019-0157-8.
- [291] Karamlou A H, Simon W A, Katabarwa A, et al. Analyzing the performance of variational quantum factoring on a superconducting quantum processor[J/OL]. *npj Quantum Information*, 2021, 7(1): 1-6. DOI: 10.1038/s41534-021-00478-z.
- [292] Lubasch M, Joo J, Moinier P, et al. Variational quantum algorithms for nonlinear problems [J/OL]. *Physical Review A*, 2020, 101(1): 010301. DOI: 10.1103/PhysRevA.101.010301.
- [293] Xu X, Sun J, Endo S, et al. Variational algorithms for linear algebra[J/OL]. *Science Bulletin*, 2021, 66(21): 2181-2188. DOI: 10.1016/j.scib.2021.06.023.
- [294] Kyriienko O, Paine A E, Elfving V E. Solving nonlinear differential equations with differentiable quantum circuits[J/OL]. *Physical Review A*, 2021, 103(5): 052416. DOI: 10.1103/PhysRevA.103.052416.
- [295] Baldi P, Vershynin R. The capacity of feedforward neural networks[J/OL]. *Neural Networks*, 2019, 116: 288-311. DOI: 10.1016/j.neunet.2019.04.009.
- [296] Vapnik V N. *Statistical Learning Theory*[M]. First ed. New York: Wiley-Interscience, 1998.
- [297] Oppen M. Learning and generalization in a two-layer neural network: The role of the Vapnik-Chervonvenkis dimension[J/OL]. *Physical Review Letters*, 1994, 72(13): 2113-2116. DOI: 10.1103/PhysRevLett.72.2113.
- [298] Geiger D, Heckerman D, Meek C. Asymptotic Model Selection for Directed Networks with Hidden Variables[M/OL]//Jordan M I. *NATO ASI Series: Learning in Graphical Models*. Dordrecht: Springer Netherlands, 1998: 461-477. DOI: 10.1007/978-94-011-5014-9_16.
- [299] Zhang N L, Kocka T. Effective Dimensions of Hierarchical Latent Class Models[J/OL]. *Journal of Artificial Intelligence Research*, 2004, 21: 1-17. DOI: 10.1613/jair.1311.
- [300] Abbas A, Sutter D, Zoufal C, et al. The power of quantum neural networks[J/OL]. *Nature Computational Science*, 2021, 1(6): 403-409. DOI: 10.1038/s43588-021-00084-1.
- [301] Abbas A, Sutter D, Figalli A, et al. Effective dimension of machine learning models[EB/OL]. 2021. <http://arxiv.org/abs/2112.04807>.
- [302] Berezniuk O, Figalli A, Ghigliazza R, et al. A scale-dependent notion of effective dimension [EB/OL]. 2020. <http://arxiv.org/abs/2001.10872>.
- [303] Frieden B R. *Science from Fisher Information: A Unification*[M/OL]. Cambridge: Cambridge University Press, 2004. DOI: 10.1017/CBO9780511616907.

REFERENCES

- [304] Rissanen J J. Fisher information and stochastic complexity[J/OL]. IEEE Transactions on Information Theory, 1996, 42(1): 40-47. DOI: 10.1109/18.481776.
- [305] Grunwald P D. The Minimum Description Length Principle[M]. Cambridge: The MIT Press, 2007.
- [306] Amari S i. Natural Gradient Works Efficiently in Learning[J/OL]. Neural Computation, 1998, 10(2): 251-276. DOI: 10.1162/089976698300017746.
- [307] McClean J R, Boixo S, Smelyanskiy V N, et al. Barren plateaus in quantum neural network training landscapes[J/OL]. Nature Communications, 2018, 9(1): 4812. DOI: 10.1038/s41467-018-07090-4.
- [308] Cerezo M, Sone A, Volkoff T, et al. Cost function dependent barren plateaus in shallow parametrized quantum circuits[J/OL]. Nature Communications, 2021, 12(1): 1791. DOI: 10.1038/s41467-021-21728-w.
- [309] Arrasmith A, Cerezo M, Czarnik P, et al. Effect of barren plateaus on gradient-free optimization [J/OL]. Quantum, 2021, 5: 558. DOI: 10.22331/q-2021-10-05-558.
- [310] Patti T L, Najafi K, Gao X, et al. Entanglement devised barren plateau mitigation[J/OL]. Physical Review Research, 2021, 3(3): 033090. DOI: 10.1103/PhysRevResearch.3.033090.
- [311] Ortiz Marrero C, Kieferová M, Wiebe N. Entanglement-Induced Barren Plateaus[J/OL]. PRX Quantum, 2021, 2(4): 040316. DOI: 10.1103/PRXQuantum.2.040316.
- [312] Jiang W, Lu Z, Deng D L. Quantum Continual Learning Overcoming Catastrophic Forgetting [J/OL]. Chinese Physics Letters, 2022, 39(5): 50303. DOI: 10.1088/0256-307X/39/5/050303.
- [313] Pascanu R, Mikolov T, Bengio Y. On the difficulty of training recurrent neural networks[C/OL]// Proceedings of the 30th International Conference on Machine Learning. PMLR, 2013: 1310-1318. <https://proceedings.mlr.press/v28/pascanu13.html>.
- [314] Pesah A, Cerezo M, Wang S, et al. Absence of Barren Plateaus in Quantum Convolutional Neural Networks[J/OL]. Physical Review X, 2021, 11(4): 041011. DOI: 10.1103/PhysRevX.11.041011.
- [315] Chakraborty A, Alam M, Dey V, et al. Adversarial Attacks and Defences: A Survey[EB/OL]. 2018. <http://arxiv.org/abs/1810.00069>.
- [316] Kurakin A, Goodfellow I, Bengio S. Adversarial Machine Learning at Scale[EB/OL]. 2017. <http://arxiv.org/abs/1611.01236>.
- [317] Lu S, Duan L M, Deng D L. Quantum adversarial machine learning[J/OL]. Physical Review Research, 2020, 2(3): 033212. DOI: 10.1103/PhysRevResearch.2.033212.
- [318] Liu N, Wittek P. Vulnerability of quantum classification to adversarial perturbations[J/OL]. Physical Review A, 2020, 101(6): 062331. DOI: 10.1103/PhysRevA.101.062331.
- [319] Gong W, Deng D L. Universal Adversarial Examples and Perturbations for Quantum Classifiers [J/OL]. National Science Review, 2021: nwab130. DOI: 10.1093/nsr/nwab130.
- [320] Poland K, Beer K, Osborne T J. No Free Lunch for Quantum Machine Learning[EB/OL]. 2020. <http://arxiv.org/abs/2003.14103>.
- [321] Ledoux M. The Concentration of Measure Phenomenon[M]. Providence: American Mathematical Society, 2001.

REFERENCES

- [322] Stanley K O, Miikkulainen R. Evolving Neural Networks through Augmenting Topologies [J/OL]. *Evolutionary Computation*, 2002, 10(2): 99-127. DOI: 10.1162/106365602320169811.
- [323] Théveniaut H, van Nieuwenburg E. A NEAT quantum error decoder[J/OL]. *SciPost Physics*, 2021, 11(1): 005. DOI: 10.21468/SciPostPhys.11.1.005.
- [324] Stanley K O, Clune J, Lehman J, et al. Designing neural networks through neuroevolution [J/OL]. *Nature Machine Intelligence*, 2019, 1(1): 24-35. DOI: 10.1038/s42256-018-0006-z.
- [325] Wolberg W, Street N, Mangasarian O. UCI Machine Learning Repository: Breast Cancer Wisconsin (Diagnostic) Data Set[EB/OL]. 1992. [https://archive.ics.uci.edu/ml/datasets/Breast+Cancer+Wisconsin+\(Diagnostic\)](https://archive.ics.uci.edu/ml/datasets/Breast+Cancer+Wisconsin+(Diagnostic)).
- [326] Kay A. Tutorial on the Quantikz Package[EB/OL]. 2019: 599290 Bytes. DOI: 10.17637/rh.7000520.
- [327] Bezanson J, Edelman A, Karpinski S, et al. Julia: A Fresh Approach to Numerical Computing [J/OL]. *SIAM Review*, 2017, 59(1): 65-98. DOI: 10.1137/141000671.
- [328] Luo X Z, Liu J G, Zhang P, et al. Yao.jl: Extensible, Efficient Framework for Quantum Algorithm Design[J/OL]. *Quantum*, 2020, 4: 341. DOI: 10.22331/q-2020-10-11-341.
- [329] Deo N. Graph Theory with Applications to Engineering and Computer Science[M]. First ed. Mineola, New York: Dover Publications, 2016.
- [330] Smacchia P, Amico L, Facchi P, et al. Statistical mechanics of the cluster Ising model[J/OL]. *Physical Review A*, 2011, 84(2): 022304. DOI: 10.1103/PhysRevA.84.022304.
- [331] Grant E, Wossnig L, Ostaszewski M, et al. An initialization strategy for addressing barren plateaus in parametrized quantum circuits[J/OL]. *Quantum*, 2019, 3: 214. DOI: 10.22331/q-2019-12-09-214.
- [332] Erickson B J, Korfiatis P, Akkus Z, et al. Machine Learning for Medical Imaging[J/OL]. *RadioGraphics*, 2017, 37(2): 505-515. DOI: 10.1148/rg.2017160130.
- [333] Zhang X, Jiang W, Deng J, et al. Observation of a symmetry-protected topological time crystal with superconducting qubits[EB/OL]. 2021. <http://arxiv.org/abs/2109.05577>.
- [334] Mackenzie A P, Maeno Y. The superconductivity of Sr_2RuO_4 and the physics of spin-triplet pairing[J/OL]. *Reviews of Modern Physics*, 2003, 75(2): 657-712. DOI: 10.1103/RevModPhys.75.657.
- [335] Fu L, Kane C L. Superconducting Proximity Effect and Majorana Fermions at the Surface of a Topological Insulator[J/OL]. *Physical Review Letters*, 2008, 100(9): 096407. DOI: 10.1103/PhysRevLett.100.096407.
- [336] Stanescu T D, Sau J D, Lutchyn R M, et al. Proximity effect at the superconductor–topological insulator interface[J/OL]. *Physical Review B*, 2010, 81(24): 241310. DOI: 10.1103/PhysRevB.81.241310.
- [337] Alicea J. New directions in the pursuit of Majorana fermions in solid state systems[J/OL]. *Reports on Progress in Physics*, 2012, 75(7): 076501. DOI: 10.1088/0034-4885/75/7/076501.
- [338] Niu Y, Chung S B, Hsu C H, et al. Majorana zero modes in a quantum Ising chain with longer-ranged interactions[J/OL]. *Physical Review B*, 2012, 85(3): 035110. DOI: 10.1103/PhysRevB.85.035110.

REFERENCES

- [339] Tsvetlik A M. Majorana Fermion Realization of a Two-Channel Kondo Effect in a Junction of Three Quantum Ising Chains[J/OL]. Physical Review Letters, 2013, 110(14): 147202. DOI: 10.1103/PhysRevLett.110.147202.
- [340] Giuliano D, Sodano P, Tagliacozzo A, et al. From four- to two-channel Kondo effect in junctions of XY spin chains[J/OL]. Nuclear Physics B, 2016, 909: 135-172. DOI: 10.1016/j.nuclphysb.2016.05.003.
- [341] Lieb E, Schultz T, Mattis D. Two soluble models of an antiferromagnetic chain[J/OL]. Annals of Physics, 1961, 16(3): 407-466. DOI: 10.1016/0003-4916(61)90115-4.
- [342] Barouch E, McCoy B M, Dresden M. Statistical mechanics of the XY Model. I[J/OL]. Physical Review A, 1970, 2(3): 1075-1092. DOI: 10.1103/PhysRevA.2.1075.
- [343] Fendley P. Parafermionic edge zero modes in \mathbb{Z}_n -invariant spin chains[J/OL]. Journal of Statistical Mechanics, 2012, 2012(11): P11020. DOI: 10.1088/1742-5468/2012/11/P11020.
- [344] Backens S, Shnirman A, Makhlin Y, et al. Emulating Majorana fermions and their braiding by Ising spin chains[J/OL]. Physical Review B, 2017, 96(19): 195402. DOI: 10.1103/PhysRevB.96.195402.
- [345] Beenakker C W J. Universal Limit of Critical-Current Fluctuations in Mesoscopic Josephson Junctions[J/OL]. Physical Review Letters, 1991, 67(27): 3836-3839. DOI: 10.1103/PhysRevLett.67.3836.
- [346] Kwon H J, Sengupta K, Yakovenko V M. Fractional ac Josephson effect in p - and d -wave superconductors[J/OL]. The European Physical Journal B, 2004, 37(3): 349-361. DOI: 10.1140/epjb/e2004-00066-4.
- [347] Martinis J M, Osborne K. Superconducting Qubits and the Physics of Josephson Junctions [EB/OL]. 2004. <http://arxiv.org/abs/cond-mat/0402415>.
- [348] Chen C Z, Sun Q F, Wang F, et al. Detection of spinons via spin transport[J/OL]. Physical Review B, 2013, 88(4): 041405. DOI: 10.1103/PhysRevB.88.041405.
- [349] Zheng J, Bender S, Armaitis J, et al. Green's function formalism for spin transport in metal-insulator-metal heterostructures[J/OL]. Physical Review B, 2017, 96(17): 174422. DOI: 10.1103/PhysRevB.96.174422.
- [350] Wen X G. Symmetry-protected topological phases in noninteracting fermion systems[J/OL]. Physical Review B, 2012, 85(8): 085103. DOI: 10.1103/PhysRevB.85.085103.
- [351] Ryu S, Moore J E, Ludwig A W W. Electromagnetic and gravitational responses and anomalies in topological insulators and superconductors[J/OL]. Physical Review B, 2012, 85(4): 045104. DOI: 10.1103/PhysRevB.85.045104.
- [352] Fu L, Kane C L. Topological insulators with inversion symmetry[J/OL]. Physical Review B, 2007, 76(4): 045302. DOI: 10.1103/PhysRevB.76.045302.
- [353] Liu X J. Andreev Bound States in a One-Dimensional Topological Superconductor[J/OL]. Physical Review Letters, 2012, 109(10): 106404. DOI: 10.1103/PhysRevLett.109.106404.
- [354] Zhang F, Kane C L, Mele E J. Topological Mirror Superconductivity[J/OL]. Physical Review Letters, 2013, 111(5): 056403. DOI: 10.1103/PhysRevLett.111.056403.

REFERENCES

- [355] Zhang F, Kane C L. Anomalous topological pumps and fractional Josephson effects[J/OL]. Physical Review B, 2014, 90(2): 020501(R). DOI: 10.1103/PhysRevB.90.020501.
- [356] Fidkowski L, Kitaev A. Effects of interactions on the topological classification of free fermion systems[J/OL]. Physical Review B, 2010, 81(13): 134509. DOI: 10.1103/PhysRevB.81.134509.
- [357] Fidkowski L, Kitaev A. Topological phases of fermions in one dimension[J/OL]. Physical Review B, 2011, 83(7): 075103. DOI: 10.1103/PhysRevB.83.075103.
- [358] Peng Y, Vinkler-Aviv Y, Brouwer P W, et al. Parity Anomaly and Spin Transmutation in Quantum Spin Hall Josephson Junctions[J/OL]. Physical Review Letters, 2016, 117(26): 267001. DOI: 10.1103/PhysRevLett.117.267001.
- [359] Hui H Y, Sau J D. 8π periodic dissipationless ac Josephson effect on a quantum spin Hall edge via a quantum magnetic impurity[J/OL]. Physical Review B, 2017, 95(1): 014505. DOI: 10.1103/PhysRevB.95.014505.
- [360] Vinkler-Aviv Y, Brouwer P W, von Oppen F. \mathbb{Z}_4 parafermions in an interacting quantum spin Hall Josephson junction coupled to an impurity spin[J/OL]. Physical Review B, 2017, 96(19): 195421. DOI: 10.1103/PhysRevB.96.195421.
- [361] Zhang F, Kane C L. Time-Reversal-Invariant \mathbb{Z}_4 Fractional Josephson Effect[J/OL]. Physical Review Letters, 2014, 113(3): 036401. DOI: 10.1103/PhysRevLett.113.036401.
- [362] Orth C P, Tiwari R P, Meng T, et al. Non-Abelian parafermions in time-reversal-invariant interacting helical systems[J/OL]. Physical Review B, 2015, 91(8): 081406. DOI: 10.1103/PhysRevB.91.081406.
- [363] Kramers H A. Théorie générale de la rotation paramagnétique dans les cristaux[J]. Proceedings of the Royal Netherlands Academy of Arts and Sciences, 1930, 33(6-10): 959-972.
- [364] Hoffman S, Loss D, Tserkovnyak Y. Superfluid Transport in Quantum Spin Chains[EB/OL]. 2018. <http://arxiv.org/abs/1810.11470>.
- [365] Bernevig B A, Hughes T L, Zhang S C. Quantum spin Hall effect and topological phase transition in HgTe quantum wells[J/OL]. Science, 2006, 314(5806): 1757-1761. DOI: 10.1126/science.1133734.
- [366] König M, Wiedmann S, Brüne C, et al. Quantum spin Hall insulator state in HgTe quantum wells[J/OL]. Science, 2007, 318(5851): 766-770. DOI: 10.1126/science.1148047.
- [367] Fu L, Kane C L. Josephson current and noise at a superconductor / quantum-spin-Hall-insulator / superconductor junction[J/OL]. Physical Review B, 2009, 79(16): 161408. DOI: 10.1103/PhysRevB.79.161408.
- [368] Lopes P L S, Boutin S, Karan P, et al. Microwave signatures of the \mathbb{Z}_2 and \mathbb{Z}_4 fractional Josephson effects[J/OL]. Physical Review B, 2019, 99(4): 045103. DOI: 10.1103/PhysRevB.99.045103.
- [369] Deng M T, Vaitiekėnas S, Hansen E B, et al. Majorana bound state in a coupled quantum-dot hybrid-nanowire system[J/OL]. Science, 2016, 354(6319): 1557-1562. DOI: 10.1126/science.aaf3961.

REFERENCES

- [370] Liu C X, Sau J D, Stanescu T D, et al. Andreev bound states versus Majorana bound states in quantum dot-nanowire-superconductor hybrid structures: Trivial versus topological zero-bias conductance peaks[J/OL]. *Physical Review B*, 2017, 96(7): 075161. DOI: 10.1103/PhysRevB.96.075161.
- [371] Zhang H, Liu C X, Gazibegovic S, et al. Quantized Majorana conductance[J/OL]. *Nature*, 2018, 556(7699): 74-79. DOI: 10.1038/nature26142.
- [372] Möttönen M, Vartiainen J J, Pekola J P. Experimental Determination of the Berry Phase in a Superconducting Charge Pump[J/OL]. *Physical Review Letters*, 2008, 100(17): 177201. DOI: 10.1103/PhysRevLett.100.177201.
- [373] Kitaev A, Preskill J. Topological Entanglement Entropy[J/OL]. *Physical Review Letters*, 2006, 96(11): 110404. DOI: 10.1103/PhysRevLett.96.110404.
- [374] Horodecki R, Horodecki P, Horodecki M, et al. Quantum entanglement[J/OL]. *Reviews of Modern Physics*, 2009, 81(2): 865-942. DOI: 10.1103/RevModPhys.81.865.
- [375] Wootters W K. Entanglement of formation and concurrence[J/OL]. *Quantum Info. Comput.*, 2001, 1(1): 27-44. <http://dl.acm.org/citation.cfm?id=2011326.2011329>.
- [376] Osborne T J, Nielsen M A. Entanglement in a simple quantum phase transition[J/OL]. *Physical Review A*, 2002, 66(3): 032110. DOI: 10.1103/PhysRevA.66.032110.
- [377] Caianiello E R, Fubini S. On the algorithm of Dirac spurs[J/OL]. *Nuovo Cimento*, 1952, 9(12): 1218-1226. DOI: 10.1007/BF02782927.
- [378] Barouch E, McCoy B M. Statistical mechanics of the XY model. II. spin-correlation functions [J/OL]. *Physical Review A*, 1971, 3(2): 786-804. DOI: 10.1103/PhysRevA.3.786.
- [379] Calabrese P, Campostrini M, Essler F, et al. Parity Effects in the Scaling of Block Entanglement in Gapless Spin Chains[J/OL]. *Physical Review Letters*, 2010, 104(9): 095701. DOI: 10.1103/PhysRevLett.104.095701.
- [380] Sinova J, Valenzuela S O, Wunderlich J, et al. Spin Hall effects[J/OL]. *Reviews of Modern Physics*, 2015, 87(4): 1213-1260. DOI: 10.1103/RevModPhys.87.1213.
- [381] Dassonneville B, Ferrier M, Guéron S, et al. Dissipation and Supercurrent Fluctuations in a Diffusive Normal-Metal–Superconductor Ring[J/OL]. *Physical Review Letters*, 2013, 110(21): 217001. DOI: 10.1103/PhysRevLett.110.217001.
- [382] Murani A, Dassonneville B, Kasumov A, et al. Microwave Signature of Topological Andreev Level Crossings in a Bismuth-Based Josephson Junction[J/OL]. *Physical Review Letters*, 2019, 122(7): 076802. DOI: 10.1103/PhysRevLett.122.076802.
- [383] Aftergood J, Trif M, Takei S. Detecting spin current noise in quantum magnets with photons [J/OL]. *Physical Review B*, 2019, 99(17): 174422. DOI: 10.1103/PhysRevB.99.174422.
- [384] Lu Y, Zhang S, Zhang K, et al. Global entangling gates on arbitrary ion qubits[J/OL]. *Nature*, 2019, 572(7769): 363-367. DOI: 10.1038/s41586-019-1428-4.
- [385] Rota R, Minganti F, Ciuti C, et al. Quantum Critical Regime in a Quadratically Driven Nonlinear Photonic Lattice[J/OL]. *Physical Review Letters*, 2019, 122(11): 110405. DOI: 10.1103/PhysRevLett.122.110405.

REFERENCES

- [386] Rota R, Savona V. Simulating frustrated antiferromagnets with quadratically driven QED cavities[J/OL]. *Physical Review A*, 2019, 100(1): 013838. DOI: 10.1103/PhysRevA.100.013838.
- [387] Zajac D M, Hazard T M, Mi X, et al. Scalable gate architecture for a one-dimensional array of semiconductor spin qubits[J/OL]. *Physical Review Applied*, 2016, 6(5): 054013. DOI: 10.1103/PhysRevApplied.6.054013.
- [388] Khajetoorians A A, Wegner D, Otte A F, et al. Creating designer quantum states of matter atom-by-atom[J/OL]. *Nature Reviews Physics*, 2019, 1(12): 703-715. DOI: 10.1038/s42254-019-0108-5.
- [389] Yang K, Paul W, Phark S H, et al. Coherent spin manipulation of individual atoms on a surface [J/OL]. *Science*, 2019, 366(6464): 509-512. DOI: 10.1126/science.aay6779.
- [390] Pedernales J S, Di Candia R, Egusquiza I L, et al. Efficient Quantum Algorithm for Computing n -time Correlation Functions[J/OL]. *Physical Review Letters*, 2014, 113(2): 020505. DOI: 10.1103/PhysRevLett.113.020505.
- [391] Francis A, Freericks J K, Kemper A F. Quantum computation of magnon spectra[J/OL]. *Physical Review B*, 2020, 101(1): 014411. DOI: 10.1103/PhysRevB.101.014411.
- [392] Posske T, Thorwart M. Winding Up Quantum Spin Helices: How Avoided Level Crossings Exile Classical Topological Protection[J/OL]. *Physical Review Letters*, 2019, 122(9): 097204. DOI: 10.1103/PhysRevLett.122.097204.
- [393] Marchukov O V, Volosniev A G, Valiente M, et al. Quantum spin transistor with a Heisenberg spin chain[J/OL]. *Nature Communications*, 2016, 7: 13070. DOI: 10.1038/ncomms13070.
- [394] ANIS M S, Abraham H, AduOffei, et al. Qiskit: An Open-Source Framework for Quantum Computing[J/OL]. *Zenodo*, 2021. DOI: 10.5281/zenodo.2573505.
- [395] Developers C. Cirq[EB/OL]. 2021. DOI: 10.5281/zenodo.5182845.
- [396] Wang Q R, Gu Z C. Construction and Classification of Symmetry-Protected Topological Phases in Interacting Fermion Systems[J/OL]. *Physical Review X*, 2020, 10(3): 031055. DOI: 10.1103/PhysRevX.10.031055.
- [397] van de Wetering J. ZX-calculus for the working quantum computer scientist[EB/OL]. 2020. <http://arxiv.org/abs/2012.13966>.
- [398] Han Y, Huang G, Song S, et al. Dynamic Neural Networks: A Survey[J/OL]. *IEEE Transactions on Pattern Analysis and Machine Intelligence*, 2021: 1-1. DOI: 10.1109/TPAMI.2021.3117837.
- [399] Martyn J M, Rossi Z M, Tan A K, et al. Grand Unification of Quantum Algorithms[J/OL]. *PRX Quantum*, 2021, 2(4): 040203. DOI: 10.1103/PRXQuantum.2.040203.
- [400] Puel T O, Chesi S, Kirchner S, et al. Mixed-Order Symmetry-Breaking Quantum Phase Transition Far from Equilibrium[J/OL]. *Physical Review Letters*, 2019, 122(23): 235701. DOI: 10.1103/PhysRevLett.122.235701.
- [401] Xiong Y. Why does bulk boundary correspondence fail in some non-hermitian topological models[J/OL]. *Journal of Physics Communications*, 2018, 2(3): 035043. DOI: 10.1088/2399-6528/aab64a.
- [402] Tserkovnyak Y. Exceptional points in dissipatively coupled spin dynamics[J/OL]. *Physical Review Research*, 2020, 2(1): 013031. DOI: 10.1103/PhysRevResearch.2.013031.

REFERENCES

- [403] Riwar R P, Houzet M, Meyer J S, et al. Multi-terminal Josephson junctions as topological matter [J/OL]. *Nature Communications*, 2016, 7(1): 1-5. DOI: 10.1038/ncomms11167.
- [404] Giuliano D, Nava A, Sodano P. Tunable Kondo screening length at a Y-junction of three inhomogeneous spin chains[J/OL]. *Nuclear Physics B*, 2020, 960: 115192. DOI: 10.1016/j.nuclphysb.2020.115192.
- [405] Chatterjee S, Rodriguez-Nieva J F, Demler E. Diagnosing phases of magnetic insulators via noise magnetometry with spin qubits[J/OL]. *Physical Review B*, 2019, 99(10): 104425. DOI: 10.1103/PhysRevB.99.104425.
- [406] Dummit D S, Foote R M. *Abstract Algebra*[M]. Third ed. Hoboken, NJ: Wiley, 2003.
- [407] Dresselhaus M S, Dresselhaus G, Jorio A. *Group Theory: Application to the Physics of Condensed Matter*[M/OL]. Berlin Heidelberg: Springer-Verlag, 2008. DOI: 10.1007/978-3-540-32899-5.
- [408] Schutz B F. *Geometrical Methods of Mathematical Physics*[M]. First ed. Cambridge ; New York: Cambridge University Press, 1980.
- [409] Puchała Z, Miszcza J. Symbolic integration with respect to the Haar measure on the unitary groups[J/OL]. *Bulletin of the Polish Academy of Sciences: Technical Sciences*, 2017, 65(No 1): 21-27. DOI: 10.1515/bpasts-2017-0003.
- [410] Mezzadri F. How to generate random matrices from the classical compact groups[EB/OL]. 2007. DOI: 10.48550/arXiv.math-ph/0609050.
- [411] Wannier G H. Antiferromagnetism. The Triangular Ising Net[J/OL]. *Physical Review*, 1950, 79(2): 357-364. DOI: 10.1103/PhysRev.79.357.
- [412] Houtappel R M F. Order-disorder in hexagonal lattices[J/OL]. *Physica*, 1950, 16(5): 425-455. DOI: 10.1016/0031-8914(50)90130-3.
- [413] Kitaev A. Anyons in an exactly solved model and beyond[J/OL]. *Annals of Physics*, 2006, 321(1): 2-111. DOI: 10.1016/j.aop.2005.10.005.
- [414] Wannier G H. The Statistical Problem in Cooperative Phenomena[J/OL]. *Reviews of Modern Physics*, 1945, 17(1): 50-60. DOI: 10.1103/RevModPhys.17.50.
- [415] Husimi K, Syôzi I. The Statistics of Honeycomb and Triangular Lattice. I[J/OL]. *Progress of Theoretical Physics*, 1950, 5(2): 177-186. DOI: 10.1143/ptp/5.2.177.
- [416] Syozi I. The Statistics of Honeycomb and Triangular Lattice. II[J/OL]. *Progress of Theoretical Physics*, 1950, 5(3): 341-351. DOI: 10.1143/ptp/5.3.341.
- [417] Fender R P, Gallo E, Jonker P G. Jet-dominated states: An alternative to advection across black hole event horizons in ‘quiescent’ X-ray binaries[J/OL]. *Monthly Notices of the Royal Astronomical Society*, 2003, 343(4): L99-L103. DOI: 10.1046/j.1365-8711.2003.06950.x.
- [418] Narayan R, McClintock J E. Advection-dominated accretion and the black hole event horizon [J/OL]. *New Astronomy Reviews*, 2008, 51(10): 733-751. DOI: 10.1016/j.newar.2008.03.002.
- [419] Blandford R D, Znajek R L. Electromagnetic extraction of energy from Kerr black holes[J/OL]. *Monthly Notices of the Royal Astronomical Society*, 1977, 179(3): 433-456. DOI: 10.1093/mnras/179.3.433.

REFERENCES

- [420] Narayan R, McClintock J E. Observational evidence for a correlation between jet power and black hole spin[J/OL]. Monthly Notices of the Royal Astronomical Society: Letters, 2012, 419 (1): L69-L73. DOI: 10.1111/j.1745-3933.2011.01181.x.
- [421] Blandford R D, Payne D G. Hydromagnetic flows from accretion discs and the production of radio jets[J/OL]. Monthly Notices of the Royal Astronomical Society, 1982, 199(4): 883-903. DOI: 10.1093/mnras/199.4.883.
- [422] Fender R P, Gallo E, Russell D. No evidence for black hole spin powering of jets in X-ray binaries[J/OL]. Monthly Notices of the Royal Astronomical Society, 2010, 406(3): 1425-1434. DOI: 10.1111/j.1365-2966.2010.16754.x.

APPENDIX A MATHEMATICAL BACKGROUND

In this Appendix, we give some elementary introduction to the mathematics that is widely used in quantum computation, condensed matter theory and machine learning, which includes algebra theory, group theory, category theory, topology theory, measure theory, and probability theory^[118,406-408].

A.1 Algebra Theory

A.1.1 Dual Space

Given any vector space V over a field F , the dual space V^* is the set of all linear maps $\varphi : V \rightarrow F$, denoted as $\text{Hom}(V, F)$. The dual space V^* itself becomes a vector space over F when equipped with an addition and a scalar multiplication satisfying:

$$(\varphi + \psi)(x) = \varphi(x) + \psi(x), (a\varphi)(x) = a(\varphi(x)), \forall \varphi, \psi \in V^*, x \in V, a \in F. \quad (\text{A.1})$$

The pairing of $\varphi \in V^*$ and $x \in V$ is denoted by $\varphi(x) = \langle x, \varphi \rangle$. The bilinear mapping $\langle \cdot, \cdot \rangle : V^* \times V \rightarrow F$ is called a natural pairing.

A.1.2 Algebra Over Field

In mathematics, an algebra over a field is a vector space equipped with a bilinear product. Let K be a field and A be a vector space over K equipped with an additional binary operation $\cdot : A \times A \rightarrow A$, then A is an algebra over K if the following identities hold for all $\mathbf{x}, \mathbf{y}, \mathbf{z} \in A$, and all $a, b \in K$:

- (i) Right distributivity: $(\mathbf{x} + \mathbf{y}) \cdot \mathbf{z} = \mathbf{x} \cdot \mathbf{z} + \mathbf{y} \cdot \mathbf{z}$;
- (ii) Left distributivity: $\mathbf{z} \cdot (\mathbf{x} + \mathbf{y}) = \mathbf{z} \cdot \mathbf{x} + \mathbf{z} \cdot \mathbf{y}$;
- (iii) Compatibility with scalars: $(a\mathbf{x}) \cdot (b\mathbf{y}) = (ab)(\mathbf{x} \cdot \mathbf{y})$.

A.1.3 Lie Algebra

A Lie algebra is a vector space \mathfrak{g} over some field F together with a binary operation $[\cdot, \cdot] : \mathfrak{g} \times \mathfrak{g} \rightarrow \mathfrak{g}$ called the Lie bracket satisfying the following axioms:

- (i) Bilinearity: $\forall a, b \in F, \quad \forall \mathbf{x}, \mathbf{y}, \mathbf{z} \in \mathfrak{g},$

$$[a\mathbf{x} + b\mathbf{y}, \mathbf{z}] = a[\mathbf{x}, \mathbf{z}] + b[\mathbf{y}, \mathbf{z}], \quad [\mathbf{z}, a\mathbf{x} + b\mathbf{y}] = a[\mathbf{z}, \mathbf{x}] + b[\mathbf{z}, \mathbf{y}].$$

- (ii) Alternativity: $[\mathbf{x}, \mathbf{x}] = 0, \quad \forall \mathbf{x} \in \mathfrak{g}.$

(iii) Jacobi identity: $[x, [y, z]] + [z, [x, y]] + [y, [z, x]] = 0$, $\forall x, y, z \in \mathfrak{g}$.

(iv) Anticommutativity: $[x, y] = -[y, x]$, $\forall x, y \in \mathfrak{g}$.

Any Lie group gives rise to a canonically determined Lie algebra (the tangent space at the identity). The generators for the Lie algebra of the special unitary group $SU(2)$ are the Pauli matrices.

A.1.4 Clifford Algebra

The Clifford algebra $Cl(V, Q)$ is a unital associative algebra generated by a vector space V over a field K with a quadratic form $Q : V \rightarrow K$ subjected to the condition,

$$v^2 = Q(v)1, \quad \forall v \in V. \quad (A.2)$$

Since V is equipped with Q , in characteristic not equal to 2, then one can rewrite this fundamental identity in the form

$$uv + vu = 2\langle u, v \rangle 1, \quad \forall u, v \in V, \quad \langle u, v \rangle = \frac{1}{2} [Q(u+v) - Q(u) - Q(v)]. \quad (A.3)$$

There exist bases for V that are orthogonal. An orthogonal basis is one such that for a symmetric bilinear form

$$\langle e_i, e_j \rangle = 0, \quad i \neq j, \quad \langle e_i, e_i \rangle = Q(e_i). \quad (A.4)$$

When V is a finite-dimensional real vector space and Q is non-degenerate, $Cl(V, Q)$ may be identified by the label $Cl_{p,q}(\mathbb{R})$, indicating that V has an orthogonal basis with p elements with $e_i^2 = +1$, q with $e_i^2 = -1$, which holds the standard diagonal form:

$$Q(v) = v_1^2 + \dots + v_p^2 - v_{p+1}^2 - \dots - v_{p+q}^2. \quad (A.5)$$

The general element of the Clifford algebra $Cl_{0,3}(\mathbb{R})$ is given by

$$A = a_0 + a_1 e_1 + a_2 e_2 + a_3 e_3 + a_4 e_2 e_3 + a_5 e_3 e_1 + a_6 e_1 e_2 + a_7 e_1 e_2 e_3. \quad (A.6)$$

The Gamma matrices, $\{\gamma_0, \gamma_1, \gamma_2, \gamma_3\}$, also known as the Dirac matrices, are a set of matrices that they generate a matrix representation of the Clifford algebra $Cl_{1,3}(\mathbb{R})$ since $\gamma_0^2 = 1, \gamma_1^2 = \gamma_2^2 = \gamma_3^2 = -1$. Majorana operators are also elements of the Clifford algebra, which can be used to construct the representation of the braiding group^[140].

A.1.5 Exterior Algebra

Like the cross product, the exterior product is anti-commutative, $u \wedge v = -(v \wedge u)$ for all vectors u and v . Yet, unlike the cross product, the exterior product is associative. The

relationship between exterior algebra and tensor algebra is given by,

$$\omega \wedge \eta = \frac{(k+m)!}{k!m!} \text{Alt}(\omega \otimes \eta), \quad (\text{A.7})$$

where k, m is the blade of multi-vectors ω, η , respectively. In a vector space of dimension n , a blade of grade $n-1$ is called a pseudo-vector or an anti-vector. The exterior algebra $\bigwedge(\mathbb{R}^1)$ of is isomorphic to the dual numbers $a + b\epsilon$, where $a, b \in \mathbb{R}$ and $\epsilon^2 = 0$.

A.2 Group Theory

A.2.1 Homotopy Group

Give a base point a in the n -sphere S^n , for a topological space X with base point b , we define $\pi_n(X)$ to be the set of homotopy classes of maps $f : S^n \rightarrow X$ that map the base point a to the base point b , whose equivalence classes form a group. Intuitively, homotopy groups record information about the basic shape, or holes, of a topological space. The first and simplest homotopy group $\pi_1(X)$ is the fundamental group, which records information about loops in a space.

A.2.2 Homology Group

Homology was originally a rigorous mathematical method for defining and categorizing holes in a manifold. Intuitively, the k -th homology group $H_k(X)$ describes the number of k -dimensional holes in a topological space X . For example, the torus is defined as a product of two circles $T = S^1 \times S^1$. Since it has a single path-connected component, two independent one-dimensional holes and one two-dimensional hole as the interior of the torus, the homology groups are

$$H_k(T) = \begin{cases} \mathbb{Z} & k = 0, 2 \\ \mathbb{Z} \times \mathbb{Z} & k = 1 \\ \{0\} & \text{otherwise} \end{cases} \quad (\text{A.8})$$

The first homology group $H_1(X)$ is the Abelianization of the first homotopy group $\pi_1(X)$.

A.2.3 Lie Group

A Lie group is a group that is also a finite-dimensional smooth manifold, in which the group operations of multiplication and inversion are smooth maps

$$\mu : G \times G \rightarrow G \quad \mu(x, y) = xy, \quad (\text{A.9})$$

The two requirements can be combined to the single requirement that the mapping

$$(x, y) \mapsto x^{-1}y \quad (\text{A.10})$$

be a smooth mapping of the product manifold into G .

A.3 Category Theory

A category C consists of the following three mathematical entities:

- (i) A class $\text{ob}(C)$, whose elements are called objects a, b .
- (ii) A class $\text{hom}(C)$, whose elements are called morphisms $f : a \rightarrow b$.
- (iii) A binary operation \circ , called composition of morphisms with associativity $h \circ (g \circ f) = (h \circ g) \circ f$ and identity $1_x : x \rightarrow x$ such that $1_b \circ f = f = f \circ 1_a$, $\forall f : a \rightarrow b$.

Functor F is a structure-preserving map between categories C . A natural transformation $\eta_X : F(X) \rightarrow G(X)$ is a relation between two functors. Objects are considered atomic in a category. Namely, we do not know whether an object A is a set, a topology, or any other abstract concept. All information is based on the relationships between objects.

A.4 Topology Theory

A.4.1 Topological Space

A topological space is a set of points X , along with a function \mathcal{N} specifying a set of neighborhoods N for each point $x \in X$, satisfying the following axioms,

- (i) If $N \in \mathcal{N}(x)$, then $x \in N$.
- (ii) If $N \subseteq M \subseteq X$, then $x \in M$.
- (iii) If $N, M \in \mathcal{N}(x)$, then $x \in N \cap M$.
- (iv) $\forall N \in \mathcal{N}(x)$, there exist $M \in \mathcal{N}(x)$ such that $\forall y \in M, N \in \mathcal{N}(y)$.

All neighborhood-preserving functions, i.e. $f : (X, \mathcal{N}) \rightarrow (Y, \mathcal{M})$, follow that if $V \in \mathcal{M}(f(x))$, then $U = f^{-1}(V) \in \mathcal{N}(x)$.

A.4.2 Open Sets

We can alternatively define the topological space (X, T) via open sets X and its collection of subsets T :

- (i) $\emptyset \in T$ and $X \in T$.
- (ii) The union of any collection of sets in T is also in T .
- (iii) The intersection of any pair of sets in T is also in T .

A.4.3 Compactness

A topological space X is called compact if each of its open covers has a finite sub-cover. Namely, X is compact if for every collection C of open subsets of X such that $X = \bigcup_{x \in C} x$, there is a finite subset F of C such that $X = \bigcup_{x \in F} x$. Any finite topological space, including the empty set, is compact.

A.4.4 Hausdorff Space

A Hausdorff space, or T_2 space is a topological space where for any two distinct points there exist neighborhoods of each which are disjoint/separated from each other. The real numbers are a Hausdorff space. More generally, all metric spaces are Hausdorff.

A.5 Measure Theory

In mathematical analysis, a measure on a set is an approach to assign a number to each suitable subset of that set. Let X be a set and Σ a σ -algebra over X , a function $\mu : \Sigma \rightarrow \overline{\mathbb{R}}$, the extended real number line $\overline{\mathbb{R}} \equiv \mathbb{R} \cup \{\infty\} \cup \{-\infty\}$, is called a measure if it satisfies the following three properties:

- (i) Non-negativity: For all E in Σ , we have $\mu(E) \geq 0$.
- (ii) Null empty set: $\mu(\emptyset) = 0$.
- (iii) Countable additivity: For all countable collections $\{E_k\}_{k=1}^{\infty}$ of pairwise disjoint sets in Σ , we have
$$\mu\left(\bigcup_{k=1}^{\infty} E_k\right) = \sum_{k=1}^{\infty} \mu(E_k).$$

A measure space is a triple (X, Σ, μ) . A *measurable space* (X, Σ) consists of the first two components without a specific measure. A *null set* is a set $S \subset X$ such that $\mu(S) = 0$. A measure space (X, Σ, μ) is *complete* if and only if $S \subseteq N \in \Sigma$ and $\mu(N) = 0 \Rightarrow S \in \Sigma$.

A.5.1 σ -algebra

Let $\mathcal{P}(X)$ be a power set on X , a subset $\Sigma \subseteq \mathcal{P}(X)$ is called a σ -algebra if it has the following three properties:

- (i) Σ contains X as an element: $X \in \Sigma$.
- (ii) Σ is closed under complementation in X : $\forall S \in \Sigma, X \setminus S \in \Sigma$.
- (iii) Σ is closed under countable unions $\bigcup_{i=1}^{\infty} S_k$.

The smallest possible σ -algebra is $\{X, \emptyset\}$, the largest possible σ -algebra is the power set $2^X \equiv \mathcal{P}(X)$. The Borel algebra on X is the smallest σ -algebra containing all open sets.

A.5.2 Measurable Function

Let (X, Σ) and (Y, T) be measurable space, a function $f : X \rightarrow Y$ is said to be measurable if $\forall E \in T$, its pre-image $f^{-1}(E) = \{x \in X | f(x) \in E\} \in \Sigma$. The choice of σ -algebras in the definition above is sometimes implicit and left up to the context. For \mathbb{R}, \mathbb{C} , or other topological spaces, the Borel algebra is a common choice.

A.5.3 Haar Measure

Let (G, \cdot) be a locally compact Hausdorff topological group, $g \in G$ and $S \subseteq G$, the left Haar measure should satisfy the following properties:

- (i) Left-translation-invariant: $\mu(gS) = \mu(S)$ for every $g \in G$ and all Borel sets $S \subseteq G$.
- (ii) Finite on every compact set: $\mu(K) < \infty$ for all compact $K \subseteq G$.
- (iii) Outer regular on Borel sets $S \subseteq G$: $\mu(S) = \inf\{\mu(U) : S \subseteq U, U \text{ open}\}$.
- (iv) Inner regular on open sets: $\mu(U) = \sup\{\mu(K) : K \subseteq U, K \text{ compact}\}$.

The Haar integral of a function $f(U)$ over the unitary group $U(N)$ satisfies

$$\int d\mu(U) f(U) = \int d\mu(U) f(VU) = \int d\mu(U) f(UV), \quad (\text{A.11})$$

for any integrable function f and group elements $U, V \in U(N)$.

A.5.4 Unitary t-Design

Let $\{p_i, V_i\}$ be an ensemble of unitary operators, with unitary $V_i \in U(N)$ being sampled with probability p_i . The ensemble $\{p_i, V_i\}$ is a t -design if

$$\sum_i p_i V_i^{\otimes t} X (V_i^\dagger)^{\otimes t} = \int d\mu(U) U^{\otimes t} X (U^\dagger)^{\otimes t}. \quad (\text{A.12})$$

This definition implies that if $f(U)$ is a polynomial of at most degree t in the matrix elements of U and their conjugate U^* , then numerically averaging arbitrary matrix X over the *finite* ensemble will yield the same result as analytically averaging X over the *whole* unitary group with the respect to the Haar measure.

The t -th moment with respect to the Haar measure $d\mu(U)$ on the unitary group can be symbolically computed with the help of the Weingarten function^[409]. Yet, for more general problems of interest, there is no obvious way of integrating it analytically or obtain a closed form. Under this circumstance, we should turn to Monte Carlo integration. Drawing unitaries uniformly with respect to the Haar measure can be numerically achieved by a slightly modified QR decomposition^[410].

A.6 Probability Theory

A.6.1 Support

Let (X, Σ, μ) be a measure space, the support of μ is defined as the set of all points x in X for which every open neighborhood N_x of x has a positive measure:

$$\text{supp}(\mu) \equiv \{x \in X \mid x \in N_x \in \mathcal{T} \implies \mu(N_x) > 0\}. \quad (\text{A.13})$$

The support of a probability distribution can be regarded as the closure of the set of possible values of a random variable drawn from that distribution.

A.6.2 The Markov Process

A Markov process, or Markov chain, is a stochastic model describing a sequence of possible states in which the probability of each state depends only on the previous state. In mathematics, a stochastic matrix is a square matrix used to describe the transitions of a Markov chain. Each of its entries is a nonnegative real number representing a probability. If the probability of moving from i to j in one time step is $\Pr(j|i) = P_{i,j}$, the stochastic matrix P is given by using $P_{i,j}$ as the i -th row and j -th column element, e.g.

$$P = \begin{bmatrix} P_{1,1} & P_{1,2} & \cdots & P_{1,j} & \cdots & P_{1,N} \\ P_{2,1} & P_{2,2} & \cdots & P_{2,j} & \cdots & P_{2,N} \\ \vdots & \vdots & \ddots & \vdots & \ddots & \vdots \\ P_{i,1} & P_{i,2} & \cdots & P_{i,j} & \cdots & P_{i,N} \\ \vdots & \vdots & \ddots & \vdots & \ddots & \vdots \\ P_{N,1} & P_{N,2} & \cdots & P_{N,j} & \cdots & P_{N,N} \end{bmatrix}, \quad (\text{A.14})$$

where the total of the transition probability from a state i to all other states must be 1, $\sum_{j=1}^N P_{i,j} = 1$. Or equivalently, $P\mathbf{1} = \mathbf{1}$, where $\mathbf{1}$ is the N -dimensional vector of all ones. An initial probability distribution of states, specifying where the system might be initially and with what probabilities, is given as a row vector. A stationary probability vector π is defined as a distribution that does not change under application of the transition matrix, i.e. $\pi P = \pi$. For an irreducible aperiodic stochastic matrix, this vector is unique and can be computed by observing that for any i we have the following limit,

$$\lim_{k \rightarrow \infty} (P^k)_{i,j} = \pi_j. \quad (\text{A.15})$$

where π_j is the j -th element of the row vector π . Among other things, this says that the long-term probability of being in a state j is independent of the initial state i .

APPENDIX B THE HONEYCOMB ISING MODEL

In the statistical physics, classical Ising models are the simplest models that exhibit phase transitions and critical phenomena. The most popular one is the isotropic Ising ferromagnet model on the square lattice, which is exactly solved and shows a critical temperature at $k_B T_c/J = 2/\sinh^{-1}(1) = 2/\ln(1 + \sqrt{2}) \approx 2.26919$, where J is the exchange coupling strength and k_B is the Boltzmann constant^[152,156-157]. The classical isotropic Ising model on the honeycomb lattice has been studied by Wannier^[411] and Houtappel^[412] and obtained the critical temperature at $k_B T_c/J = 2/\cosh^{-1}(2) = 2/\ln(2 + \sqrt{3}) \approx 3.0373$. Apart from the *classical* Ising model, *quantum* spin models such as the Kitaev model^[413] on the honeycomb lattice has received tremendous attention, as this model contains intriguing anyonic excitations which can be used as the building-blocks for topological quantum computation. Recently, it is shown that the partition function of the classical Ising honeycomb model could be used to prove the barren plateau problem in the field of quantum machine learning^[158]. To this end, we elaborate on the technical details of transfer matrix technique.

B.1 Periodic Boundary Condition

B.1.1 General Case

The honeycomb lattice is labelled in a pattern as shown in Figure B.1, i.e., $N = 4nm$ vertices placed in $2m$ rows and $2n$ columns, whose Hamiltonian reads:

$$H(s_1, s_2, \dots, s_{4nm}) = -K_1 \sum_{(k,l)_1} s_k s_l - K_2 \sum_{(k,l)_2} s_k s_l - K_3 \sum_{(k,l)_3} s_k s_l, \quad (\text{B.1})$$

$$\begin{aligned} &= - \sum_{i=1}^{2m} \sum_{j=1}^{2n} \left[K_1 (s_{2i-1,2j-1} s_{2i,2j-1} + s_{2i,2j} s_{2i+1,2j}) \right. \\ &\quad \left. + K_2 (s_{2i-1,2j} s_{2i,2j} + s_{2i,2j-1} s_{2i+1,2j-1}) \right. \\ &\quad \left. + K_3 (s_{2i,2j} s_{2i,2j+1} + s_{2i+1,2j-1} s_{2i+1,2j}) \right]. \quad (\text{B.2}) \end{aligned}$$

The state of each vertex is indicated by its classical spin variable $s_k = \pm 1$. Here $(k, l)_{1,2,3}$ in Equation (B.1) denotes that the sum is to be taken over pairs of nearest neighbors with exchange couplings $K_{1,2,3}$ along three directions. Concretely, we index the Hamiltonian in the form of Equation (B.2) under the two-dimensional configuration of Figure B.1.

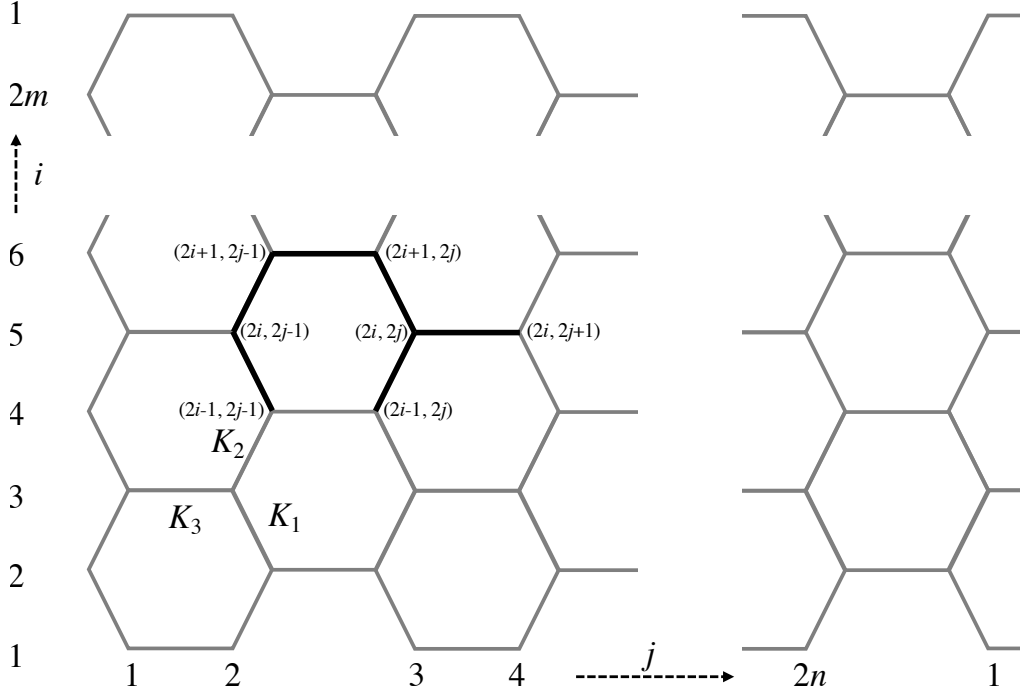


Figure B.1 Honeycomb lattice under periodic boundary condition.

Since each unit cell (full black lines) contains two rows, we denote μ_i ($i = 1, \dots, m$) to be the collection of all spin coordinates of the i -th unit cell along the i direction:

$$\mu_i = \bigcup_{j=1}^{2n} \{s_{2i,2j-1}, s_{2i+1,2j-1}, s_{2i,2j}, s_{2i+1,2j}\}. \quad (\text{B.3})$$

Under the periodic boundary condition along the i -direction, the calculation of the partition function is reduced to the trace of the powers of the transfer matrix^[154]:

$$\begin{aligned} Z &= \sum_{s_1=\pm 1} \sum_{s_2=\pm 1} \cdots \sum_{s_{4nm}=\pm 1} \exp[-\beta H(s_1, s_2, \dots, s_{4nm})] \\ &= \sum_{\mu_1} \cdots \sum_{\mu_m} \langle \mu_1 | \mathbb{P} | \mu_2 \rangle \langle \mu_2 | \mathbb{P} | \mu_3 \rangle \cdots \langle \mu_{m-1} | \mathbb{P} | \mu_m \rangle \langle \mu_m | \mathbb{P} | \mu_1 \rangle \\ &= \text{Tr } \mathbb{P}^m, \end{aligned} \quad (\text{B.4})$$

where we set $\beta = 1/k_B T = 1$ for simplicity. Since $|\mu_i| = 4n$, the dimension of \mathbb{P} is $2^{2n} \times 2^{2n}$. We can further decompose \mathbb{P} into four $2^{2n} \times 2^{2n}$ matrices under the representation of Pauli spin operators : $\mathbb{P} = (4 \sinh 2K_1 \sinh 2K_2)^n \mathbb{V}_0$, and $\mathbb{V}_0 = \mathbb{V}_1 \mathbb{V}_2 \mathbb{V}_3 \mathbb{V}_4$ with

$$\mathbb{V}_1 = \exp [K_1^* (\hat{\sigma}_1^x + \hat{\sigma}_3^x + \dots + \hat{\sigma}_{2n-1}^x) + K_2^* (\hat{\sigma}_2^x + \hat{\sigma}_4^x + \dots + \hat{\sigma}_{2n}^x)] , \quad (\text{B.5})$$

$$\mathbb{V}_2 = \exp [K_3 (\hat{\sigma}_2^z \hat{\sigma}_3^z + \hat{\sigma}_4^z \hat{\sigma}_5^z + \dots + \hat{\sigma}_{2n}^z \hat{\sigma}_1^z)] , \quad (\text{B.6})$$

$$\mathbb{V}_3 = \exp [K_2^* (\hat{\sigma}_1^x + \hat{\sigma}_3^x + \dots + \hat{\sigma}_{2n-1}^x) + K_1^* (\hat{\sigma}_2^x + \hat{\sigma}_4^x + \dots + \hat{\sigma}_{2n}^x)] , \quad (\text{B.7})$$

$$\mathbb{V}_4 = \exp [K_3 (\hat{\sigma}_1^z \hat{\sigma}_2^z + \hat{\sigma}_3^z \hat{\sigma}_4^z + \dots + \hat{\sigma}_{2n-1}^z \hat{\sigma}_{2n}^z)] , \quad (\text{B.8})$$

where another periodic boundary condition is imposed in Equation (B.6) and wraps the lattice into a torus. The duals of couplings are defined by $K_i^* = \frac{1}{2} \ln \coth K_i$. With Jordan-Wigner transformation and Clifford algebra^[154], the above \mathbb{V}_i matrices are reduced into $\omega_{\mu,\nu}(\theta) \in \text{SO}(4n)$ rotations under the Majorana basis, i.e. $\Omega_0^\pm = \Omega_1 \Omega_2^\pm \Omega_3 \Omega_4$, with

$$\Omega_1 = \prod_{j=1,3,\dots}^{2n-1} \omega_{2j-1,2j}(-2iK_1^*) \prod_{j=2,4,\dots}^{2n} \omega_{2j-1,2j}(-2iK_2^*), \quad (\text{B.9})$$

$$\Omega_2^\pm = \prod_{j=2,4,\dots}^{2n-2} \omega_{2j,2j+1}(-2iK_3) \cdot \omega_{4n,1}(\pm 2iK_3), \quad (\text{B.10})$$

$$\Omega_3 = \prod_{j=1,3,\dots}^{2n-1} \omega_{2j-1,2j}(-2iK_2^*) \prod_{j=2,4,\dots}^{2n} \omega_{2j-1,2j}(-2iK_1^*), \quad (\text{B.11})$$

$$\Omega_4 = \prod_{j=1,3,\dots}^{2n-1} \omega_{2j,2j+1}(-2iK_3). \quad (\text{B.12})$$

More specifically, $\omega_{\mu,\nu}(\theta)$ is the matrix that rotates by θ in the plane spanned by μ and ν in the $4n$ -dimensional Euclidean space. Since Ω_0^\pm belong to circulant Toeplitz matrices (see Equation (B.37) for details), the diagonalization of Ω_0^\pm is reduced to solve the eigenvalues of a 4×4 matrix $\mathbb{m}_k = \mathbb{a} + e^{+i\pi k/n} \mathbb{b} + e^{-i\pi k/n} \mathbb{c}$, where $k \in \{1, 3, 5, \dots, 2n-1\}$ for $\mathbb{U} = +1$, and $k \in \{0, 2, 4, \dots, 2n-2\}$ for $\mathbb{U} = -1$, and \mathbb{U} is the parity operator. Originally there are $4n$ eigenvalues in each subspace in the form of $\exp(\pm \theta_k^{\updownarrow})$ ^①, while it is sufficient for us to utilize $2n$ values of θ_k^{\updownarrow} to evaluate the partition function^②:

$$Z = (4 \sinh 2K_1 \sinh 2K_2)^{mn} \times \left[\sum_{\text{even "−"}} \exp\left(\frac{m}{2} \sum_{k=1,3,\dots}^{2n-1} \pm \theta_k^{\updownarrow}\right) + \sum_{\text{odd "−"}} \exp\left(\frac{m}{2} \sum_{k=0,2,\dots}^{2n-2} \pm \theta_k^{\updownarrow}\right) \right]. \quad (\text{B.13})$$

Moreover, the ratio of the largest and the second largest eigenvalues of \mathbb{V}_0 is

$$\frac{\lambda_1}{\lambda_2} = \exp\left(\frac{1}{2} \sum_{j=1}^n \theta_{2j-1}^{\updownarrow}\right) / \exp\left(\frac{1}{2} \sum_{j=1}^n \theta_{2j-2}^{\updownarrow}\right) \xrightarrow{n \rightarrow \infty} 1, \quad (\text{B.14})$$

for the ferromagnetic phase, and

$$\frac{\lambda_1}{\lambda_2} = \exp\left(\frac{1}{2} \sum_{j=1}^n \theta_{2j-1}^{\updownarrow}\right) / \exp\left(\frac{1}{2} \sum_{j=1}^n \theta_{2j-2}^{\updownarrow} - \theta_m\right) \xrightarrow{n \rightarrow \infty} \exp \theta_m, \quad (\text{B.15})$$

① Note that here θ_k^{\updownarrow} is a notation for a pair of θ_k solved from the same k , and the subscript \uparrow and \downarrow refer to the large and small one, respectively.

② This expression is only valid for the paramagnetic phase, as for the ferromagnetic phase, we should select even “−” for both of them.

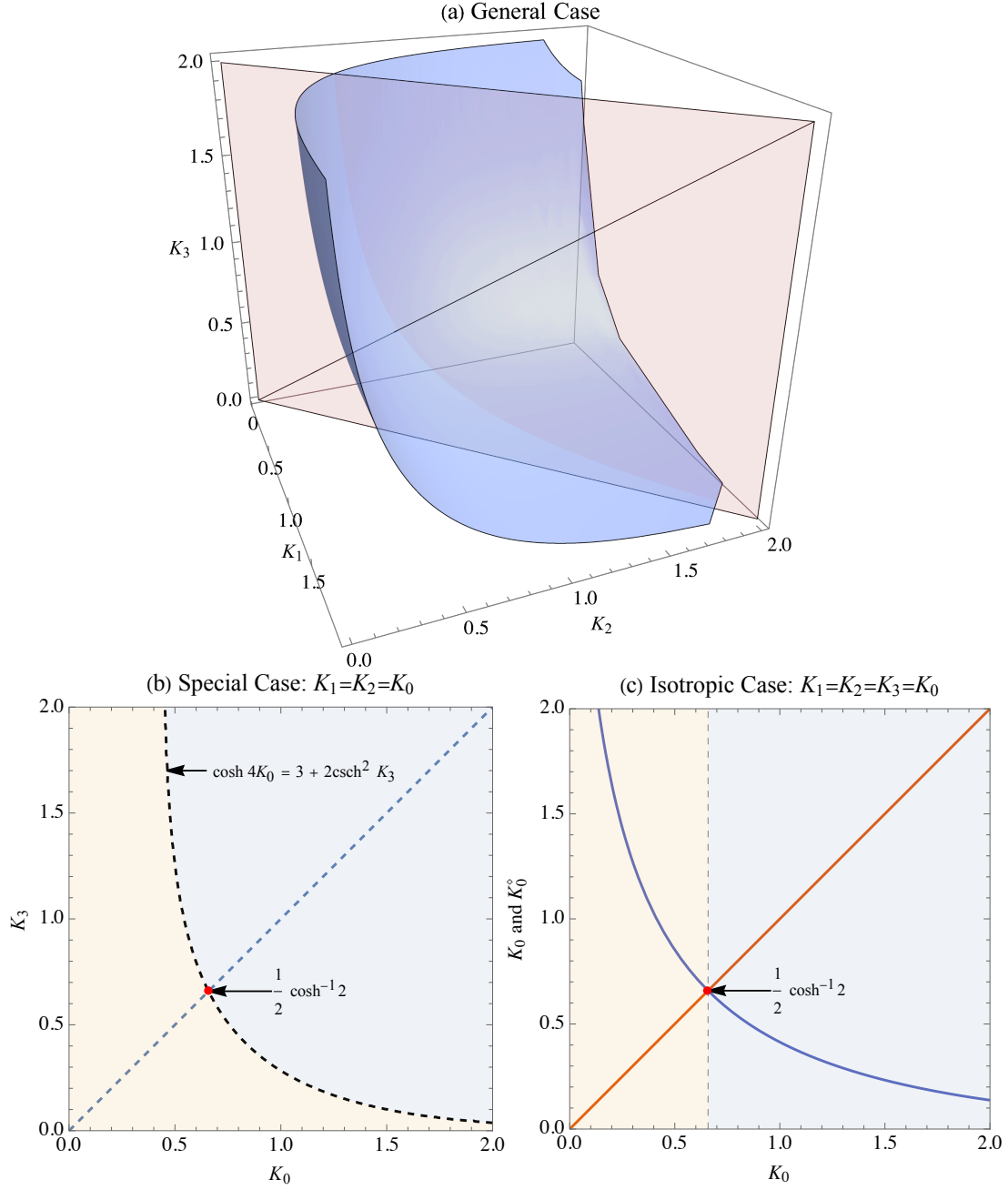


Figure B.2 Phase diagrams in different cases

for the paramagnetic phase, where θ_m is the element with the smallest real part in the set of $\{\theta_{2j-2}^{\uparrow\downarrow}\}_{j=1}^n$, which is calculated as $\cosh \theta_m = B_0 - \sqrt{B_0^2 - C_0}$,

$$B_0 = \cosh 2K_1^* \cosh 2K_2^* \cosh 2K_3 + \sinh 2K_1^* \sinh 2K_2^* + (\sinh 2K_1^* + \sinh 2K_2^*)^2 \sinh^2 2K_3/4, \quad (\text{B.16})$$

$$C_0 = (1 + \cosh 4K_1^* \cosh 4K_2^* + \sinh 4K_1^* \sinh 4K_2^* \cosh 2K_3)/2 + (3 + \cosh 4K_1^* \cosh 4K_2^* - 4 \sinh 2K_1^* \sinh 2K_2^*) \sinh^2 2K_3/4. \quad (\text{B.17})$$

The phase transition occurs at $\theta_m = 0$, which can be determined by $B_0 - \sqrt{B_0^2 - C_0} = 1 \Leftrightarrow 2B_0 = C_0 + 1$. Figure B.2(a) depicts the phase transition “surface” (blue) of the general case. To verify Equation (B.14) and Equation (B.15), we explicitly plot $\ln(\lambda_1/\lambda_2)$ as a function of n in Figure B.3 for both the ferromagnetic phase and the paramagnetic phase. It is seen that, under the thermodynamic limit $n \rightarrow \infty$, the ground state (λ_1 or λ_2) in the ferromagnetic phase is doubly degenerate due to the fact that the sum of all eigenvalues of $\mathbb{U} = \pm 1$ sectors converge. Since the unitary t -design calculation can be reduced into the scaling properties of $\ln(\lambda_1/\lambda_2)$, our results can be used to prove the presence and absence of barren plateau phenomena in tensor-network based machine learning models^[158].

B.1.2 Special Case: $K_1 = K_2$

In the special case of $K_1 = K_2 = K_0$, the solutions of θ_k^\updownarrow can be explicitly calculated as $\cosh \theta_k^\updownarrow = B_k \pm \sqrt{B_k^2 - C_k}$ with

$$B_k = \cosh 2K_3 \cosh 2K_0^\diamond - \sin^2(k\pi/2n) \sinh^2 2K_0^* \sinh^2 2K_3, \quad (\text{B.18})$$

$$C_k = \cosh^2 2K_3 + \sinh^2 4K_0 \cosh^4 K_3 - \cos(k\pi/n) \sinh^2 2K_0^* \sinh^2 2K_3, \quad (\text{B.19})$$

where we introduce $\cosh 2K_0^\diamond = \cosh^2 2K_0^* + \sinh^2 2K_0^* \cosh 2K_3$. The partition function in Equation (B.13) is reduced into ^①

$$Z = \frac{4^n (2 \sinh 2K_0)^{N/2}}{2} \left[\prod_{j=1}^n \cosh \left(\frac{m}{2} \theta_{2j-1}^\updownarrow \right) + \prod_{j=1}^n \sinh \left(\frac{m}{2} \theta_{2j-1}^\updownarrow \right) + \prod_{j=1}^n \cosh \left(\frac{m}{2} \theta_{2j-2}^\updownarrow \right) - \prod_{j=1}^n \sinh \left(\frac{m}{2} \theta_{2j-2}^\updownarrow \right) \right]. \quad (\text{B.20})$$

Under this specific circumstance, the smallest real part of $\{\theta_{2j-2}^\updownarrow\}_{j=1}^n$ is determined by

$$\cosh \theta_m = \cosh \theta_0^\updownarrow = B_0 - \sqrt{B_0^2 - C_0} = \cosh(2K_3 - 2K_0^\diamond) \Leftrightarrow \theta_m = |2K_3 - 2K_0^\diamond|.$$

The phase transition “line” is determined by $\theta_m = 0 \Leftrightarrow K_3 = K_0^\diamond \Leftrightarrow \cosh 4K_0 = 3 + 2\text{csch}^2 K_3$, which is shown in Figure B.2(b).

By use of Equation (B.14) and Equation (B.15), under the thermodynamic limit, $\ln(\lambda_1/\lambda_2) = \theta_m \approx 0.242385$ for $K_0 = K_1 = K_2 = K_3 = 0.6$. Likewise, as for the ferromagnetic phase, $\ln(\lambda_1/\lambda_2) = 0$, which are demonstrated in Figure B.3.

^① Again, this expression is only applicable to the paramagnetic phase, “−” of the last term should be replaced with “+” in the ferromagnetic phase.

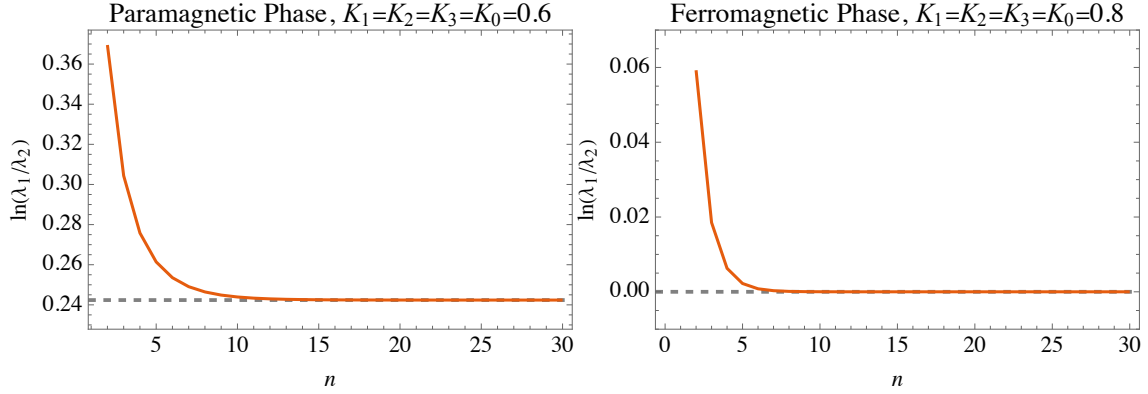


Figure B.3 Logarithms of eigenvalue ratio in two phases under periodic boundary conditions.

B.1.3 Isotropic Case: $K_1 = K_2 = K_3$

Here we briefly discuss the isotropic case of $K_1 = K_2 = K_3 = K_0$, we find that B_k , C_k are reduced into

$$B_k = \cosh 2K_0 \cosh 2K_0^\diamond - \sin^2(k\pi/2n), \quad (\text{B.21})$$

$$C_k = \cosh^2 2K_0 + \cosh^2 2K_0^\diamond - \cos(k\pi/n), \quad (\text{B.22})$$

and the solutions of $\theta_k^{\uparrow\downarrow}$ can be fully simplified as

$$\begin{aligned} \cosh \theta_k^{\uparrow\downarrow} = & \cosh 2K_0 \cosh 2K_0^\diamond - \sin^2(k\pi/2n) \\ & \pm \cos(k\pi/2n) \sqrt{\sinh^2 2K_0 \sinh^2 2K_0^\diamond - \sin^2(k\pi/2n)}, \end{aligned} \quad (\text{B.23})$$

where $\cosh 2K_0^\diamond = \cosh^2 2K_0^* + \sinh 2K_0^* \cosh 2K_0^*$. The expression of the partition function is the same as Equation (B.20), and $\theta_m = |2K_0 - 2K_0^\diamond|$. By use of the identity $(\cosh 2K_0 - 1)(\cosh 2K_0^\diamond - 1) = 1$ to solve $\theta_m = 0$, it is easy to observe that the phase transition point takes at $K_0 = K_0^\diamond = K_c = \frac{1}{2} \cosh^{-1} 2 = \frac{1}{2} \ln(2 + \sqrt{3}) \approx 0.658479$, which is plotted in Figure B.2(c) and agrees with the previous results in^[159,414-416].

B.2 Open Boundary Condition

B.2.1 Cylinder Case

In the cylinder boundary condition case, we need to rewrite Equation (B.6) to be

$$\mathbb{V}_1 = \exp \left[K_1^* (\hat{\sigma}_1^x + \hat{\sigma}_3^x + \dots + \hat{\sigma}_{2n-1}^x) + K_2^* (\hat{\sigma}_2^x + \hat{\sigma}_4^x + \dots + \hat{\sigma}_{2n}^x) \right], \quad (\text{B.24})$$

$$\mathbb{V}_2 = \exp \left[K_3 (\hat{\sigma}_2^z \hat{\sigma}_3^z + \hat{\sigma}_4^z \hat{\sigma}_5^z + \dots + \hat{\sigma}_{2n-2}^z \hat{\sigma}_{2n-1}^z) \right], \quad (\text{B.25})$$

$$\mathbb{V}_3 = \exp \left[K_2^* (\hat{\sigma}_1^x + \hat{\sigma}_3^x + \dots + \hat{\sigma}_{2n-1}^x) + K_1^* (\hat{\sigma}_2^x + \hat{\sigma}_4^x + \dots + \hat{\sigma}_{2n}^x) \right], \quad (\text{B.26})$$

$$\mathbb{V}_4 = \exp \left[K_3 (\hat{\sigma}_1^z \hat{\sigma}_2^z + \hat{\sigma}_3^z \hat{\sigma}_4^z + \dots + \hat{\sigma}_{2n-1}^z \hat{\sigma}_{2n}^z) \right], \quad (\text{B.27})$$

and Equation (B.10) to be

$$\Omega_1 = \prod_{j=1,3,\dots}^{2n-1} \omega_{2j-1,2j}(-2iK_1^*) \prod_{j=2,4,\dots}^{2n} \omega_{2j-1,2j}(-2iK_2^*), \quad (\text{B.28})$$

$$\Omega_2 = \prod_{j=2,4,\dots}^{2n-2} \omega_{2j,2j+1}(-2iK_3), \quad (\text{B.29})$$

$$\Omega_3 = \prod_{j=1,3,\dots}^{2n-1} \omega_{2j-1,2j}(-2iK_2^*) \prod_{j=2,4,\dots}^{2n} \omega_{2j-1,2j}(-2iK_1^*), \quad (\text{B.30})$$

$$\Omega_4 = \prod_{j=1,3,\dots}^{2n-1} \omega_{2j,2j+1}(-2iK_3). \quad (\text{B.31})$$

The bad news is that $\Omega_0 = \Omega_1\Omega_2\Omega_3\Omega_4$ is not circulant matrix anymore (see Equation (B.37) for details), while the good news is that we do not need to separate two subspaces, due to the disappearance of the parity operator. Thus the partition function is simply given by

$$Z = (4 \sinh 2K_1 \sinh 2K_2)^{mn} \sum_{\text{all } \pm} \exp \left(\frac{m}{2} \sum_{k=1}^n \pm \theta_k^{\uparrow\downarrow} \right). \quad (\text{B.32})$$

Furthermore, $\ln(\lambda_1/\lambda_2)$ is strictly equal to θ_m^o , which is the smallest real part in the set of $\{\theta_k^{\uparrow\downarrow}\}_{k=1}^n$. One should bear in mind that, here in the open boundary condition, θ_m^o is not a constant anymore, in stark contrast to θ_m in the periodic boundary condition. Nevertheless, from numerical results, we observe that

$$\frac{\lambda_1}{\lambda_2} = \exp \theta_m^o \xrightarrow{n \rightarrow \infty} \begin{cases} 1, & \text{ferromagnetic phase} \\ \exp \theta_m, & \text{paramagnetic phase} \end{cases}, \quad (\text{B.33})$$

which is shown in Figure B.4. In the paramagnetic phase of $K_1 = K_2 = K_3 = K_0 = 0.6$, $\ln(\lambda_1/\lambda_2)$ retains the same limit as Figure B.3(a), but with smoother curvature.

B.2.2 Free and Fixed Boundary

If the lattice are set with a freely open boundary (i.e., a surface with the honeycomb pattern), the partition function is no longer the trace of the powers of the transfer matrix \mathbb{P} , which can be seen in the following equation:

$$\begin{aligned} Z &= \sum_{\mu_1} \cdots \sum_{\mu_m} \langle \mu_1 | \mathbb{P} | \mu_2 \rangle \langle \mu_2 | \mathbb{P} | \mu_3 \rangle \cdots \langle \mu_{m-1} | \mathbb{P} | \mu_m \rangle \langle \mu_m | \mathbb{Q} | \mu_m \rangle \\ &= \sum_{\mu_1, \mu_m} \langle \mu_1 | \mathbb{P}^{m-1} \mathbb{Q} | \mu_m \rangle, \end{aligned} \quad (\text{B.34})$$

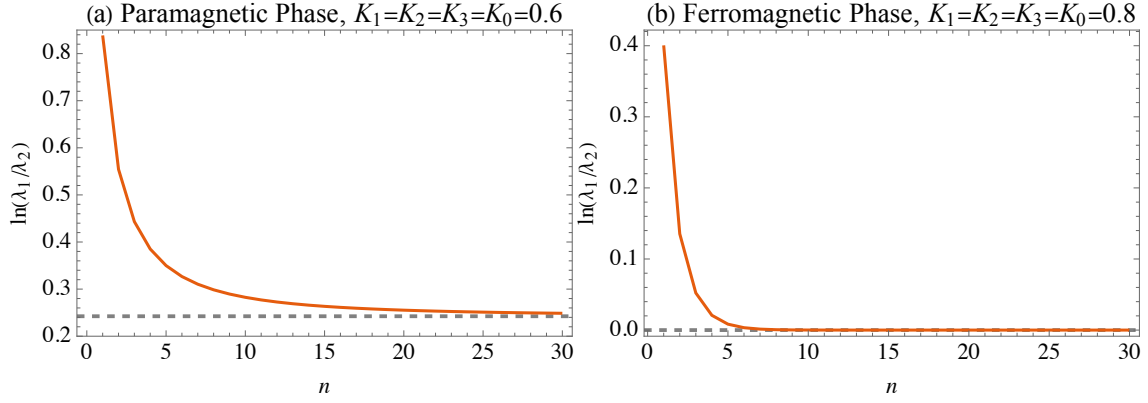


Figure B.4 Logarithms of eigenvalue ratio in two phases under open boundary conditions.

where \mathbb{Q} is a revised transfer matrix specific for the m -th row. Hence, under the freely open boundary condition, Z should be evaluated as the sum of all entries of the $2^{2n} \times 2^{2n}$ matrix $\mathbb{P}^{m-1} \mathbb{Q}$. This is not an eigenvalue problem any more, since the the sum of all entries relies on the specific basis we choose. However, we can select specific configurations of μ_1, μ_m to compute the partition function of the desired fixed boundary condition, although this approach is fairly inefficient. Nonetheless, if we are only interested in the transfer matrix \mathbb{P} itself, instead of fully solving out the partition function Z , we can still try to analyze the spectrum of \mathbb{P} under the fixed boundary condition.

B.3 Useful Identities

In order to simplify the analytical expressions, we utilize following mathematical identities between X , $X^* = 1/2 \ln \coth X$, $\cosh 2X^\diamond = \cosh^2 2X^* + \sinh^2 2X^* \cosh 2X$,

$$\sinh 2X \sinh 2X^* = \cosh 2X \tanh 2X^* = \tanh 2X \cosh 2X^* = 1,$$

$$\coth 2X = \cosh 2X^*, \quad \operatorname{sech} 2X = \tanh 2X^*, \quad \operatorname{csch} 2X = \sinh 2X^*,$$

$$\cosh 2X \sinh 2X^* = \cosh 2X^*, \quad \sinh 2X \cosh 2X^* = \cosh 2X,$$

$$2 \cosh 2X^\diamond = \coth^2 X + 1, \quad (\cosh 2X - 1)(\cosh 2X^\diamond - 1) = 1,$$

$$2 \cosh^2 X \cosh^2 2X^* = \cosh 2X \cosh 2X^\diamond,$$

$$\cosh^4 X \sinh^2 4X^* = \cosh^2 2X^\diamond, \quad 2 \cosh 2X \cosh 2X^\diamond + 1 = \sinh^2 2X \sinh^2 2X^\diamond.$$

To simplify the partition function from Equation (B.13) to Equation (B.20), we use

$$\sum_{\text{even } \alpha_j} \prod_{j=1}^n e^{\pm \alpha_j} = \frac{1}{2} \left(\prod_{j=1}^n 2 \cosh \alpha_j + \prod_{j=1}^n 2 \sinh \alpha_j \right), \quad (\text{B.35})$$

$$\sum_{\text{odd } \alpha_j} \prod_{j=1}^n e^{\pm \alpha_j} = \frac{1}{2} \left(\prod_{j=1}^n 2 \cosh \alpha_j - \prod_{j=1}^n 2 \sinh \alpha_j \right). \quad (\text{B.36})$$

B.4 Toeplitz Matrices

There are three kinds of $n \times n$ matrices found to be useful in our project, two of them are Toeplitz matrices with nicely analytical solutions of eigenvalues (the circulant one and the open one), while the rest one is more complicated,

$$\Omega_0^\pm = \begin{pmatrix} a & b & & \mp c \\ & c & a & b \\ & & c & a \\ & & & \ddots & b \\ \mp b & & & c & a \end{pmatrix}, \quad (\text{B.37})$$

$$\Omega = \begin{pmatrix} a & b & & 0 \\ & c & a & b \\ & & c & a \\ & & & \ddots & b \\ 0 & & & c & a \end{pmatrix}, \quad (\text{B.38})$$

$$\Omega_0 = \begin{pmatrix} c & b & & 0 \\ & b & a & b \\ & & b & a \\ & & & \ddots & b \\ 0 & & & b & d \end{pmatrix}. \quad (\text{B.39})$$

The eigenvalues of Ω_0^\pm is $\mathfrak{m}_k = a + e^{+i\pi k/n}b + e^{-i\pi k/n}c$, where $k \in \{1, 3, 5, \dots, 2n-1\}$ for Ω_0^+ , and $k \in \{0, 2, 4, \dots, 2n-2\}$ for Ω_0^- . And the eigenvalues of Ω is given by $\mathfrak{m}_k = a + 2\sqrt{bc} \cos[\pi k/(n+1)]$, where $k \in \{1, 2, \dots, n\}$. The last matrix Ω_0 is related to the cylinder open boundary condition, while the expressions of its eigenvalues are much more complicated. The explicit form of a, b, c, d can be found on the *Mathematica* notebook^[70].

APPENDIX C INTRODUCTION TO X-RAY BINARIES

Most stars in the Universe are in the form of binary systems. When one of these two stars evolves into a black hole or a neutron star, its companion star may provide materials to be accreted by the compact object and form an accretion disk and a jet outflow. This process will release large amounts of gravitational energy and radiate bright X-ray from the disk, which is known as X-ray binaries, together with radio emission from the jet. Generally, X-ray binaries are classified into black hole X-ray binaries and neutron star X-ray binaries, according to the type of central accretor. It is recently shown that the type of the central accretor can be identified directly based on the observational data via the machine learning approach^[181]. The radiation properties are quite different between black hole X-ray binaries and neutron star X-ray binaries: in the quiescent state, black hole X-ray binaries are typically two to three orders of magnitude less luminous than neutron star X-ray binaries^[417-418], but are more radio loud than neutron star X-ray binaries, which indicates that the jet power in black hole X-ray binaries will be more powerful than that in neutron star X-ray binaries; while in high/soft state, jet activities fade away for both black hole X-ray binaries and neutron star X-ray binaries.

In addition, how the relativistic jet forms, and how much power it carries are the key questions. It has long been suggested that relativistic jets could be powered not by the accretion flow but by the spin of the black hole^[419-420]. However, there is also another point of view that the jet power mainly comes from the accretion disk rather than the spin of the black hole due to the disk-jet coupling phenomenon from observation^[421-422]. Under the assumption that the origin of jet power is related to the internal energy of the inner disk, Shen et al.^[180] applied a magnetized, radiatively efficient thin disk model and the well-known radiatively inefficient accretion flow model to neutron star X-ray binaries and black hole X-ray binaries. They showed that the observed radio/X-ray correlations in X-ray binaries can be well understood by the disc–jet couplings. This theoretical model also provides a valuable guide for determining whether an X-ray binary system hosts a black hole or a neutron star.

ACKNOWLEDGEMENTS

First and foremost, I would like to acknowledge my advisor, Professor Dong-Ling Deng for his patient and kind guidance. Prof. Deng's broad knowledge of the quantum artificial intelligence field was an invaluable resource, helping me a lot in exploring various aspects, ranging from quantum information and computational complexity to AMO physics and topological phases of matter. In research, Prof. Deng always stays enthusiastic and approachable to answer me many subtle questions on numerical simulations and machine learning techniques. I have learned a lot from our discussions, and his detailed comments on scientific writing have substantially improved the quality of the papers covered in this dissertation. In daily life, Prof. Deng always keeps a low-profile and is willing to share his precious life experience with the students like a close friend. I feel very fortunate and blessed to have him as my advisor.

I also want to thank my co-supervisor, Prof. Mircea Trif, who has a vibrant attitude to research and life. Also as one of my close friends, his care and support are in every stage and aspect of my graduate life, even in the first few years when I was very dumb and behind. I clearly remember he taught me the fermionization of quantum spin systems, hand by hand, on the blackboard of his office. During the time of my rehabilitation when I still could not move alone, he visited my apartment and showed me how to obtain an effective low-field theory face-to-face. We have been keeping in touch to discuss the spin transport in open quantum systems online when he moved to Warsaw. It has always been very inspirational talking to him, and he generously shared with me a lot of his insights into various problems.

I am grateful to Prof. Luming Duan, Prof. Luyan Sun, Prof. Yipu Song, Prof. Haifeng Yu, and Prof. Dongning Zheng for accepting to be members of my PhD committee. I have also enjoyed the discussion with other faculty members at the Institute of Interdisciplinary Information Sciences, Prof. Yong Xu, Prof. Xiongfeng Ma, and Prof. Yu-Kai Wu. I would like to thank Prof. Zhao-Hui Wei for his guidance when I was a teaching assistant for the optimization theory course.

I am indebted to my undergraduate supervisor, Prof. Wei-Min Gu, for guiding me to unveil the beauty of the Universe and finish the manuscript about the black hole and neutron star X-ray binaries. When I told him I would like to switch my research direction

from high-energy astrophysics to quantum computation, he gave me generous support and encouraged me to enter this fledging field. During the period of COVID-19 quarantine, he still spent time revising my manuscript, which was later published in one of the longest established astronomical journals and became my first scientific paper.

During my PhD, I learned a lot from the members of the quantum artificial intelligence group, to whom I wish to express my gratitude. Special thanks to Zhide Lu, we worked in collaboration on the quantum architecture search project, which has become a vital part of this dissertation. The expansive brainstorming with Zidu Liu were very fruitful and led to nice collaborative efforts and many interesting results about quantum capsule networks. In addition to gourmet and photography, I have always enjoyed the discussion with Wenjie Jiang about the quantum continual learning and Floquet time crystals. I can always have countless discussions with Weikang Li about various aspects of life, ranging from electronic sports to quantum classifiers. It has been a wonderful experience discussing with Dr. Li-Wei Yu and Dr. Shun-Yao Zhang, whose humor often made my day. I still remember the evening when we were buried in an intense discussion about the non-Hermitian topological band theory and did not realize the first day of 2021 had just arrived. It was a pleasure to chat with Sirui Lu, Yuan-Hang Zhang, Dong Yuan, Si Jiang, Weiyuan Gong, Qi Ye, and Zizhao Han, whose enthusiasm has always been a great source of motivation.

Thanks to all my not yet mentioned friends who shared with me on topics beyond the scope of this dissertation. I am thankful to Dr. Tie-Cheng Guo for the time-order phase, Dr. Yan-Bin Yang for high-order topological insulators, Dr. You Zhou for the quantum resource theory, Dr. Pei Zeng for quantum key distribution, Yi-Hong Zhang for quantum channels, Zhi-Ling Wang for a flying Schrödinger's cat in a superconducting qubit, Wen-Ding Zhao, Wen-Tao Chen and Yue Jiang for the trapped ion setup, Quan-Xin Mei and Mu Qiao for the trapped ion theory, Xi-Yue Han for the quantum butterfly effect, Xiao-Xuan Pan for the superconducting setup, Ye-Fei Yu for the nitrogen-vacancy center, etc. Special thanks to Dr. Wei-Zhou Cai and Dr. Xue-Gang Li for the interesting discussions about the physics behind The Wandering Earth during the Chinese new year at Tsinghua.

I have also benefited from numerous collaborations and discussions outside Tsinghua. I want to thank Prof. Sias Hoffman for the beneficial discussions about the spin transport, Prof. Peter Zoller for the fractional Josephson effect, Prof. Tomasz Dietl for the spin current, Prof. Posske Thore for the quantum spin helices, Prof. Lei Wang for deep learn-

ACKNOWLEDGEMENTS

ing, Dr. Xun Gao for the cross-entropy benchmark, Dr. Fang-Li Liu for anyonic statistics, Dr. Shang-Jie Guo for giant atoms, Dr. Victor Fernandez Becerra for the spin pumping, etc. I am very appreciative of the hospitality of Tania Paul and Minh Nguyen Nguyen in Warsaw. I would not forget the hotpot we tried near the building of the Polish Academy of Sciences, which turned out to be Chuan-Chuan.

In the year of 2018, the deteriorating of my body and the leaving of kith and kin threw me into the darkest abyss, where I suffered extreme pain, both physically and psychologically. I have spent nearly one year doing rehabilitation. First and foremost, I would like to immensely express my gratitude to my loving parents, Bi-Lin Shen and Li-Yun He, who took care of my health for more than three months after the surgery in the summer. I am also thankful to my sister Xin-Xin Shen and other relatives for being always supportive. I am especially thankful to the doctors and the physiotherapists who brought me mirth during the period of rehabilitation in the hospital: Dr. Lin Xu, Dr. Xiao-Hong Mu, Chuan-Yu Hu, Hao Mi, Xiao-Yun Chen, Si-Fan Wang, Qin Zhang, Bao-Ming Hao, Liang Lv. I will never forget the time when I celebrated the new year of 2019 with my wardmates in the hospital. Specifically, I would like to thank the backbone members of the Student Society for Accessibility Development Study, including but not limited to, Xiao-Peng Zhu, Bin Chen, Meng-Nan Jiang, and Dr. Xiao-Yuan Yi. I also thank the administration staffs at the Institute of Interdisciplinary Information Sciences, Xia-Min Lv, Shuai Sun, Yu-Chan Shang, Jia Ma, Jia Liu and Di Sun, who gave me generous support during the whole graduate life. I would also like to sincerely thank my friends who gave me hands during this exhausting period, including but not limited to, Tian-Liang Bi, Fang-Jun Cheng, Shu-Yan Dong, Yi-Ze Dong, Hao He, Xiao-Cong Hu, Hong-Yi Huang, Bing-Yan Jiang, Yuan-Qi Li, Wei-Yu Shen, Yi Shen, Ze-Yu Shen, Yu Shi, Hang-Yu Si, Siddhant Singh, Yan-Jun Tian, Tsek-Peng Tok, Jia-Shen Wang, Xun Wang, Yu-Kun Wu, Qiong-Cong Xu, Xue-Chun Xu, Wen-Tan Xue, Shu-Xi Ye, Sheng-Tao Zheng, Bo-Cheng Zhu, etc. Special thanks to the one who accompanied me to the Mayday's concert hosted at the Beijing Bird's Nest. Without any of them, I would never escape from the endless swamp and come back to the normal research life.

I've seen things many people wouldn't believe. Supercurrents dance along the junction of quantum spin chains. I wondered X-ray shines in the dark near V404 Cygnus. All those moments will be lost in time, like gravitational waves in the Universe.

Time to recommence.

声 明

本人郑重声明：所呈交的学位论文，是本人在导师指导下，独立进行研究工作所取得的成果。尽我所知，除文中已经注明引用的内容外，本学位论文的研究成果不包含任何他人享有著作权的内容。对本论文所涉及的研究工作做出贡献的其他个人和集体，均已在文中以明确方式标明。

签 名：_____ 日 期：_____

RESUME

个人简历

1995 年 6 月 8 日出生于福建省漳州市诏安县。

2013 年 9 月考入厦门大学物理科学与技术学院天文学系。

2017 年 7 月本科毕业并获得理学学士学位。

2017 年 9 月免试进入清华大学交叉信息研究院攻读物理学博士至今。

在学期间完成的相关学术成果

- [1] Lu Z*, Shen P X*, Deng D L. Markovian Quantum Neuroevolution for Machine Learning [J/OL]. Physical Review Applied, 2021, 16(4): 044039. DOI: 10.1103/PhysRevApplied.16.044039.
- [2] Shen P X, Hoffman S, Trif M. Theory of topological spin Josephson junctions [J/OL]. Physical Review Research, 2021, 3(1): 013003. DOI: 10.1103/PhysRevResearch.3.013003.
- [3] Shen P X, Jiang W J, Li W K, et al. Adversarial learning in quantum artificial intelligence [J/OL]. Acta Physica Sinica, 2021, 70(14): 140302-140302-12. DOI: 10.7498/aps.70.20210789.
- [4] Liu Z*, Shen P X*, Li W, et al. Quantum Capsule Networks [EB/OL]. 2022. <http://arxiv.org/abs/2201.01778>.
- [5] Shen P X, Gu W M. Accretion disc–jet couplings in X-ray binaries [J/OL]. Monthly Notices of the Royal Astronomical Society, 2020, 495 (2): 2408-2415. DOI: 10.1093/mnras/staa1349.

COMMENTS FROM THESIS SUPERVISOR

沈培鑫同学的论文主要研究量子机器学习与信息处理相关问题，这对于展示近期量子技术的优越性有着重要的意义。

在量子机器学习方面，论文引入了一种量子神经进化算法，该算法可以自动地为不同的机器学习任务找到接近最优的量子神经网络。在嘈杂中等规模量子器件时代，搜索具有较小深度的、性能良好的量子线路对于量子机器学习实验演示乃至实际应用都至关重要。为展示此算法的优势，论文设计了一个量子分类器进行手写字体和拓扑态的识别。其结果展示了神经进化算法在量子架构搜索中的巨大潜力。此项工作由沈培鑫与合作者共同完成。

在量子信息处理方面，论文详细讨论了一维量子 Ising-XY-Ising 自旋链的自旋输运。通过运用对称性分析、数值模拟和解析方法，论文揭示了几种与涌现的马约拉纳费米子有关的分数自旋约瑟夫森效应。论文进一步分析了自旋电流对自旋纠缠的影响，并提出使用腔量子电动力学装置中的色散读出技术来探测自旋约瑟夫森效应。此项工作由沈培鑫在导师的指导下独立完成。

此外，该博士论文还回顾了量子机器学习中一些著名的量子算法和量子模拟技术，并展望了一些新的量子机器学习架构和算法。

总的来说，该博士论文内容充实详细，选题紧靠当前量子物理研究前沿，所得成果具有较高的原创性。论文涉及量子信息与计算，机器学习，凝聚态物理等领域，具有很强的交叉属性。作者对论文所涉及的领域有广泛的了解，引述全面，写作能力突出。总体而言，这是一篇非常优秀的博士论文。

RESOLUTION OF THESIS DEFENSE COMMITTEE

量子计算与机器学习的快速发展催生了一个新的研究前沿——量子机器学习。在有噪声中等规模量子器件时代，搜索具有较小深度、性能良好的量子线路对于量子机器学习实验演示及实际应用都至关重要。沈培鑫同学围绕量子机器学习的架构优化和量子自旋链中的信息处理两个问题，开展了系统的理论研究，取得了如下创新性成果：

1、引入了一种量子神经进化算法，该算法可以自动地为不同的机器学习任务找到接近最优的量子神经网络。

2、设计了一个量子分类器进行手写字体和拓扑态的识别，并展示了神经进化算法在量子架构搜索中的潜力。

3、系统研究了一维量子 Ising-XY-Ising 自旋链的自旋输运，揭示了自旋电流对自旋纠缠的影响。

论文工作表明沈培鑫同学在量子计算、凝聚态物理、机器学习等领域具有扎实的基础，和很强的独立科研能力。论文观点清晰，格式规范，逻辑严密，结论合理，文献引述全面。答辩条理清晰，论述严谨，回答问题精炼。经答辩委员会无记名投票，一致同意通过沈培鑫同学的博士学位答辩，并建议授予理学博士学位。